EXPERIMENTAL CONSTRAINTS ON THE GENERATION AND EVOLUTION OF MID-OCEAN RIDGE BASALTS

by

Rosamond Joyce Kinzler

s.B. Geology, Massachusetts Institute of Technology
(1984)
s.M. Geology, Massachusetts Institute of Technology
(1985)

Submitted to the Department of Earth, Atmospheric and Planetary Sciences in partial fulfillment of the requirements for the degree of

DOCTOR OF PHILOSOPHY

in

GEOLOGY

at the

Massachusetts Institute of Technology

May, 1991

Signature of Author: _____
Department of Earth, Atmospheric, &
Planetary Sciences, M.I.T.
May, 1991

Certified by: _____
Dr. Timothy L. Grove
Thesis Supervisor

Accepted by: _____
Dr. Thomas H. Jordan
Chairman, Departmental Committee on Graduate Students

EXPERIMENTAL CONSTRAINTS ON THE GENERATION AND EVOLUTION OF MID-OCEAN RIDGE BASALTS

by

Rosamond Joyce Kinzler

Submitted to the Department of Earth, Atmospheric and Planetary Sciences in partial fulfillment of the requirements for the degree of

Doctor of Philosophy

May, 1991

ABSTRACT

Experimental petrology and major element chemistry are used to infer the melting processes that operate in the upper oceanic mantle to yield basaltic magma, and the subsequent cooling processes by which these magmas chill to form the oceanic crust.

THE PRIMARY MAGMAS OF MID-OCEAN RIDGE BASALTS

This paper reports experiments carried out between 9 and 16 kbar (0.9 - 1.6 GPa) using natural, primitive mid-ocean ridge basalt (MORB) compositions and synthetic analogs of MORB to investigate the effects of pressure, temperature and variable bulk chemistry on the composition of liquids multiply saturated with the minerals present in the upper oceanic mantle: olivine, orthopyroxene, augite and plagioclase or spinel. For this low-variance, 5-phase assemblage, expressions involving pressure, liquid NaK# $(Na_2O+K_2O)/(Na_2O+K_2O+CaO)$, Mg# $(Mg/[Mg+Fe^{2+}]$; total iron as Fe^{2+}) and wt. % TiO_2 predict temperature and major element compositions of magmas produced by melting spinel and plagioclase lherzolites over the pressure range of 0.001 - 16 kbar. The expressions are derived using data from this experimental study and published experimental studies that report compositions of glasses coexisting with olivine, orthopyroxene, augite and plagioclase and/or spinel. A two-part quantitative framework for evaluating the systematics of MORB chemistry is presented: 1) for estimating melts from a depleted MORB-mantle source as a function of pressure and changing mantle composition, and 2) for evaluating the effects of fractional crystallization on these

estimated primary melts over a range of pressures corresponding to depths in the uppermost oceanic mantle and in the oceanic crust. This framework yields the following observations: the total extents of depletion achieved by the decompression melting process range from ~5 - 20 %, the range of pressures of melting is relatively narrow, from 8 - 15 kbar, and much of the variation in major element chemistry observed in MORB can be explained by melting a similar depleted MORB-mantle source (primitive upper mantle, [Hart and Zindler, 1986] - ~1 % melt). The inverse correlation between Na_2O and FeO observed by Klein and Langmuir (1987) in the global MORB data set is also present in the array of the estimated primary magmas of MORB. The operation of fractional crystallization over a range of pressures is responsible for the rotation of the steep, primary Na_2O-FeO trend to the more shallow trend observed in the evolved (MgO = 8.00 wt.%) MORB. The dominant compositional vector associated with mixing between melts generated at different pressures within the same decompression melting 'column' resembles the compositional vectors associated with varying extent of melting and pressure of melting (i.e., an inverse correlation between Na_2O and FeO in the mixed melts). The mixing vector is not similar to the 'local' trends observed by Klein and Langmuir (1989). These 'local' trends are identified within MORB sampled over a limited portion of mid-ocean ridge, and are characterized by a positive correlation between Na_2O and FeO, and an inverse correlation between Na_2O and SiO_2. Fractional crystallization of estimated primary magmas over a range of pressures (0.001 - 4 kbar, and possibly greater) generates variability in derivative magmas that resembles the local trends observed at several areas along the mid-Atlantic ridge. The correlation between pressure of melting (10 - 15 kbar), extent of melting (3 - 20 %) and Na_2O-FeO systematics observed by Klein and Langmuir (1987, 1989) generally holds for normal (not hot-spot influenced) MORB. The primary magmas of some low-Na_2O, hot-spot MORBs may have been derived by melting a more fertile mantle source, to a greater extent, at similar pressures to the intermediate -Na_2O, normal MORB.

MAGMATIC DIVERSITY AT THE OVER-LAPPING SPREADING CENTER AT $11^{O}45'$ N ON THE EAST PACIFIC RISE

Major element chemical data, experimentally determined phase equilibria and geological observations obtained with the ALVIN submersible are combined to investigate the petrological processes responsible for generating the compositional diversity sampled in lavas from both rifts of the $11^{O}45'$N over-lapping spreading center (OSC) on the East Pacific Rise (EPR). Lavas on the tectonically active, migrating, eastern rift of the OSC show a greater diversity in major element composition relative to those on the western rift, which is less active volcanically and tectonically (north of $11^{O}45'$N). The geochemical signatures of the lavas erupted on both the eastern and western rifts of the OSC require the operation of crystallization of magmas along the olivine - augite - plagioclase - liquid boundary, however, few, if any of the lavas erupted at the OSC contain augite as a phenocryst phase. The diversity of major element compositions of the lavas sampled from the western rift is well explained by simple

mixing between moderately evolved magmas saturated with olivine + augite + plagioclase near 1-atm., and parental magma. The resulting mixed magma is no longer saturated with augite at 1-atm., however the magma composition retains the signature of the fractionation of augite contributed by the evolved component in the mixture. The major element compositions of lavas sampled from the eastern rift are well explained by fractionation from parental magmas similar to the primitive lavas sampled at the eastern rift and further to the north on the EPR, at pressures equivalent to ~3 - ~6 km depth. Although these magmas appear to have evolved by fractionation of olivine + plagioclase + augite, upon emplacement to shallower pressures and eruption, they are no longer saturated with augite and are thus erupted with only olivine and plagioclase as phenocryst or micro-phenocryst phases. The diversity of chemical compositions erupted during the recent history of the eastern rift and the lack of a continuous seismic reflector along this portion of the EPR preclude the existence of a continuous 'magma chamber' beneath the eastern rift of the OSC, however, the occurrence of lavas of similar major element chemistry and similar age along approximately 25 km of ridge requires extensive lateral injection from the source of magma differentiation, possibly at pressures equivalent to near the base of the oceanic crust.

Thesis Supervisor: Dr. Timothy L. Grove
Professor of Geology

TABLE OF CONTENTS

LIST OF FIGURES

LIST OF TABLES

ACKNOWLEDGEMENTS

You will find something more in woods than in books. Trees and stones will teach you that which you can never learn from masters.

- ST. BERNARD OF CLAIRVAUX

- except that it is often through the skills we acquire from masters, combined with the support of our peers and loved ones, that we learn to approach the 'trees and stones' with confidence and creativity. First and foremost, I gratefully acknowledge my advisor and friend, Tim Grove, for being my mentor through nine years (and three degrees) at M.I.T. Several other 'masters' have contributed to my graduate school experience. Bill Bryan introduced me to the petrology of ocean floor basalts, provided guidance and the opportunity to do field work through ocean-going scientific research, and through his expertise in oceanic basalts has contributed greatly to the research presented in this thesis. Fred Frey's trace element geochemistry course improved my ability to think critically about published scientific work, and through discussion and his presence on my thesis committee, Fred has also contributed significantly to this thesis. Encountering Tom Jordan within the final year of the work presented here has been both challenging and rewarding; one definitely keeps learning right up to the end of this PhD process! Dave Walker provided a fresh and challenging perspective as the 'out-side' member on my thesis committee and the work presented in this revised version benefitted from his contribution. Steve Recca's expert advice on matters from electron microprobes to computers was a welcome contribution, not to mention his excellent shoulder rubs and generally good-humored presence.

I also acknowledge the support and considerable input from several graduate students. Michael Baker, Tom Juster, Karen Bartels and Tom Sisson shared advice, elation and commiseration over the challenges of experimental petrology. Early on Michael welcomed even the dumbest question (and continues to do so, to this day); Tom J. is an invaluable resource for fun and challenging scientific discussion, we got through J.B.T.'s course together; Tom S. is always available for careful, considered discussions about tricky problems, with just the right touch of humorous insight, and Karen and I shared the joys of riding the red-line and trudging through Harvard Yard at all hours to put up piston-cylinder experiments. The active participation of Tom Wagner and Glenn Gaetani in our experimental petrology lab have been welcome, light-hearted additions to the final stages of the research presented here. Matt Cordery patiently and expertly integrated some aspects of the work in this thesis into his research, teaching me much about mantle dynamics in the process of doing so. Just as important, however, has been the support Matt has provided over the past 9 months, as we have been 'through this' together.

I acknowledge my family's example through work ethic, as well as their support and enthusiasm for this achievement (especially at the points when my enthusiasm had dwindled considerably); in particular my mother, Kennen Kinzler, who consistently demonstrated the ability to empathize with a process relatively foreign to her. I hope to honor my grandparents, Robert H. Pratt and Frances M. Kinzler with this work. My parents-in-law, Karin and Bill Bespolka, have provided a considerable amount of care and support throughout the graduate school experience. I dedicate this thesis to my brother, Karl Kinzler, who's love and confidence in me will remain with me always.

Carl Bespolka has consistently, lovingly and patiently supported me throughout the PhD process. His sense of humor and his care and respect are gifts that I gratefully acknowledge and cherish.

INTRODUCTORY NOTE

This thesis consists of two independent and free-standing chapters that pertain to processes of melting in the upper oceanic mantle and crystallization of basaltic magma in the upper oceanic mantle and oceanic crust. Mid-ocean ridge basalts have long been recognized as potential 'windows' through which we may 'see' processes of melt generation in and chemical compositions of the upper oceanic mantle. Observable products of the processes that yield mid-ocean ridge basalt include the thickness and rate of generation of the oceanic crust, and the chemical compositions and mineral assemblages of the mid-ocean ridge basalts and depleted abyssal peridotites. Mid-ocean ridge basalts and depleted abyssal peridotites are direct samples of the end-products of the melting and freezing process that forms oceanic crust. The thickness and rate of formation of the oceanic crust informs us of the volumes and rates of magma generation in the upper oceanic mantle. Samples of abyssal peridotite contain information on the nature of the melting processes. Pieces of the oceanic crust (mid-ocean ridge basalt) contain information on the composition(s) of the upper oceanic mantle, the nature and depth(s) of the melting process(es), and the processes that occur after magma formation, during the freezing of the magma to form the oceanic crust.

The purpose of the research presented in the two chapters of this thesis is to contribute to the framework required to extract information about processes of thermal evolution and chemical mass transfer in the earth's upper mantle from data on the thickness and chemistry of the oceanic crust. The approach taken in Chapters I and II is fourfold: 1) to examine the melting process directly by carrying out melting experiments in the laboratory on analogs of mantle material at pressures and temperatures similar to those that occur in the earth up to approximately 50 km depth, 2) to examine the freezing process directly by carrying out melting experiments in the laboratory on natural basalt at ambient pressures, 3) to relate the experimental data generated in the

laboratory to the chemical compositions of basalts using the framework of phase equilibria, and 4) to use geologic observations of basalt occurrences at mid-ocean ridges to form models of magma generation and freezing.

Chapter I provides new experimental data on the pressures and temperatures at which upper-mantle peridotite melts, and on the composition of melts that are generated by this melting process. Quantitative descriptions of the phase equilibria that control melt generation from mantle peridotite are presented that are constrained by the data presented in this study, as well as data from the literature. Chemical variations observed in mid-ocean ridge basalt from the global data set are then used in the context of the phase equilibria to infer depths and volumes of melt generation required to produce these basalts. The basalts we sample have been through the freezing process, and thus their chemical compositions have been modified. A method is described and employed to remove the modifying effects of the freezing process on the melts generated in the mantle, which may occur over the range of pressures between magma generation and segregation from the source region, and emplacement within the mid-ocean ridge. The chemical systematics of the basalts that are associated with the melting process are then identified.

Chapter II examines the chemistry and geology of a portion of the mid-ocean ridge at $11^{o}45'$N on the East Pacific rise. The nature of the freezing process that resulted in the formation of the oceanic crust in the vicinity of a small ridge offset feature is investigated in the context of detailed geological observations from the ALVIN submersible and chemical compositions of the sampled crust. Experimentally determined, low-pressure phase equilibria are employed to 'see' through the effects of low pressure crystallization and magma mixing processes on the chemistry of the sampled basalts. The phase equilibria framework developed in Chapter 1 for quantifying freezing processes at higher pressures is employed to determine the range of depths over which the basalts cooled and crystallized.

Each chapter is presented as a self-contained article including references. Figures and tables are placed at the end of the text for each chapter. The abstracts from each chapter have been combined into the thesis abstract presented at the beginning of the document.

CHAPTER I

Primary magmas of mid-ocean ridge basalts

INTRODUCTION

State of the problem of melting in the upper oceanic mantle

Melting in the upper mantle occurs as the result of adiabatic up-welling that accompanies crustal extension at mid-ocean ridge spreading centers. Thermal evolution of the upper mantle causes decompression melting which results in a large amount of chemical differentiation. Oceanic crust, which covers approximately 80 % of the earth's surface, and is created at a rate of roughly 20 km^3/yr at mid-ocean ridge spreading centers, is the end-product of this melting process. A simple schematic diagram of the decompression melting process is shown in Fig. 1. 'Fertile' mantle (mantle that has not yet contributed any melt to the spreading center) rises along an adiabat beneath the active spreading axis. At some depth (shown in Fig. 1 at approximately 50 km), the ambient temperature crosses the solidus of the mantle material and melting begins. Melting continues as the mantle rises further, ceasing at the depth at which the temperature of the mantle parcel is lower than the solidus temperature for the mantle. Two physical conditions control the point at which the ambient mantle temperature crosses below the mantle solidus and melting stops: 1) conductive cooling from above lowers the mantle temperature in the upper part of the oceanic mantle (i.e. Cordery and Phipps-Morgan, 1991), and 2) melting proceeds to the extent that the extraction of one or more phases from the mantle residue occurs (the mantle becomes depleted in the 'basaltic' component), at which point the mantle solidus steepens so that the solidus temperature rises above the ambient temperature. McKenzie and Bickle (1988) suggest that conductive cooling will not be a significant factor in the upper oceanic mantle, although Cordery and Phipps-Morgan (1991) show that under certain conditions, specifically at slow spreading rates, conductive cooling may impose a significant control. In any case, the more significant control on the degree to which the mantle melts is most likely imposed by the total extent of depletion achieved. The point at which a phase is

eliminated from the mantle residue, or the degree of depletion achieved during melting, will be a function of how (and if) the melt is extracted from the mantle residue as it is produced.

What happens to the melt, as it is produced? Does it stay with its solid residue (batch melting in a diapir; i.e., Presnall et al., 1979), or does it separate and rise on its own (i.e., McKenzie and Bickle, 1984, 1988)? These questions are important because whether or not the melt remains in equilibrium with its solid residue as the mantle rises through the melting regime controls the volume and the compositions of the melts and the residues of the melting process. If the melt stays with the solid as the solid rises through the melting regime, and separates at the top, then the bulk composition of the melting system (residue + melt) stays constant, and the pressure signature of the melt produced will be equivalent to the pressure of segregation (the pressure at the top of the melting regime). In this batch melting case, bulk system composition and pressure of melting are effectively constant for the melting process that yields MORB, and the volume and composition of magma produced will be a function of the starting composition of the mantle, the pressure of segregation and the extent of melting achieved, which is a function of temperature. If, on the other hand, melts segregate from the rising mantle in small fractions, as they are produced, then the bulk composition of the melting system changes continuously as melting proceeds (near-fractional melting). Furthermore, as long as the fractions of melt do not equilibrate with the overlying mantle as they rise, then the pressure signature associated with the magma formed by aggregating these small fractions of melt at some depth shallower than the melting regime will reflect the range of pressures over which each of the small melt fractions were produced. In this near-fractional melting case, then, the volume and composition of the resulting aggregate magma composition will be a function of temperature, the range of pressures over which the melting occurred, and the changing system composition.

Theoretical models of melt generation and segregation (i.e., McKenzie, 1984) favor polybaric, near-fractional melting over diapiric, batch melting for producing magmas during decompression melting. The recent experimental study of basaltic melt segregation from a deforming matrix of olivine (Riley and Kohlstedt, 1991) suggests that melts segregate at small fractions (0.1-1%) as they are produced. Johnson et al. (1990) suggest that the chemical variations observed in abyssal peridotites, the residues of the partial melting process that produces MORB, reflect a process of melt extraction that involves the removal of small increments of melt as they are produced (near-fractional melting). Geodynamic models (Cordery and Phipps-Morgan, 1991) suggest that buoyancy forces resulting from the change in density associated with the extraction of melt from the rising mantle will enhance convection of mantle through the melting regime, and thus enhance melting. Given these theoretical, experimental and geochemical observations it is clear that decompression melting is a dynamic process during which pressure, temperature and system composition change as melting proceeds, and the changes in system composition associated with melt extraction result in changes in density that feed back to drive the melting process.

Recent efforts to more realistically model the decompression melting process in the upper oceanic mantle include Klein and Langmuir (1987, 1989) and McKenzie and Bickle (1988). Klein and Langmuir utilized the melting experiments of Jaques and Green (1980) and Fujii and Scarfe (1985), as well as the method of Langmuir and Hanson (1980) for estimating the distribution of FeO and MgO during mantle melting, to examine the case of polybaric, batch melting for the generation of MORB at mid-ocean ridges; in their treatment the pressure of melting and the extent of melting varied but the solid composition melting at any given pressure was constant. McKenzie and Bickle (1988) used an empirical parameterization of an unabridged set of the existing mantle peridotite melting experiments to model the melting process that produces MORB as a polybaric, near-fractional melting process. In their treatment both pressure

and the solid composition varied as melting proceeded. The present study provides new experimental data that pertains to the mantle melting process. A quantitative, experimentally constrained description of the melting equilibria as a function of pressure, temperature and solid composition is presented. This quantitative description is guided by thermodynamic constraints on the mantle melting equilibrium, and is calibrated over the data presented in this study as well as a comprehensive but more critically evaluated set of melting experiments as compared to the data sets of McKenzie and Bickle (1988) and Klein and Langmuir (1987, 1989).

Our approach is guided by the theoretical framework of the mantle melting process provided by McKenzie and Bickle (1988) and by the insightful observations of Klein and Langmuir (1987, 1989) about the geochemical systematics of sampled MORB, and how these systematics may relate to the mantle melting process. The approaches taken by Klein and Langmuir (1987, 1989) and McKenzie and Bickle (1988) to estimating compositions of melts from mantle peridotites are based on peridotite melting experiments that are analogs to larger extents of melting of the mantle (> 20 %) and are not directly applicable to modelling melting processes that involve extraction of small (0.1 - 1 %) melt fractions. Fig. 2 presents NaK# vs. Mg# for experimentally produced melts that coexist with the phases present in the mantle source, olivine, orthopyroxene, augite and spinel and/or plagioclase. The open squares represent existing data, the solid squares show the data added by this study (and that of Grove et al., 1990; and Bartels et al., 1991). Small increment melts produced from a spinel-lherzolite rising into the melting region beneath a mid-ocean ridge are anticipated to have high NaK# ($\sim$0.4). With further depletion by extraction of melt the NaK# decreases. The Mg# of the melts increases relatively slightly. These melt compositional parameters impose a significant control on the major element compositions of melts from spinel-lherzolites. Our approach provides an improvement over the earlier approaches because it is calibrated over a data set that better describes the variations of

melt composition anticipated during near-fractional melting of mantle lherzolite. The parameterization is designed for calculating melts over the range of melt percents relevant for the mantle melting process (1 - 20%). Moreover, it allows a quantitative calculation of the melt composition at small melt percentages as a function of changing residue composition. The description we present can be used to constrain mantle melting processes, whether batch, near-fractional, or in-between.

Background on question of primary magmas of MORB

The oceanic crust provides samples of the end-product of the mantle melting process. In order to use the chemistry of the oceanic crust (or its thickness) to infer characteristics of this melting process, we need to evaluate and correct for any post-melting processes that may have modified the mantle melt compositions and volumes to yield the sampled MORB. For the purpose of this discussion we define a liquid produced by partial melting of a source region and unmodified by any post-segregation process as a 'primary magma' (B.V.S.P., 1981). Thus it is the primary magmas of MORB that provide direct constraints on the mantle melting process. The identity of the primary magmas of MORB has been the subject of on-going debate. Three general views have evolved over the past 25 years. The first view is that the primary magmas of MORB are essentially picritic melts that segregated from their mantle source at relatively high pressures (20-25 kbar, O'Hara, 1968a; Stolper, 1980; Elthon and Scarfe, 1984; Elthon, 1989). This view holds that a major amount of chemical modification has occurred to these picritic, primary magmas after separation from their mantle residue to produce chemically evolved MORB sampled at mid-ocean ridge spreading centers.

The second view is that many primitive MORBs are potential primary magmas that segregated from their mantle source at relatively low pressures (9-11 kbar, e.g., Presnall et al., 1979, Fujii and Scarfe, 1985; Fujii, 1989). For the purpose of this discussion, we define 'primitive' MORB to be those MORB glasses that contain greater than 9.00 wt.% MgO. A third approach to the primary magmas of MORB has evolved

along with the more recent models of the decompression melting process beneath mid-ocean ridges discussed above (O'Hara, 1985; McKenzie and Bickle, 1988; Klein and Langmuir, 1987, 1989). This approach regards the magma that is emplaced into the spreading center as an aggregate of melts collected from a range of degrees and depths of melting and segregation. In this third view, the magma being fed into spreading centers no longer represents a primary magma in the strict sense of the definition provided above, but rather consists of a blend of primary magmas, segregated from a range of pressures, referred to in later discussion as aggregate primary magmas.

In this paper, two approaches are used to constrain the mantle melting processes that yield MORB. A *forward approach* consists of using the experimentally constrained, quantitative description of the mantle melting equilibria presented below to predict primary magma compositions produced by batch and near-fractional, isobaric and polybaric melting of a depleted MORB-mantle source. Fractional crystallization processes are then applied to correct these estimated primary magma compositions 'down temperature' to 8.00 wt.% MgO so that they can be directly compared to the corrected global data set of MORB compiled by Klein and Langmuir (1987,1989). An *inverse approach* consists of subtracting out the effects of fractional crystallization and other post-segregation magmatic processes from a subset of sampled MORBs that span the range of compositions covered by the global data set of Klein and Langmuir (1987,1989) in order to track the sampled MORBs 'up temperature', back to parental, primary magma compositions. These parental, primary magma compositions are compared to those estimated by the mantle melting models presented below to place constraints on the generation of the primary magmas of these MORB, as well as to evaluate the nature of the composition of the depleted MORB-mantle source(s).

EXPERIMENTAL AND ANALYTICAL METHODS

Starting Material

Two primitive and one parental mid-ocean ridge basalt (MORB), and several synthetic MORB analog compositions were chosen for experimental study. The samples consist of fresh glassy to aphyric pillow fragments, and the freshest parts of the pillows were separated, reduced to powder by grinding in a SPEX shatterbox for 3 minutes, and then used as starting material. Three types of experiments were carried out: the first used the natural basalts, the second used mixtures of natural basalt with small proportions of mafic minerals and the third used synthetic compositions prepared by combining mixes of oxides with small proportions of mafic minerals. Mixes for the second type of experiment were prepared by grinding powdered natural basalt with hand-picked, cleaned, crushed Kragero orthopyroxene or San Carlos olivine in an automatic agate mortar and pestle for 3 hours. The synthetic starting compositions were prepared in three steps. The first step entailed grinding Johnson-Matthey high purity SiO_2, TiO_2, Al_2O_3, Cr_2O_3, Fe_2O_3, MgO, MnO with prepared mixes of $CaSiO_3$, Na_2SiO_3 and $K_2Si_4O_9$ together in an automatic agate mortar and pestle for 5 hours, Fe sponge was then added and the mix was ground for an additional 1.5 hours (Lindsley et al., 1974). The second step entailed adding small proportions of powdered San Carlos olivine and in some cases powdered spinel separated from a Kilbourne Hole lherzolite (KH-5-4, T.L. Grove, pers. comm.). The third step entailed holding the synthetic mix at $\sim 1300^{o}C$ at an oxygen fugacity controlled at the quartz-magnetite-fayalite buffer on Pt-Fe loops fabricated after the method of Grove (1981). This step was necessary to ensure that the Fe was present in the starting composition as dominantly FeO. Table 1 provides chemical analyses of the starting compositions used in this study.

Experimental procedure

Melting experiments were carried out at 9, 10, 11, 12, 13 and 16 kbar, under volatile-free conditions, in a 1/2" solid-medium piston cylinder apparatus (Boyd and England, 1960) using the piston-in method (Johannes et al., 1971). Experimental conditions are reported in Table 2. The temperature was monitored and controlled using Pt-$Pt_{90}Rh_{10}$. The pressure medium consisted of an outer cell of NaCl and an inner cell of Pyrex. This pressure cell was calibrated against the melting point of gold at 10 kbar (Akella and Kennedy, 1971) and the observed effect of friction within the assembly was < 1 kbar. This effect on total pressure lies within the uncertainties of the calibration and the pressures reported in Table 2 do not include a friction correction. Approximately 4 - 10 mg of starting material was packed into a graphite container, closed with a graphite lid and welded into an outer Pt capsule. The graphite isolates the sample from the Pt outer capsule and prevents Fe loss. The graphite-Pt capsule assembly keeps the redox conditions constant near the C-CO_2-CO buffer. The 32 mm sample assembly was placed in a ceramic sleeve and centered in the hot spot of a graphite furnace using crushable alumina (An_{900}) spacers. The thermocouple was located 3.5 mm above the center of the furnace, or 1.75 mm above the top of the sample capsule, and separated from the capsule by a 1.75 mm wafer of An_{900}. The temperature gradient between the thermocouple position and the center of the sample was measured to be 45 ^{o}C. Temperatures reported in Table 2 are corrected for this temperature difference. Failure to reproduce the sample geometry from experiment to experiment results in inconsistent temperature measurements. Temperatures were reproduced in the assembly described above to at least within +/- 15 ^{o} C.

Analytical methods

Experimentally produced run products were analyzed with the MIT 4-spectrometer JEOL 733 Superprobe, using an accelerating voltage of 15 keV and a beam current of 10 nA for all phases. Data was reduced using Bence and Albee (1968)

matrix corrections with modifications of Albee and Ray (1970). A beam spot size of 10 microns was used for glass analyses, a 1 micron beam spot size was used for the crystalline run products. Analytical precision is estimated by replicate measurements of a MORB glass (PROTEA-9-70-002, Table 1). One standard deviations of replicate glass analyses expressed as relative percent oxides are SiO_2:0.2%, TiO_2:1.7%, Al_2O_3:1.3%, FeO:0.8%, MgO:0.7%, MnO:17.6%, CaO:0.8%, K_2O:10%, Na_2O:2.2%, P_2O_5:33.3%, based on 368 individual analyses over 46 analytical sessions. The mean sum of the analyses of the MORB glass is 99.2%. Major element compositions of all the run products are presented in Table 3.

Conservation of Mass

Three approaches were used to evaluate if the bulk composition of the experimental charge remained constant. We inspected each polished charge in reflected light to determine if large cracks had formed in the graphite containers during the experiment. If cracks were apparent, and melt was observed to be in contact with the outer Pt sleeve, then Fe loss is certain to be greater than 5 % relative and such experiments were discarded. It is possible that cracks may form that are not apparent upon inspection of the polished charge in reflected light, and thus each charge was examined with the back-scattered electron imaging system (brightness = average atomic number) on the electron microprobe. If significant Fe-loss has occurred then the Fe-Mg bearing minerals will often show reverse zoning with respect to Fe and Mg, because Fe is diffusing out of the minerals and glass and into the platinum outer capsule throughout the course of the experiment. Even in charges with no observed reverse-zoned crystals, Fe-loss may still have occurred, and thus a third approach that entailed computing mass balances between the compositions of phases (Table 3) and the bulk composition of each experiment (using the method of unweighted least squares; Bryan et al., 1969, reported in Table 2) was necessary to ensure conservation of Fe in the charge. In a successful experiment, the composition estimated by the mass balance of the phases

present closely approximates the bulk composition of the starting basalt or basalt-mineral mix. In general, only experiments with < 10 % relative Fe loss were considered acceptable. The mass balance calculations for several of the experiments containing glass, olivine and orthopyroxene yielded negative phase proportions. The negative phase proportions result from the arrangement of the phases, particularly the melt, olivine and orthopyroxene phases, in composition space, relative to the bulk composition. Mass balance results with negative phase proportions are physically unreasonable because all of the phases included in the mass balance are observed to be present in the experiment. These results therefore cannot be used to evaluate whether mass was conserved during the experiment. We forced positive phase proportions on the mass balance results by excluding the phases that had negative coefficients in the initial calculation (in many cases, orthopyroxene; and in three experiments, the alumina-rich phase as well) from the mass balance calculation. This treatment forces the glass and the other crystalline phases to incorporate the components present in the excluded phases and thus results in overestimates of the proportions of these included phases. We used the equilibrium batch melting equation and treated K_2O as incompatible in the crystalline phases to estimate the melt % present in each charge (Table 2). As expected, in all but one of the experiments, the glass fractions estimated with the equilibrium batch melting equation are lower than those predicted by the mass balance calculations. The purpose of the three measures described above are to provide maximum surety that Fe-loss is identified in the experiments. Maintaining a constant bulk composition of the starting material is a necessary first step for an approach to equilibrium in an experiment. An experiment that is undergoing mass transfer of Fe with respect to an outer platinum capsule, for example, can not reach equilibrium unless and until loss of Fe to the capsule has ceased and the bulk composition of the sample has stabilized. The outer platinum capsule may provide a large sink for the Fe in the silicate charge, and potentially buffer the FeO content in the resulting glass which would then yield

misleading experimental results (see section below on Experimental data used to develop the model).

Attainment of equilibrium

All of the experiments presented in this study are direct syntheses; phase appearance sequences and temperatures have not been reversed. However, several lines of observation lead us to conclude that the experiments approached equilibrium sufficiently that they can be used to constrain the processes of mantle melting. First, the Fe-Mg bearing crystalline phases show generally consistent partitioning with respect to iron and magnesian (with the exception of experiments H177, H179, H181, H154 and H156, which have low Fe-Mg K_Ds for all Fe-Mg bearing crystalline phases present, and are discussed below). The average $K_D^{Fe\text{-}Mg_s}$ ($[FeO^{xtl}MgO^{liq}]/[FeO^{liq}MgO^{xtl}]$) are 0.30 ($1\sigma$=0.04), 0.30 ($1\sigma$=0.04), 0.27 ($1\sigma$=0.05), and 0.42 ($1\sigma$=0.07) for olivines, augites, orthopyroxenes and spinels, respectively. These K_Ds are as expected from other phase equilibrium studies and provide evidence for a close approach to equilibrium. Second, we have succeeded in maintaining reasonably constant sample bulk compositions with little or no loss of iron to the platinum outer capsule (see above). Third, replicate analyses of the glass phases present in the melting experiments show that the majority of the experimental liquids were homogeneous within the precision of the microprobe analytical technique (+/- 2 σ). Fourth, the experimental minerals, with the exception of augites, are generally sub- to euhedral, and equant or tabular; and individual crystals commonly reach sizes of 50 to 100 microns across, (the augites, in contrast, are often anhedral, see below).

Nevertheless, individual mineral analyses vary outside of the practical reproducibility established above from replicate glass analyses. Back-scattered electron imaging shows that most of the experimentally produced minerals are weakly zoned, and that sector and patchy zoning are often the norm for augites. The presence of sector zoning and the small heterogeneities in compositions of the experimentally produced

minerals are inconsistent with attainment of total equilibrium. We run our experiments for as long as possible, however, experiments of far greater duration than are presently feasible would be required to produce true equilibrium mineral phase compositions. We used the compositions of the experimentally produced augites to guide the choice of optimum run durations. Augite compositional variation is a sensitive function of pressure and temperature, and the composition of the melt produced and the nature of the melt-producing reaction for a mantle peridotite are dependent on the composition of the coexisting augite (Stolper, 1980). A series of experiments were conducted on a primitive MORB composition (ALVIN 2004-3-1) at 10 kbar and 1270 ^{o}C for durations from 0.5 to 48 hours in order to investigate the effect of run duration on the homogeneity and average composition of experimentally produced augite. Augite and plagioclase are liquidus phases at 10 kbar for this MORB. Augites produced in experiments of 0.5 to 6 hours duration were very heterogeneous in composition. Longer run times (>14 hours) produced more homogeneous augites, but compositional heterogeneity persists in even the longest runs. Furthermore, the average composition of the experimentally produced augites appears to become constant for experiments with durations between 6 and 24 hours. Obviously, longer run times are almost always desirable when trying to reproduce processes that occur in the earth, however our run times were chosen to maximize the achievement of near equilibrium results within the practical limits of our experimental setup.

Experiments H177, H179, H181, H154 and H156 have anomalously low Fe-Mg K_Ds for all the Fe-Mg bearing crystalline phases (<0.25 for olivine, <0.25 for augite, <0.23 for orthopyroxene and <0.34 for spinel). These experiments are all highly crystalline (~ 20-30 wt.% glass) and the fact that the Fe-Mg K_Ds are low for all the Fe-Mg bearing crystalline phases present in each experiment suggests that a significant portion of the total iron measured in the melt phase is actually present as Fe^{3+}. If this were true, then the measured amount of total iron yielded by the electron microprobe

would be an over-estimate of the actual amount of Fe^{2+} in the glass, which would then result in a lower apparent K_D for Fe-Mg exchange between minerals and melt (FeO^{liq} occurs in the denominator of the K_D formulation). Thompson (1974) noted a similar dependance of observed Fe-Mg K_D for olivine on temperature (melt fraction) in 10-kbar melting experiments on a natural basalt, and attributed it to the increased activity of Fe_2O_3 which was not being accounted for because all the Fe was measured as FeO. A simple calculation suggests that if the MORB glass used in the starting composition for the four of the five experiments listed above (H177, H156, H154 and H181: 90 wt.% MORB and 10 wt.% powdered San Carlos olivine) contained ~10 % of the total iron as Fe^{3+}, then the amount of Fe^{3+} present in the starting material would be ~0.9 wt. %. If Fe^{3+} is assumed to be totally incompatible with respect to all of the crystalline phases present, then the amount of Fe^{3+} estimated to be present in an experiment with 22 wt.% liquid is 0.9/.22 = 4.1 wt.%. In the case of experiment H181, for example, the total FeO measured in the glass phase by the electron microprobe is 11.8 (Table 3), and the observed Fe-Mg olivine K_D is 0.21. If 4.1 wt. % of the total Fe is present as Fe_2O_3 then a simple approximation of the 'true' Fe-Mg olivine K_D for this experiment is (18.7*5.70)/(7.71*42.3), or 0.33; similar estimates of the 'true' augite, orthopyroxene and spinel Fe-Mg K_Ds are 0.31, 0.28 and 0.50. These estimated values are well within the expected range. Experiments are currently under way to determine if reducing the starting composition in Fe capsules in evacuated silica tubes at 1 atm. prior to using it in the melting experiments will result in higher observed Fe-Mg K_Ds. The presence of a significant portion of the total Fe as Fe^{2+} in the 5 experiments discussed in this section also affects the observed Mg# of the melt (true Mg# will be higher), and may also affect the stability of spinel. As the descriptions of the mantle melting equilibria discussed below depend critically on both the identity of the phases with which the melt is saturated (i.e., spinel or plagioclase, both, or neither) and the Mg# of the melt, these 5 experiments were used only in the description of the plagioclase melting equilibrium (the

stability of which is assumed not to depend critically on the amount of Fe^{3+} present in the melt). The melt compositions were recalculated by assuming that the true Fe-Mg olivine K_D in each experiment is equal to the average experimentally determined Fe-Mg olivine K_D (0.30) to estimate the amount of FeO, and then estimating the amount of Fe_2O_3 by difference from the total measured FeO.

Philosophy behind the experimental approach

Realistic models of the melting process in the upper mantle require the capacity to predict the compositions of small extent partial melts of the mantle as a function of temperature, pressure, and changing bulk mantle composition. A powerful constraint on these small extent melts is that they are produced in equilibrium with the minerals present in the solid residue. The major phases present over the extents of melting achieved during the melting processes that yield MORB are: olivine, low-Ca pyroxene (orthopyroxene or pigeonite), high-Ca pyroxene (augite), and an aluminous phase (spinel and/or plagioclase) in the pressure range 0.001 - 16 kbar. The phrase 'mantle residual assemblage' is used to refer to the phases olivine + augite + low-Ca pyroxene + spinel +/- plagioclase. The constraint that augite and spinel are residual to the melting process that yields MORB stems from the presence of these phases in even the most depleted abyssal peridotites sampled on the sea floor (Dick et al., 1984). We therefore designed experiments that would yield melts of a range of compositions that coexist with the mantle residual assemblage over a range of pressures and temperatures. To achieve this goal, mixtures of basalt powder and small amounts of either powdered orthopyroxene or olivine were melted over a range of temperatures and pressures. Initially, the phase equilibria for a powdered primitive MORB glass (ALVIN 2004-3-1, Table 1) were determined at 9, 11 and 13 kbar. None of the experiments on ALVIN 2004-3-1 contained coexisting melt, olivine, augite, low-Ca pyroxene, spinel and/or plagioclase, but we used the olivine-augite-plagioclase, olivine-plagioclase and augite-plagioclase boundaries located with ALVIN 2004-3-1 as a guide for changing the bulk

composition to create a starting composition that would saturate with the mantle residual assemblage. Using this approach, bulk compositions were generated that yielded the experimental assemblage: liquid + olivine + augite + low-Ca pyroxene + spinel and or plagioclase at a range of temperatures at 9 - 16 kbar. By-products of this effort to locate these low-variance boundaries over a range of pressures, temperatures and bulk compositions were experiments that contain melt coexisting with only a subset of the desired crystalline phases. Several experiments containing melt coexisting with olivine +/- orthopyroxene +/- augite are also reported in Tables 2 and 3.

Comparison to other experimental approaches to mantle melting

Three approaches have been taken to investigate melting processes in the mantle: peridotite melting (forward approach), determination of liquidus phase equilibria on primitive natural basalt compositions (inverse approach) and melting basalt glass compositions in contact with natural mantle minerals (the sandwich technique). The peridotite melting, or forward approach consists of melting mantle material over a range of pressures and temperatures. Some of the earliest experimental studies on the nature of mantle melting were done using this approach (e.g., Ito and Kennedy, 1967; Green and Ringwood, 1967; Kushiro, 1968; Mysen and Kushiro, 1977; Jaques and Green, 1980, Takahashi, 1986) and these studies have provided important first order observations. Measuring the compositions of the melt produced and the coexisting phases is limited, however, by the small melt fractions present.

Several of the experimental studies carried out to investigate the nature of mantle melting used the inverse approach (e.g. Kushiro, 1973; Fujii and Kushiro, 1977; Bender, et al, 1978; Fujii and Bougault, 1983; Elthon and Scarfe, 1984). This approach consists of choosing a primitive natural basalt composition that is assumed to represent a liquid composition and testing whether this primitive composition represents a primary melt from some depth. In order to test the primary nature of this primitive basalt, the liquidus phase assemblage is determined by melting it over a range of pressures and

temperatures. If the primitive melt's composition is similar to that of a primary melt from some depth, then at experimental pressure, temperature and volatile conditions equal to those conditions at which the natural melt was produced, the liquidus assemblage for the natural composition will be the same as the mineral phase assemblage present in the mantle residue upon segregation.

In general, none of the primitive natural compositions tested by the inverse approach were shown to crystallize the mantle residual assemblage on their liquidus. Only a few of these primitive compositions ever crystallize orthopyroxene (or pigeonite) at all, and these compositions only do so at temperatures well below their liquidus. (e.g. up to 30 - 40 degrees below the liquidus temperature for the FAMOUS primitive basalt 527-1-1 at 15 kbar, as determined by Bender et al., 1978).

Several recent experimental studies have applied the sandwich technique (e.g., Stolper, 1980; Takahashi and Kushiro, 1983; Fujii and Scarfe, 1985; Falloon and Green, 1987). This approach forces saturation of a primitive basalt with a natural mineral assemblage representing the mantle source, over a range of pressures and temperatures. The sandwich technique successfully produces large pools of silicate melt in contact with the starting mineral assemblage (generally olivine + orthopyroxene +/- augite +/- spinel +/- plagioclase).

EXPERIMENTAL RESULTS

We have produced 20 assemblages consisting of glass plus the mantle residual assemblage over a range of temperatures from 1220 to 1340 ^{o}C, in the pressure range of 9 - 16 kbar. Liquids saturated with olivine, two pyroxenes, and at least one aluminous phase will be referred to as 'multiply saturated' in the following sections. Each provides a constraint on the reaction boundary described by silicate liquids coexisting with the mantle residual assemblage in composition, pressure, temperature space.

A simplified liquidus phase diagram (Fig. 3) shows the effect of pressure on the position of liquidus boundaries in composition space. Glass and pyroxene compositions from a subset of the experiments reported in Tables 2 and 3 are recalculated in terms of end-member mineral components, and then projected into the pseudo-quaternary Oliv-Cpx-Plag-Qtz (olivine - clinopyroxene - plagioclase - quartz) using the projection scheme of Tormey et al. (1987). The liquids in Fig. 3 are saturated with plagioclase and thus can be projected through the Plag component onto an Oliv-Cpx-Qtz pseudo-ternary diagram. This simplified liquidus phase diagram is suitable for interpreting liquid lines of descent for MORB compositions similar to those used in the experiments. Multiply saturated liquids produced at 9, 11 and 13 kbar project as points for each given pressure. The curves that emanate from these points are boundaries defined by the projected compositions of liquids coexisting with 3 solid phases (olivine + orthopyroxene + plagioclase, olivine + augite + plagioclase, orthopyroxene + augite + plagioclase, compositions in Grove et al., 1991). When these multiply saturated liquids are plotted as points on mineral component projection schemes as functions of pressure, they constitute one point in a multi-dimensional volume, or on the 'reaction boundary' defined by liquids that can coexist with the mantle residual assemblage in temperature, composition space. Their projected positions are functions of temperature and major element chemistry, i.e., Mg#, alkali content and TiO_2 (see discussion below). As such, this simplified liquidus phase diagram is useful for qualitatively depicting the relationship between pressure and compositions of liquids and coexisting solid phases. The effect of increased pressure on the projected composition of silicate liquids that coexist with the mantle residual assemblage, as inferred from our experimental study and depicted in Fig. 3, is to decrease the Qtz component and increase the Oliv component in the multiply saturated liquids. This observation is consistent with observations of several previous studies in both natural and simple systems (i.e., O'Hara, 1968b; Presnall et al., 1979; Stolper, 1980).

Melting reactions for the mantle residue assemblage

One important question in basalt petrogenesis is the nature of the melting reaction by which primary basalts are generated in the mantle (Mysen and Kushiro, 1977; Stolper, 1980). Stoichiometric coefficients of the melting reaction are required as input for models of melting processes in the upper mantle. Reaction boundary coefficients presented in Table 4 were estimated by mass balancing a higher temperature liquid on a reaction boundary against a lower temperature liquid on that same boundary plus the solid phases coexisting with that lower temperature liquid (Juster et al., 1989). The most accurate result is achieved by choosing two liquids produced by melting the same starting composition at two slightly different temperatures, however such pairs of experiments and the compositional data required are not common in the elevated pressure experimental literature. Experiments B52 and B30 were carried out at 12 kbar, 15^{o} apart on similar starting compositions (SYN2 and SYN3, Table 1), and both contain melt coexisting with olivine + augite + orthopyroxene + spinel. Based on the estimates of the coefficients for the melt reaction relating the lower temperature B30 melt and crystalline phases to the higher temperature B52 melt (Table 4) we suggest that melting spinel lherzolite at 12 kbar consumes augite, orthopyroxene and spinel and produces liquid plus olivine. The nature of the suggested melt reaction is similar to that observed in the simple mantle analog system CaO-MgO-Al_2O_3-SiO_2 (Presnall et al, 1979). Reaction boundary coefficients for the melting of spinel lherzolite were also estimated from pairs of 10-kbar experiments presented in the study of Falloon and Green (1987). The melt reactions estimated from these data are qualitatively similar to that of the B30-B52 melt reaction, the quantitative differences most likely stem from the difference in pressure and the resulting differences in melt and pyroxene compositions. The estimated spinel-lherzolite melting reaction obtained by averaging the reaction estimates from experiments B30-B52 and a subset of the Falloon and Green (1987) 10-kbar data (Table 4) is shown graphically in Fig. 4. The 10-kbar

phase compositions are projected into the Oliv - Spinel - Di-Hd - En-Fs tetrahedron. The nature (which phases are consumed or produced during melting) of the melting reaction can be determined using this projection (Grove et al., 1983a). The projected composition of the multiply saturated liquid at 10 kbar lies outside the phase volume defined by olivine, orthopyroxene, augite and spinel. Thus, the geometry depicted in Fig. 4 indicates that augite + orthopyroxene + spinel are being consumed to produce liquid + olivine at 10 kbar. The coefficients of the melting reaction are extremely sensitive to the liquid and augite compositions (see Table 4). Therefore, the melting reaction observed at a given pressure and temperature varies as the compositions of these experimentally produced phases vary. Appropriate melt reactions for modelling mantle melting are obtained from experiments containing minerals and melts reasonably similar in composition to mantle phases.

Two sets of reaction coefficients for the melting of spinel lherzolite estimated from data at 16 kbar from this study and from the study of Bartels et al. (1991) suggest that the melting reaction consumes augite + spinel to produce liquid + olivine + orthopyroxene at 16 kbar. The Mg#s of the melts in the 16 kbar experiments are lower than those expected for melts in equilibrium with peridotite, and thus it is difficult to evaluate whether the change in the nature of the melting reaction observed between the 10-12 kbar and 16 kbar experiments is caused by melt composition variations, or by the effect of pressure on the coexisting augite and orthopyroxene compositions.

Reaction coefficients were determined for the plagioclase-lherzolite melting boundary at 8 kbar using experiments H130, H164 and H13. Because the starting composition for H13 is significantly different from the starting composition for H130 and H164 these coefficients are approximate, however, they provide a guide for modelling plagioclase lherzolite melting. Reaction coefficients were also determined for the melt + olivine + augite + orthopyroxene + plagioclase + spinel using experiments H162, H156, H154 and H181. These experiments were carried out on the same starting

composition between 1280 and 1295 ^{o}C at 13 kbar and the estimated melt reactions (Table 4) suggest that when plagioclase - spinel lherzolites melt, augite + orthopyroxene + spinel are consumed to produce liquid + olivine + plagioclase. The melt compositions present in these experiments have low Cr_2O_3 contents and Mg#s (and potentially high Fe_2O_3 contents, see above), however and thus the inferred melt reaction coefficients may not be directly applicable to melting of mantle peridotite.

In summary, mantle melting is not modal and the coefficients of the melting reaction (and potentially the nature) change with increasing pressure. With the possible exception of the pressure range of 4-6 kbar where melting may be at a eutectic boundary (Grove et al., 1990), melts produced at higher and lower pressures in the mantle are generated along a peritectic-type boundary. Based on the coefficients provided in Table 4 it is apparent that melt composition, bulk system composition and pyroxene compositions strongly influence the way mantle peridotite melts. Three areas of further work are required to better constrain how melting of lherzolite proceeds: 1) experiments at 15 - 20 kbar are required to produce experiments containing melts with mantle characteristics that coexist with the mantle residual assemblage in order to evaluate the effect of the changing pyroxene compositions on the melt reaction, 2) experiments are required to more accurately estimate the reaction boundary for plagioclase lherzolite melting over the pressure range of 8 - 12 kbar, and 3) experiments are required to establish the nature of the melt reaction at conditions equivalent to the plagioclase to spinel transition in the upper mantle.

Composition of experimentally produced melts saturated with the mantle residue assemblage

Presnall and Hoover (1987) and Grove et al. (1990) observed that many experimentally produced, multiply saturated liquids were not directly suitable as partial melts of a natural mantle lherzolite. Many experimentally produced liquids are too rich in FeO, Na_2O, K_2O and TiO_2 to be parental to basalts that we sample, and too rich in

FeO, relative to MgO, to be in equilibrium with a mantle residue. The Mg# in the multiply saturated liquids reported in this study ranges from 0.46 - 0.69, the Na_2O content from 1.87 - 5.94 and the TiO_2 content from 1.15 - 2.56. Only a small subset of these melts are direct analogs of mantle melts, however all of them can be used to describe the multi-dimensional volume occupied by liquids coexisting with the mantle residual assemblage in pressure, temperature and composition space. In the following discussion we present a method for using constraints provided by experiments containing multiply saturated liquids (from this study and the literature) to predict how the natural upper mantle will melt as a function of pressure and changing mantle composition.

A QUANTITATIVE MODEL FOR MANTLE MELTING

Experimental data used to develop the model

Multiply saturated experiments covering a broad range of composition space, 12 from this study (the Series H experiments in Table 2) and 49 from natural system experiments presented in the literature (Kushiro, 1973; Fujii and Kushiro, 1977; Stolper, 1980; Fujii and Bougault, 1983; Grove and Bryan, 1983b; Takahashi and Kushiro, 1983; Fujii and Scarfe, 1985; Takahashi, 1986; Falloon and Green, 1987; Baker and Eggler, 1987; Grove et al., 1990; Bartels et al., 1991), are used to develop a model for predicting the compositions of melts produced in the mantle over the pressure range 0.001 - 16 kbar. We also include 5 multiply saturated experiments produced in the simple-analog system CMAS (CaO-MgO-Al_2O_3-SiO_2) by Presnall et al. (1979). Table 5 presents a summary of the experimental studies included in our data set. To most completely describe the mantle-melting equilibria, we have incorporated as many data from the literature as possible. Fig. 5 presents temperature vs. Mg# of multiply saturated melts from the literature (Table 5) and from this study, broadly contoured for increasing pressure. Multiply saturated liquids from experiments in the simple system CMAS (Presnall et al., 1979) at 0.001, 7, 9, 9.3, 11 and 14 kbar provide upper limits on the

temperatures at which silicate melts can coexist with the mantle residual assemblage over this pressure range. The data show generally systematic variations between Mg#, temperature and pressure, with the exception of the 10-kbar data of Falloon and Green (1987) (solid circles in Fig. 5). These melts were produced with the sandwich technique described above and they define a temperature - Mg# trend that cuts across the main trend defined by all the data. They also span a range of temperatures at one pressure (10 kbar) similar to that spanned by the 10 - 15 kbar data of the other studies shown, and the upper end of which exceeds the 14-kbar melt temperature in the simple system CMAS. It is possible that the chromium could stabilize the assemblage olivine + orthopyroxene + augite + spinel + melt to higher temperatures in the natural system relative to the temperatures observed for the analog assemblage in the simple system. However the chromium effect would have to be great enough to overcome the temperature-lowering effects caused by the presence of FeO and Na_2O, in particular, in the natural system, Falloon and Green (1987) 10-kbar experiments. Given the lack of data available to quantify the effect of chromium on the assemblage melt + olivine + orthopyroxene + augite + spinel, relative to the simple system, it is not possible to rule out the chromium effect, however we interpret the temperature-Mg# variation of the Falloon and Green (1987) 10-kbar sandwich experiments in Fig. 5 to indicate a lack of equilibrium between the sandwich minerals and melt (for further discussion, see below). Only the lowest temperature experiment of the Falloon and Green 10-kbar data was included in the data set used for the regressions described below.

Quantitative description of the mantle melting equilibria

The upper limit upon the thermodynamic variance of the melting equilibrium is obtained from the Gibbs phase rule: $F = C + 2 - \Phi$, where F refers to the number of degrees of freedom, C to the number of system components and Φ to the number of phases. For mantle melting Φ is five: melt - olivine - orthopyroxene - augite - Al-phase (plagioclase, spinel). In the simple, mantle analog system, CMAS, the melting

equilibrium has one degree of freedom. Therefore, fixing pressure of melting in the CMAS system also fixes both temperature and composition of the melt. To describe the major element, bulk composition of the natural upper mantle, however, more components must be considered. We have chosen eight system components that are necessary and nearly sufficient to describe the chemical variation in the mantle-melt system: Mg_2SiO_4, $CaMgSi_2O_6$, $FeMg_{-1}$, $CaAl_2Si_2O_8$, $NaSiCa_{-1}Al_{-1}$, $KSiCa_{-1}Al_{-1}$, TiO_2, SiO_2. The components with $_{-1}$ notation are exchange components, and describe the effect of replacing one constituent with another (i.e. an Fe^{2+} cation for a Mg cation). The system components listed above can be used to describe the melt phase components: Ol (olivine), Cpx (clinopyroxene), Pl (plagioclase), Qz (SiO_2), TiO_2, Mg#, $NaSiCa_{-1}Al_{-1}$, and $KSiCa_{-1}Al_{-1}$, where Ol, Cpx, Pl and Qz are oxygen normalized mineral components chosen to describe the melt. Application of the Gibbs phase rule: F = 8 + 2 - 5, indicates five degrees of freedom for the melting equilibrium in the natural system. In order to predict the temperature or composition of partial melts of the natural upper mantle, we have to fix five variables, i.e., pressure and four compositional variables.

The increase in variance from one in the CMAS system to five in the natural system occurs as a result of the added components: FeO, TiO_2, Na_2O and K_2O in the natural system, relative to CMAS. We have developed a method for predicting the composition and temperature of a liquid in the 8 component system in equilibrium with the mantle residual assemblage using easily calculated parameters. Our treatment is justified on thermodynamic grounds but is not rigorous, in part because we use mixed weight and molar values. For example, in place of the exchange components $NaSiCa_{-1}Al_{-1}$ and $KSiCa_{-1}Al_{-1}$ in the melt we found that the weight ratio $(Na_2O+K_2O)/(Na_2O+K_2O+CaO)$ (NaK#) was sufficient to describe the effects of changing alkali content on the major element composition of a melt coexisting with the mantle residual assemblage. This simplification is justified because MORBs are

generally very low in K_2O. Similarly, we used wt.% units for TiO_2 because these are the units in which this element is most commonly expressed. An obvious shortcoming of our approach is that we do not include Cr in our component description of the mantle system. We have excluded Cr/Al variation in spinel and the coexisting melt because of the lack of adequate data. We calculate the changes in the composition of a liquid in equilibrium with olivine + orthopyroxene + augite + plagioclase or olivine + orthopyroxene + augite + spinel as pressure and the key major element parameters, Mg#, NaK# and TiO_2, vary. The calculation expresses the change in liquid composition in terms of oxygen based mineral components. These mineral components can be transformed to oxide weight percent through a linear transformation.

We estimate the relationships between our variables as linear, and use multiple linear regression to obtain expressions that reflect the best fits for T, and the melt components: Ol, Cpx, Pl and Qz, in terms of P (in Kbar), Mg# (molar), NaK# (wt.) and TiO_2 (wt. %). The 66 experiments contained in the data set described above were used to constrain the fit. We estimated two expressions over the range of 0.001-16 kbar because mantle mineralogy changes over this pressure range, from plagioclase-(+/- sp) lherzolite at lower pressures to spinel-lherzolite at higher pressures.

The regressions for plagioclase-lherzolite melting (constrained with 30 experiments):

										R	
T	=	1242 +	9	(P-0.001) +	-120	(1-Mg#) +	-88.8	NaK# +	-6.6	TiO_2	0.88	(1)
Ol	=	.120 +	.008	(P-0.001) +	.229	(1-Mg#) +	-.335	NaK# +	-.009	TiO_2	0.97	(2)
Cpx	=	.261 +	-.008	(P-0.001) +	-.069	(1-Mg#) +	-.104	NaK# +	.012	TiO_2	0.95	(3)
Pl	=	.419 +	.012	(P-0.001) +	-.135	(1-Mg#) +	.691	NaK# +	.000	TiO_2	0.95	(4)
Qz	=	.200 +	-.012	(P-0.001) +	.000	(1-Mg#) +	-.252	NaK# +	.000	TiO_2	0.97	(5)

The regressions for spinel-lherzolite melting (constrained with 38 experiments):

T	=	1146 +	17	(P-0.001) +	-85.6	(1-Mg#) +	-70.0	NaK# +	0.00	TiO_2	0.89	(6)
Ol	=	.177 +	.005	(P-0.001) +	.111	(1-Mg#) +	-.249	NaK# +	.000	TiO_2	0.61	(7)
Cpx	=	.265 +	-.006	(P-0.001) +	.243	(1-Mg#) +	-.434	NaK# +	.000	TiO_2	0.67	(8)
Pl	=	.383 +	.010	(P-0.001) +	-.319	(1-Mg#) +	1.22	NaK# +	.000	TiO_2	0.90	(9)

$$Qz = .176 + -.008\ (P\text{-}0.001) + .000\ (1\text{-}Mg\#) + -.539\ NaK\# + .047\ TiO_2 \qquad 0.88 \qquad (10)$$

The constant terms in the regressions for eqns. 1-5 were fixed to the values of T and melt components Ol, Cpx, Pl and Qz determined by Presnall et al. (1979) for the CMAS system at 1 atm., because these expressions simplify to this simple system, 5-phase equilibrium when the independent variables (1-Mg#), NaK# and TiO_2 are zero. In the CMAS end member case, the 5-phase equilibrium is univariant, and both the temperature and composition of a melt coexisting with olivine - orthopyroxene - augite - plagioclase are described by pressure alone. The pressure dependent terms goes to zero at 1 atm. and a set of constant terms are left in the expressions for plagioclase-lherzolite melting that reflect the temperature and composition of a melt in the CMAS system that coexists with the mantle residual assemblage at 1 atm. We did not fix the constant terms in the spinel-lherzolite melting expressions (eqns. 6-10) because the 5-phase assemblage olivine - orthopyroxene - augite - spinel - melt is metastable in CMAS at 1 atm. The constant terms in eqns. 6-10 were determined by the regressions.

Equations. 1-10 are preliminary in that they represent best fits to the existing data set of assemblages of melt coexisting with olivine, orthopyroxene, augite, and plagioclase and/or spinel produced experimentally at pressures up to 16 kbar. In order to maximize the number of constraints we have used as many experiments as possible. We include experiments performed using a variety of techniques from 6 different laboratories. The resulting data set provides a good, first approximation of the multi-dimensional volume defined by silicate melts coexisting with mantle residual assemblage in pressure, temperature, composition space. Values of the adjusted correlation coefficient (R) for the regressions that yielded eqns. 1-10 range from 0.61 to 0.97. For a perfect fit of the right-hand side variables to the left-hand side variable, R is 1.0. The values of R for the temperature regressions (eqns 1 and 6) are 0.88 and 0.89. Fig. 6a provides a comparison of temperatures predicted by eqns. 1 and 6 to the experimental temperature.

Temperatures for 56 of the 64 experiments used to constrain eqns. 1 and 6 are predicted to within +/- 25 ^{o}. The goodness of fit for eqns. 1-5 to the plagioclase-saturated experiments and 6-10 to the spinel-saturated experiments has been evaluated (Fig. 6b) by using the temperature, and Mg#, NaK# and wt. % TiO_2 in the melt phase for each experiment, and eqns. 1-5 and 6-10 to predict pressure. Pressures for 59 of the 64 experiments used to constrain eqns. 1-10 are predicted to within +/- 2 kbar of the experimental pressure, a reasonable estimate of the interlaboratory pressure differences in piston cylinder devices (Johannes et al., 1971). The 'best' and 'worst' case fits for the melt component eqns. are shown in Fig. 7. As an example of a best case, values of the Qz component are predicted for each of the spinel-saturated experiments with eqn. 10 and compared to the experimentally observed values. As an example of the worst case, values of the Ol component for the same melts are predicted with eqn. 7 and compared to the experimentally determined values of Ol.

The lower values of R for eqns. 7 and 8 may reflect limitations of the various experimental approaches represented in the data set, as well as inter-laboratory, analytical differences. For example, the lower temperature, peridotite-basalt sandwich experiments of Fujii and Scarfe (1985) are fit well by eqns. 6-10. The higher temperature sandwich experiments, however, are not. This difference could reflect a lack of equilibrium between the melt and the sandwich minerals in these higher temperature experiments. The lack of equilibrium in the higher temperature experiments might result because the rate of dissolution of the augite may be too slow for the experiment to attain the true equilibrium phase assemblage. Alternatively, the difference could be due to the absence of a Cr variable in our quantitative description. To test the first hypothesis, a synthetic analog of one of the higher temperature melts (melt composition # 10 from Table 6) of Fujii and Scarfe (1985) was prepared for a series of melting experiments. If this melt composition (F&S,#10) is multiply saturated at 10 kbar then it should have augite + orthopyroxene + spinel (+/- olivine, as olivine is

in reaction with melt along the multiple saturation boundary). The F&S,#10 experimental composition (solid square) is compared to the composition predicted with eqns. 7-10 (open square with cross) in Fig. 8, using the same projection schemes described in Fig. 3. The predicted composition projects at lower Cpx contents in the Oliv - Cpx - Qtz projection (Fig. 8a) and at lower Plag contents in the Oliv - Cpx - Plag projection (Fig. 8b), relative to the projected position of F&S,#10. Based on the position of the estimated 10-kbar multiple saturation boundary and the inferred olivine + augite + liquid boundary, F&S,#10 should have augite on its liquidus, followed by the assemblage olivine + augite at lower temperatures. The melting experiments reported in Table 6 confirm that F&S,#10 crystallizes augite on its liquidus at temperatures between 1295 and 1310^{o}C (within 15^{o} of the reported liquidus temperature; Fujii and Scarfe, 1985). A melting experiment 30^{o} below the liquidus also contained only augite + liquid. The F&S,#10 composition is representative of a subset of the 'multiply saturated' experiments reported in the literature, and included in the data set to constrain eqns. 1-10, that are not well fit by the resulting equations. The melting experiments reported in Table 6 suggest that the F&S,#10 composition is poorly fit by description of the spinel-multiple saturation boundary provided by eqns. 6-10 because this composition is not multiply saturated with the sandwich minerals present in the charge at the reported pressure and temperature.

An additional test of the quantitative descriptions of the plagioclase- and spinel-multiple saturation boundaries is provided by comparing the temperatures and melt compositions in the B-series experiments presented in Tables 2 and 3 to the temperatures and melts compositions predicted for these melts by eqns. 1-10 (Table 7). The B-series experiments presented in Tables 2 and 3 were not used to constrain the quantitative descriptions of the spinel- and plagioclase melting equilibria presented in the text. The choice of starting compositions and temperatures for the B-series experiments was guided with eqns. 1-10. The temperatures of the experiments are

predicted to within 15^{o} for 4 of the 5 examples shown in Table 7. Melt compositions in experiments B30 and B52 are poorly fit by the compositions predicted with eqns. 7-10 with respect to SiO_2 and Al_2O_3 in particular, however the melt compositions in experiments B54 and B56 are well matched by the predicted compositions using the same eqns. The melt composition in experiments B63 is close to the composition predicted with eqns. 2-5. Work is currently underway to refine the descriptions of the multiple saturation boundaries provided by eqns. 1-10 by 1) using a more robust technique to describe the multiple saturation surfaces with the experimental data, and to describe the errors associated with the fits, 2) excluding data such as the F&S,#10 composition that are demonstrated not to be multiply saturated with the mantle residual assemblage, 3) incorporating more data such as the B-series experiments in Tables 2 and 3, and 4) incorporating the effects of Cr/Al variations into the treatment.

The coefficients for the independent variables in the temperature expressions are positive for (P-0.001), and negative (or zero) for the compositional variables (1-Mg#), NaK# and TiO_2. The two-fold increase in the magnitude of the positive dependence of temperature on (P-0.001) between the plagioclase-lherzolite (eqn. 1) and the spinel-lherzolite (eqn. 6) melting expressions is similar to that observed in CMAS (Presnall et al, 1979). The negative coefficients for (1-Mg#), NaK# and TiO_2 reflect melting point lowering effects caused by the addition of FeO, Na_2O, K_2O and TiO_2, respectively.

Equations 1-10 quantify the observations of many experimentalists (Takahashi and Kushiro, 1983; Fujii and Scarfe, 1985; Falloon and Green, 1987). These authors have pointed out that the boundary defined by melts saturated with the mantle residue phases is not univariant in the natural system, and melts in equilibrium with the mantle residual assemblage can vary over a range of compositions. In other words, mantle melts do not all plot at a single point on a temperature - composition phase diagram (e.g., a projection) at a given pressure, the composition of a multiply saturated melt depends on the bulk composition of the system. The magnitudes of the effects of variation in Mg#

and NaK# on the projected compositions of liquids in equilibrium with a plagioclase-lherzolite mantle residue at 8 kbar are shown for a range of melt compositions (Mg# = 0.5 to 1.0 and NaK# = 0.0 to 0.5, TiO_2 = 0.75 wt. %) in Fig 9. The composition of a liquid (shown here in terms of normative Oliv, Cpx, Qtz and Plag components) saturated with olivine + orthopyroxene + augite + plagioclase varies dramatically as NaK# and Mg# vary. Increasing NaK# decreases the Qtz component in the projected compositions of predicted primary melts (Fig. 9a), and melts range in composition from Qtz-undersaturated through Qtz-saturated.

At a given pressure, the effect of decreasing Mg# is to shift the projected positions of melts from plagioclase-lherzolite sources to lower normative Cpx and higher normative Oliv (Fig. 9a and 9b). This effect is similar to that observed in the simple system CaO-MgO-Al_2O_3-SiO_2-FeO at 1 atm. on the phase boundaries olivine + low-Ca pyroxene + plagioclase + augite + liquid and olivine + plagioclase + augite + liquid (Shi and Libourel, 1991). As the Mg# of the system decreases, the piercing point defined by the boundary olivine + plagioclase + augite + liquid in the Anorthite - Olivine - Cpx plane shifts towards Olivine. At a given pressure, increasing NaK# increases the Plag component in the projected compositions of predicted primary melts (Fig. 9b). This effect is qualitatively similar to that depicted for 1-atm, multiply saturated, natural system liquids by Grove and Juster (1989). It is also consistent with the study of Biggar and Humphries (1981) on the effect of increasing Na_2O on the 4-phase piercing point forsterite + diopside + plagioclase + liquid in the system CMAS+Na_2O at 1 atm. In this simple system study, increasing Na_2O content of the liquid saturated with forsterite, diopside and plagioclase shifts the composition of that liquid towards higher normative plagioclase content.

MELTING IN THE UPPER OCEANIC MANTLE, ESTIMATING THE PRIMARY MAGMAS OF MORB

Assumptions and model input

To model the mantle-melting process we make three simplifying assumptions. The first is that the MORB-mantle source is uniform in its mineralogy at the onset of melting, consisting of olivine, two pyroxenes and at least one aluminous phase. Although uniform in mineralogy, we assume that the bulk composition of the mantle may vary, and are interested in predicting the effect of varying bulk mantle composition on the partial melt produced at a given pressure. The third assumption is that melting in the upper oceanic mantle is volatile-free. To model the mantle melting process we need to 1) estimate partition coefficients, 2) estimate the mantle source composition, 3) estimate the modal mineralogy of the source, 4) estimate the melting reaction, and 5) specify the melting model, extent of melting or depletion and pressure of melting.

Estimating melt compositions with eqns. 2-5 and 7-10

Equations 2-5 and 7-10 provide mineral component descriptions of melts in equilibrium with the mantle residual assemblage. The Mg#, NaK# and TiO_2 contents of potential primary melts must be estimated to use these equations. Estimates of TiO_2 and NaK# for melts of the upper oceanic mantle are obtained with the batch melting equation:

$$C_l=C_o/(D_B+F(1-P_B)) \qquad (11)$$

where C_l is the concentration of TiO_2, for example, in the melt, C_o is the initial concentration of TiO_2 in the solid, D_B is the bulk partition coefficient for TiO_2 between the solid and the melt, weighted by the initial mode of the solid, F is the extent of melting, and P_B is the bulk partition coefficient for TiO_2 between the solid and the melt, weighted by the stoichiometric coefficients of the melting equation. We use eqn. 11 to model both batch melting and fractional melting processes. By setting F=0.01-0.20 we estimate the TiO_2 contents of melts produced in single increments (or 'batches') of melting. By calculating increments of F=0.01-0.001 and removing most of the melt at

each increment, we use the batch melting equation to approximate fractional melting, modeled as incremental batch melting with incomplete melt withdrawal.

Partitioning of elements between mantle minerals and melt. Distribution coefficients for CaO, Na_2O, K_2O and TiO_2 between mineral phases and melt were calculated from experimental data provided in Table 3, data of Bartels et al. (1991) and Grove et al. (1991) and Grove et al. (in prep). We do not assume any temperature and composition dependence for the distribution coefficients, and treat the pressure dependence very simply: one set of distribution coefficients are used for calculations at pressures less than 9 kbar and another for calculations at pressures greater than 9 kbar. The Mg#s of melts coexisting with the mantle source were estimated by applying an olivine/melt $K_D^{Fe\text{-}Mg}$ ($FeO^{ol}MgO^{liq}/FeO^{liq}MgO^{ol}$) of 0.30, the average of 109 $K_D^{Fe\text{-}Mg}$ determinations (1σ=0.05) over the pressure range of 8 - 20 kbar (Thompson, 1974; Thompson, 1975; Takahashi and Kushiro, 1983; Elthon and Scarfe, 1984; Takahashi, 1986; Falloon and Green, 1987; Baker and Eggler, 1987; Ulmer, 1989; Bartels et al., 1991; Grove et al., 1990; this study). The Mg# of olivine in the mantle source was estimated by using mineral-mineral Fe-Mg exchange K_Ds for olivine, orthopyroxene, augite and spinel and the modal proportions of these minerals to calculate a mass balance with the Mg# of the bulk mantle. This method of estimating the Mg# of the melt works well for small melt fractions, because it determines the Mg# of the melt that would be in exchange equilibrium with the mantle source at the beginning of melting. To better model Fe-Mg systematics for larger melt fractions, work is currently underway to solve the mass balance for FeO and MgO between a fraction of melt and the residue, given the quantity of melt produced, initial mantle composition, initial mantle phase proportions, stoichiometric coefficients of the melting reaction, mineral/mineral Fe-Mg exchange coefficients and the olivine/melt K_D (i.e. after the method of Langmuir and Hanson, 1980).

Estimates of the depleted mantle source composition. A composition for the depleted MORB mantle is estimated by assuming that it represents the residue left by extracting a small degree melt from the primitive mantle composition. The actual extent of melting that occurred to produce the MORB mantle from the primitive mantle is not precisely known. The extent of depletion estimated from Sm-Nd isotopic systematics (Hart and Zindler, 1986) is < 3%. Hofmann (1988) proposed 1-2% depletion, based on mass balance constraints between primitive mantle, average continental crust and average MORB. We have estimated a MORB mantle composition by depleting the primitive mantle composition of Hart and Zindler (1986) by 1.3 %. The calculation entailed extracting melts from the primitive mantle over the pressure range 1 - 25 kbar, using melt model 3 (see below). Melting over a range of pressures produces a range of primary melt compositions and therefore a range of mantle residue compositions. The residues from each of the pressure steps were averaged together to obtain a well mixed, depleted MORB-mantle composition (Table 8).

Estimates of modal proportions of mineral phases in the mantle. We calculated the modal mineralogy of the upper oceanic mantle in the plagioclase-lherzolite and spinel-lherzolite fields using materials balance methods. Mineral phases similar to those produced in our experiments at appropriate pressures were balanced against the primitive mantle composition of Hart and Zindler (1986). The experimentally produced phases chosen for the mass balance have Mg#s similar to those inferred to be present in the mantle source (mineral phase compositions from Table 3; Bartels et al., 1991; Falloon and Green, 1987; Takahashi, 1986). The modes of the depleted MORB-mantle composition are estimated by calculating the change in the modal assemblage with progressive melting with the stoichiometric coefficients of the melting reaction. Representative modes for spinel-lherzolite at 10 kbar and plagioclase-lherzolite at 8 kbar are provided in Table 8.

Estimates of the melting reaction. Estimates of the stoichiometric coefficients for the melting reactions are provided in Table 4 and assumed constant over the melting interval. To model spinel-lherzolite melting (pressures > 9 kbar) we used the reaction 0.82 augite + 0.40 orthopyroxene + 0.08 spinel = 1 liquid + 0.30 olivine, and for plagioclase-lherzolite melting (pressures < 9 kbar) we used the reaction 0.28 augite + 0.19 orthopyroxene + 0.58 plagioclase = 1 liquid + 0.05 olivine.

Model primary melts from the depleted MORB-mantle source (the forward approach)

In this section we estimate Mg#, NaK# and TiO_2 contents for melts generated over a range of pressures and extents of melting, by batch melting and incremental batch (or 'fractional') melting, from the estimated depleted MORB-mantle composition. Given these estimates of Mg#, NaK# and TiO_2 contents, eqns. 2-5 and 7-10 provide mineral component descriptions of these melts. The mineral component description, together with the Mg#, NaK# and wt.% TiO_2 contents are then transformed to a wt.% oxide description. Compositions of partial melts have been estimated over the pressure interval of 20 to 4 kbar (within the spinel and plagioclase stability fields). Several recent studies have suggested that melts produced at pressures higher than 25 kbar (the stability field of garnet) constitute some part of the magmas erupted at mid-ocean ridge spreading centers (Bender et al., 1984; McKenzie and Bickle, 1988; Klein and Langmuir, 1987; Salters and Hart, 1989). We have extrapolated our experimental data set only to 20 kbar. Experimental data are not sufficient to constrain the compositions and temperatures of melts coexisting with garnet, olivine, orthopyroxene and augite.

Compositions of primary magmas and aggregate primary magmas are estimated using the predictive method presented above with the following melting models: 1) isobaric, batch melting; 2) isobaric, incremental-batch, accumulated melting with incomplete melt withdrawal; and 3) polybaric, incremental-batch, accumulated melting with incomplete melt withdrawal.

Model 1: Isobaric batch melts

Model 1 melts are produced by a single increment of melting (a 'batch') of a specified extent, at a single pressure. Equation 11 is used to estimate TiO_2 and NaK# for these melts, with F (extent of melting) equal to the desired batch increment. Mg# is estimated as described above. These estimated values are plugged into eqns. 1-10 along with pressure to predict major element composition and temperature of melting. The effects of changing pressure and extent of melting on the major element compositions of the magmas produced are apparent in the model 1 melts predicted for extents of melting of 5, 10 and 20 % and pressures between 5 and 20 kbar (Table 8, model 1 melts).

The extent of melting that can occur before exhausting one of the 4 phases, olivine, orthopyroxene, augite and plagioclase or spinel, is estimated using the stoichiometric coefficients of the mantle-melting reaction combined with the estimated modal mineralogy of the mantle source. For the depleted mantle 1 composition (assuming batch melting) plagioclase is exhausted from the plagioclase-lherzolite residue at approximately 10 % melting; spinel appears to disappear from spinel-lherzolite at approximately 38% melting. Augite is exhausted at approximately 39 % melting from the plagioclase-lherzolite source and at approximately 23 % melting from the spinel-lherzolite source. We have chosen a melt % of 20 % as the outside limit for our batch melting models because evidence from abyssal peridotites suggests that the primary magmas of MORB coexisted with olivine, orthopyroxene, augite and an aluminous phase (Cr-Al spinel) when they were formed (Dick et al., 1984; Fujii, 1989). The effect of near-fractional melting on the extents of depletions at which phases will be exhausted cannot be directly assessed without a quantification of the dependance of the mantle melting reaction on mantle melt composition.

The melt compositions produced with the batch melting model, from the depleted mantle 1 model composition at pressures between 8 and 15 kbar, and melt extents of 10 - 20 % are broadly similar to primitive MORB, particularly in terms of

K_2O, Na_2O and TiO_2. These characteristics reflect both the depleted nature of our MORB-mantle source (Table 8, depleted mantle 1) and the relatively low extents of melting (<25%). At a constant pressure, increasing the extent of melting decreases the abundances of TiO_2, Na_2O, K_2O, SiO_2, and Al_2O_3, and increases the abundances of FeO, MgO, and CaO in the melt. These effects can be largely understood in terms of the changing NaK# of the melts produced as extent of melting increases. At low melt extents, NaK# is high, and thus the multiply saturated melts have higher contents of normative plagioclase (higher SiO_2, Al_2O_3, Na_2O). As the melt extent increases, the NaK# drops, and the multiply saturated melts have lower contents of normative plagioclase (higher FeO, MgO, CaO). At constant extent of melting, increasing pressure of melting results in lower SiO_2, and higher Al_2O_3, FeO, and MgO. Calculated batch melts that illustrate the relation between pressure and extent of melting are shown in Fig. 10a on a Na_2O vs. FeO diagram. Klein and Langmuir (1987) observed a negative correlation between FeO and Na_2O in their global data set of MORB compositions, and inferred that this negative correlation resulted from the coupling of increased extent of melting (which decreases Na_2O in primary magmas), and increased pressure of melting (which increases FeO in primary magmas; Langmuir and Hanson, 1980). This inference led them to suggest that the Na_2O-FeO correlation observed in the global MORB data set reflected a melting process in the upper oceanic mantle that resulted in the production of greater extents of melting, when melting began at deeper pressures (40 kbar), and the lesser extents of melting when melting began at lower pressures (14 kbar). The trends shown in Fig. 10a are consistent with Klein and Langmuir's suggestion of the general effects of pressure and extent of melting, or mantle composition, on the resulting mantle melt composition. It is also apparent from Fig. 10a, that another process that can lead to a negative correlation between Na_2O and FeO is increasing the extent of melting at a fixed pressure, or over a limited range of pressures.

The effects of pressure and extent of melting on the CaO/Al_2O_3 vs. FeO characteristics of calculated batch primary magmas are shown in Fig. 10b. At a fixed pressure, increased extent of melting results in higher CaO/Al_2O_3 and FeO in the calculated magma compositions. At fixed extent of melting, increased pressure of melting results in lower CaO/Al_2O_3 and higher FeO. The correlation observed between CaO/Al_2O_3 and FeO in the batch melts calculated over a increased pressures and extent of melting is positive, and is opposite to the inverse correlation observed between Na_2O and FeO for the same calculated melts.

Effect of mantle composition on the compositions of batch melts

Melts produced by the model 1 melting process at 8 and 15 kbar from the primitive and depleted mantle compositions shown in Table 8 are compared on Na_2O vs. FeO and CaO/Al_2O_3 diagram in Fig. 11. Compositions of primary magmas produced from the depleted mantle source are shifted to lower Na_2O contents, and slightly higher FeO contents at the same pressure and extent of melting, relative to compositions of primary magmas produced from a more fertile source.

Model 2: Isobaric, incremental-batch, accumulated melting with incomplete melt withdrawal

In their recent trace element study of abyssal peridotites, Johnson et al. (1990) suggested that upper mantle peridotite is depleted of its basaltic component through a fractional melting process. Isobaric incremental, accumulated melting with incomplete melt withdrawal is a step-wise process calculated to model isobaric, progressive depletion of a mantle source similar to near-fractional melting at a single pressure. The process of incremental, accumulated melting with incomplete melt withdrawal is similar to the melting process described by Langmuir et al. (1977) as 'continuous but incomplete removal of melt as melting proceeds'. During a single step, a small (1 %) batch of melt is produced. The composition of this increment of melt is calculated in the same way as the model 1 batch melts described above, with F=.01. Most (90%) of this increment of

melt is then drawn off and pooled, and the bulk composition, mineral mode and Mg# of the olivine in the residue is recalculated. The new bulk composition, mineral mode, and olivine Mg# of the mantle residue then used as the starting points for the next step. Calculated compositions of accumulated primary melts generated from this process at pressures between 5 and 20 kbar and melt %s of 5.2, 10.3 and 20.2 are presented in Table 8 (model 2 melts). The outside limit of melting extent was again chosen to be less than the extent of melting (assuming the batch model) at which augite is exhausted.

Calculated model 2 melts are shown on Na_2O vs. FeO and CaO/Al_2O_3 vs. FeO diagrams (Figs. 12a and 12b). The compositions of the model 2 melts differ from the model 1 melts generated at similar pressures and extents of melting. The fractional nature of the process that produced the model 2 melts effectively scavenges more Na_2O from the residue as melting proceeds. The difference between the model 1 and model 2 melts is less marked in the case of plagioclase-lherzolite melting because the presence of plagioclase in the source makes Na_2O more compatible in the plagioclase-lherzolite residue than in the spinel-lherzolite residue.

The differences in Na_2O content (and K_2O) between the model 1 and model 2 melts generated at the same pressures and extents of melting but by different melting processes are in part responsible for the differences in the CaO/Al_2O_3 ratios observed for the same melts (Figs. 10 and 12). The higher contents of Na_2O and K_2O in the melts produced by the model 2 process result in higher values of NaK#. NaK# is one of the parameters used in eqns. 2-5 and 7-10 to estimate the major element composition of melts saturated with a plagioclase- or spinel- lherzolite assemblage. Increased NaK# results in a predicted melt composition that has a higher normative Plag content, relative to Cpx, Oliv and Qtz (see earlier discussion). Magma compositions with higher normative plagioclase, relative to normative clinopyroxene, olivine and quartz, have higher Al_2O_3 contents, lower CaO contents, and thus lower CaO/Al_2O_3 ratios. Estimated spinel-lherzolite melt compositions with higher NaK# also have higher SiO_2

and lower total FeO and MgO contents, relative to spinel-lherzolite melt compositions with lower NaK#, although both will have similar Mg#. Compare, for example, melts in experiments B52 and B54 (Table 3). These melts were produced at the same pressure, and have similar Mg#s and TiO_2 contents, but different NaK# values (0.15 and 0.28, respectively). The melt composition in B54, which has the higher NaK# value, has a lower CaO/Al_2O_3, higher SiO_2, higher Al_2O_3, and lower FeO, MgO and CaO. This effect of NaK# is significant for near-fractional melting models in the upper oceanic mantle that involve removal of the melt fractions as they are produced and for batch melting models that involve varying the extent of melting between batches. The NaK# values of melts change substantially over the melt extent range appropriate for magma generation in the upper oceanic mantle as the result of stripping away melt fractions, or increasing the extent of melting, because Na_2O and K_2O are incompatible in the spinel-lherzolite assemblage. The Mg# variation will be less because Mg# is buffered, to a certain extent by the large proportion of olivine (+ orthopyroxene) in the residue (see Fig. 2). Thus, both the FeO and MgO contents of the melts increase as the residue becomes more depleted (during near-fractional melting), or as the melt extent increases (during batch melting), even as the Mg# increases, because the NaK# is decreasing.

Temperature of melting in the upper oceanic mantle

Fig. 13 depicts the mantle solidus in the simple system CMAS determined by Presnall et al. (1979); the temperatures of the depleted mantle residue predicted using the expressions presented above, the depleted mantle 1 composition and the model 2 melting assumptions; and the solidus inferred by McKenzie and Bickle (1988) from natural system experiments. Curves representing the temperature of the residue after 3 and 6 % incremental-batch, accumulated melting steps with partial melt withdrawal, and the temperature of the residue at which an initial 0.1 % batch melt is present are shown. The incremental-batch, accumulated melting process involves removing 90% of 1 % melt batches from the mantle, 3 and 7 times, to accumulate 2.7 % and 6.1 % total

fractions of melt, respectively. Thus, the accumulated, batch melting temperatures presented in Fig. 13 represent the temperature of the mantle residue at the extraction of the final increment. Note that the initial 0.1 % batch melt increment is produced at a temperature that is considerably higher than the mantle solidus inferred by McKenzie and Bickle (1988) (dashed line) from natural system experimental data. This difference may stem from a variety of sources. Small amounts of hydrous phases (serpentine, talc, etc.) may have been present in the natural starting material of the peridotite melting experiments used to constrain the McKenzie and Bickle (1988) solidus. Initial dehydration of these minerals could lower the observed solidus, relative to that of an anhydrous mantle peridotite. Furthermore, as discussed above, determining the solidus directly by peridotite melting at pressure is difficult given current experimental and analytical techniques. Such solidus determinations are thus likely to be subject to error.

Model 3: Polybaric, incremental-batch, accumulated melting with incomplete melt withdrawal

Melt generation below mid-ocean ridge spreading centers is best modeled by an adiabatic melting and melt extraction process that occurs over a range of pressures in the upper mantle (McKenzie, 1984; Klein and Langmuir, 1987, 1989; McKenzie and Bickle, 1988). We have formulated a simple melting column model to estimate the compositions of an aggregate primary magma consisting of a blend of primary magmas produced over a range of pressures. This model is different from the melting column model presented by Klein and Langmuir (1987, 1989), in that we model polybaric, near-fractional melting, during which 90% of the melt produced is removed at each step. Thus, in this simple model, the amount of melt generated at any pressure within the melting column is always the same, and the average pressure of melting is simply the mean pressure of the melting column (compare to the mean melt extent and pressure of Klein and Langmuir, 1987; which are weighted towards the upper (more shallow) part of the melting column.). An incremental-batch, accumulated melting process with

incomplete melt withdrawal is calculated over a range of pressures to simulate melting of mantle rising adiabatically. The increment of melting that occurs in mantle peridotite per kbar of adiabatic rise is assumed to be 1.0% (similar to the value of Ahern and Turcotte, 1979, of 1.2%). At some initial pressure, during the ascent of a parcel of mantle, its temperature intersects that of the mantle solidus, and melting begins. The parcel of mantle rises 1 kbar and melts 1.%. Of this 1.% melt, 90% is removed and accumulated elsewhere. The depleted parcel of mantle, retaining a small amount of melt, rises another kbar, and melts another 1.%. 90% of this batch is removed and accumulated with the previous batch, etc. The melts are accumulated and mixed to become an aggregate of primary melts sampled from a range of pressures. Between each step of melt production, the composition, mineral mode and Mg# of the residual olivine in the mantle parcel is recalculated.

The composition of the aggregate primary magma depends on the depth of solidus intersection, the total extent of depletion of the mantle source achieved and the degree to which the sampling process is representative of all the melts generated. The total extent of depletion, or maximum extent of melting reached at the top of the melting regime, is in turn a function of the depth of solidus intersection, or onset of melting, as well as the thermal regime in the upper mantle beneath the spreading center. If melting starts deep enough, and continues to relatively shallow levels beneath the spreading center, then the limiting factor to generating melt from the mantle residue will be the amount of augite present. If melting starts shallower, and/or if cooler isotherms established by conductive cooling at the top of the mantle extend to deeper levels in the upper mantle then melting of the rising mantle may be terminated prior to the exhaustion of augite. We have calculated the arrays of melt increment compositions for 6 examples of the model 3 process. In examples 1 - 3, the depleted mantle 1 composition (Table 8) is used. In examples 4 - 6, the fertile mantle of Hart and Zindler (1986) is used. In these models, upwelling mantle peridotite of the depleted mantle composition

intersects the solidus at 25, 20 and 15 kbar (example 1, 2 and 3, respectively). Melts are extracted from the residue until a depth of 4 kbar (arbitrary imposition of the depth at which cooling by conduction lowers the ambient temperature below the mantle solidus) is reached. In all the models presented in Table 9, melting proceeds until the cut-off pressure of 4 kbar without exhausting the augite in the residue. The aggregate primary magma, or average of the increments, for each example is presented in Table 9. Compositions of the increments and the aggregate primary magma composition are shown for the first three models on a Na_2O vs. FeO diagram in Fig. 14.

The curvature of the arrays of melt increments arise from the combined effects of decreasing pressure, and increasing 'depleted' character of the mantle peridotite. The Na_2O variation is a function solely of extent of depletion of the source peridotite; as a parcel of peridotite rises in the mantle and melts are produced and stripped away, the residual solid becomes increasingly depleted in incompatible components. Increments of melts produced from the increasingly depleted residual solid contain less Na_2O. The FeO variation during the model 3 melting process, however, is a function of both increasing extent of depletion, which increases the amount of FeO in the melt produced, and decreasing the pressure of melting, which decreases the amount of FeO in the melt produced. These competing effects result in the FeO variations shown in Fig. 14. The effect of pressure on the FeO content of the melt is demonstrated by the shift in the arrays of melts present in each model melting column towards higher FeO with increased pressure.

The aggregate primary magma from one melting path (or column) is the average composition of the individual increments if all the increments from that path are sampled equally, and mixed completely. These aggregate primary magmas are shown in Fig. 14 for each of the 3 melting paths discussed. As anticipated (Klein and Langmuir, 1987), the FeO content of an aggregate primary magma from a melting column increases with increasing depth of the melting column. The Na_2O variation is controlled by the

extent of depletion of the peridotite, which in turn is controlled by the depth at which melting begins and the depth at which melting terminates. For all 3 examples in Fig. 14, melting does not proceed to the extent that augite is exhausted from the lherzolite source, but rather is terminated by intersection of the rising mantle with an assumed lithospheric boundary, above which it is too cool to melt. Because melting is initiated at different depths, however, the total extent of melting achieved from the melting column in each example, varies from ~ 18% in the 25-4 kbar example to 10% in the 15-4 kbar example. The high Na_2O, low FeO end of the array defined by the aggregate primary magmas (open symbols) in Fig. 14 is thus from the shallowest melting column, in which the total extent of depletion achieved of the mantle source is the smallest. The low Na_2O, high FeO end of the array is from the deepest melting column, in which the mantle achieves the highest extent of melting (systematics similar to those suggested by Klein and Langmuir [1987] to explain the variations observed in the MORB global array, see below; although the range in pressure spanned by these three melting columns of 25 - 4 kbar is significantly lower than the range suggested by Klein and Langmuir of 40 - 1 kbar in their Table 3, 1987 to explain the observed diversity of MORB compositions).

Extent of depletion achieved of the mantle source and thickness of the oceanic crust

An important parameter that varies systematically with the Na_2O and FeO variations between the 3 melting column models described above is the implied mantle temperature. The ambient mantle temperatures implied by the three simple, one-dimensional melting models varies from ~ 1500 ^{o}C in example 1, to ~ 1340 ^{o}C in example 3. The crustal thickness (simple calculation for estimating crustal thickness for each melt model is presented in notes for Table 9) yielded by each column also varies. Resulting crustal thickness, assuming that all the melt produced in the melting column is extracted to form the oceanic crust, increases by a factor of 3 between the high-Na_2O and low-Na_2O ends of the aggregate primary magma array (from 4 km to 13 km). The observed average thickness of young oceanic crust is ~ 6 km (range of 3 - 8 km, Reid

and Jackson, 1981). The observed variation in crustal thickness shows a systematic decrease with increasing spreading rate (Chen and Sandwell, 1990). The larger variation in crustal thickness observed at slower spreading rates is associated with fracture zones and is interpreted by Chen and Sandwell (1990) to reflect a transition from a 3-D structure of crustal accretion at slow ridges to a 2-D accretion pattern at fast spreading ridges. Klein and Langmuir (1987) have suggested that crustal thickness and MORB chemistry are correlated. This suggestion is based primarily on the observation of thicker crust at Iceland (~ 15 km, seismically determined; low Na_2O, high FeO) and thinner crust at the mid-Cayman Rise (~ 3 km, estimated from geologic evidence; high Na_2O, low FeO). The observed crustal thicknesses intermediate between these extremes do not show a significant correlation with basalt chemistry. The lack of a correlation between the estimates of intermediate crustal thickness and basalt chemistry may result from inadequate data coverage; alternatively it may suggest that crustal thickness and basalt chemistry are decoupled. In the latter case, additional variables must operate during the decompression melting process to buffer the crustal thickness to a more constant value while still allowing for the observance of the geochemical signatures associated with extent and pressure of melting variations in MORB (see below). For example, we use a simple, one-dimensional melting column model that assumes a fixed melt production rate upon decompression. This model may be too simple to predict observables such as crustal thickness associated with melting in the upper oceanic mantle realistically.

Mantle melting systematics and fractional crystallization of MORB magmas, global and local trends revisited

Klein and Langmuir (1987) observed an inverse correlation between FeO and Na_2O in their corrected, global MORB data set. Their observations were based on a data set of evolved MORB (MgO contents < 8.5 wt.%). In this study we find a similar

inverse correlation between FeO and Na_2O for compositions of primary melts generated over a range of pressures and extents of melting, and thus confirm their insightful interpretation linking the inverse correlation observed in evolved MORB to the interplay between the effects of pressure and extent of melting on the compositions of melts generated in the upper oceanic mantle.

The main trend of Na_2O vs. FeO observed by Klein and Langmuir (1989, their Fig. 5) in the global MORB data set corrected to 8.0 wt.% MgO is shown in Fig. 15a. The global data set presented by Klein and Langmuir (1987,1989) is corrected to 8.00 wt.% MgO to normalize out the effects of 'low-pressure' fractional crystallization. They applied a correction to the Na_2O and FeO contents of MORB that was estimated by fitting Na_2O vs. MgO and FeO vs. MgO curves for suites of MORBs, over the compositional range of 5 - 8.5 wt. % MgO. The solid curves in Fig. 15a show the compositions of melts calculated with the near-fractional melting model (model 2) at 8, 10, 12 and 15 kbar from the depleted mantle 1 source composition (Table 8), for total extents of depletion of the mantle source ranging from < 5% - 20.2 %. The primary magma trend is steeper than the main Na_2O-FeO trend defined by evolved MORB, and the two do not coincide. In order to directly compare the estimated primary melts to the sampled lavas, the primary melts need to be 'corrected' forward to 8.00 wt.% MgO.

Correcting estimated primary magmas 'down temperature'

We corrected the primary magmas 'down temperature' by fractionally crystallizing them at low (near 1-atm.) pressures. The fractionation paths were calculated by estimating the positions of the 1-atm. phase boundaries (olivine + plagioclase + liquid, and olivine + plagioclase + augite + liquid) for a given primary magma in both the Oliv - Cpx - Qtz and the Oliv - Cpx - Plag projections. The boundaries were estimated by calculating the normative Ol, Cpx, Pl and Qz components of the liquid on the olivine - plagioclase - augite - orthopyroxene - liquid 5-phase boundary with equations 2-5. To use these equations, we fixed pressure at 0.001 kbar,

and specified the Mg#, NaK# and TiO_2 contents of the primary magma. The positions of the 3-phase olivine + plagioclase + liquid - and the 4-phase olivine + plagioclase + augite + liquid boundaries were then inferred from the position of the 5-phase boundary (see below for more discussion). The 3 and 4-phase boundaries were then used to determine the fractional crystallization path that would evolve the primary magma to 8.00 wt.% MgO at near-ocean floor pressures. The hatchered lines in Fig. 15a show the estimated primary magmas corrected to 8.00 wt.% MgO; the solid arrows connect estimated primary melts representing 5.3%, 10.3% and 20.2% depletion of the mantle source at 12 kbar (10.2, 11.5 and 12.8 wt.% MgO, respectively) to the fractionated melts, each with 8.00 wt. % MgO.

The 5.3% aggregate primary magma from 12 kbar contains 10.2 wt.% MgO and is in the olivine primary phase volume at near-ocean floor pressures, relative to the estimated 1-atm. phase boundaries. The fractional crystallization path (all of the fractional crystallization models were calculated as described in the notes for table 10) that evolves this aggregate primary magma from 10.2 wt.% MgO (Mg# = 0.727) consists of one, 0.02 mass increment of olivine subtraction, followed by 12, 0.02 increments of 30% olivine + 70% plagioclase subtraction (MgO = 8.03 wt.%, Mg# = 0.65). The total % crystallized for this path is 23. The 5.3% aggregate primary melt from 12 kbar does not reach augite saturation at 1-atm. conditions over the crystallization interval of 10.2 - 8.00 wt. % MgO. The fractional crystallization path that evolves the 10.3% (MgO = 11.5 wt.%; Mg# = 0.733) aggregate primary magma to 8.00 wt.% MgO consists of the subtraction of two, 0.02 increments of olivine, followed by 19, 0.02 increments of 30% olivine and 70% plagioclase subtraction (MgO = 8.00 wt.%, Mg# = 0.61). The total % crystallized for this path is 35. The 10.3% aggregate primary melt from 12 kbar also does not reach augite saturation at 1 atm. over the crystallization interval of 11.5 - 8.00 wt.% MgO. The cumulate rock types produced from the low-pressure fractional crystallization paths that evolve both the 5.3 and the 10.3% aggregate primary magmas

to 8.00 wt.% MgO are dunite and troctolite. In contrast, the 12-kbar, 20.2% aggregate primary melt does reach augite saturation during 1-atm. fractional crystallization to 8.00 wt.% MgO. The 1-atm. fractional crystallization path that evolves this primary magma from 12.8 wt. % MgO (Mg# = 0.742) to 8.00 wt. % MgO consists of 3, 0.02 increments of olivine subtraction, followed by 12, 0.02 increments of 33% olivine + 67% plagioclase subtraction, followed by 14, 0.02 increments of 12% olivine + 39% augite + 49% plagioclase subtraction (MgO = 7.98 wt.%, Mg# = 0.57). The total % crystallized for this path is 44, and the cumulate rock types produced are dunite, troctolite and gabbro.

The primary magmas from 8 - 15 kbar corrected forward by low-pressure fractionation overlap much of the variation in Na_2O and FeO (with the exception of the higher FeO MORB) spanned by the global array of Klein and Langmuir (1987,1989) (Fig. 15a). The relatively closely spaced curves defined by the estimated primary magmas are displaced to higher FeO and Na_2O as a result of the forward correction by fractional crystallization at near ocean floor conditions. The slopes of the isobaric melting curves become more shallow. Much of the range of variation in FeO and Na_2O spanned by the global array can be produced by melting the depleted MORB mantle source (Table 8) to achieve ~5 - ~20 % total depletion, over the pressure range of 8 - 15 kbar; and then subsequent fractionation at near-ocean floor conditions. The closely spaced curves of melt compositions are shifted to more widely spaced fractionated magma compositions, however, and thus the full span of the global array of MORB is not covered by the magma compositions yielded by low-pressure fractionation of aggregate primary magmas from the same mantle source. Variations in mantle source composition vary the Na_2O and FeO contents of mantle melts (see Fig. 11), and will therefore vary the resulting Na_2O and FeO contents of 'corrected' primary magma compositions at 8.00 wt.% MgO. Major element source variations may be partly responsible for the generation of the spread of compositions observed in the global array of MORB at 8.00 wt.% MgO. However, an additional variable that affects the

compositions of primary melts as they evolve to sampled MORB is the pressure at which crystallization occurs.

The effects of differentiation to 8.00 wt.% MgO by fractional crystallization over the pressure range of 4 -0.001 kbar (within the upper oceanic mantle and oceanic crust) are shown in Fig. 15b. In this figure the aggregate primary magmas are 'corrected' to 8.00 wt.% MgO by estimating fractional crystallization paths at 4 kbar for several aggregate primary magmas generated at 8 - 15 kbar using the same approach as described above for estimating near-ocean floor fractional crystallization paths. The effect of fractionating the same aggregate primary magma to 8.00 wt.% MgO at a higher pressure relative to the low-pressure fractionation paths discussed above can be to achieve higher Na_2O and FeO contents in the magmas fractionated at higher pressure. For example, the 10.3% aggregate primary magma from 12 kbar contains 2.94 wt.% Na_2O and 9.06 wt. % FeO at 8.00 wt.% MgO as the result of fractionation at low pressures (0.001 kbar) and 3.10 wt.% Na_2O and 9.82 wt.% FeO at 8.00 wt.% MgO as the result of fractionation at 4 kbar. The higher Na_2O and FeO contents in the magma fractionated at the higher pressure result from the earlier appearance of augite in the higher pressure fractionation path. Both Na_2O and FeO are incompatible in the assemblages olivine + plagioclase and olivine + plagioclase + augite. The crystallization of both assemblages therefore enriches the liquid in Na_2O and FeO. However, the crystallization of the assemblage olivine + plagioclase + augite takes out less MgO as compared to the crystallization of the assemblage olivine + plagioclase (for a given mass of the assemblage crystallized). The controlling factor in the extents of fractional crystallization for the paths presented in Fig. 15 is MgO content. It requires more fractional crystallization to evolve a magma from 11.5 wt.% MgO to 8.00 wt.% MgO by subtracting out olivine + plagioclase + augite, as compared to subtracting out olivine + plagioclase. Therefore, if augite appears in the fractional crystallization path, then greater enrichments in the incompatible FeO and Na_2O occur. For example, the

10-kbar, 10.3% aggregate primary magma (MgO = 11.2 wt.%) is in the olivine primary phase volume at 4 kbar. The fractional crystallization path that evolves this magma to 8.00 wt.% MgO at 4 kbar consists of 2, 0.02 mass increments of olivine subtraction, followed by 8, 0.02 increments of 30% olivine + 70% plagioclase subtraction, followed by 11, 0.02 increments of 14% olivine + 31% augite + 56% plagioclase subtraction (MgO = 8.00 wt%, Mg# = 61). The total % crystallized for this path is 35. The same 10-kbar, 10.3% aggregate primary magma is also in the olivine primary phase volume at 1 atm. The fractional crystallization path that evolves this magma to 8.00 wt.% MgO at 1 atm. consists of 2, 0.02 mass increments of olivine subtraction, followed by 15, 0.02 increments of 30% olivine + 70% plagioclase subtraction (MgO = 8.02 wt.%, Mg# = 63). The total % crystallized for this path is 29. As shown in Fig. 15b, the range of Na_2O and FeO contents spanned by the global array of MORB at 8.00 wt.% MgO (including the high FeO MORB) can be produced by melting a depleted MORB mantle source from 5 - 20 % total extent over the pressure range of 8 - 15 kbar, and then fractionating these primary magmas within the upper 25 km of the oceanic mantle and oceanic crust.

The origin of 'local trends'

In addition to effectively rotating and translating the Na_2O-FeO trend from the steeper, primary trend, to the more shallow, global trend, fractional crystallization over a range of pressures may play a significant role in generating the dispersion of MORB compositions from the corrected global array that is responsible for 'local trends' or cross trends identified by Klein and Langmuir (1987, 1989) and Brodholt and Batiza (1989) for locations along the mid-Atlantic ridge. The cross trends are observed because MORB corrected to 8.00 wt.% MgO from the same region sometimes contain variable amounts of Na_2O and FeO contents at the same MgO contents. These MORB are characterized by a positive correlation between Na_2O and FeO at 8.00 wt.% MgO (and an inverse correlation between Na_2O and SiO_2) as compared to the inverse correlation between Na_2O and FeO associated with the global array. The cross trends are found in

some MORB suites that show the parent-derivative relationships recognized in several MORB suites and ascribed to fractional crystallization (Grove and Bryan, 1983; Tormey et al., 1987; Grove et al., 1990, Grove et al., 1991).

Three of the local trends identified by Klein and Langmuir (1989, their Fig. 5a) are shown in Fig. 15c. As discussed above, aggregate melts produced at the same pressure (10 kbar for these isobaric models) and representing the same total extent of depletion of the same mantle source will evolve to different Na_2O and FeO contents at 8.00 wt.% MgO by fractional crystallization at elevated pressures (for example, 4 kbar) and near-ocean floor pressures (1 atm.). Thus, fractional crystallization of the same aggregate primary magma over a range of pressures from the top of the melting regime in the upper mantle to shallow levels in the oceanic crust can produce variations in the basalts sampled at one location along a ridge that cut across the global array. The trends in Na_2O and FeO shown by the curves connecting the 1-atm. and 4-kbar fractionated magmas from each of the three 10-kbar, aggregate primary magmas are similar in slope to the cross trends identified at the mid-Cayman rise, $11.4^{o}N$-$11.97^{o}N$ on the mid-Atlantic ridge and the Reykjanes peninsula. There is a slight shallowing in slope in the three cross trends identified by Klein and Langmuir (1989) with increasing FeO and decreasing Na_2O in the corrected MORB, which is also apparent in the trends indicated by the forward corrected primary magmas at 1 atm. and 4 kbar. The positively correlated 'cross' trends defined by primary magmas fractionated forward at 4 kbar and 1 atm. shown in Fig. 15b and c with respect to FeO and Na_2O are also characterized by decreasing SiO_2 and CaO/Al_2O_3 with increasing FeO and Na_2O. The span of Na_2O and FeO indicated by the observed cross trends along the mid-Atlantic ridge may indicate fractional crystallization over a greater range of pressures than that modelled (increasing the difference in pressures increases the amount of enrichment of FeO and Na_2O achieved in the magmas fractionating at higher pressures, because augite appears earlier in the fractionation path at higher pressures). Alternatively, variations in

aggregate primary magma compositions fed to the spreading center may contribute to the observed span. The cross trends observed at the mid-Cayman rise and the Reykjanes peninsula are shifted to lower and higher FeO contents, respectively, relative to the forward corrected 10-kbar aggregate melts in Fig. 15c. In terms of the simple isobaric models used for this discussion, these shifts can be explained by deriving the aggregate primary magmas from slightly lower and higher pressures (9 and 12 kbar), respectively (detailed models starting from MORB lavas sampled at these locations are presented below).

In the previous discussion we assumed that the primary magmas were generated isobarically. As discussed earlier, however, melting in the mantle beneath mid-ocean ridges is most likely a polybaric and near-fractional process. Aggregate primary magmas estimated from the depleted MORB-mantle source using the polybaric melting model (model 3, Table 9) are compared to the global array of Klein and Langmuir (1987) and the local trends of Klein and Langmuir (1989) in Fig. 16a on a wt.% Na_2O vs. wt.% FeO diagram and in Figs. 16b and c on wt.% Na_2O vs. wt.% SiO_2 diagrams. The polybaric, aggregate primary magmas show an inverse correlation with FeO and Na_2O that is steeper than the global array defined by MORB corrected to 8.00 wt.% MgO, and a positive correlation between Na_2O and SiO_2 (Figs. 16a and b). The polybaric, aggregate primary magmas corrected 'down temperature' to 8.00 wt.% MgO by fractional crystallization at near-ocean floor conditions and at 4 kbar fall within the global array defined in terms of Na_2O and FeO (Fig. 16a). The corrected primary magmas fall within the roughly triangular region of MORB corrected to 8.00 wt.% MgO in terms of Na_2O and SiO_2 (Fig. 16c, after Klein and Langmuir, 1989; their Fig. 6b). The 'down-temperature' fractionation corrections were carried out as described above for the isobaric aggregate primary magmas. For example, the polybaric, aggregate primary magma generated in a melting column with a mean pressure of melting corresponding to 12 kbar, and representing 14% depletion of the depleted MORB-mantle source (wt.%

MgO = 12.00, Mg# = 0.736), follows the following crystallization path to 8.00 wt.% MgO at near-ocean floor conditions: 5, 0.01 mass increments of olivine subtraction, followed by 16, 0.02 increments of 31% olivine + 69% plagioclase subtraction, followed by 4, 0.02 increments of 13% olivine + 56% plagioclase + 31% augite subtraction (8.03 wt.% MgO, Mg# = 0.60). The total amount crystallized for this low-pressure path is 35%. The same aggregate, polybaric primary magma follows the following crystallization path at 4 kbar (pressure corresponding to the top of the melting regime): 5, 0.01 mass increments of olivine subtraction, followed by 7, 0.02 increments of 31% olivine + 69% plagioclase subtraction, followed by 18, 0.02 increments of 11% olivine + 51% plagioclase + 38% augite subtraction (8.01 wt.% MgO, Mg# = 0.58). The amount crystallized for this high-pressure path is 41%. The slopes of the positive correlation between Na_2O and FeO, and the inverse correlation between SiO_2 and Na_2O at 8.00 wt.% MgO caused by fractionating these polybaric, aggregate primary magmas at 0.001 and 4 kbar are similar to the local trends shown again in Fig. 16a and c and discussed above. The correspondence between the corrected primary magmas and the global array of MORB is in agreement with the interpretation of Klein and Langmuir (1987,1989) that the low FeO, high Na_2O MORB come from more shallow melting regimes (mean pressure of melting ~ 8-9 kbar) in which the mantle is melted to a lesser extent, and the high FeO, low Na_2O MORB come from deeper melting regimes (mean pressure of melting ~ 15 kbar) in which the mantle is melted to a greater extent. For the mantle composition used in these calculations, the high FeO, low Na_2O portion of the global array can be produced by melting at a mean pressure of 15 kbar, to a total extent of ~ 18% (similar to the deepest melting column calculation presented in Table 9 and Fig. 16a). The low FeO, high Na_2O portion of the global array can be produced by melting at a mean pressure of < 9.5 kbar (the mean pressure of the most shallow melting column calculation), and/or a total extent of melting of < 10%. The greater span in the observed local trends, relative to that produced solely by fractionating the

same primary magma at different pressures is most likely indicative of a range of incoming primary magma compositions. The range could result from variations in the mantle source composition, and/or from variations in the aggregation process (i.e. Klein and Langmuir, 1989, see below for further discussion), and/or by interaction between the mantle melts and the overlying mantle (see below).

For polybaric fractionation of primary MORBs to occur, favorable thermal conditions are required in the uppermost oceanic mantle. The models discussed above suggest that fractionation over the range of 0.001 - 4 kbar pressures (and possibly greater) are required to generate the dispersion of Na_2O and FeO that characterizes the local trends observed by Klein and Langmuir (1989). Primary MORB magma will only experience fractionation at pressures of 4 kbar and lower in the upper mantle if the temperatures are cool enough at these depths.

Klein and Langmuir have interpreted the cross trends as representative of within-column mixing of melts produced by differing extents of melting at different pressures, i.e., small degree melts generated at high pressures mixing with high degree melts generated at lower pressures, within the same mantle column. It is apparent from Fig. 17, that incomplete mixing of the individual increments of melt produced over a range of pressures along the same melting path, in this case example number 2 from Table 9, is capable of generating an array of trends of FeO vs. Na_2O. However, mixing the compositional extremes generated along a single melting path (e.g., mixing the increment from the most fertile mantle, at 20 kbar with the increment from the most depleted mantle at 4 kbar, Fig. 17) in differing proportions yields a Na_2O - FeO correlation that is similar to the global trend, not perpendicular to it. Mixing increments from more shallow, more depleted portions of the melting column (e.g., melt increments from 10 and 4 kbar depth in the melting column) in varying proportions yields a positive Na_2O-FeO correlation, however these melts, sampled directly would be more depleted, with respect to Na_2O, and will also have a more shallow level melting signature than

most MORB sampled from the sea-floor. Three stage mixtures of variable proportions within the melting column can be envisioned that would exhibit the positive correlation between Na_2O and FeO, with the appropriate absolute abundances of Na_2O to resemble the local trends (i.e. a 2:1 mix of the most fertile increment and the most depleted increment, which then mixes with varying amounts of the increment produced at 13 kbar). Clearly, in a three-dimensional melting regime, characterized by near-fractional, polybaric melting processes, the potential exists for incomplete sampling and mixing between various melt fractions to generate a variety of partial aggregate primary magmas. The overall vector associated with the intra-column mixing processes, however, is similar to the vector associated with varying mean extents and pressures of melting (see open symbols in Fig. 14), rather than orthogonal, as suggested by Klein and Langmuir (1989).

We have also discuss briefly below two additional post-segregation processes that impart a chemical signature to the derivative magmas that could be similar to polybaric fractionation involving aug as a crystallizing phase. These processes can also generate the dispersion of Na_2O and FeO at similar MgO contents in the derivative magmas. Mixing of a range of evolved magma compositions that achieved their compositions by varying amounts of fractional crystallization from the same primary, or near-primary magma in a crustal level magma chamber, with a replenishment of that near-primary magma can produce Na_2O-FeO trends similar to the local trends. If primary MORB magmas percolate through the upper mantle en route to the spreading axis, then assimilation of mantle material may occur to modify the melt composition. It may be possible to generate the Na_2O-FeO systematics observed in the local trends with this process, however the melting process is not well enough constrained at this point to quantify the process. In the discussion above of calculating estimated primary magmas forward to 8.00 wt.% MgO and in the discussion below of correcting observed MORB with ~8.00 wt.% MgO back to estimated primary magma compositions, we have made

the simplifying assumption that fractional crystallization over a range of pressures is the dominant post-segregation process operating to modify the primary magmas of MORB. This assumption allows us to correct for the fractional crystallization processes that relate primary magmas to MORB and see the trend in terms of Na_2O and FeO contents generated by melting processes that produced the primary magmas of MORB. The trend that emerges is similar to that produced by increased extents of melting over a limited pressure range (8 - 15 kbar).

Back-calculation of 'parental' and primitive MORB to primary magma compositions (the inverse approach)

Although several have been tested experimentally, no sampled MORB has been demonstrated to be multiply saturated at elevated pressure with the mantle phases olivine, orthopyroxene, augite, and an aluminous phase. Furthermore, most MORB glasses have Mg#s lower than 0.70 (total Fe as Fe^{2+}), which should be considered as a minimum Mg# for melts that could be in equilibrium with mantle ol (composition Fo_{89}-Fo_{90}). Thus sampled MORB are not primary melts. To use the chemical compositions of sampled MORB to constrain the melting processes beneath mid-ocean ridge spreading centers we need to remove, or 'see through' the compositional signatures of post-segregation magmatic processes. These processes may include any or all of the following: 1) low pressure fractionation and mixing processes that occur within the oceanic crust, 2) fractional crystallization of primary magmas in the upper mantle, en route to emplacement into the spreading center, and 3) assimilation of mantle (or lithosphere) by primary magmas as they move through the upper mantle.

The occurrence of low pressure fractional crystallization has been demonstrated in almost all MORB suites discussed in the literature, and is also suggested by the presence of the cumulate rocks that make up layer 3 of the oceanic crust. Further compositional modification can occur within crustal level magmas chambers as the result of mixing between evolved magmas produced by low pressure fractional crystallization

of olivine + augite + plagioclase and more primitive magmas delivered to the magma chamber as it is replenished with near-primary magma from depth (O'Hara and Mathews, 1981). This mixing process yields a chemical signature, distinct from that of crustal level, low-pressure fractionation of olivine + augite + plagioclase, that might resemble crystallization of olivine + augite + plagioclase at pressures in the mantle below the oceanic crust (see below). A similar chemical signature may be imparted to MORB in crustal-level magma chambers as the result of 'in situ' or side-wall crystallization (Langmuir, 1989). In this process, cooler, highly evolved liquids are generated in boundary layers, along the walls of magma chambers, while the interior of the chamber remains hotter and less fractionated. Residual liquids from the boundary layer are incorporated into the hotter, less evolved interior, yielding a mixed chemical signature, distinct from low pressure fractional crystallization.

A second process that may modify the chemical composition of a MORB primary magma is fractional crystallization of primary magmas en route to the surface. As discussed above, primary magmas become saturated with ol upon emplacement to lower pressures relative to the pressure at which they were last equilibrated with their mantle residue. As these primary magmas move up into the cooler, uppermost mantle, they crystallize olivine. Further crystallization involves plagioclase and augite; the crystallization assemblage depends on the pressure at which fractionation occurs. Evidence for high pressure (pressures greater than oceanic crustal pressures, i.e. 3 - 8 kbar) crystallization of olivine + augite + plagioclase is found in high pressure gabbros sampled at the mid-Cayman Rise (Elthon, 1987) and in the MORB liquid trends observed at the Kane Fracture Zone (Tormey et al., 1987). A method for removing the effects of fractional crystallization of primary magmas en route to emplacement into the spreading center is presented below.

The chemical composition of a primary magma may be modified by the assimilation of (incorporation of, or reaction with) mantle material as the magma rises

through the upper mantle. Assimilation may occur as melts percolate through the mantle, or it may occur within the region where the increments of melts are collected or 'aggregated'. Evidence for melt percolation is found in the plagioclase-bearing peridotites that occur in the abyssal peridotite suite and have been interpreted as depleted mantle peridotite that was 'injected' with melt at shallow levels in the upper mantle (Dick, 1989). Evidence for melt aggregation in the mantle beneath spreading centers has been inferred from structures in ophiolites (Nicolas and Prinzhofer, 1983). The residual peridotite in the uppermost mantle is most likely a harzburgite, containing only a few % of augite. A MORB primary magma, saturated with olivine, orthopyroxene, augite and a Cr-Al spinel upon leaving its mantle residue, is saturated with olivine only upon decompression. If this magma is allowed to equilibrate with the overlying mantle, lower pressure partial melting will result. Olivine will crystallize from the magma, and orthopyroxene (+ any residual augite left in the depleted uppermost mantle) will melt and be incorporated into the magma (Kelemen, 1990). This process increases the SiO_2 content and decreases the total FeO and MgO contents of the magma, while buffering the Mg# at mantle-melt values. CaO and Al_2O_3 also increase slightly in the magma. The chemical variation among a range of magmas that initially stemmed from the same primary magma composition and subsequently underwent differing amounts of this mantle assimilation process, followed by olivine fractionation, may resemble the chemical variation produced by the crystallization of olivine + augite + plagioclase from this same primary magma at pressures in the uppermost mantle, below the oceanic crust (see below).

Correcting MORBs for 'up temperature' to remove the effects of fractionation

Two different groups of MORB glasses were calculated back to hypothetical primary magma compositions. The parental MORB group consists of 4 MORB glasses with MgO less than 9 wt.% that span the range of Na_2O-FeO variation observed by Klein and Langmuir (1987) in the global MORB data set. In addition, each of the

glasses in this group represent a 'parental' lava composition for their respective regions (i.e. Bryan et al., 1981). The term parental implies that these compositions can be related to the more evolved lava compositions sampled in the same region by processes of near ocean-floor fractional crystallization. The primitive MORB group consists of 5 MORB glasses that represent the extremes in Na_2O-FeO variation in the primitive MORB data set compiled by Elthon (1990). The inversion technique described below provides a prediction of the fractionation processes that have modified a MORB after it was separated from its mantle source, and is used to calculate each of the selected MORBs back to a potential primary magma composition. This technique assumes that the primary magma segregated at one pressure.

The technique uses mineral component projection schemes, eqns. 2-5 and 7-10, a test of Mg#, and experimentally constrained estimates of phase proportions and mineral compositions involved in the fractionation processes. The inversion technique starts by using the $NaK^{\#}$, Mg# and TiO_2 of the MORB to calculate the values of mineral components of liquids multiply saturated with the pl- and sp-mantle residue assemblage over a range of pressures (using eqns 2-5 and 7-10). The MORB composition is also expressed in terms of mineral components. If the MORB mineral components and the calculated mineral components of a predicted primary magma at one pressure coincide, and if its Mg# is appropriate for a liquid in equilibrium with a mantle residue (i.e. μ 0.70), then the MORB may be a primary magma. If none of the calculated multiply saturated compositions coincide with the MORB, and/or if the Mg# is not appropriate for a liquid in equilibrium with a mantle residue, the next step is to determine the simplest fractionation process that would allow the MORB to be brought into coincidence with one of the multiple saturation boundaries. This approach assumes that fractional crystallization is the process that modified the MORB from its primary magma composition. The relative projected positions of the MORB and the calculated multiply saturated liquids are used to determine the minimum pressure of fractionation that

could bring the MORB back to a calculated primary magma composition. The compositional changes caused by this fractionation process are added back to the MORB composition by carrying out a backward fractionation process. Phase compositions and proportions estimated from experimentally determined olivine-plagioclase-liquid or olivine-augite-plagioclase liquid boundaries are used (Grove et al., 1990; Grove et al., 1991). Once the MORB has been corrected by this back fractionation process, the revised composition is used with eqns. 2-5 and 7-10 to calculate a new set of liquids saturated with the mantle residue assemblage over a range of pressures. These are compared to the revised MORB composition and, if necessary, the process of back fractionation is adjusted until a 'back-fractionated' MORB composition is obtained that has the appropriate Mg# and mineral components to be in equilibrium with the mantle residual assemblage. Primary magma compositions estimated with this technique will be referred to as 'back-fractionated primary magmas'.

A parental MORB from the mid-Cayman rise (KN-54-2-2; Thompson et al., 1980) serves as an example to illustrate this inversion technique. Fig. 18 shows the Oliv - Cpx - Qtz and Oliv - Cpx - Plag pseudo-ternary projections with the composition of KN-54-2-2 and the compositions of multiply saturated liquids calculated with eqns 2-5 and 7-10, over a range of pressures using the $NaK^{\#}$, Mg# and TiO_2 content of KN-54-2-2. Note that the projected position of KN-54-2-2 closely resembles the position of the 9-kbar, spinel saturated multiply saturated liquid. However KN-54-2-2 does not pass the Mg# test for a melt in equilibrium with a mantle residue, and thus must have been modified since its primary magma separated from the mantle source. At each one of the plagioclase-bearing calculated multiply saturated liquids, the orientations of the olivine-plagioclase-augite-liquid (4-phase boundary) and olivine-plagioclase-liquid (3-phase boundary) boundaries may be inferred. The 1-atm. boundaries are shown in Fig. 18. To infer the orientations of the higher pressure boundaries, move the 1-atm. phase boundaries to the multiple saturation point for the desired pressure, keeping the 4 and 3-

phase boundaries parallel to their 1-atm orientations. This is a simplification of the phase relationships that is justified on the grounds that the slopes of the 3 and 4-phase boundaries do not change significantly with increasing pressure (Grove et al. 1991). These boundaries can be used to infer the liquid line of descent for a given MORB at that pressure. At 1-atm, KN-54-2-2 would have olivine + plagioclase as liquidus phases, and would follow the 3-phase boundary to the 1-atm. 4-phase boundary. By comparing the 3 and 4-phase boundaries at successively higher pressures with the projected composition of KN-54-2-2, an estimate can be made of the minimum pressure at which KN-54-2-2 may have experienced olivine + plagioclase + augite fractionation. For KN-54-2-2 the minimum pressure of olivine + augite + plagioclase fractionation is 8 kbar. At this pressure, the KN-54-2-2 composition and the position of the 4-phase boundary coincide. Therefore, we suggest that at 8 kbar the parental magma for KN-54-2-2 underwent some amount of olivine + plagioclase + augite fractionation. Olivine, augite and plagioclase are added to correct for this 8-kbar fractionation, and new projected compositions of liquids saturated with the mantle residue are then calculated using this revised MORB composition. For KN-54-2-2 a small amount of olivine addition returns the revised MORB composition to the calculated 10 kbar, spinel-multiple saturation boundary.

All the MORBs discussed in this section were returned to primary magma compositions using this technique. The back-fractionation paths that returned each MORB to a primary magma composition are summarized in Table 10. The degree of difficulty encountered in trying to return a fractionated MORB to its primary magma composition will be proportional to the complexity of the magmatic processes that have occurred. In the case of KN-54-2-2 the back-calculation procedure was not difficult. If the parental MORB for a given region is more evolved in terms of Mg# and near the 4-phase boundary at 1-atm (i.e. the composition from the Reykjanes peninsula), then the

solution becomes less constrained, because a number of possible paths could be followed back to a primary composition.

An important constraint on the elevated pressure liquid line of descent for the primary magmas of MORB is visible in Fig. 18. All of the MORBs we investigated (with the possible exception of #102, from the primitive MORB compilation of Elthon (1990) had primary compositions estimated by back-calculation that were derived from sp-saturated mantle residues. These primary liquids always plot in the olivine-primary phase volume relative to the 3 and 4-phase boundaries. If the primary magma segregates from its residue and then fractionates at pressures only slightly lower than the melting/segregation pressure (pressure of fractionation within 2 kbar of pressure of melting), then olivine fractionation (cumulate = dunite) is followed by olivine-augite fractionation (cumulate = wherlite), then olivine-augite-plagioclase fractionation (cumulate = gabbro). If the primary magma is removed from its residue and emplaced to a pressure more than 2 kbar lower than the segregation pressure, then olivine fractionation is followed by olivine-plagioclase fractionation (cumulate = troctolite), then olivine-augite-plagioclase fractionation.

Polybaric fractionation is demonstrated to account for the modification of the primary magmas of the diverse set of MORB examined above, and some combination of olivine, olivine-plagioclase and/or olivine-augite-plagioclase fractionation all play significant roles in generating the evolved compositions of the lavas we examined in detail. Augite may play a significant role even if the sampled lavas are not saturated with augite upon eruption because of the close proximity of the olivine-augite and the olivine-augite-plagioclase phase boundaries to compositions of partial melts from a spinel-lherzolite residue at elevated pressures.

Pressure of derivation of primary MORB and the relationship between primitive MORB and primary MORB

With the possible exception of one of the 9 MORB compositions, which has an Mg# of 0.70, and appears to be very close to a primary composition (ELT 102, Fig. 19), in general the MORB compositions considered above do not resemble predicted primary magma compositions, but have experienced post-segregation modification by fractional crystallization. This is not a new conclusion. As discussed earlier in this study and as pointed out by many authors (e.g. B.V.S.P., 1981), experimental petrology studies have generally failed to demonstrate that any MORB is saturated with the mantle residual assemblage at elevated pressure. In general, primitive and parental MORBs are <u>not</u> primary melts. The pressure of melting estimates for the back-fractionated primary magma compositions range from 9 - 15 kbar (Table 10). Therefore, most of the melting that produces the primary magmas of MORB appears to occur in the spinel-stability field and pressures greater than 15 kbar are not necessarily required to explain the major element chemical variations of parental and primitive MORB. Furthermore, the primary magmas of MORBs predicted with eqns 2-5 and 7-10, and estimated with the back-fractionation technique are <u>not</u> picritic, and contain 8.82 to 12.8 wt. % MgO (Tables 8, 9 and 10).

The calculated paths from the MORBs back to the parental primary magma compositions are shown on Na_2O vs. FeO and CaO/Al_2O_3 vs. FeO diagrams in Fig. 19. The trend defined by the spectrum of predicted primary magmas from the depleted MORB-mantle source provided in Table 8, produced at several pressures and over a range of extents of melting, coincides with primary compositions estimated for a range of parental and primitive MORBs by subtracting out the effects of fractional crystallization. The model 1, batch melting curves from Fig. 12 are also shown for comparison. The range of % melting obtained by comparing these back-fractionated primary magma compositions to melts produced by the model 1 melting process from the depleted

mantle 1 composition is 5 - 20 %. The back-fractionated primary magma compositions for the 9 parental and primitive MORBs are generally similar to the primary magma compositions estimated with eqns. 7-10 (spinel-lherzolite melting) and the melt models discussed above (compare Tables 8, 9 and 10). The pressure estimates indicated by the compositions of the back-fractionated primary magmas for the parental and primitive MORB (with the exception of ELT-102) are consistent with the melting pressures (within about 2 kbar) for the forward-calculated, model 2 melts of similar FeO, Na_2O and CaO/Al_2O_3.

In addition to pressure and extent of melting, mantle source composition controls the composition of primary magmas. The 9 MORB compositions discussed above were chosen because they have a wide range of FeO and Na_2O contents, which might, in turn, reflect a range of mantle source compositions. With the exception of ELT-102 and perhaps IOTJ, however, the array of MORBs chosen have major element characteristics similar to a range of extents of melts derived by melting a source similar to depleted mantle 1 (Table 8) between ~10 and 15 kbar. As shown above (Fig. 11), melts produced at similar extents of melting and pressure from a less depleted mantle have higher Na_2O and lower FeO. The low Na_2O - low FeO back-fractionated primary magma estimate for ELT-102 may reflect larger extent melts from a more fertile source mantle.

Klein and Langmuir (1987, 1989) have interpreted the negative correlation between Na_2O and FeO observed in the corrected global MORB data set as follows: high-Na_2O, low-FeO MORBs are produced by melting over a limited range of pressures (i.e. small extents of melting), with a shallow mean pressure. Low-Na_2O, high-FeO MORBs are produced by melting over a larger range of pressures (i.e. high extents of melting), with a deeper mean pressure. The high-Na_2O (>3 wt. %), low FeO portion of the primary global array is defined by the back-fractionated primary parents for the Indian Ocean triple Junction (IOTJ) and the mid-Cayman rise lavas (MCR). Both of the

primary magmas for these MORBs were produced by relatively small extents of melting (~3 - 6 %) at roughly 10 - 12 kbar. The back-fractionated primary magmas for the Kane Fracture Zone (23°N, MAR), and primitive MORB compositions 65, 45, and 72 have intermediate Na_2O (2 - 3 wt. %) and FeO, and were produced by a higher extent of melting (8 - 18 %), at a slightly higher pressure (13-15 kbar). Thus, the correlation between depth and extent of melting suggested by Klein and Langmuir (1987, 89) to explain the Na_2O-FeO systematics of MORB holds for these regions.

The correlation breaks down for the MORBs at the low-Na_2O (<2 wt.%) extreme of the array. The results presented in this study suggest that two other processes may contribute to the global trend of decreasing Na_2O with increasing pressure: increased extent of melting from the same source at the same pressure, and melting sources of variously depleted character at the same pressure. The back-fractionated primary magmas for MORBs from the Reykjanes Peninsula near Iceland and from 46°-32° S on the MAR have low Na_2O and lower FeO (see Fig. 19). These primary magmas were produced by melting at 11 - 15 kbar, roughly the same range of pressures of melting for the back-fractionated primary magmas with higher Na_2O, and similar, or lower FeO (Table 8). The difference may be that these magmas were produced by melting a more fertile mantle, but to greater extents. MORB from the Reykjanes Peninsula near Iceland, the FAMOUS region at 37°N on the MAR, and from 46°-32° S on the MAR are all 'enriched' or hot-spot influenced MORB. Enriched MORB have long been recognized as different from 'normal' MORB (e.g., Bryan, 1979). Dick et al. (1984) compared abyssal peridotites and associated basalt from the mid-Cayman rise, from just south of the Kane Fracture Zone and from FAMOUS, and concluded that the highest degree of melting occurred in the vicinity of mantle hot spots. We have shown that melts generated at the same pressure, but from a more fertile mantle source composition have lower FeO relative to melts from a less depleted source composition (Fig. 11). Thus, the MORB at the low Na_2O end of the array in the global

data set may have been produced by melting a more fertile mantle source, to a greater extent, and at a similar pressure, rather than by melting a similar mantle source at a greater depth.

CONCLUSION

Two types of information are necessary to understand the processes by which mantle is melted to produce MORB magma: 1) the compositions of melts produced in the mantle as a function of pressure, melting regime and mantle composition, and 2) methods for relating these estimated primary magmas to sampled MORB. This paper provides a step towards obtaining these types of information by presenting a quantitative framework for estimating melts of mantle peridotite and for evaluating the effects of fractional crystallization over a range of pressures on these melts. Calculated compositions of primary magmas produced by melting in the upper oceanic mantle are corrected 'down temperature' to 8.00 wt. % in order to directly compare them to sampled MORB corrected to 8.00 wt. % MgO. Selected MORB that span the range of Na_2O and FeO defined by the global array identified by Klein and Langmuir (1987) are corrected 'up temperature' to parental primary magmas and compared directly to estimated mantle melts. These comparisons yield the following observations: the total extents of depletion achieved by the decompression melting process range from ~5 - 20 %, the range of pressures of melting is relatively narrow, from 8 - 15 kbar, and much of the variation in major element chemistry observed in MORB can be explained by melting a similar depleted MORB mantle source. Further conclusions are: 1) the negative correlation between Na_2O and FeO observed by Klein and Langmuir (1987, 1989) in the global MORB data set is also present in the array of the primary magmas of MORB. 2) The operation of fractional crystallization over a range of pressures is responsible for the rotation of the steep, primary Na_2O-FeO trend to the more shallow trend observed in the evolved (non-primary) MORB. 3) The dominant vector

associated with intra-column mixing is not similar to the observed local trends, but is rather more similar to the vectors associated with varying extent and pressure of melting on the compositions of the melts produced. Fractional crystallization over a range of pressures (0.001 - 4 kbar) can generate the local trends observed at several areas along the mid-Atlantic ridge. 4) The correlation between pressure of melting (8 - 15 kbar), extent of melting (3 - 20 %) and Na_2O-FeO systematics observed by Klein and Langmuir (1987, 1989) generally holds for normal (not hot-spot influenced) MORB. 5) The primary magmas of low-Na_2O, hot-spot MORBs may have been derived by melting a more fertile mantle source, to a greater extent, at similar pressures to the intermediate -Na_2O normal MORB.

REFERENCES

Ahern, J. L., and Turcotte, D. L., Magma migration beneath an ocean ridge, Earth Planet. Sci. Lett., 45, 115-122, 1979.

Akella, J. and Kennedy, G. C., Melting of Gold, Silver and Copper-Proposal for a new high-pressure calibration scale. J. Geophys. Res., 76, 4969-4977, 1971.

Albee, A. L. and Ray, L., Correction factors for electron microprobe analysis of silicates, oxides, carbonates, phosphates and sulfates. Anal. Chem., 42, 1408-1414, 1970.

Baker, D. R., and Eggler, D. H., Compositions of anhydrous and hydrous melts coexisting with plagioclase, augite and olivine or low-Ca pyroxene from 1 atm to 8 kbar: Application to the Aleutian volcanic center of Atka. Am. Mineral., 72, 12-28, 1987.

Bartels, K. S., Kinzler, R. J., and Grove, T. L., High pressure phase relations of a near primary high alumina basalt from Medicine Lake Highland, N. California. Contrib. Mineral. Petrol., submitted.

Basaltic Volcanism Study Project, Basaltic Volcanism on the Terrestrial Planets. Pergamon Press, Inc., New York. 1286 pp, (1981).

Bence, A. E., and Albee, A. L., Empirical correction factors for the electron microanalysis of silicates and oxides. J. Geol., 76, 382-403, 1968.

Bender, J. F., Hodges, F. N., and Bence, A. E., Petrogenesis of basalts from the project FAMOUS area: Experimental study from 0 to 15 kbars. Earth Planet. Sci. Lett., 41, 277-302, 1978.

Bender, J. F., Langmuir, C. H. and Hanson, G. N., Petrogenesis of Basalt Glasses from the Tamayo Region, East Pacific Rise. J. Pet., 25, 213-254, 1984.

Biggar, G. M., and Humphries, D. J., The plagioclase, forsterite diopside, liquid equilibrium in the system CaO-Na_2O-MgO-Al_2O_3-SiO_2. Mineral. Mag., 44,309-314, 1981.

Boyd, F. R., and England, J. L., Apparatus for phase equilibrium studies at pressures up to 50 kbars and temperatures up to 1750žC. J. Geophys. Res., 65, 741-748, 1960.

Brodholt, J. P., and Batiza, R., Global systematics of unaveraged mid-ocean ridge basalt compositions: comment on "Global correlations of ocean ridge basalt chemistry with axial depth and crustal thickness" by E. M. Klein and C. H. Langmuir. J. Geophys. Res., 94, 4231-4239, 1989.

Bryan, W. B., Regional Variation and Petrogenesis of Basalt Glasses from the FAMOUS area, mid-Atlantic ridge. J. Pet., 20, 293-325, (1979).

Bryan, W. B., Finger, L. W., and Chayes, F., Estimating proportions in petrographic mixing equations by least squares approximation. Science, 163, 926-927, 1969.

Bryan, W. B., Thompson, G., and Ludden, J. N., Compositional variation in normal MORB from 22^{o} - 25^{o} N; mid-Atlantic ridge and Kane Fracture Zone. J. Geophys. Res., 86, 11815-11836, 1981.

Cordery, M. J., and Phipps-Morgan, J., A new approach to the problem of melt migration at mid-ocean ridges. J. Geophys. Res., submitted, 1991.

Dick, H. J. B., Fisher, R. L., and Bryan, W. B., Mineralogic variability of the uppermost mantle along mid-ocean ridges. Earth Planet. Sci. Lett., 69, 88-106, 1984.

Dick, H. J. B., Abyssal peridotites, very slow spreading ridges and ocean ridge magmatism. In: Magmatism in the Ocean Basins, eds.: Sounders, A. D., & Norry, M. J., Geol. Soc. Spec. Publ. No. 42, 71-105, 1989.

Elthon, D., The petrogenesis of primary mid-ocean ridge basalts. Reviews in Aquatic Sciences, 2, 1, 27-53, 1990.

Elthon, D., Pressure of origin of primary mid-ocean ridge basalts. In: Magmatism in the Ocean Basins, eds.: Saunders, A. D., & Norry, M. J., Geol. Soc. Spec. Publ. No. 42, 125-136, 1989.

Elthon, D., Petrology of gabbroic rocks from the mid-Cayman Rise spreading center. J. Geophys. Res., 92, 658-682, 1987.

Elthon, D. and Scarfe, C. M., High pressure phase equilibria of a high-magnesia basalt and the genesis of primary oceanic basalts. Amer. Mineral., 69, 1-15, 1984.

Falloon, T. J., and Green, D. H., Anhydrous partial melting of MORB pyrolite and other peridotite compositions at 10 kbar: Implication for the origin of primitive MORB glasses. Mineral. Petrol., 37, 181-219, 1987.

Fujii, T., Genesis of mid-ocean ridge basalts. In: Magmatism in the Ocean Basins, eds.: Saunders, A. D., & Norry, M. J., Geol. Soc. Spec. Publ. No. 42, 137-146, 1989

Fujii, T., and Bougault, H., Melting relations of a magnesian abyssal tholeiite and the origin of MORBs. Earth Planet. Sci. Lett., 62, 283-295, 1983.

Fujii, T., and Kushiro, I., Melting relations and viscosity of an abyssal tholeiite. Carnegie Inst. Yrb. 76, 1977.

Fujii, T., and Scarfe, C. M., Composition of liquids coexisting with spinel lherzolite at 10 kbar and the genesis of MORBs. Contrib. Mineral. Petrol., 90, 18-28, 1985.

Green, D. H., and Ringwood, A. E., The genesis of basaltic magma. Contrib. Mineral. Petrol., 15, 103-190, 1967.

Grove, T. L., Use of FePt alloys to eliminate the iron loss problem in 1-atmosphere gas mixing experiments: Theoretical and practical considerations. Contrib. Mineral. Petrol., 78, 298-304, 1981.

Grove, T. L., Gerlach, D. C., Sando., T. W., and Baker, M. B., Origin of calc-alkaline series lavas at Medicine Lake volcano by fractionation, assimilation and

mixing: Corrections and clarifications. Contrib. Mineral. Petrol., 82, 407-408, 1983a.

Grove, T. L., and Bryan, W. B., Fractionation of pyroxene-phyric MORB at low pressure: an experimental study. Contrib. Mineral. Petrol., 84, 293-309, 1983b.

Grove, T. L., and Baker, M. B., Phase equilibrium controls on the tholeiitic versus calc-alkaline differentiation trends. J. Geophys. Res., 89, 3253-3274, 1984.

Grove, T. L., and Juster, T. C., Experimental investigations of low-Ca pyroxene stability and olivine - pyroxene - liquid equilibria at 1-atm in natural basaltic and andesitic liquids. Contrib. Mineral. Petrol., 103, 287-305, 1989.

Grove, T. L., Kinzler, R. J., and Bryan, W. B., Natural and experimental phase relations of lavas from Serocki Volcano. Proc. Ocean Drill. Proc., Scientific Results, 106/109, 9-17, 1990.

Hart, S. R., and Zindler, A., In search of a bulk-earth composition. Chem. Geol., 57, 247-267, 1986.

Hofmann, A. W., Chemical differentiation of the Earth: the relationship between mantle, continental crust, and oceanic crust. Earth Planet. Sci. Lett., 90, 297-314, 1988.

Ito, K., and Kennedy, G. C., Melting and phase relations in a natural peridotite to 40 kilobars. Am. J. Sci., 265, 519-538, 1967.

Jaques, A. L., and Green, D. H., Anhydrous melting of peridotite at 0-15 kbar pressure and the genesis of the tholeiitic basalts, Contrib. Mineral. Petrol., 73, 287-310, 1980.

Johannes, W., Bell, P. M., Mao, H. K., Boettcher, A. L., Chipman, D. W., Hays, J. F., Newton, R. S., and Seifert, F., An interlaboratory comparison of piston-cylinder pressure calibration using the albite breakdown reaction. Contrib. Mineral. Petrol., 32, 24-38, 1971.

Johnson, K. T. M., Dick, H. J. B., and Shimizu, N., Melting in the oceanic mantle: an ion microprobe study of diopsides in abyssal peridotites. J. Geophys. Res., 95, 2661-2678, 1990.

Kelemen, P. B., Reaction between ultramafic rock and fractionating basaltic magma, Part I: Phase relations, the origin of calc-alkaline magma series, and the formation of discordant dunite. J. Pet., 31, 51-98, 1990.

Juster, T. C., Grove, T. L., and Perfit, M. R., Experimental constraints on the generation of FeTi basalts, andesites, and rhyodacites at the Galapagos spreading center, 85°W and 95°W. J. Geophys. Res., 94, 9251-9274, 1989.

Klein, E. M., and Langmuir, C. H., Global correlations of ocean ridge basalt chemistry with axial depth and crustal thickness. J. Geophys. Res., 92, 8089-8115, 1987.

Klein, E. M., and Langmuir, C. H., Local versus global variations in ocean ridge basalt composition: a reply. J. Geophys. Res., 94, 4241-4252, 1989.

Kushiro, I., Compositions of magmas formed by partial zone melting of the earth's upper mantle. J. Geophys. Res., 73, 619-634, 1968.

Kushiro, I., Origin of some magmas in oceanic and circumoceanic regions. Tectonophys., 17, 211-222, 1973.

Langmuir, C. H., Bender, J. F., Bence, A. E., Hanson, G. N., and Taylor, S. R., Petrogenesis of basalts from the FAMOUS area: mid-Atlantic ridge. Earth and Planet. Sci. Lett., 36, 133-156, 1977.

Langmuir, C. H., and Hanson, G. N., An evaluation of major element heterogeneity in the mantle sources of basalts. Philos. Trans. R. Soc. London, Ser. A, 297, 383-407, 1980.

Langmuir, C. H., Geochemical consequences of in situ crystallization. Nature, 340, 199-205.

Lindsley, D. H., Kesson, S. E., Hartzman, M. J., and Cushman, M. K., The stability of armalcolite: Experimental studies in the system MgO-Fe-Ti-O. Proc. 5th Lunar Sci. Conf., 521-534, 1974.

McKenzie, D., The generation and compaction of partially molten rock, J. Petrol., 25, 713-765, 1984.

McKenzie, D., and Bickle, M. J., The volume and composition of melt generated by extension of the lithosphere. J. Petrol, 29, 625-629, 1988.

Mysen, B. O., and Kushiro, I., Compositional variations of coexisting phases with degree of melting of peridotite in the upper mantle, Am. Mineral., 62, 843-865, 1977.

Nicolas, A. and Prinzhofer, A., Cumulative or residual origin for the transition zone in ophiolites: structural evidence. J. Pet., 24, 188-206, 1983.

O'Hara, M. J., Are any ocean floor basalts primary magma? Nature, 220, 683-686, 1968a.

O'Hara, M. J., The bearing of phase equilibria studies in synthetic and natural systems on the origin and evolution of basic and ultrabasic rocks. Earth Sci. Rev., 4, 69-133, 1968b.

O'Hara, M. J., Importance of the "shape" of the melting regime during partial melting of the mantle. Nature, 314, 58-62, 1985.

O'Hara, M. J., and Mathews, Geochemical evolution in an advancing, periodically replenished, periodically tapped, continuously fractionated magma chamber. J. Geol. Soc. London, 138, 237-277, 1981.

Presnall, D. C., Dixon, T. H., O'Donell, T. H., and Dixon, S. A., Generation of mid-ocean ridge tholeiites, J. Petrol., 20, 3-35, 1979.

Presnall, D. C., and Hoover, J. D., High pressure phase equilibrium constraints on the origin of mid-ocean ridge basalts. In: Magmatic processes: physicochemical principles, ed.. B. O. Mysen, 75-89, 1987.

Price, R. C., Kennedy, A. K., Riggs-Sneeringer, M., and Frey, F. A., Geochemistry of basalts from the Indian Ocean triple junction: implications for the generation and evolution of Indian Ocean ridge basalts. Earth Planet. Sci. Lett., 78, 378-396, 1986.

Reid, I., and Jackson, H. R., Oceanic spreading rate and crustal thickness. Marine Geophys. Res., 5, 165-172, 1981.

Riley, G. N. and Kolhstedt, D. L., Melt migration in silicate melt-olivine systems. Submitted to Earth Planet. Sci. Lett. (1991).

Stolper, E., A phase diagram for mid-ocean ridge basalts: Preliminary results and implications for petrogenesis. Contrib. Mineral. Petrol., 74, 13-27, 1980.

Salters, V. J. M., and Hart, S. R., The Hf-paradox and the role of garnet in the source of mid-ocean ridge basalts, Nature, 342,420-422, 1989.

Schilling, J. G., Zajac, M., Evans, R., Johnston, T., White, W., Devine, J. D., and Kingsley, R., Petrologic and geochemical variations along the mid-Atlantic ridge from 29^{o} N to 73^{o} N. Amer. J. Sci., 283, 510-586, 1983.

Shi, P. and Libourel, G. The effects of FeO on the system CMAS at low pressure and implications for basalt crystallization processes. Contrib. Mineral. Petrol., submitted, 1991.

Takahashi, E., Melting of a dry peridotite KLB-1 up to 14 GPa: Implications on the origin of peridotitic upper mantle. J. Geophys. Res., 91, 9367-9382, 1986.

Takahashi, E., and Kushiro, I., Melting of a dry peridotite at high pressures and basalt magma genesis. Am. Mineral., 68, 859-879, 1983.

Thompson, R. N., Primary basalts and magma genesis I. Skye, North-west Scotland. Contrib. Mineral. Petrol., 454, 317-341, 1974.

Thompson, R. N., Primary Basalts and magma genesis II. Snake River Plain, Idaho, U.S.A. Contrib. Mineral. Petrol., 52, 213-232, 1975.

Thompson, G., Bryan, W. B., and Melson, W. G., Geological and geophysical investigation of the mid-Cayman rise spreading center: geochemical variation and petrogenesis of basalt glasses. J. Geol., 88, 41-55, 1980.

Tormey, D. R., Grove, T. L., and Bryan, W. B., Experimental petrology of normal MORB near the Kane Fracture Zone: 22ž-25žN, mid-Atlantic ridge. Contrib. Mineral. Petrol., 96,121-139, 1987.

Ulmer, P., The dependence of the Fe^{2+}-Mg cation-partitioning between olivine and basaltic liquid on pressure, temperature and composition. An experimental study to 30 kbars. Contrib. Mineral. Petrol., 101, 261-273.

Fig. 1-1 Schematic diagram of decompression melting in the upper oceanic mantle (not to scale).

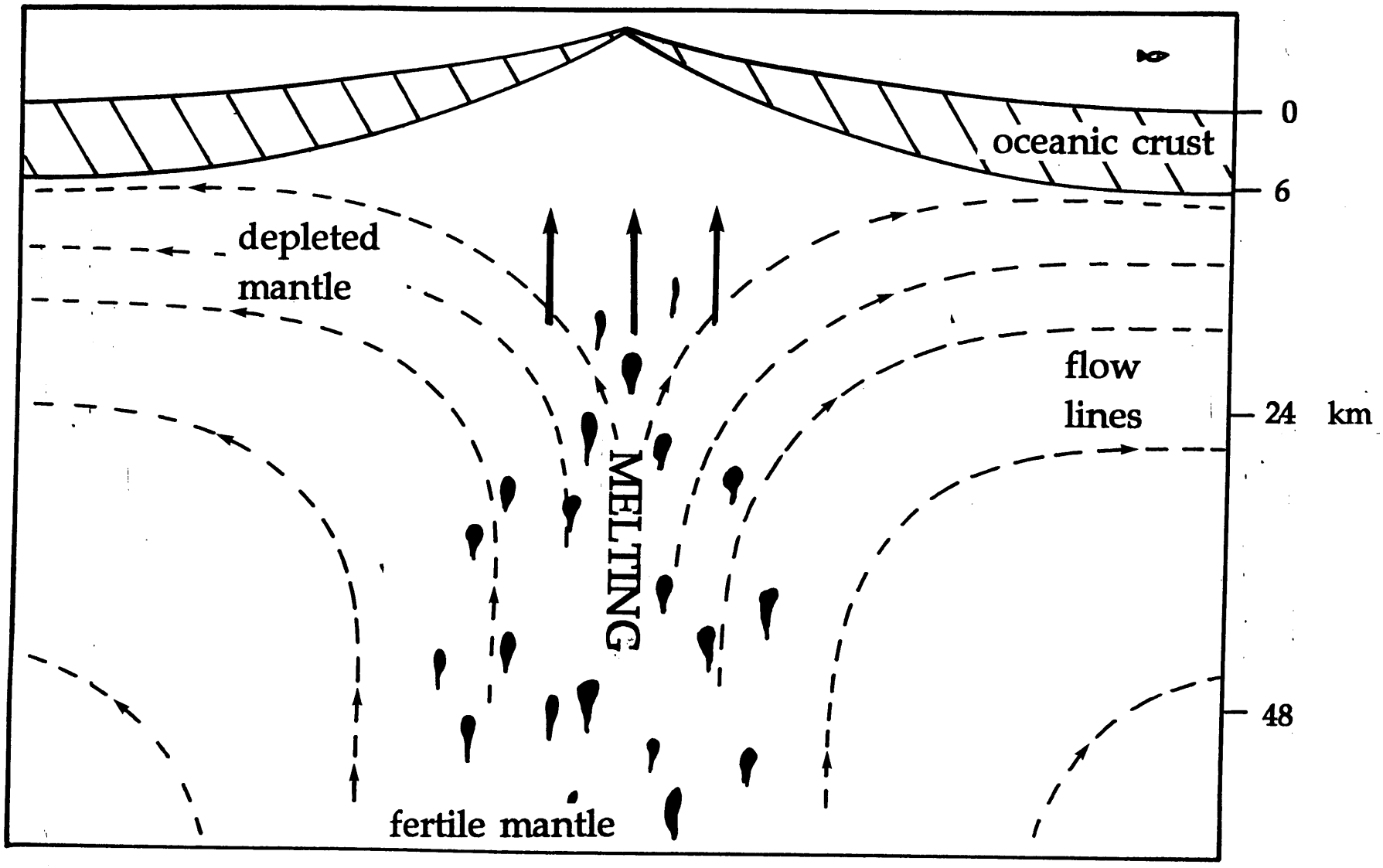
0
oceanic crust
6
depleted
mantle
flow
lines
24 km
MELTING
48
fertile mantle

Fig. 1-2 NaK# vs Mg# of experimentally produced melts that coexist with olivine, augite, low-Ca pyroxene (orthopyroxene or pigeonite) and spinel or plagioclase (or both) at 0.001 kbar (pluses), and elevated pressures up to 16 kbar. The open squares are the existing experimentally produced, multiply saturated mantle analog melts, the solid squares are the data added by this study (also include data from Grove, et al., 1990; and Bartels et al., 1991). Small extent (~ 1%) melts from spinel-lherzolite (sp-lherz) are anticipated to have high values of NaK# (~ 0.40) and Mg# of ~ 0.70 (shown as open diamond). With further melting of an increasingly depleted spinel-lherzolite (i.e., near-fractional melting), the NaK# drops steeply, while the Mg# increases only slightly (path shown by solid arrow).

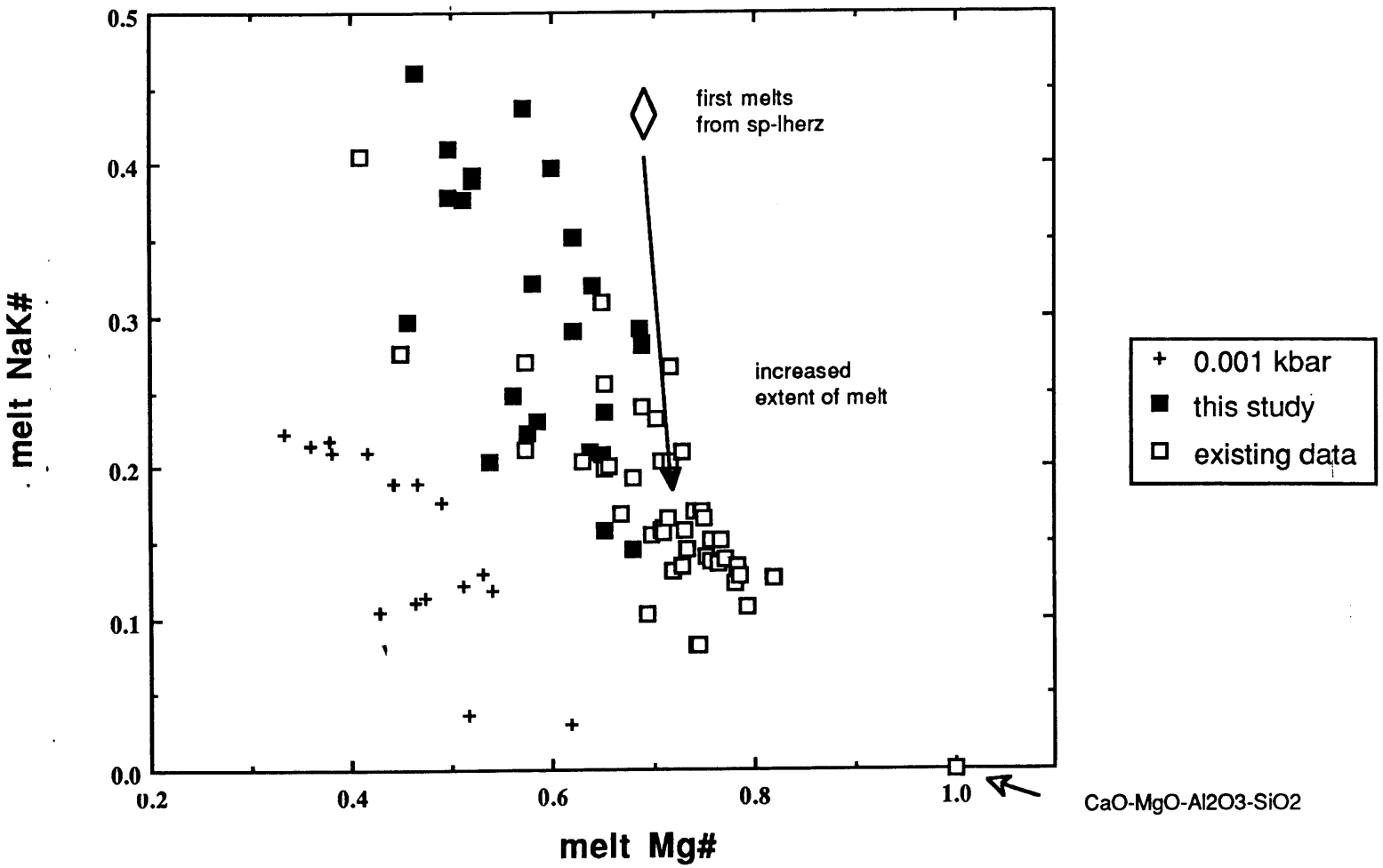
melt NaK#
melt Mg#
0.0
0.1
0.2
0.3
0.4
0.5
0.2
0.4
0.6
0.8
1.0
first melts
from sp-lherz
increased
extent of melt
0.001 kbar
this study
existing data
CaO-MgO-Al2O3-SiO2

Fig. 1-3 Pseudo-ternary liquidus phase diagram constructed from experiments conducted on mixtures of the primitive MORB composition ALV-2004-3-1 + small fractions of Kragero orthopyroxene or San Carlos olivine. Experimentally produced glass and pyroxene compositions are recalculated in terms of mineral components using the projection scheme of Tormey et al. (1987) and oxygen units, and projected through Plag onto the Oliv-Cpx-Qtz plane. The filled boxes locate the projected positions of the compositions of glasses saturated with 3 crystalline phases (olivine-augite-plagioclase, augite-orthopyroxene-plagioclase); phase compositions for these experiments are presented in Grove et al. (1991) and Grove et al. (in prep). The stars locate the projected positions of the compositions of glasses saturated with 4 or 5 crystalline phases (olivine-augite-orthopyroxene-plagioclase at 9 and 11 kbar, olivine-augite-orthopyroxene-plagioclase-spinel at 13 kbar), and the coexisting pyroxenes; phase compositions for these experiments are presented in Table 3. The ellipse shows the standard deviation of the mean of 7 microprobe analyses of an experimentally produced glass.

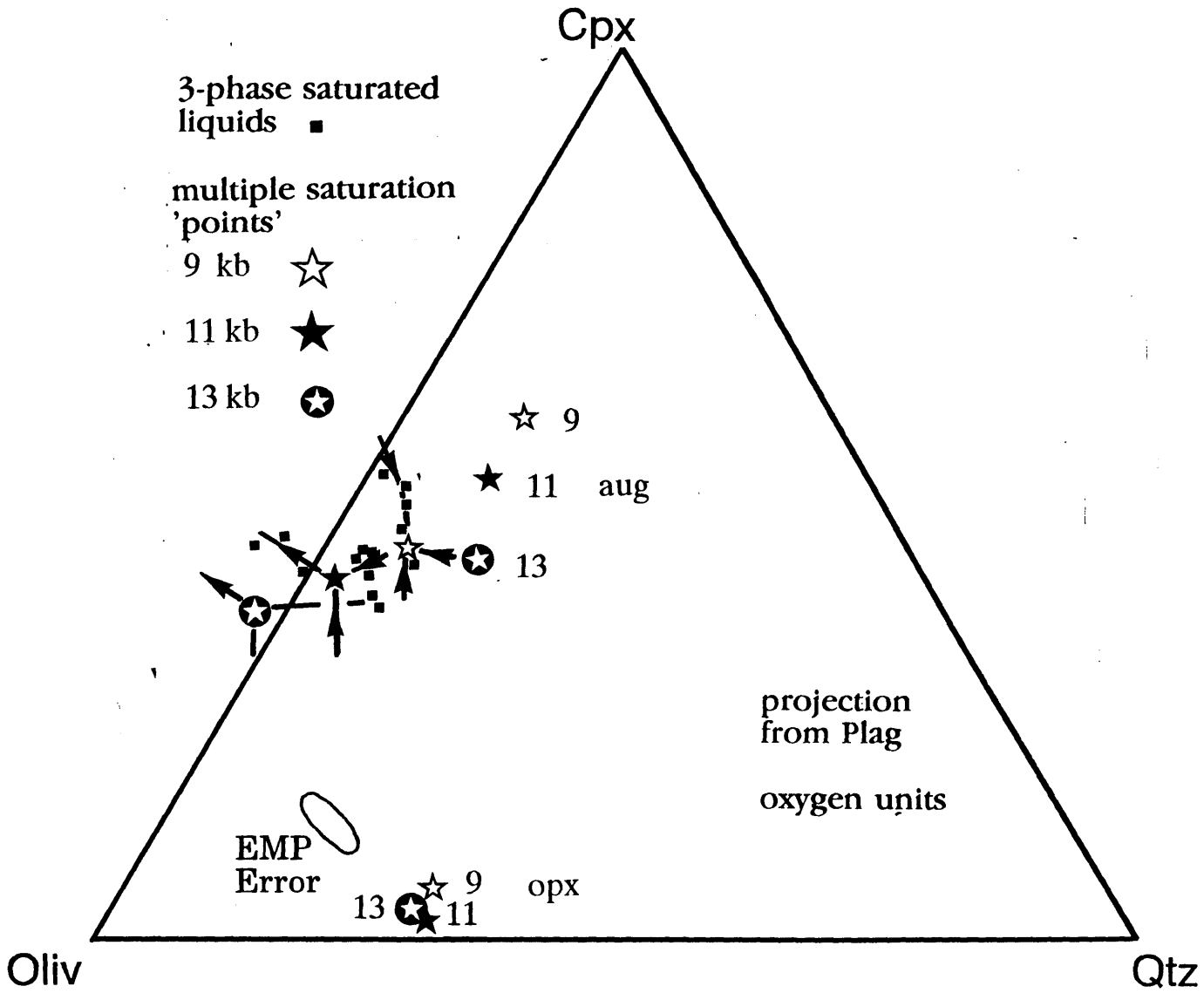
Cpx
3-phase saturated liquids
multiple saturation 'points'
9 kb
11 kb
13 kb
9
11 aug
13
projection from Plag
oxygen units
EMP Error
9 opx
13
11
Oliv
Qtz

Fig. 1-4 Graphical representation of the 10-kbar melt reaction for spinel lherzolite estimated from experiments B30, B52 and a subset of the 10-kbar experiments of Falloon and Green (1987). The projection scheme casts the experimentally produced mineral and melt phases in terms of the oxygen based mineral components: Oliv, Spinel, En-Fs (enstatite-ferrosilite) and Di-Hd (diopside-hedenbergite). The circles show the phases being consumed during melting (augite + orthopyroxene + spinel) and the stars show the phases being produced (melt + olivine). The reaction is 0.82 augite + 0.40 orthopyroxene + 0.08 spinel = 1.0 liquid + 0.30 olivine.

10-kbar melting reaction:

0.82 Aug + 0.40 Opx + 0.08 Spinel

= 1.0 Melt + 0.30 Olivine

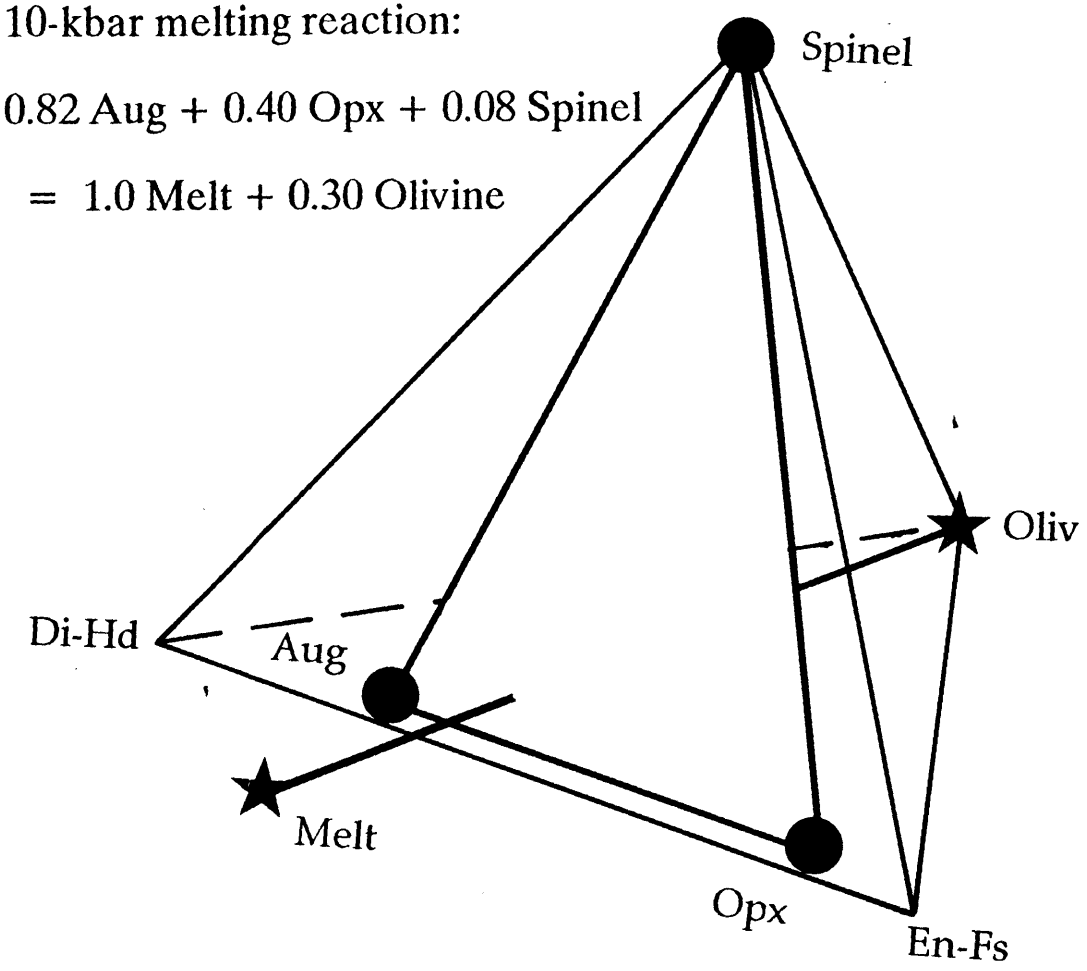

Fig. 1-5 Temperature of multiple saturation experiments vs. Mg# systematics of multiply saturated, experimentally produced melts from the literature and this study. Increased pressure increases the temperature at which the experimental liquids coexist with the mantle residual assemblage, as does increased Mg#. The simple system CaO-MgO-Al_2O_3-SiO_2 data of Presnall et al. (1979) define the maximum temperature at 0.001, 7, 9, 9.3, 11 and 14 kbar at which silicate melts can coexist with the mantle residual assemblage. Overall, the data show consistent variations. The 10-kbar data of Falloon and Green (1987) (F & G 10 kbar, solid circles), show a large variation in temperature, over a limited range in Mg#. These data are not included in the data set used for the descriptions of the multiple saturation boundaries provided in the text.

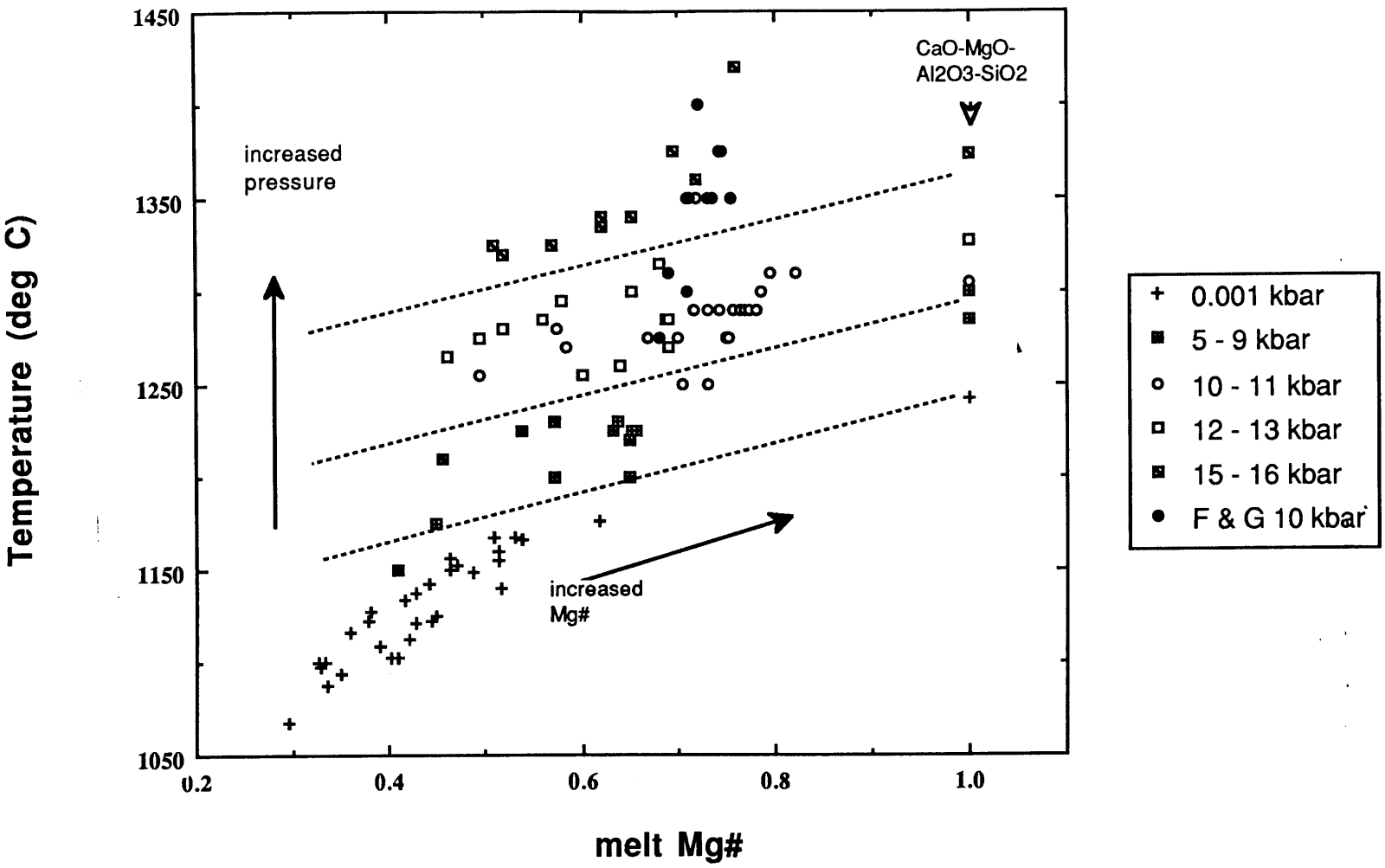
Temperature (deg C)
1450
1350
1250
1150
1050
0.2
0.4
0.6
0.8
1.0
melt Mg#
CaO-MgO-
Al2O3-SiO2
increased
pressure
increased
Mg#
0.001 kbar
5 - 9 kbar
10 - 11 kbar
12 - 13 kbar
15 - 16 kbar
F & G 10 kbar

Fig. 1-6 (A) Predicted temperature vs. reported experimental temperature for the experimental data set used to constrain the temperature expressions (eqns. 1 and 5 in the text). R-squared refers to the correlation coefficient; for a perfect fit, R-squared = 1.0.

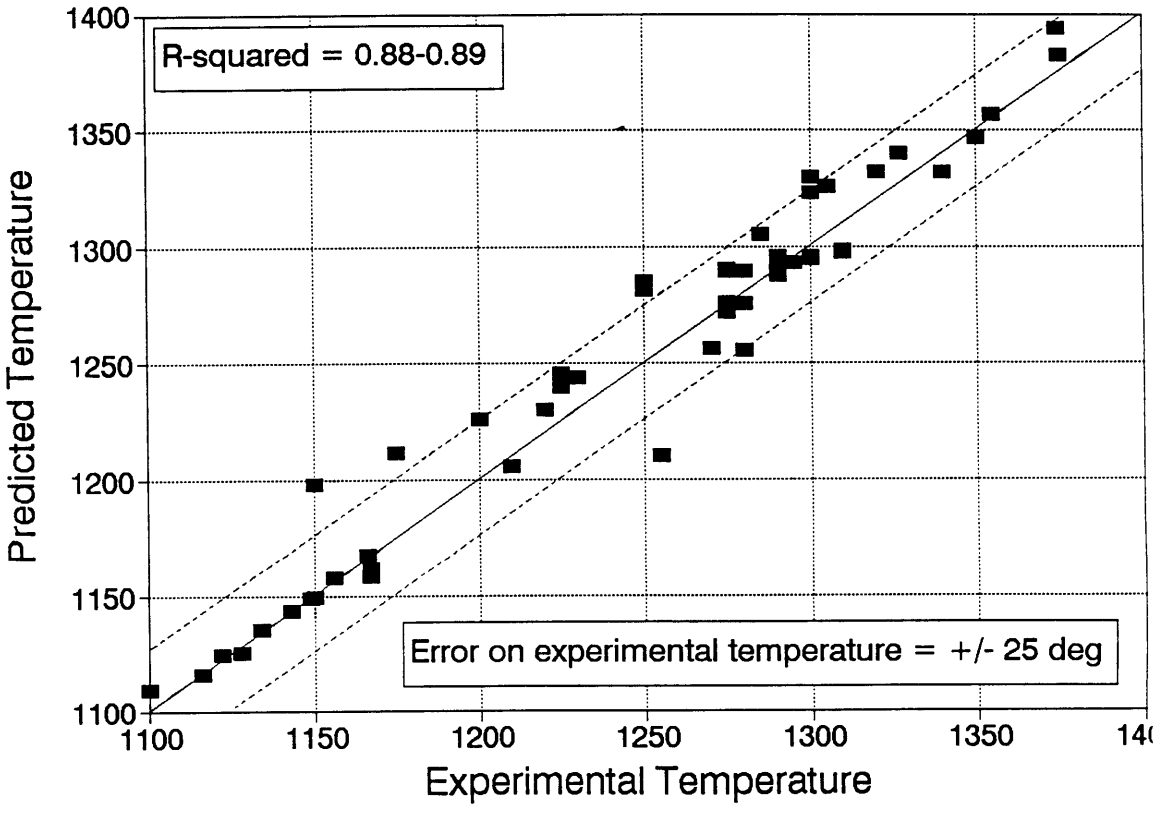
R-squared = 0.88-0.89
Error on experimental temperature = +/- 25 deg
Predicted Temperature
Experimental Temperature
1400
1350
1300
1250
1200
1150
1100
1100
1150
1200
1250
1300
1350

Fig. 1-6 (B) Predicted pressure vs. reported experimental pressure for the same data set. The predicted pressure is the average of the pressures predicted by eqns. 1-5 for the plagioclase-saturated melting equilibrium and the average of the pressures predicted by eqns. 6-10 for the spinel-saturated melting equilibrium, and thus portrays the overall 'goodness of fit' for eqns. 1-10 to the experimental data set.

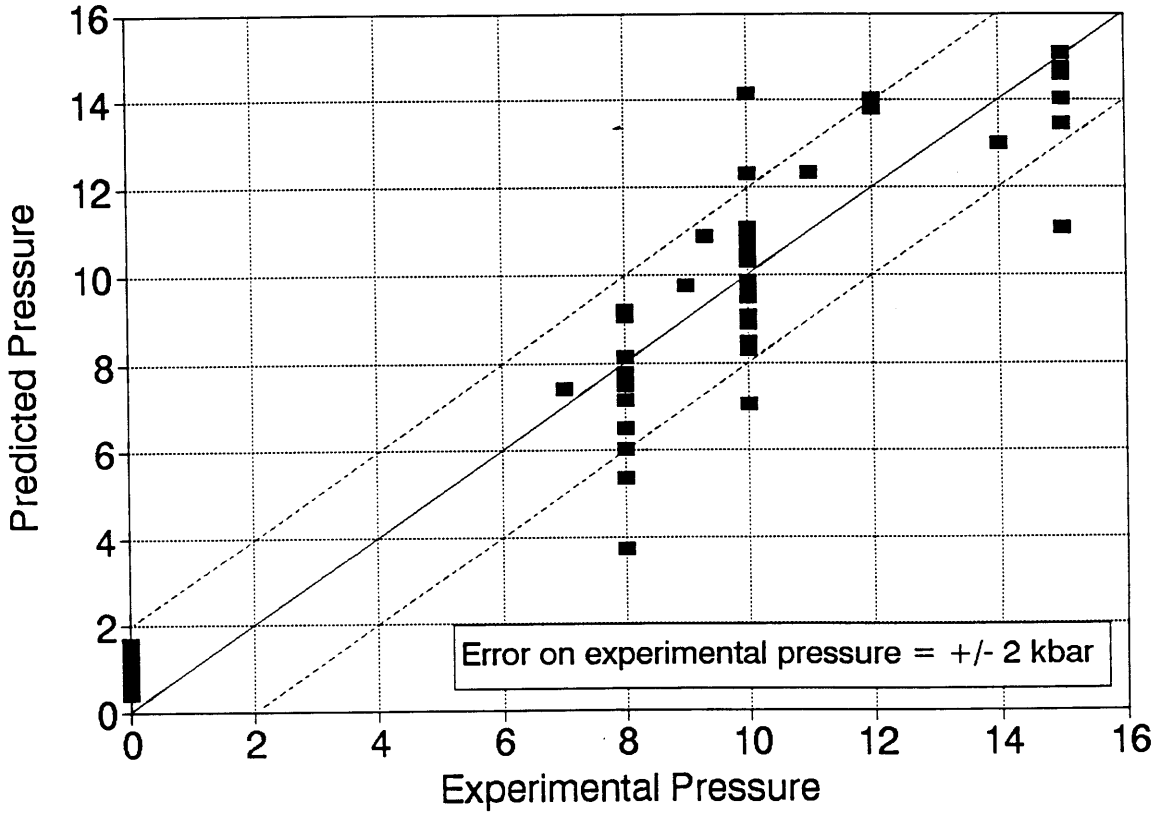
Predicted Pressure
Experimental Pressure
Error on experimental pressure = +/- 2 kbar
0
2
4
6
8
10
12
14
16

Fig. 1-7 (A) Predicted Qz values vs. experimentally observed Qz values for the sp-saturated melting equilibrium (eqn. 10). Qz refers to the oxygen-normalized mineral component of SiO_2 in the melt.

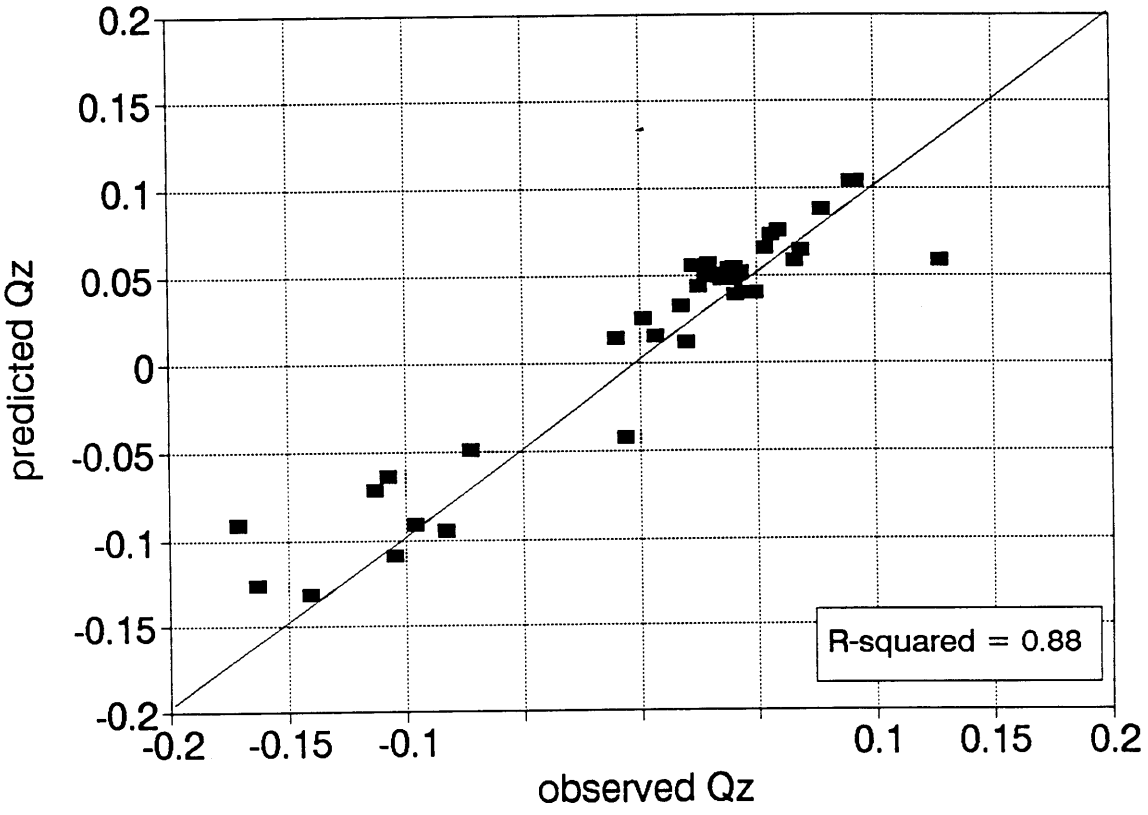
0.2
0.15
0.1
0.05
0
-0.05
-0.1
-0.15
-0.2
predicted Qz
-0.2
-0.15
-0.1
0.1
0.15
0.2
observed Qz
R-squared = 0.88

Fig. 1-7 (B) Predicted Ol values vs. experimentally observed Ol values for the sp-saturated melting equilibrium (eqn. 6). Ol refers to the oxygen-normalized mineral component of olivine in the melt.

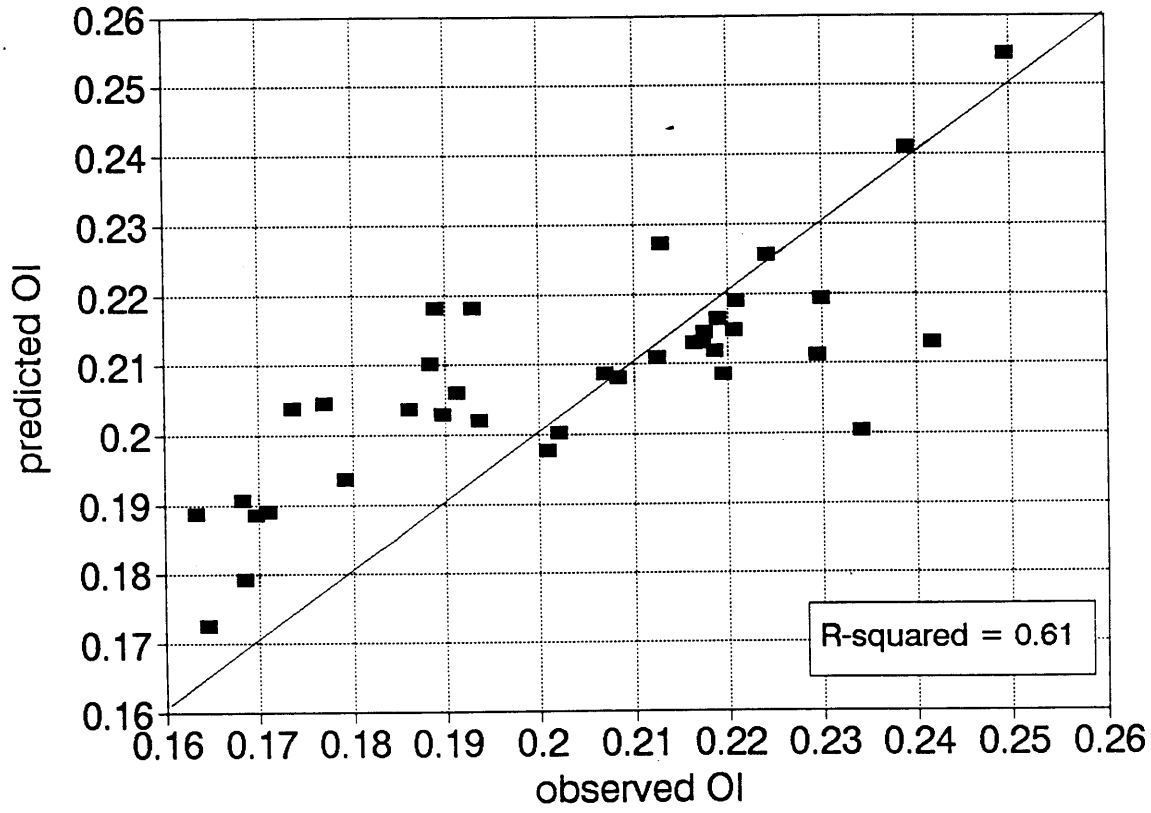
predicted OI
observed OI
0.26
0.25
0.24
0.23
0.22
0.21
0.2
0.19
0.18
0.17
0.16
0.16 0.17 0.18 0.19 0.2 0.21 0.22 0.23 0.24 0.25 0.26
R-squared = 0.61

Fig. 1-8 (A) Comparison of predicted spinel-lherzolite-melt multiple saturation boundary (open square with cross) for melt composition #10 from Table 6 of Fujii and Scarfe (1985) (F&S, #10), to the melt composition (solid square). This melt composition was reported to coexist with olivine + augite + orthopyroxene + spinel at 10 kbar and 1310^{o}C. It is representative of a group of melt compositions used in the data set to constrain the spinel-lherzolite-melt multiple saturation boundary that are not well fit by the resulting description (equations 6 - 10). Pseudo-ternary projection schemes calculated as in Fig. 3. In both the projections through Plag (A) and Qtz (B), the F&S,#10 composition projects into the augite primary phase volume relative to the estimated 10-kbar multiple saturation boundary and inferred olivine + augite + liquid boundary. Given the estimated phase boundaries, this composition should have augite on its liquidus, followed by the assemblage augite + olivine. Melting experiments on a synthetic analog of the F&S,#10 composition (Table 6) confirm this prediction.

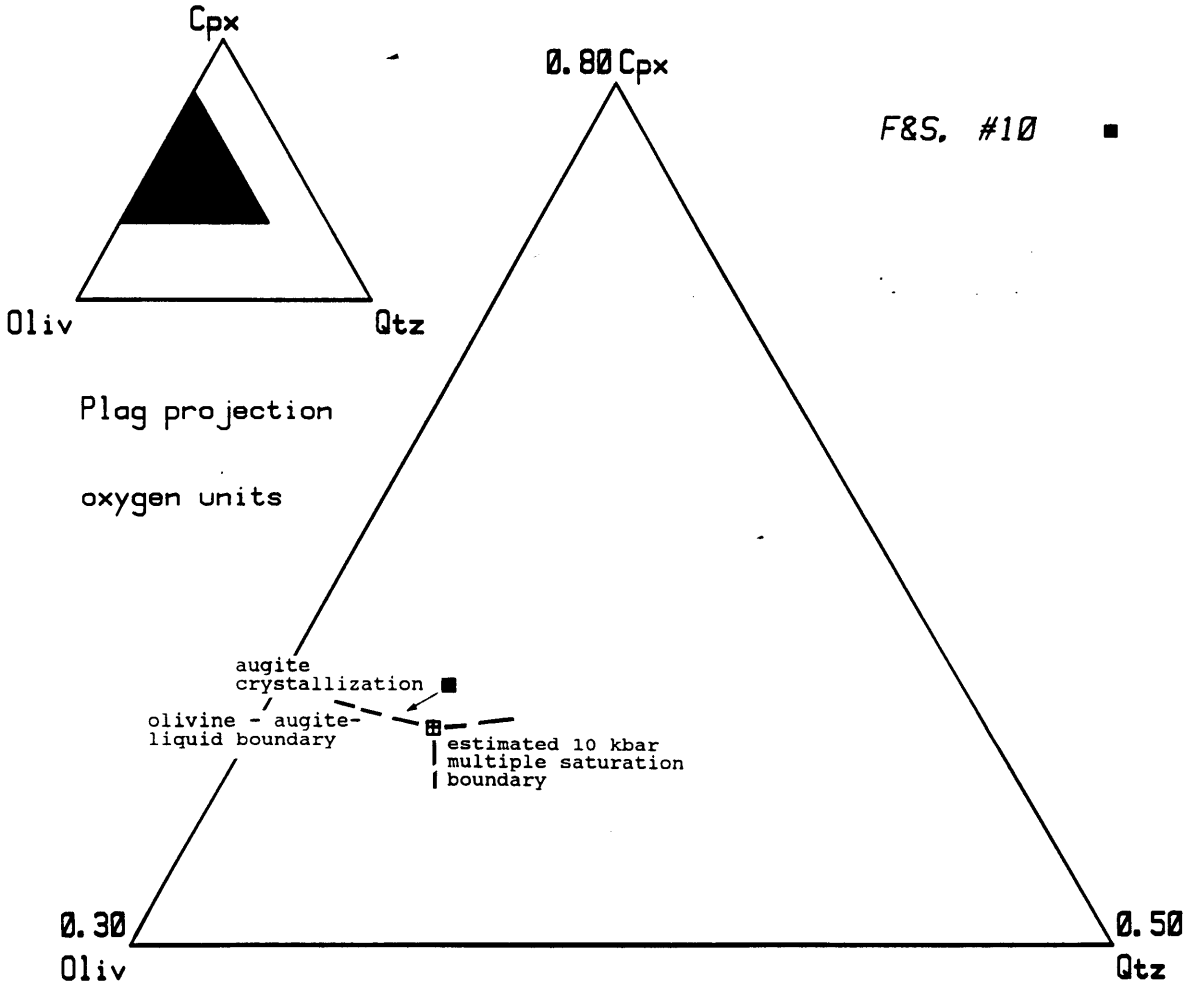
Cpx
Oliv
Qtz
Plag projection
oxygen units
0.80 Cpx
F&S. #10
augite
crystallization
olivine - augite-
liquid boundary
estimated 10 kbar
multiple saturation
boundary
0.30
Oliv
0.50
Qtz

Fig. 1-8 (B) (see fig. caption for Fig. 8a)

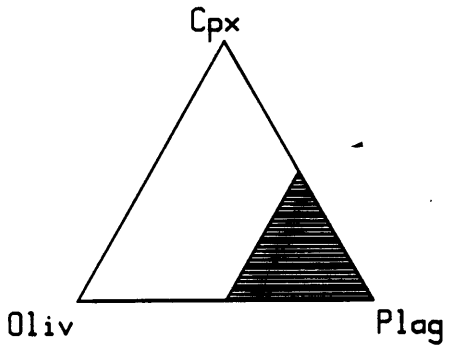

Qtz projection

oxygen units

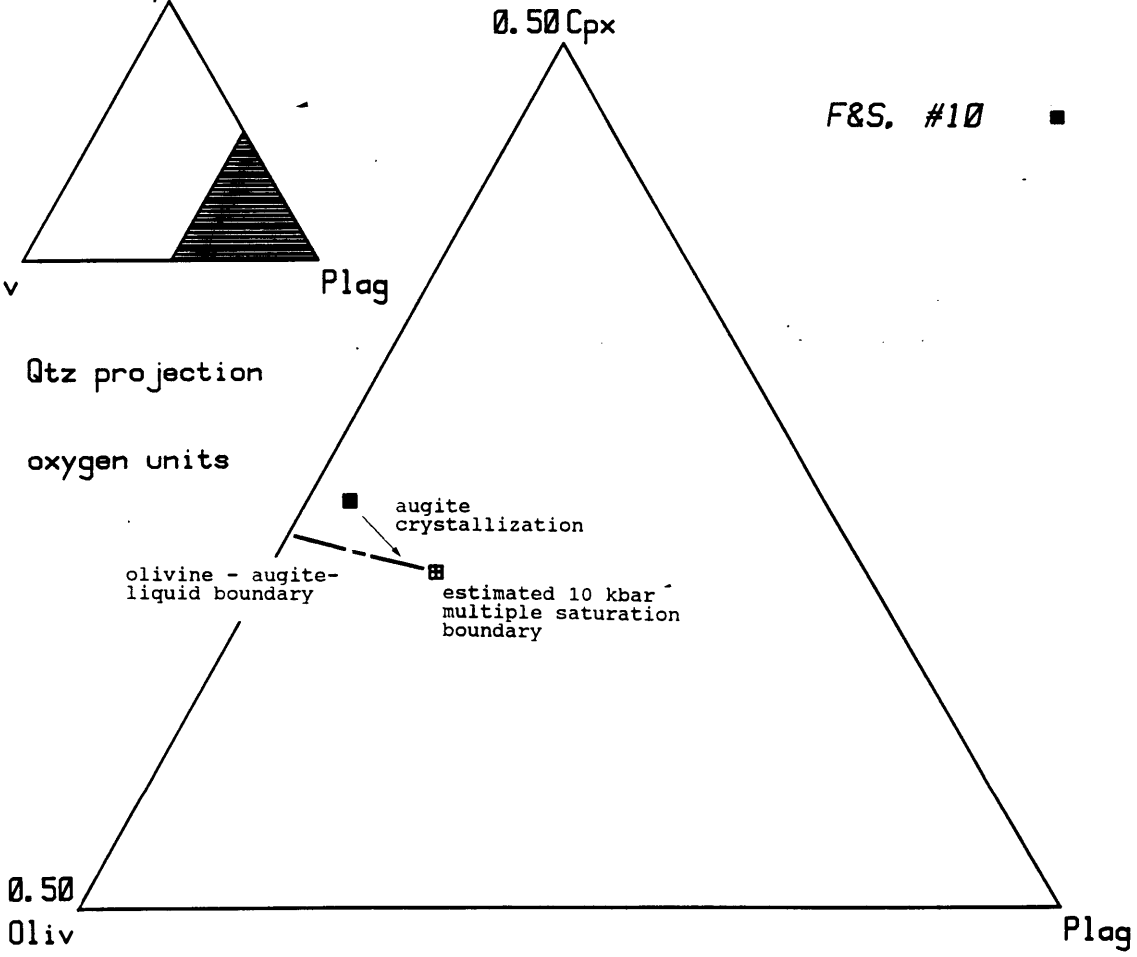

Fig. 1-9 (A) Grid of melt compositions produced from a plagioclase-lherzolite source at 8 kbar, projected through Plag onto the Oliv - Cpx - Qtz pseudo-ternary. Pseudo-ternary projection schemes calculated as in Fig. 3. Grids (spaced at 0.1 unit increments) show the effects of variations in Mg# and NaK# of the multiply saturated liquid on the projected position of this liquid; wt.% TiO_2 in each of the projected melts is 0.75. (B) Same melt compositions as in (A), projected through Qtz onto the Oliv - Cpx - Plag pseudo-ternary.

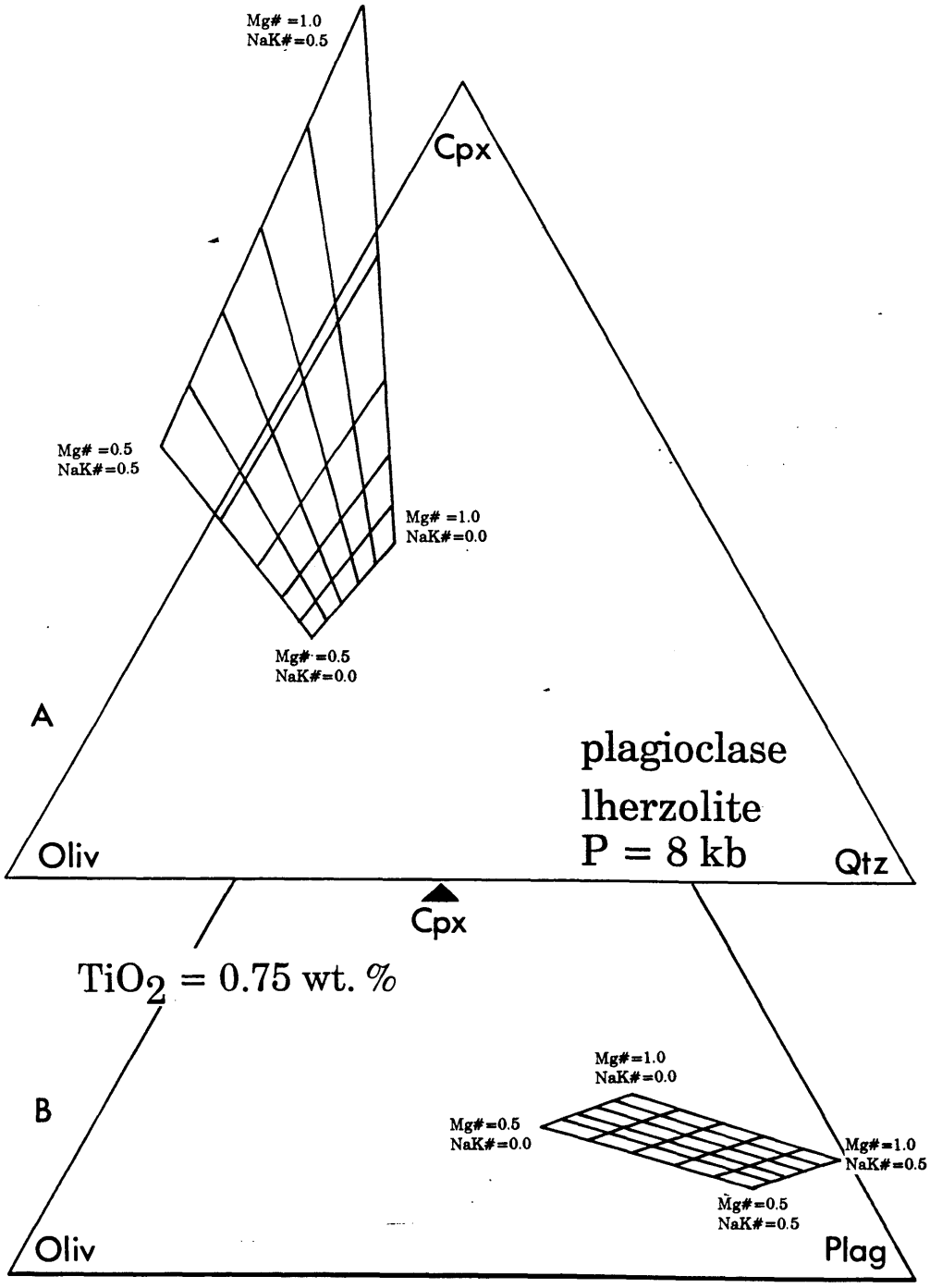
Mg# =1.0
NaK#=0.5
Cpx
Mg# =0.5
NaK#=0.5
Mg# =1.0
NaK#=0.0
Mg# =0.5
NaK#=0.0
A
plagioclase
lherzolite
P = 8 kb
Oliv
Qtz
Cpx
TiO2 = 0.75 wt. %
Mg#=1.0
NaK#=0.0
Mg#=0.5
NaK#=0.0
Mg#=1.0
NaK#=0.5
Mg#=0.5
NaK#=0.5
B
Oliv
Plag

Fig. 1-10 (A) Wt.% Na_2O vs FeO for model 1 melts of the upper oceanic mantle (Table 8), using the depleted mantle 1 composition. Solid squares represent 1, 5, 10 and 20 % batch melts from a plagioclase-lherzolite source at 5 and 8 kbar, and open squares represent 1, 5, 10 and 20 % batch melts from a spinel-lherzolite source at 10, 15 and 20 kbar.

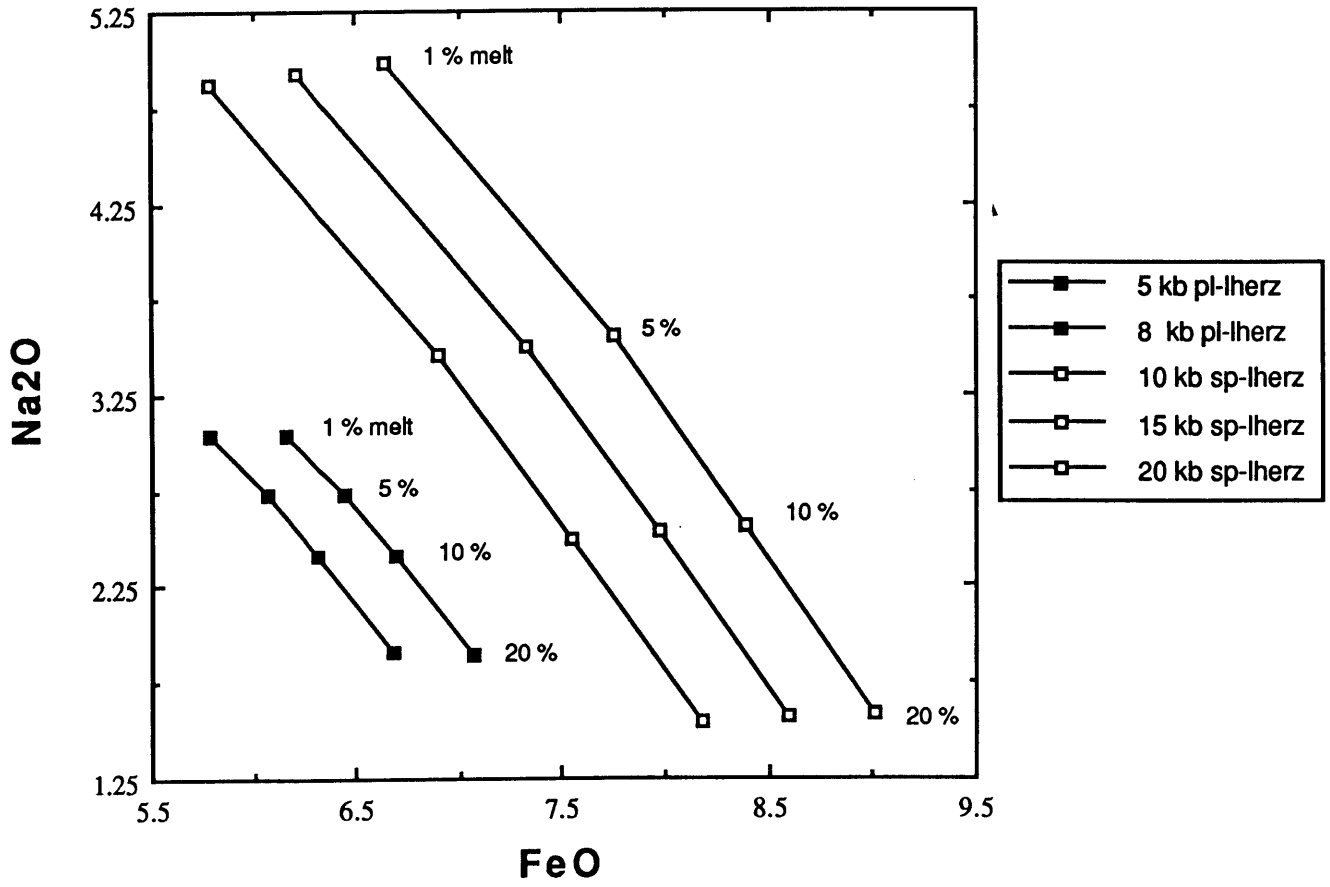
5.25
4.25
3.25
2.25
1.25
Na2O
5.5
6.5
7.5
8.5
9.5
FeO
1 % melt
5 %
10 %
20 %
1 % melt
5 %
10 %
20 %
5 kb pl-lherz
8 kb pl-lherz
10 kb sp-lherz
15 kb sp-lherz
20 kb sp-lherz

Fig. 1-10 (B) CaO/Al_2O_3 vs. FeO for the same melts described in (A).

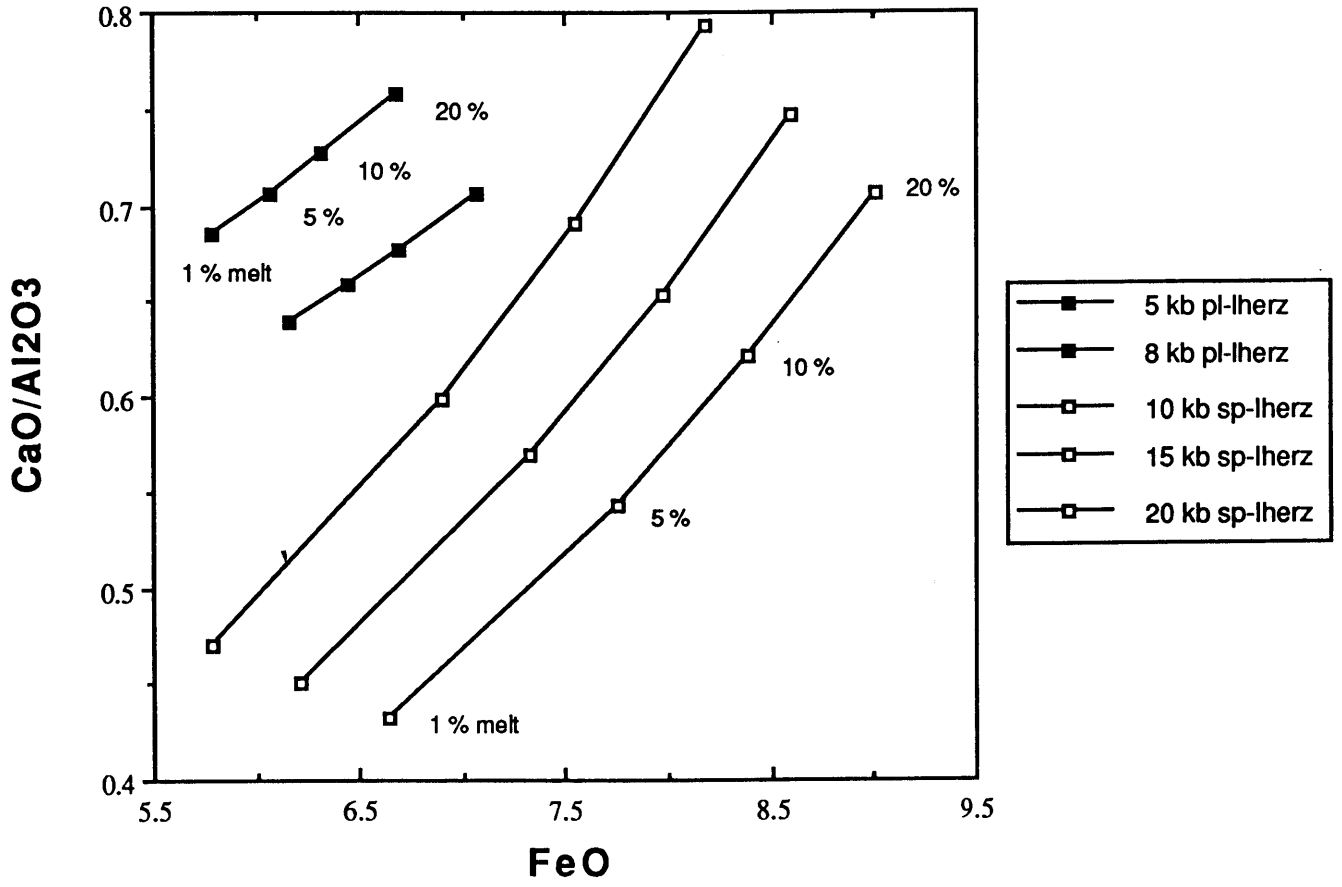
0.8
0.7
0.6
0.5
0.4
CaO/Al2O3
5.5
6.5
7.5
8.5
9.5
FeO
20 %
10 %
5 %
1 % melt
20 %
10 %
5 %
1 % melt
5 kb pl-lherz
8 kb pl-lherz
10 kb sp-lherz
15 kb sp-lherz
20 kb sp-lherz

Fig. 1-11 (A) Na_2O vs. FeO for batch melts from 2 different mantle sources, a primitive upper mantle composition of Hart and Zindler (1986) and a depleted mantle composition (Table 8). The curve for each of the two mantles is defined by batch melts calculated at 1, 5, 10 and 20 % melting. One set of curves was calculated at 8 kbar from a plagioclase-lherzolite source, the other at 15 kbar from a spinel-lherzolite source.

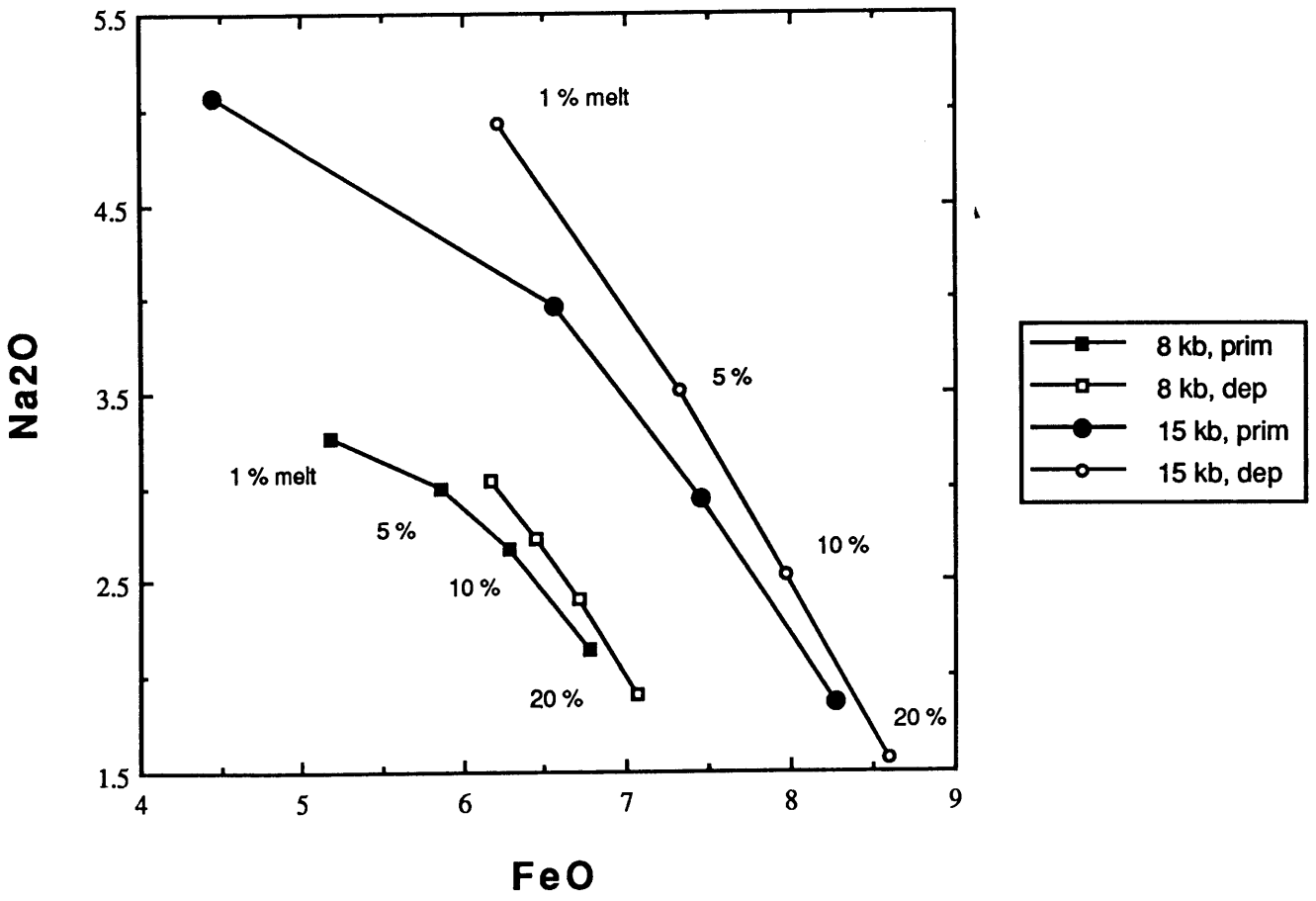
5.5
4.5
3.5
2.5
1.5
4
5
6
7
8
9
Na2O
FeO
1 % melt
5 %
10 %
20 %
1 % melt
5 %
10 %
20 %
8 kb, prim
8 kb, dep
15 kb, prim
15 kb, dep

Fig. 1-11 (B) CaO/Al_2O_3 vs. FeO for same melts shown in (A).

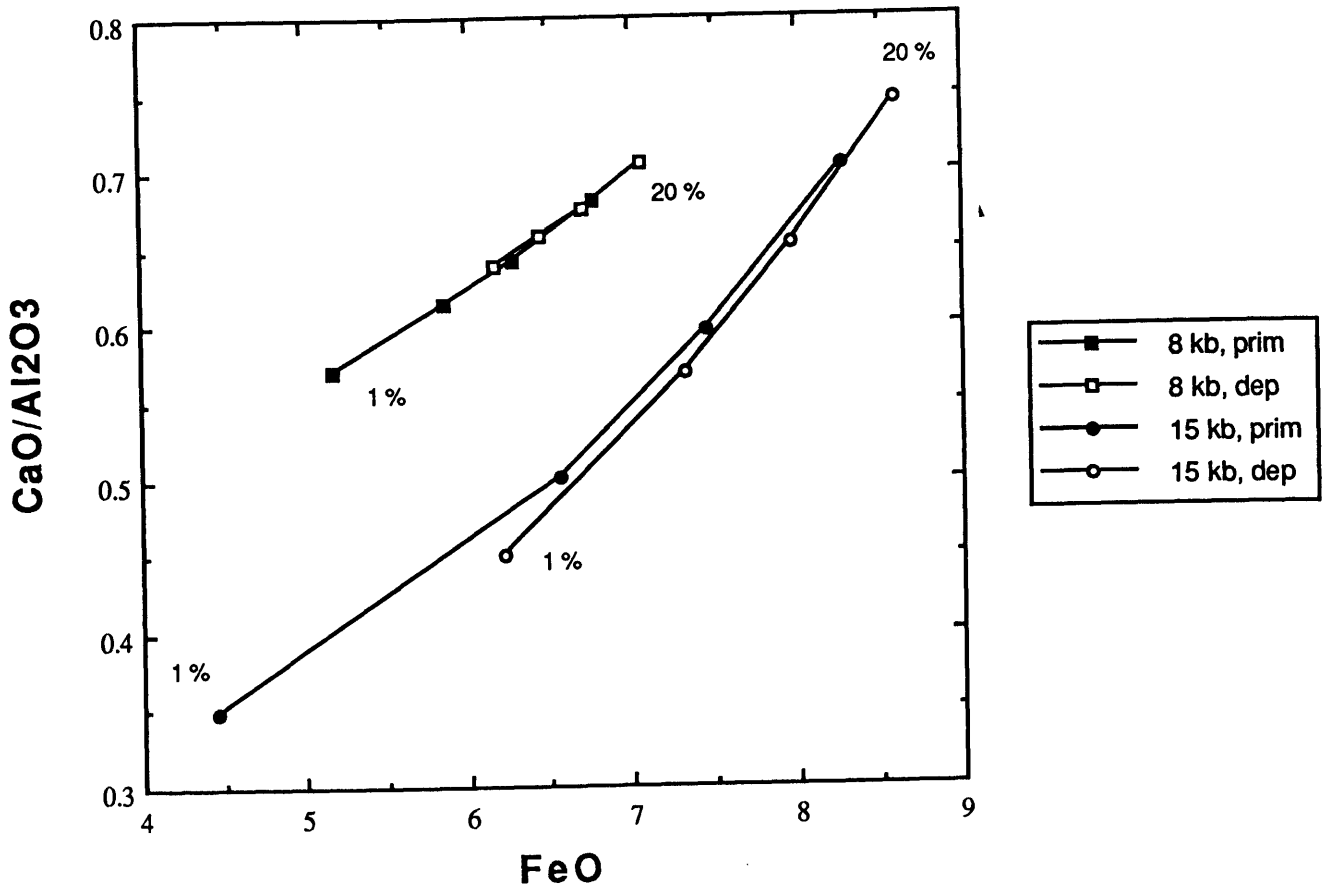
0.8
0.7
0.6
0.5
0.4
0.3
4
5
6
7
8
9
CaO/Al2O3
FeO
20 %
20 %
1 %
1 %
1 %
8 kb, prim
8 kb, dep
15 kb, prim
15 kb, dep

Fig. 1-12 (A) Wt.% Na_2O vs FeO for model 2 melts of the upper oceanic mantle (Table 8), using the depleted mantle 1 composition. Solid circles represent 1, 5.2, 10.3 and 20.2 % incremental-batch accumulated melts from a plagioclase-lherzolite source at 5 and 8 kbar, and from a spinel-lherzolite source at 10, 15 and 20 kbar.

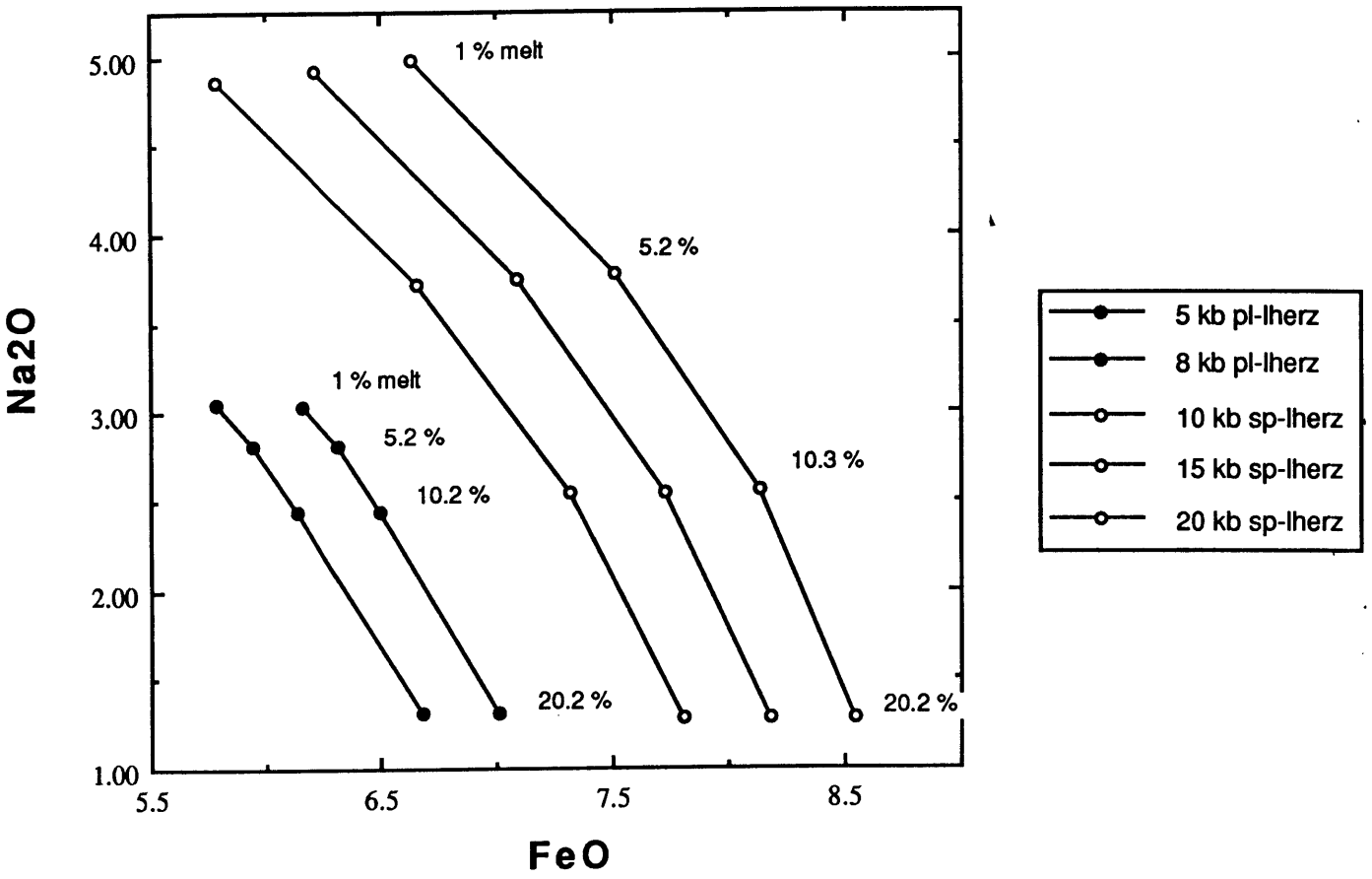
Na2O
FeO
5.00
4.00
3.00
2.00
1.00
5.5
6.5
7.5
8.5
1 % melt
5.2 %
10.3 %
20.2 %
1 % melt
5.2 %
10.2 %
20.2 %
5 kb pl-lherz
8 kb pl-lherz
10 kb sp-lherz
15 kb sp-lherz
20 kb sp-lherz

Fig. 1-12 (B) CaO/Al_2O_3 vs. FeO for the same melts described in (A).

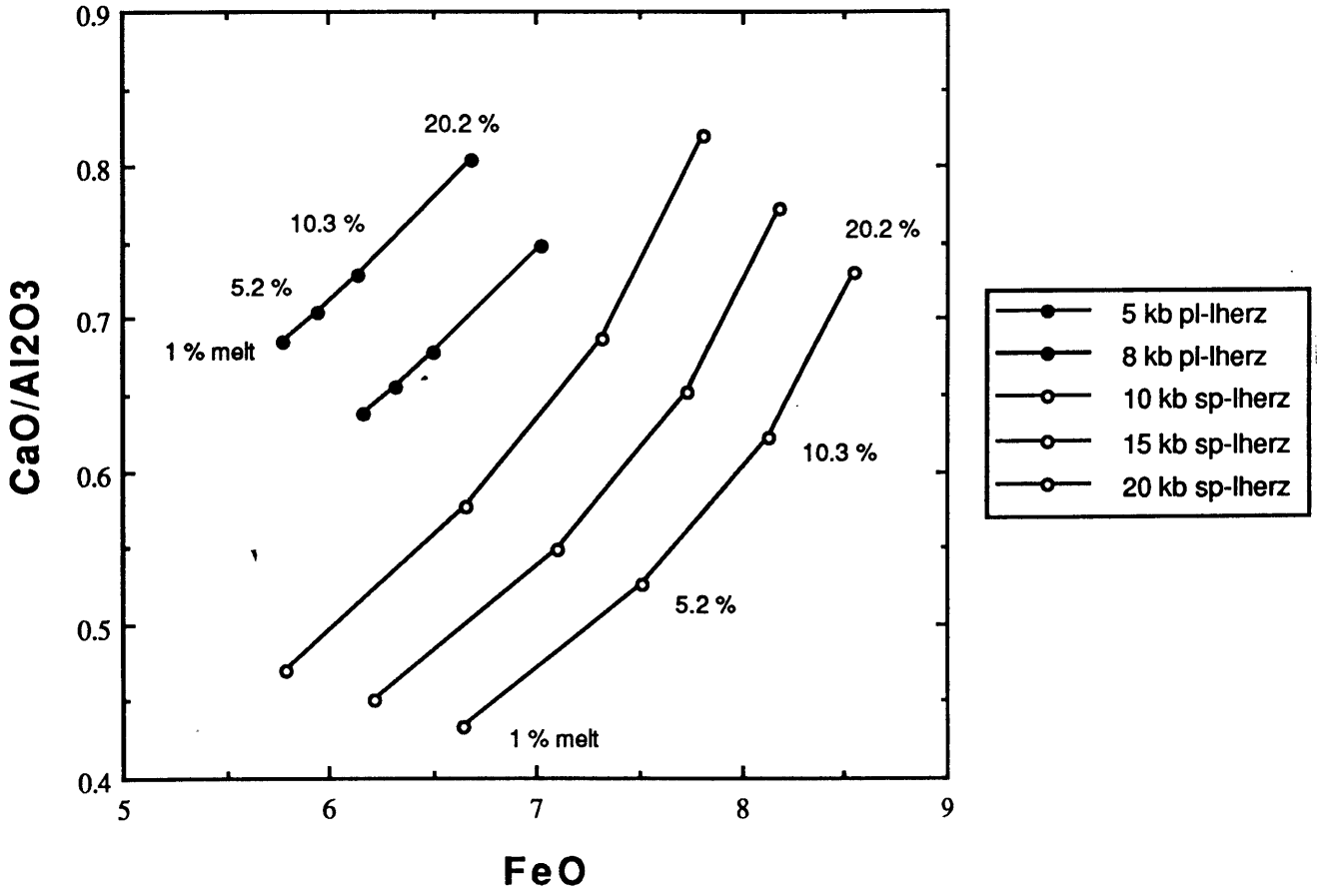
0.9
0.8
0.7
0.6
0.5
0.4
5
6
7
8
9
CaO/Al2O3
FeO
20.2 %
10.3 %
5.2 %
1 % melt
20.2 %
10.3 %
5.2 %
1 % melt
5 kb pl-lherz
8 kb pl-lherz
10 kb sp-lherz
15 kb sp-lherz
20 kb sp-lherz

Fig. 1-13 Temperature - Pressure diagram for melting in the mantle. The upper most, dash-dot curve represents the mantle solidus in the simple system CaO-MgO-Al_2O_3-SiO_2 determined by Presnall et al. (1979); the lower most, dashed curve is the mantle solidus inferred by McKenzie and Bickle (1988) from natural system experiments; and the three curves in between represent 6 % and 3 % accumulated batch melts, and 0.1% batch melt from the depleted MORB-mantle composition 1 presented in Table 8 (see text for discussion).

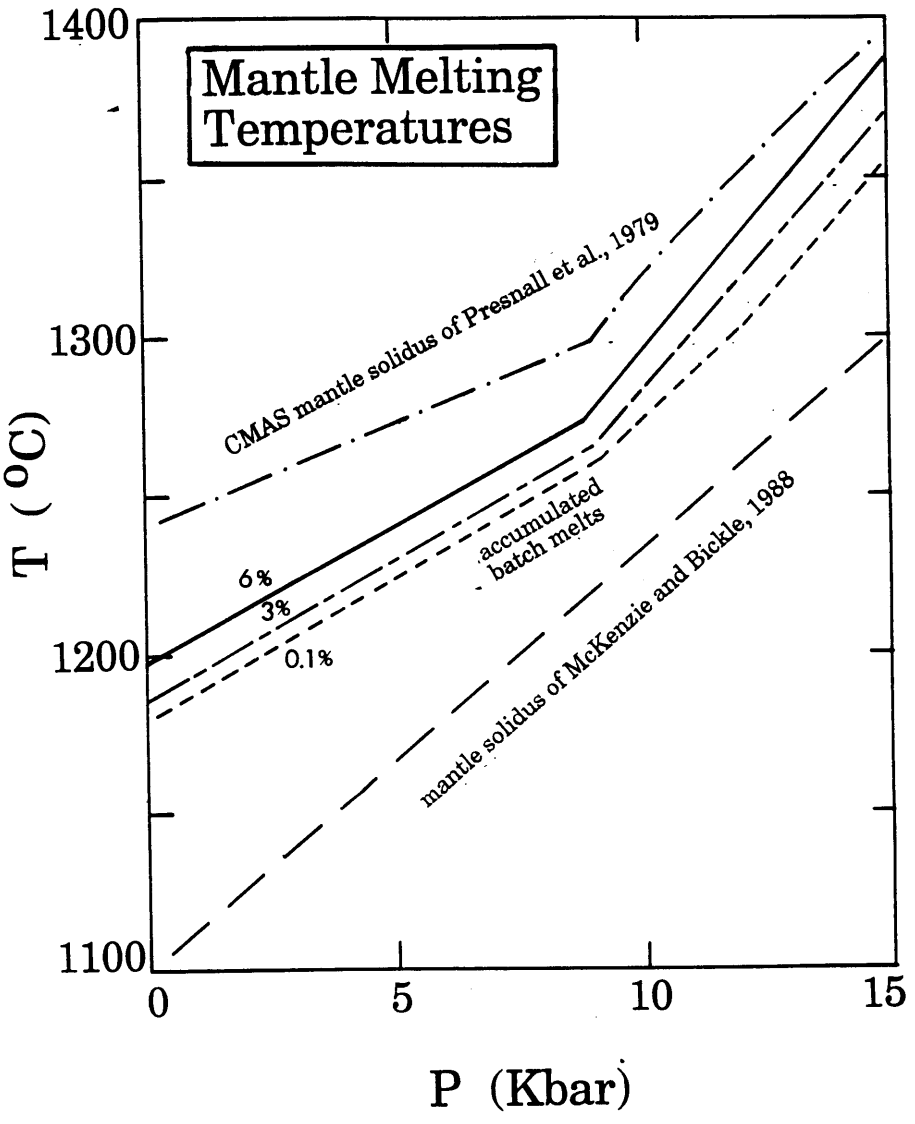
Mantle Melting Temperatures
1400
1300
1200
1100
T (°C)
0
5
10
15
P (Kbar)
CMAS mantle solidus of Presnall et al., 1979
6%
3%
0.1%
accumulated
batch melts
mantle solidus of McKenzie and Bickle, 1988

Fig. 1-14 Na_2O vs. FeO for model 3 melting paths (# 1, 2 and 3, Table 9). Each solid symbol shows the composition of an increment of melt produced as mantle of the depleted mantle 1 composition rises and undergoes incremental, batch melting, in response to adiabatic decompression. Like symbols represent increments of melt produced within the same column. The high-Na_2O melts are the first melts produced, at the greatest pressure. The low-Na_2O melts are the last melts produced, at the shallowest pressure. As pressure decreases, the mantle composition becomes increasingly depleted in Na_2O. The 3 melting paths correspond to the first three melt models in Table 9. The averages of all the increments produced along each of the melting paths, respectively, are shown as open symbols.

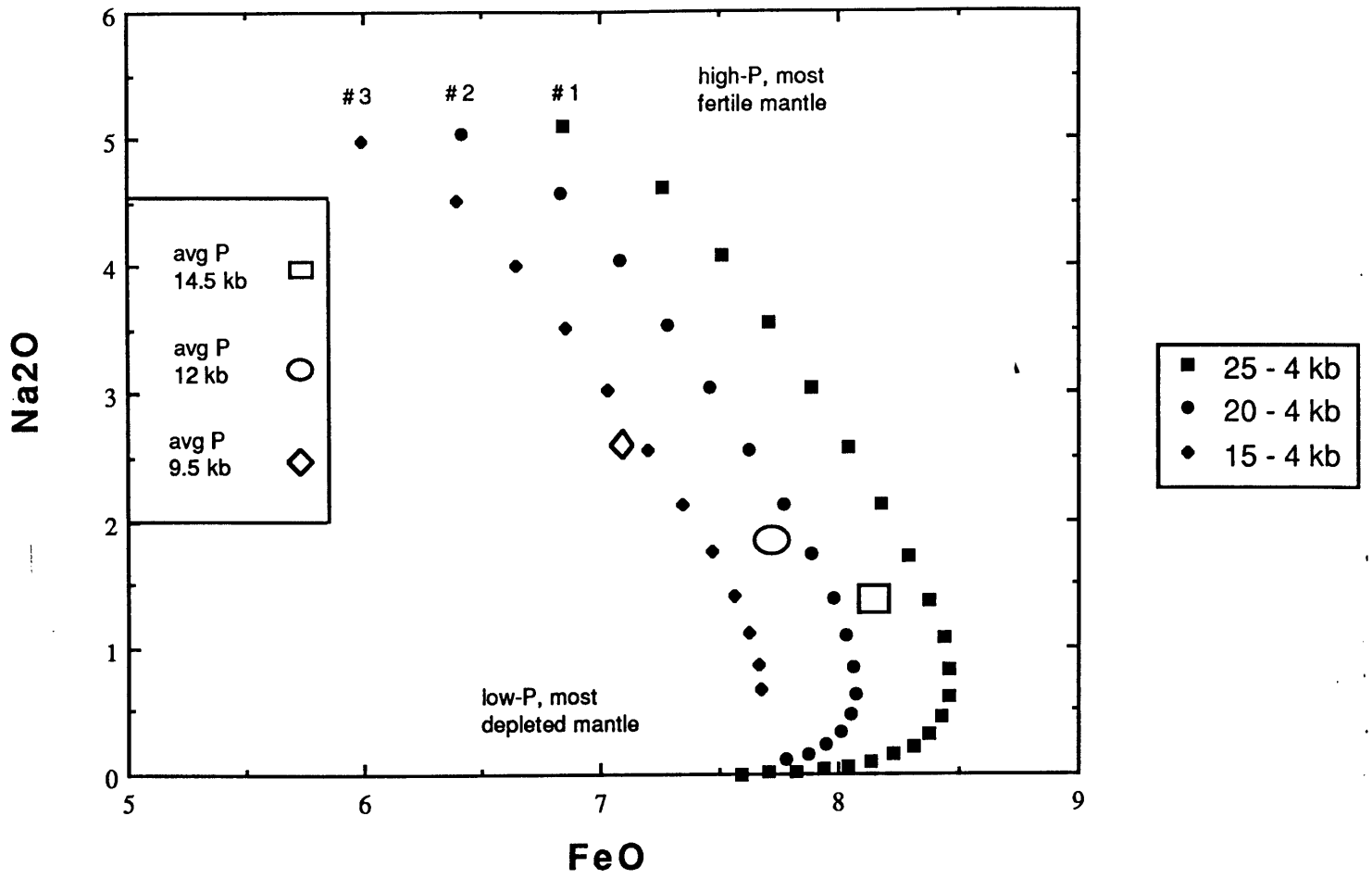
Na2O
FeO
#3
#2
#1
high-P, most
fertile mantle
low-P, most
depleted mantle
avg P
14.5 kb
avg P
12 kb
avg P
9.5 kb
25 - 4 kb
20 - 4 kb
15 - 4 kb
0
1
2
3
4
5
6
5
6
7
8
9

Fig. 1-15 (A) Na_2O vs. FeO comparing the main trend of Klein and Langmuir (1989, their Fig. 5a) for the global MORB data set corrected to MgO = 8.0 (enclosed within the dashed curve), to the trend defined by the primary magma compositions calculated in this study. The primary magmas are produced by melting depleted mantle 1 using an isobaric, near-fractional melting model between 8 and 20 kbar, from < 5% - 20% (shown as solid curves). The entire region occupied by the data presented in Klein and Langmuir (1989, their Fig. 5) is also delimited with the dash-dot curves. The hatchered curves show the compositions of the estimated primary melts corrected 'down temperature' to 8.00 wt.% MgO by applying fractional crystallization processes at near-ocean floor conditions. The solid arrows connect estimated primary magmas from 12 kbar to the corrected magmas at 8.00 wt.% MgO.

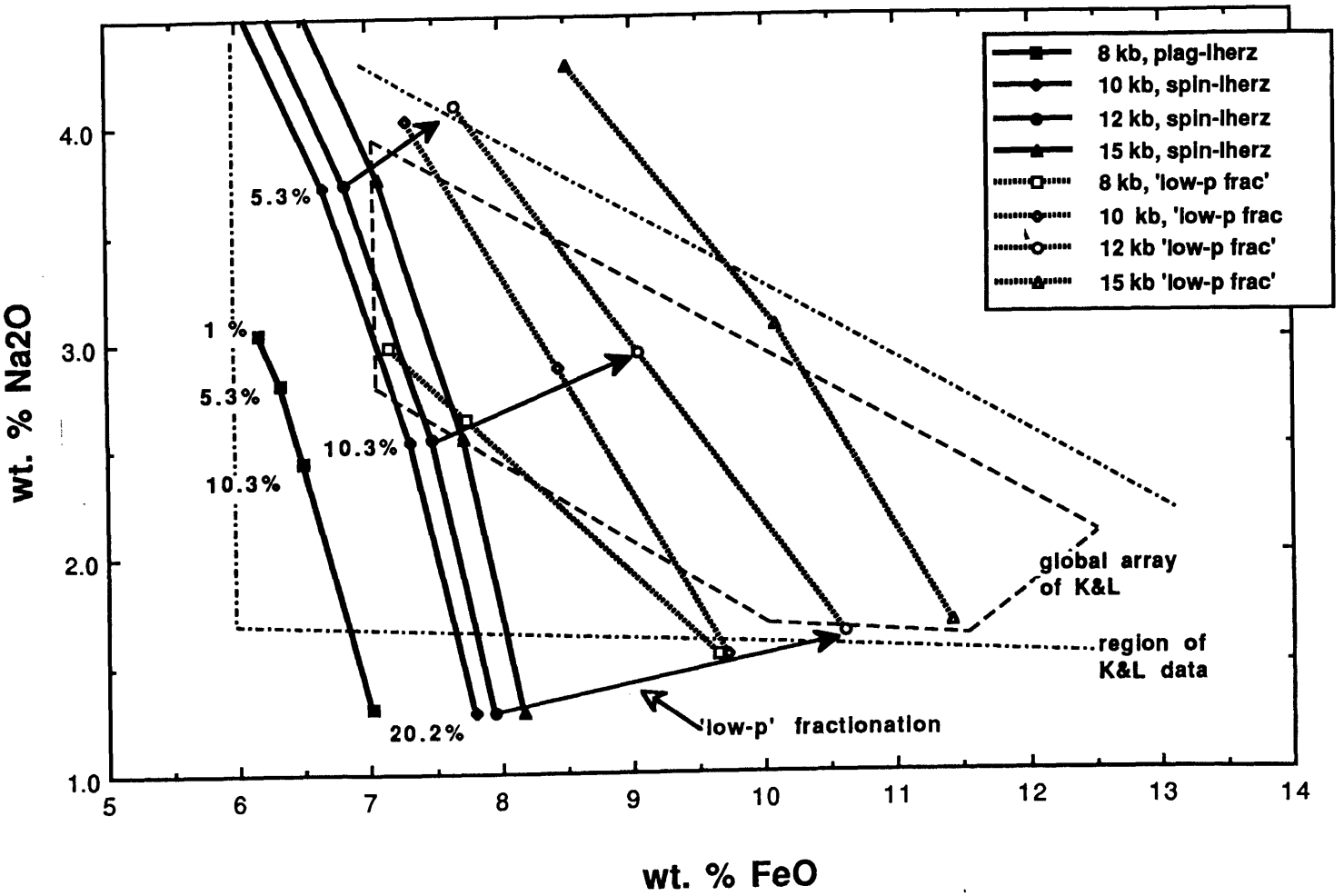
8 kb, plag-lherz
10 kb, spin-lherz
12 kb, spin-lherz
15 kb, spin-lherz
8 kb, 'low-p frac'
10 kb, 'low-p frac
12 kb 'low-p frac'
15 kb 'low-p frac'
5.3%
1 %
5.3%
10.3%
10.3%
20.2%
global array of K&L
region of K&L data
'low-p' fractionation
wt. % Na2O
wt. % FeO
4.0
3.0
2.0
1.0
5
6
7
8
9
10
11
12
13
14

Fig. 1-15 (B) The global MORB data corrected to 8.00 wt.% MgO described in the caption to Fig. 15a is shown again on an Na_2O vs. FeO diagram. Also shown are curves indicating the compositions of the estimated primary magmas shown in Fig. 15a corrected 'down temperature' by applying fractional crystallization processes at near-ocean floor conditions and at pressures of ~ 4 kbar. Like line types indicate curves corrected from the same primary magmas at each of the two pressures. Closed symbols along the curves indicate 'low-p', or near-ocean floor conditions of fractional crystallization, open symbols indicate fractional crystallization at 'elev-p' or ~ 4 kbar.

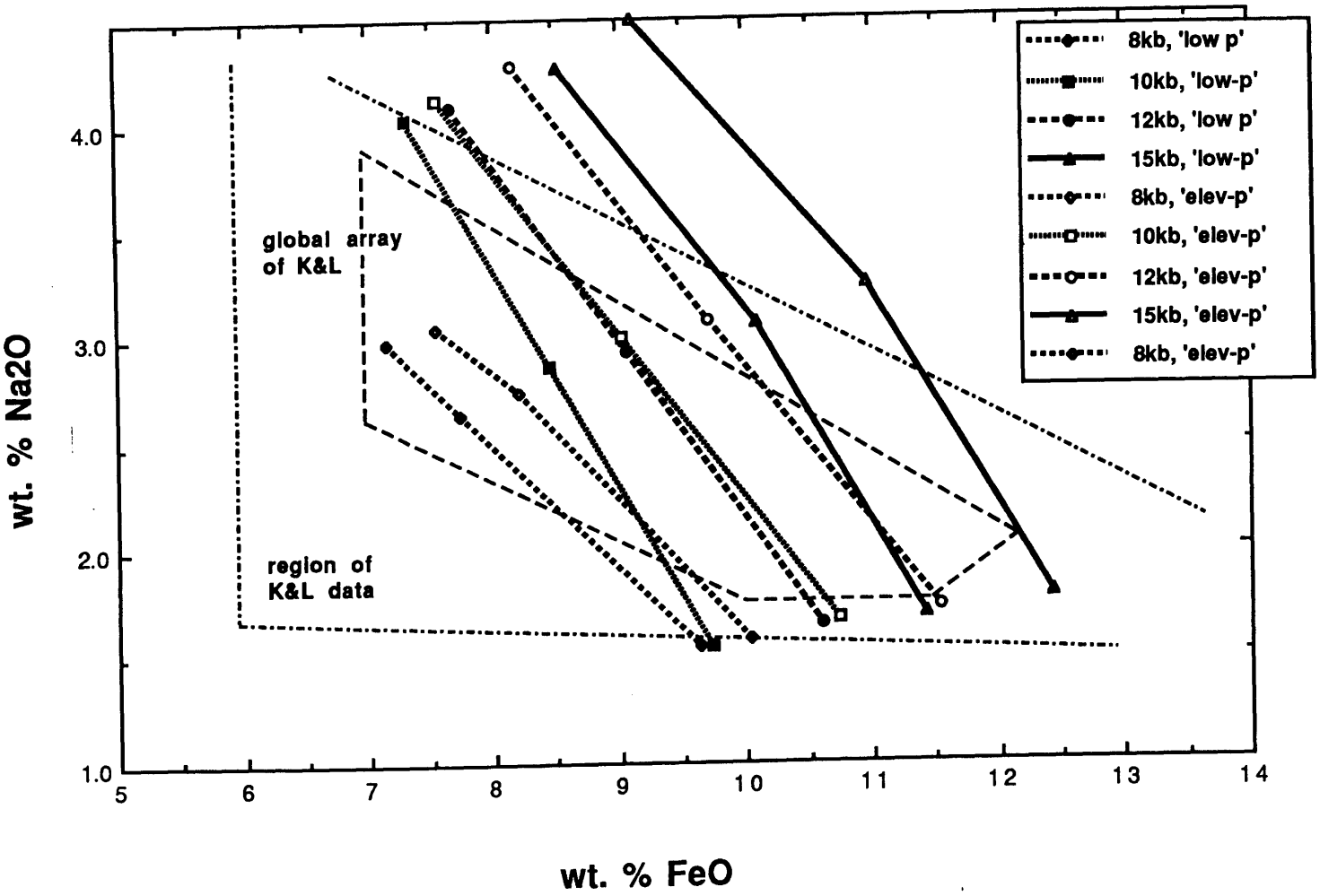
8kb, 'low p'
10kb, 'low-p'
12kb, 'low p'
15kb, 'low-p'
8kb, 'elev-p'
10kb, 'elev-p'
12kb, 'elev-p'
15kb, 'elev-p'
8kb, 'elev-p'
global array of K&L
region of K&L data
wt. % Na2O
wt. % FeO
1.0
2.0
3.0
4.0
5
6
7
8
9
10
11
12
13
14

Fig. 1-15 (C) The global MORB data corrected to 8.00 wt.% MgO described in the caption to Fig. 15a is shown again on an Na_2O vs. FeO diagram. Also shown are three of the local trends observed by Klein and Langmuir (1989, their Fig. 5b) (heavy solid curves; MCR = mid-Cayman rise, MAR = 11.4°N-11.97°N on the mid-Atlantic ridge, RP = Reykjanes Peninsula), and the corrected primary magmas from 10 kbar, the solid curve that connects the solid squares shows the 10-kbar melts corrected 'down temperature' to 8.00 wt.% MgO by fractional crystallization at 'low-p' or near-ocean floor conditions, the hatchered line connecting the open squares shows the same 10-kbar melts corrected 'down temperature' to 8.00 wt.% MgO by fractional crystallization at ~4 kbar. The solid lines connecting the solid and open squares indicate the potential cross trends in Na_2O vs. FeO caused by fractional crystallization of a similar primary magma at near 1-atm. conditions and ~4 kbar.

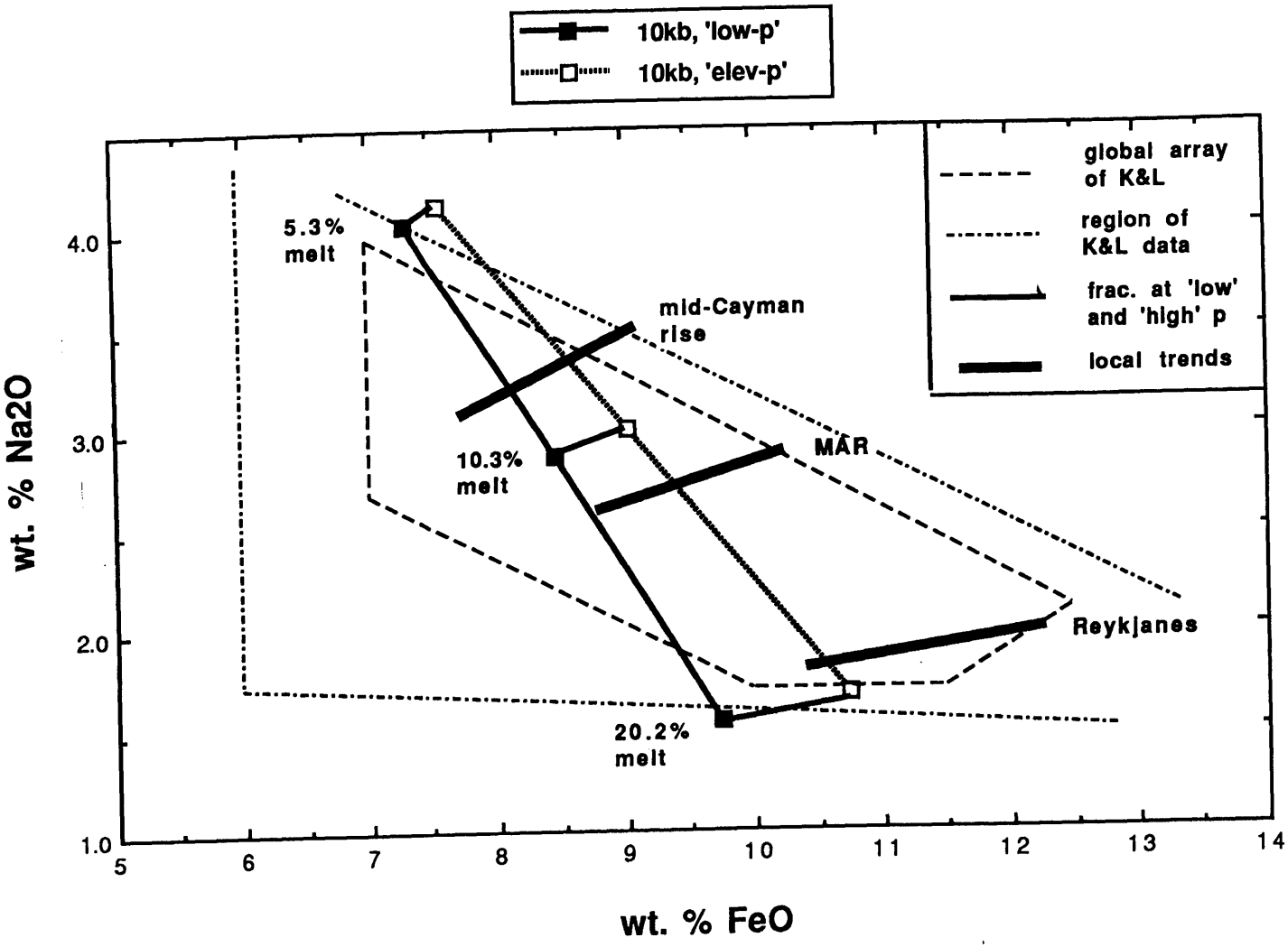
10kb, 'low-p'
10kb, 'elev-p'
global array of K&L
region of K&L data
frac. at 'low' and 'high' p
local trends
5.3% melt
mid-Cayman rise
MAR
10.3% melt
Reykjanes
20.2% melt
wt. % Na2O
wt. % FeO
4.0
3.0
2.0
1.0
5
6
7
8
9
10
11
12
13
14

Fig. 1-16 (A) Na_2O vs. FeO comparing the main trend of Klein and Langmuir (1989, their Fig. 5a) for the global MORB data set corrected to MgO = 8.0 (enclosed within the dashed curve), to the trend defined by the polybaric, aggregate primary magmas estimated in this study (solid curve connecting solid squares). The dash-dot curve contains all of the global MORB data. The labels 10, 14 and 18% associated with the solid squares indicate the extent of depletion of the mantle source achieved during the polybaric, near-fractional melting process. The polybaric, aggregate primary magmas are corrected 'down temperature' to 8.00 wt.% MgO by fractionally crystallizing them at 0.001 kbar ('low' p frac, shown by hatchered curve connecting open squares) and at 4 kbar ('high' p frac, shown by curve connecting open circles). The heavy solid curves labelled MCR (mid-Cayman rise), MAR (11.4°N-11.97°N on the mid-Atlantic ridge) and RP (Reykjanes Peninsula) indicate the position and slope of the local trends observed at these locations by Klein and Langmuir (1989, their Fig. 5b).

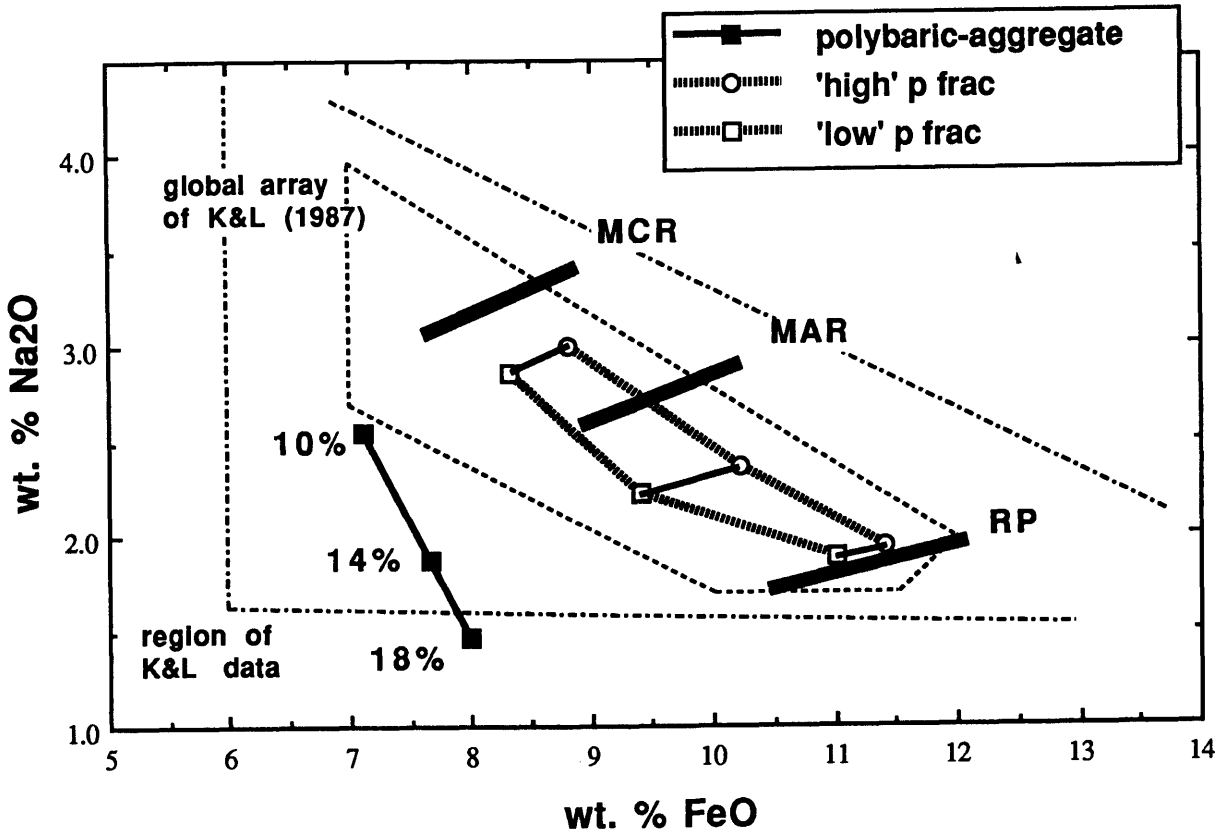
polybaric-aggregate
'high' p frac
'low' p frac
global array
of K&L (1987)
MCR
MAR
RP
10%
14%
18%
region of
K&L data
wt. % Na2O
wt. % FeO
4.0
3.0
2.0
1.0
5
6
7
8
9
10
11
12
13
14

Fig. 1-16 (B) Wt.% Na_2O vs. wt.% SiO_2 comparing the trend defined by the polybaric, aggregate primary magmas estimated in this study (solid curve connecting solid squares) to the same primary magmas corrected 'down temperature' to 8.00 wt.% MgO by fractional crystallization at 0.001 kbar ('low' p, dashed line connecting solid circles) and at 4 kbar ('high' p, dashed line connecting solid triangles).

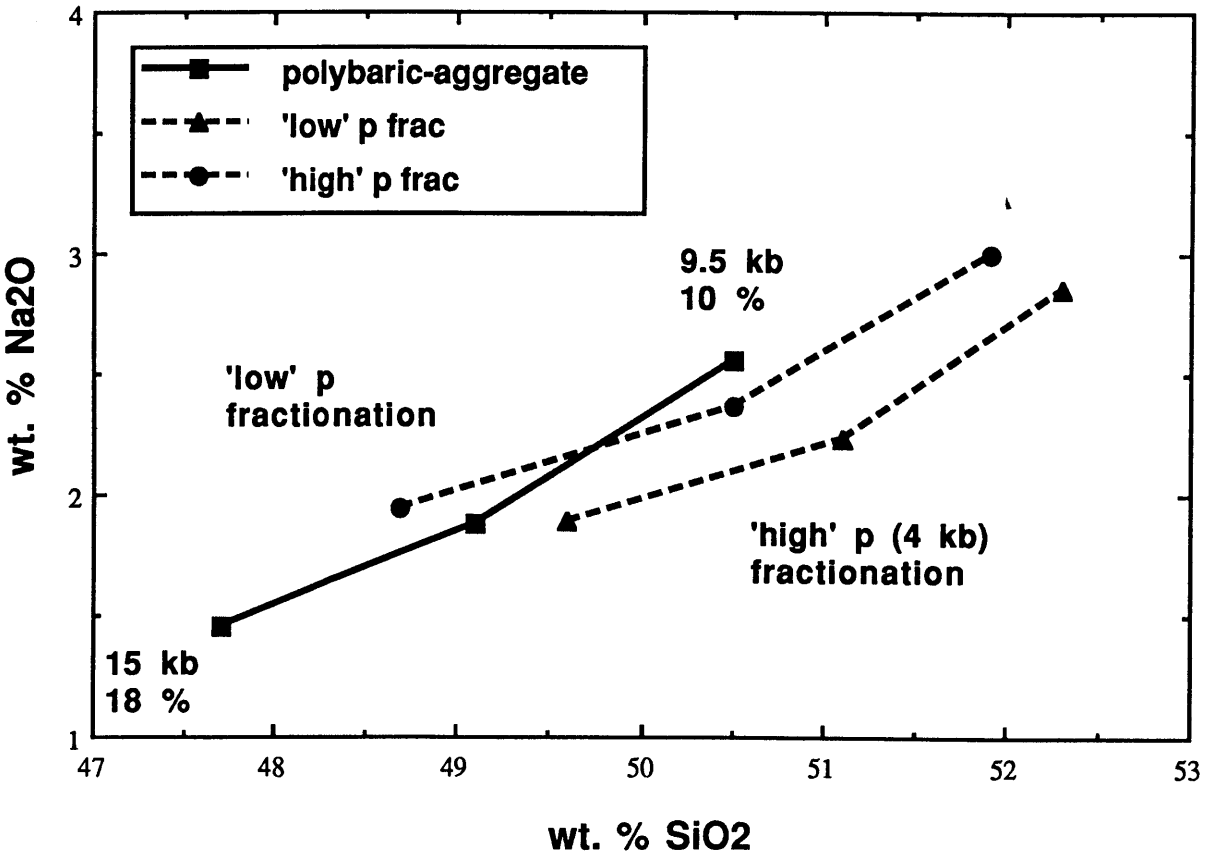
polybaric-aggregate
'low' p frac
'high' p frac
9.5 kb
10 %
'low' p
fractionation
'high' p (4 kb)
fractionation
15 kb
18 %
wt. % Na2O
wt. % SiO2
4
3
2
1
47
48
49
50
51
52
53

Fig. 1-16 (C) Wt.% Na_2O vs. wt.% SiO_2 comparing the forward corrected polybaric, aggregate primary magmas (0.001 kbar = solid curve connecting solid triangles; 4 kbar = solid curve connecting solid circles) to the region occupied by MORB corrected to 8.00 wt.% MgO by Klein and Langmuir (1989, their Fig. 6b) (outlined by dashed line), and to the local trends (labelled as in Fig. 16a). The forward corrected primary magmas are labelled with the extent of depletion achieved in the melting regime that yielded each aggregate primary magma.

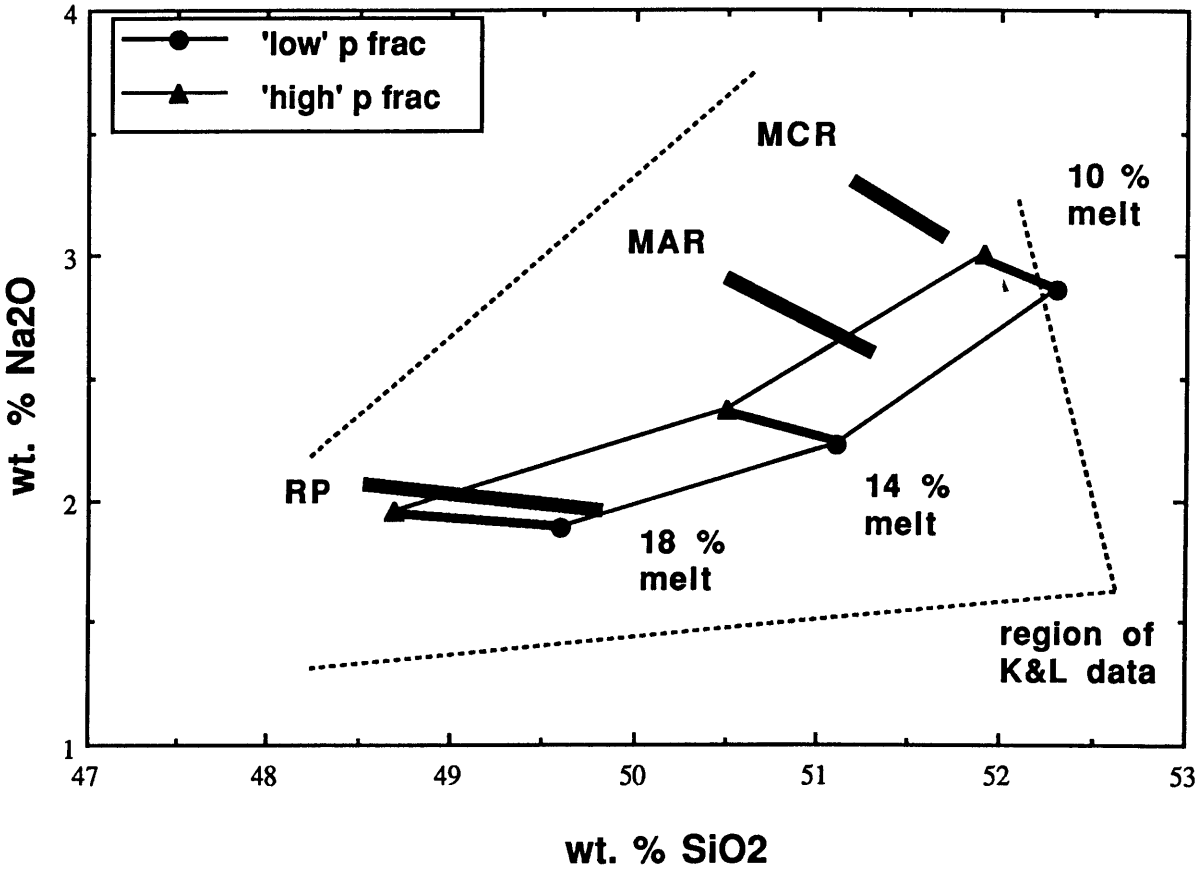
'low' p frac
'high' p frac
MCR
MAR
RP
10 %
melt
14 %
melt
18 %
melt
region of
K&L data
wt. % Na2O
wt. % SiO2
4
3
2
1
47
48
49
50
51
52
53

Fig. 1-17 Na_2O vs. FeO for the polybaric, incremental melting with incomplete melt withdrawal model calculated over the pressure range of 20 - 4 kbar (presented in Fig. 14, solid diamonds). The open squares represent the increments of melt present in the 'melting column' beneath a mid-ocean ridges spreading axis. If all these increments were sampled and thoroughly mixed, then an aggregate primary magma composition (shown as the open circle in Fig. 14) representing the average of all the increments would be delivered to the ridge axis. If incomplete mixing were to occur beneath a given portion of a mid-ocean ridge (as suggested by Klein and Langmuir, 1989, as a mechanism to explain the 'local trends' observed in the global MORB data set, characterized by a positive correlation between Na_2O and FeO at 8.0 wt.% MgO) then a variety of partial aggregate primary magmas may be delivered to the spreading axis. Three possible mixing vectors are indicated with the heavy solid lines. A positive correlation between Na_2O and FeO is generated by incomplete mixing within only the most shallow portion of the melting column. These shallow level melts, however, are also characterized by extremely low Na_2O (<1 wt.%) because they are derived from the most depleted mantle.

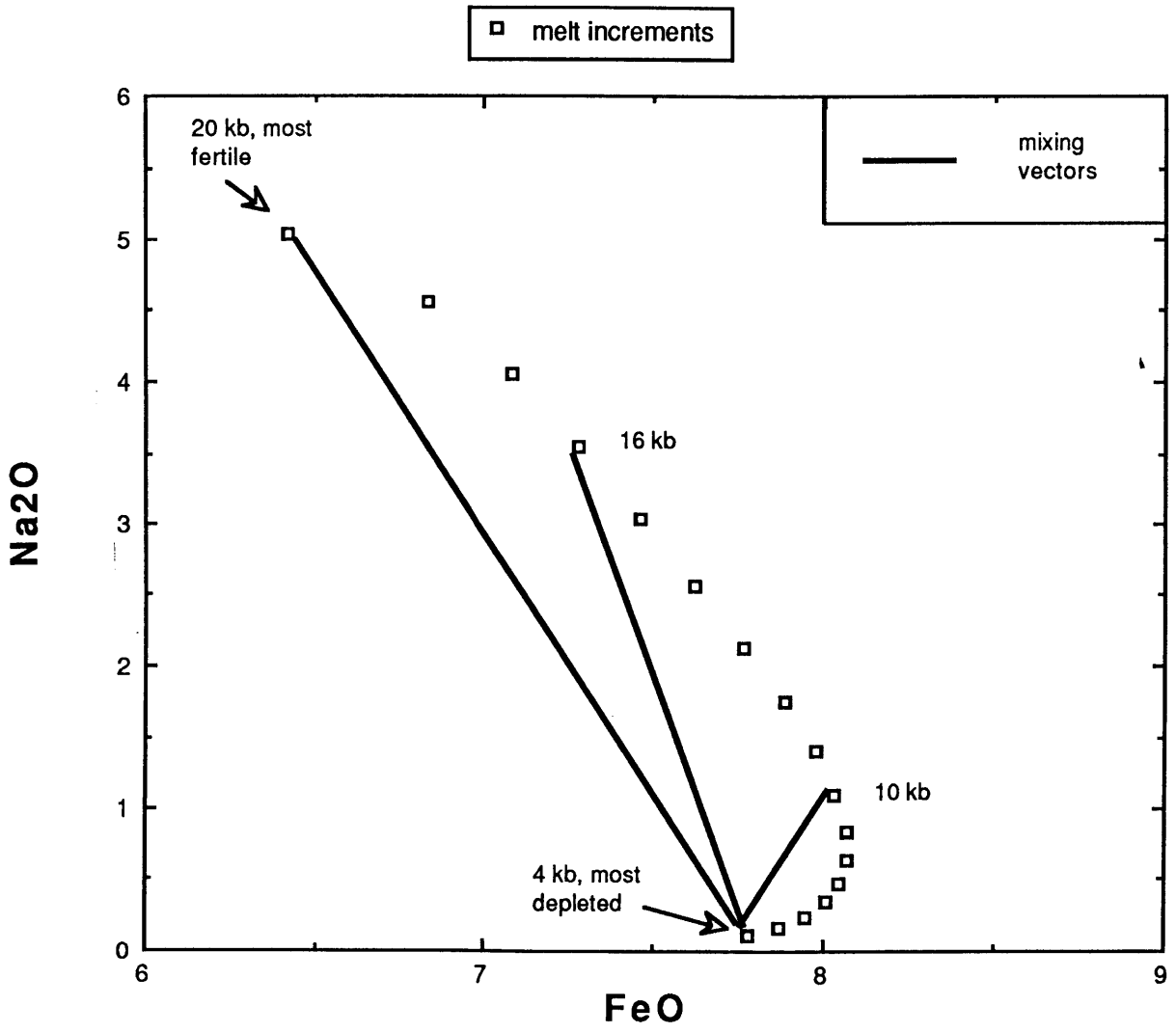
melt increments
mixing vectors
20 kb, most fertile
16 kb
10 kb
4 kb, most depleted
Na2O
FeO
0
1
2
3
4
5
6
6
7
8
9

Fig. 1-18 Pseudo-ternary projection schemes from Plag onto the Oliv-Cpx-Qtz pseudo-ternary (upper), and from Qtz onto the Oliv-Cpx-Plag pseudo-ternary (lower). The projection scheme is the same as that described for Fig. 3. The projected position of the parental mid-Cayman rise lava KN-54-2-2 (c) is shown on each, along with the projected positions for the calculated liquids at 0.001, 2, 4, 6, 8 and 10 kbar (solid squares) saturated with olivine-orthopyroxene-augite-plagioclase; and at 5, 7, 9, 11, 13 and 15 kbar (solid triangles) saturated with olivine-orthopyroxene-augite-spinel. These liquid compositions were calculated at each of these pressures with eqns. 2 - 5 and 7 - 10 in the text, for the Mg#, NaK# and wt.% TiO_2 of KN-54-2-2. The olivine-augite-plagioclase-liquid and olivine-plagioclase-liquid boundaries are sketched in at 1 atm.. The olivine-augite-plagioclase-liquid boundary tracks with the olivine-orthopyroxene-augite-plagioclase-liquid boundary with increasing pressure. The trace of the olivine-orthopyroxene-augite-plagioclase-liquid boundary with increasing pressure is similar to the olivine-plagioclase-liquid boundary. The olivine-plagioclase-liquid boundary does not appear to shift with increased pressure. Thus, the olivine-augite-plagioclase-liquid boundary and the olivine-plagioclase-liquid boundary can be inferred at each of the pressures from the positions of the multiple saturation points. Note that composition C lies on olivine-plagioclase-liquid boundary at 1-atm, but coincides with the inferred 8-kbar olivine-plagioclase-augite-liquid boundary. This boundary projects onto the 8-kbar olivine-orthopyroxene-augite-plagioclase-liquid point in the Oliv-Cpx-Plag pseudo-ternary.

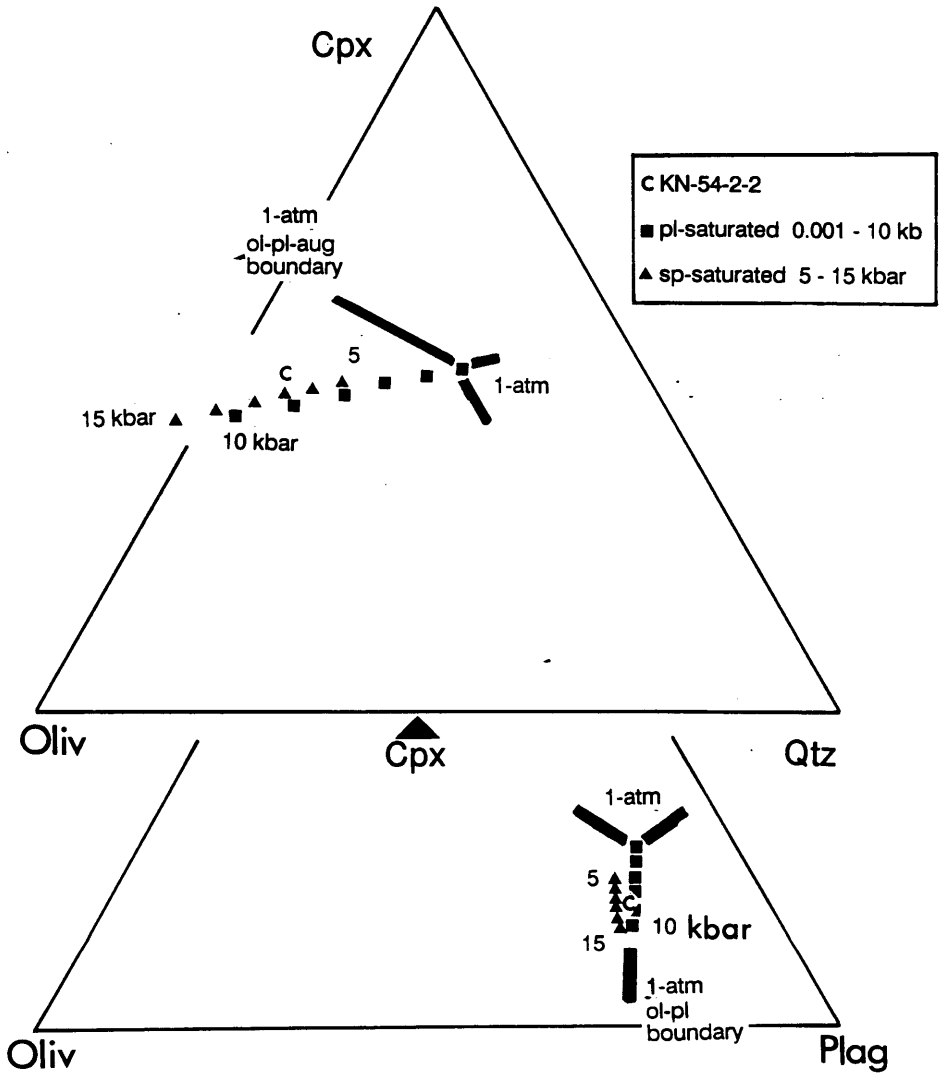
Cpx
C KN-54-2-2
pl-saturated 0.001 - 10 kb
sp-saturated 5 - 15 kbar
1-atm
ol-pl-aug
boundary
5
C
1-atm
15 kbar
10 kbar
Oliv
Cpx
Qtz
1-atm
5
C
10 kbar
15
1-atm
ol-pl
boundary
Oliv
Plag

Fig. 1-19 (A) Wt.% Na_2O vs. wt.% FeO showing the back-fractionation paths (dashed lines) generated with the inverse technique described in the text (see also Table 10) for 9 MORB compositions. Each lava and the model magma compositions associated with its back-fractionation path is designated with a different symbol. Dashed lines connect the natural lavas back to the model, parental, primary magma compositions. The group labelled with letters are the parental group MORBs: IOTJ = Indian Ocean triple junction (sample 6/2; Price et al., 1986); MCR = mid-Cayman rise (sample KN-54-2-2; Thompson et al., 1980); KFZ = just south of the Kane Fracture Zone, 23^{o} N on the MAR (sample GS-104-20); RP = Reykjanes Peninsula (sample TR-139-180-1; Schilling, 1983). The group labelled with numbers are the primitive group MORBs, the numbers are the same as the numbers in Table 5 of Elthon (1990). The solid curves are defined by the model 2 melts from the depleted mantle 1 (Fig. 12). The solid symbols indicate 5.2, 10.3 and 20.2 % melts, circles, squares and triangles represent melts from 10, 15 and 20 kbar, respectively.

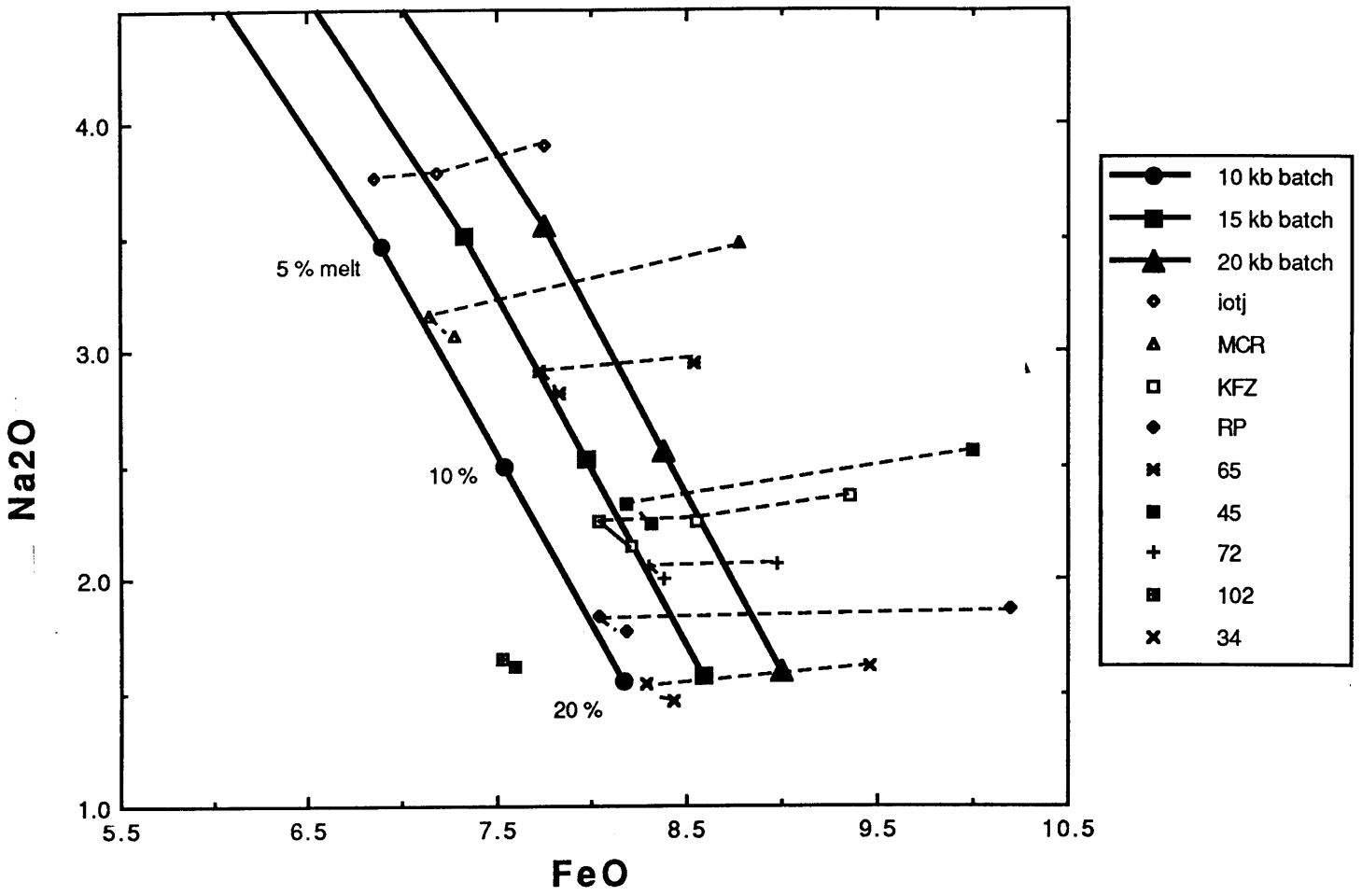
Na2O
FeO
4.0
3.0
2.0
1.0
5.5
6.5
7.5
8.5
9.5
10.5
5 % melt
10 %
20 %
10 kb batch
15 kb batch
20 kb batch
iotj
MCR
KFZ
RP
65
45
72
102
34

Fig. 1-19 (B) CaO/Al_2O_3 vs wt.% FeO for same lavas, back-fractionation paths and melting curves shown in (A). Note that #102, from the primitive MORB data set of Elthon (1990), is very close to being primary.

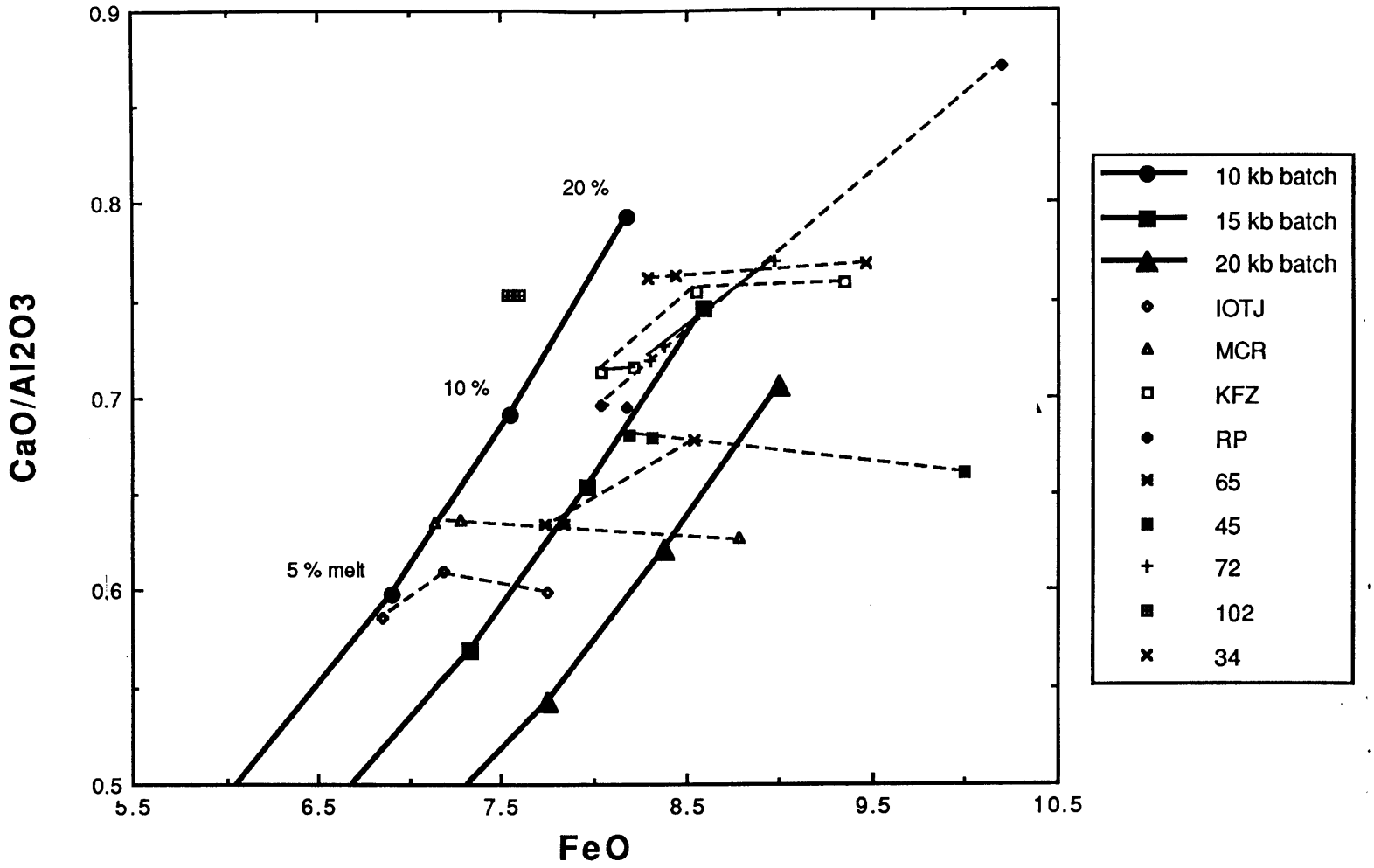
0.9
0.8
0.7
0.6
0.5
CaO/Al2O3
5.5
6.5
7.5
8.5
9.5
10.5
FeO
20 %
10 %
5 % melt
10 kb batch
15 kb batch
20 kb batch
IOTJ
MCR
KFZ
RP
65
45
72
102
34

Table 1-1 Starting compositions used in 9, 11, 13 and 16 kb multiple saturation experiments

	528-1-1	70-002	2004-3-1	79-35g	Kragero opx	San Carlos olivine	KH-4-5 spinel	SYN[a]1	SYN2	SYN3	SYN4	SYN5	SYN6
n	(10)	(368)	(7)		(3)								
SiO_2	48.8(1)[a]	49.6(1)	49.1(2)	47.5(1)	57.3	39.9	0.00	46.5	47.5	45.6	47.3	46.4	47.5
TiO_2	0.80(2)	1.20(2)	1.19(2)	0.59(2)	0.06		0.10(1)	0.30	0.31	0.30	0.33	0.33	0.30
Al_2O_3	15.7(1)	15.8(2)	16.3(8)	18.0(1)	0.10		58.7(1)	13.4	12.3	14.3	14.6	15.5	14.7
Cr_2O_3				0.04(3)			9.84(13)	0.03	0.04	0.20	0.03	0.23	0.0
FeO	9.26(9)	8.98(7)	8.65(9)	8.82(10)	9.49	11.2	10.0(1)	9.40	9.59	9.41	8.07	8.12	7.84
MgO	10.2(1)	8.66(6)	9.13(5)	10.2(1)	33.5	48.9	20.7(2)	21.3	21.0	21.3	20.0	20.0	20.5
MnO	0.19(3)	0.17(3)	0.09(5)	0.17(3)	-[b]		0.12(1)	0.04	0.04	0.04	0.06	0.06	0.09
CaO	11.9(1)	11.9(1)	11.7(2)	11.6(2)	0.26		0.02(1)	8.04	8.28	7.88	7.09	6.96	6.52
K_2O	0.10(1)	0.10(1)	0.10(1)	0.09(2)	-		-	0.04	0.04	0.04	0.07	0.07	0.07
Na_2O	2.09(8)	2.67(6)	2.66(9)	2.43(9)	-		-	0.99	1.02	0.97	2.44	2.39	2.56
P_2O_5	-	0.12(4)	0.04(2)	0.03(3)	-		-						
Total	99.0	99.2	99.0	99.4	100.7		99.9	100.0	100.0	100.0	100.0	100.0	100.0
100.0													

MORB glasses 528-1-1, 70-002 and 2004-3-1, fused bulk rock 79-35g (Bartels et al., 1991), Kragero orthopyroxene and spinel from Kilborne Hole (KH-5-4) were analyzed with the MIT JEOL Superprobe. San Carlos olivine was calculated as Fo_{89} olivine

[a] numbers in parentheses represent 1 r deviation in terms of least units cited, thus 48.8(1) should be read as 48.8 +/- 0.1.
[b] element not analyzed.
[c] SYN compositions calculated by combining weighed amounts of mixes of oxides and powdered San Carlos olivine +/- Kilbourne Hole spinel.

Table 1-2 Experimental run conditions (see Table 1 for starting compositions and Table 3 for run product compositions)

Composition[a]	Run #	T °C	P Kb	t hrs	Run products[b]	K_D Fe-Mg ol/liq	aug/liq	opx/liq	sp/liq	% gl[c]	Phase[d] proportions (wt. %)	ΣR^{2e}	%Fe[f] loss
528-1-1	H13	1220	9	10	gl,pl,ol,aug,pig	0.26	0.29	0.25	-	41	42:27:5:26:-	0.61	2.11
79-35g	H251	1250	9	18	gl,pl,ol,aug,opx	0.34	0.33	0.30	-	67	45:14:29:12:-	0.56	1.75
+16 wt.% opx													
70-002	H129	1270	9	3	gl,ol,opx	0.32	-	0.29	-	90	93:7:-	1.74	-[g]
+20 wt.% opx	H128	1250	9	5	gl,ol,opx	0.31	-	0.26	-	90	91:9:-	2.55	0.59
	H130	1230	9	12	gl,pl,ol,aug,opx	0.38	0.34	0.31	-	66	77:-:8:15:-	2.47	5.00
	H164	1225	9	9	gl,pl,ol,aug,opx	0.31	0.33	0.29	-	61	79:-:9:13:-	2.90	-
2004-3-1	H184	1260	11	24	gl,ol,aug,opx	0.32	0.34	0.31	-	64	79:14:6:-	0.94	9.60
+10 wt.% ol	H177	1255	11	18	gl,pl,ol,aug,opx	0.24	0.23	0.20	-	22	29:24:12:35:-	0.28	2.47
	H165	1310	13	12	gl,ol,aug,opx	0.29	0.28	0.25	-	64	74:3:23:-	0.39	5.60
	H178	1295	13	10	gl,ol,aug,opx	0.32	0.28	0.33	-	73	91:6:3:-	0.03	0.97
	H162	1295	13	15	gl,pl,ol,aug,opx,sp	0.31	0.31	0.27	0.49	37	52:-:2:44:-:-	1.52	-
	H156	1290	13	15	gl,pl,ol,aug,opx,sp	0.23	0.26	0.23	0.34	34	40:4:1:53:-:2	0.10	0.45
	H154	1280	13	15	gl,pl,ol,aug,opx,sp	0.22	0.22	0.21	0.33	31	39:5:1:52:-:3	0.14	0.43
	H181	1280	13	18	gl,pl,ol,aug,opx,sp	0.21	0.21	0.18	0.33	22	31:8:1:58:-:2	0.25	1.27
2004-3-1	H179	1320	16	15	gl,ol,aug,opx,sp	0.21	0.25	0.19	0.33	23	19:4:74:-:3	0.33	3.36
+20 wt.% ol	H193	1345	16	24	gl,ol,aug,opx	0.30	0.35	0.31	-	53	82:6:12:-	1.05	5.65
2004-3-1	H253	1360	16	30	gl,ol,opx	0.32	-	0.38	-	50	96:4:-:-	3.58	13.1
+25 wt.% ol	H200	1340	16	23	gl,ol,aug,opx,sp	0.25	0.28	0.24	0.39	27	33:14:51:-:2	0.53	4.89
	H199	1325	16	22	gl,ol,aug,opx,sp	0.26	0.26	0.34	0.41	24	25:11:61:-:3	0.80	3.74
2004-3-1	H176	1330	16	22	gl,ol,aug,opx	0.29	0.34	0.29	-	54	70:5:25:-	2.83	12.0
+30 wt.% ol													

Table 1-2 (cont.)

Composition[a]	Run #	T °C	P Kb	t hrs	Run products[b]	K_D Fe-Mg ol/liq	aug/liq	opx/liq	sp/liq	% gl[c]	Phase[d] proportions (wt. %)	ΣR^{2e}	%Fe[f] loss
79-35g	H195	1300	13	9	gl,ol,aug	0.30	0.30	-	-		73:21:6	0.87	5.11
+20 wt.% ol	H196	1285	13	17	gl,ol,aug,opx	0.31	0.32	0.29	-	70	76:20:4:-	0.82	3.85
	H185	1350	16	11	gl,ol,aug,opx	0.32	0.36	0.31	-	58	83:17:-:-	1.56	14.5
SYN1	B29	1315	12	13	gl,ol,opx	0.33	-	0.33	-	57	78:22:-	0.20	4.12
	B32	1285	12	12	gl,ol,aug,opx,sp	0.28	0.24	0.19	0.40		51:15:15:18:1	0.01	0.13
SYN2	B30	1300	12	11	gl,ol,aug,opx,sp	0.33	0.33	0.26	0.48		25:10:37:24:4	0.01	0.15
SYN3	B52	1315	12	18	gl,ol,aug,opx,sp	0.31	0.27	0.27	0.54		58:19:5:15:3	0.03	0.40
SYN4	B54	1285	12	22	gl,ol,aug,opx,sp	0.32	0.34	0.29	0.47		59:16:6:17:2	0.03	-
	B55	1270	12	24	gl,ol,aug,opx,sp	0.32	0.33	0.29	0.47		57:15:7:19:2	0.05	-
SYN5	B59	1285	12	26	gl,ol,aug,opx,sp	0.34	0.34	0.28	0.48		54:13:9:20:4	0.07	-
	B56	1255	12	15	gl,pl,ol,aug,opx,sp	0.30	0.25	0.21	0.44		25:17:23:19:12:4	0.02	-
SYN6	B63	1260	10	23	gl,pl,ol,aug,opx	0.30	0.28	0.22	-	21	25:35:40:-:-	0.05	0.86

a opx refers to Kragero orthopyroxene, ol refers to San Carlos olivine.

b abbreviations: gl=liquid, pl=plagioclase, ol=olivine, aug=augite, pig=pigeonite, opx=orthopyroxene and sp=spinel.

c liquid fraction calculated for experiments with negative phase proportions (see note [d]), estimated assuming K_2O behaves incompatibly and using an equilibrium batch crystallization equation.

d phase proportions listed in same order as given for run products; "-" = excluded from mass balance. Phase proportions solved with gl,ol,aug (+/- pl, sp) to ensure a physically reasonable mass balance of the run products against the bulk compositions. When low-Ca pyroxene (pyx) (and in three cases, pl) was included in the mass balance, negative proportions resulted because of the arrangement of the run products in composition space. Exclusion of low-Ca pyx in the mass balance forces the liquid (gl), the ol and aug to take up the difference. Therefore the mass balance will overpredict the fractions of these phases. The gl fraction predicted by the mass balance is generally larger than that estimated with the equilibrium crystallization equation, assuming K_2O behaves incompatibly (see previous column). The purpose of the mass balance is solely to evaluate whether Fe was lost from the sample to the outer Pt capsule.

e sum of the residuals squared for the mass balance described in note c.

f % relative Fe loss.

g no discernable Fe loss within the constraints of the mass balance calculation.

Table 1-3 Run product compositions for melting experiments at 9 - 16 kbar (see Table 2 for run conditions)

Run	Phase[a]	#	SiO_2	TiO_2	Al_2O_3	Cr_2O_3	FeO	MgO	MnO	CaO	K_2O	Na_2O	P_2O_5	total
H13	gl	9	48.1(4)	1.35(22)	14.4(2)	0.04(2)	13.4(8)	7.91(24)	0.25(3)	10.3(2)	0.20(2)	2.36(14)	0.11(5)	98.4
	pl	5	51.0(6)	-[c]	29.9(1)	-	0.82(21)	0.40(16)	-	11.9(3)	0.06(1)	3.41(21)	-	99.5
	ol	3	39.4(2)	0.00[d]	0.08(-)	0.03(1)	18.9(1)	42.4(4)	0.21(2)	0.37(-)	-	-	-	101.2
	aug	9	51.6(1.2)	0.55(14)	4.79(3.2)	0.39(20)	9.37(1.9)	18.8(1.8)	0.26(3)	14.3(3.2)	-	0.31(28)	-	100.4
	pig	8	54.7(1.1)	0.14(10)	1.95(39)	0.00	11.5(2.)	27.0(1.7)	0.27(12)	4.66(67)	-	0.12(10)	-	100.5
H251	gl	11	49.9(4)	0.74(26)	16.6(3)	0.02(1)	8.58(33)	8.49(24)	0.21(8)	10.5(2)	0.12(2)	2.84(1)	0.06(4)	98.1
	pl	4	51.5(2)	-	29.8(5)	-	0.34(18)	0.32(12)	-	13.7(1)	0.03(1)	3.60(15)	-	99.2
	ol	5	39.7(3)	0.03(1)	0.14(6)	0.00	15.4(1)	44.5(3)	0.13(4)	0.41(6)	-	-	-	100.2
	aug	14	53.2(8)	0.38(8)	4.71(1.1)	0.09(3)	6.81(81)	20.5(1.5)	0.15(3)	14.3(2.0)	-	0.31(7)	-	100.4
	opx	14	56.3(1.)	0.16(7)	2.28(1.17)	0.05(3)	9.49(40)	30.9(1.3)	0.18(2)	2.21(71)	-	0.00	-	101.5
H129	gl	10	50.4(2)	1.02(5)	14.7(2)	0.09(3)	9.05(12)	11.0(2)	0.14(2)	10.9(1)	0.10(1)	2.37(8)	0.11(2)	99.8
	ol	5	40.4(2)	0.03(1)	0.08(1)	0.06(1)	12.4(1)	47.5(2)	0.15(3)	0.37(2)	-	-	-	100.7
	opx	2	56.2	0.16	2.33	0.10	7.66	32.0	0.09	2.51	-	0.03	-	101.0
H128	gl	10	51.5(4)	1.02(5)	15.3(1)	0.09(3)	8.81(11)	9.94(13)	0.14(3)	11.1(2)	0.10(1)	2.36(12)	0.12(2)	100.4
	ol	4	40.4(2)	0.04(1)	0.07(1)	0.06(1)	13.0(1)	46.8(4)	0.14(2)	0.38(3)	-	-	-	100.9
	opx	4	56.7(3)	0.13(8)	1.46(56)	0.11(7)	8.19(17)	32.1(7)	0.12(5)	2.16(32)	-	0.05(2)	-	101.0
H130	gl	10	50.1(1)	1.15(6)	16.3(2)	0.09(3)	9.12(16)	9.01(10)	0.13(3)	10.9(1)	0.12(2)	2.77(6)	0.12(2)	99.7
	pl	3	50.6(5)	-	30.0(9)	-	0.78(13)	0.70(18)	-	14.4(4)	0.04(1)	3.29(28)	-	99.8
	ol	5	39.1(1)	0.05(4)	0.07(5)	0.00	16.9(4)	43.6(4)	0.17(4)	0.38(2)	-	-	-	100.3
	aug	10	53.1(5)	0.52(9)	3.64(8)	0.17(3)	7.11(4)	20.5(8)	0.13(7)	14.9(7)	-	0.30(9)	-	100.2
	opx	1	55.1	0.30	3.13	0.11	9.45	29.8	0.23	3.09	-	0.06	-	101.2
H164	gl	7	50.1(1)	1.15(3)	16.2(1)	0.07(2)	8.93(6)	9.26(7)	0.12(2)	11.0(5)	0.13(1)	2.76(1)	0.09(2)	99.8
	pl	6	50.4(3)	-	29.7(1.)	-	0.52(18)	0.60(44)	-	13.5(4)	0.03(1)	3.80(15)	-	100.6
	ol	4	40.5(3)	0.04(1)	0.10(1)	0.04(2)	13.7(1)	45.8(3)	0.20(1)	0.38(3)	-	-	-	100.7
	aug	26	52.8(1.5)	0.65(25)	4.45(1.91)	0.13(3)	6.43(1.03)	20.1(9)	0.17(3)	15.0(1.7)	-	0.37(20)	-	100.0
	opx	9	56.0(8)	0.23(8)	2.37(1.15)	0.07(4)	8.62(60)	31.7(1.0)	0.16(5)	2.31(75)	-	0.06(3)	-	101.4

Table 1-3 (cont.)

Run	Phase[a]	#	SiO_2	TiO_2	Al_2O_3	Cr_2O_3	FeO	MgO	MnO	CaO	K_2O	Na_2O	P_2O_5	total
H184	gl	9	48.7(7)	1.24(4)	17.7(2)	0.03(1)	8.14(16)	9.56(34)	0.17(2)	10.5(7)	0.14(1)	3.14(1)	0.13(3)	99.4
	ol	5	40.2(1)	0.02(1)	0.05(2)	0.02(1)	12.7(3)	47.1(2)	0.15(1)	0.33(1)	-	-	-	100.6
	aug	10	51.3(1.)	0.58(20)	7.01(82)	0.18(3)	5.80(30)	19.9(9)	0.16(3)	14.3(1.)	-	0.50(7)	-	99.6
	opx	12	53.4(1.1)	0.27(5)	6.19(1.4)	0.13(3)	7.94(17)	29.8(6)	0.19(3)	2.40(21)	-	0.10(1)	-	100.3
H177	gl	8	46.9(1.3)	2.56(10)	17.7(7)	0.00	11.5(1.3)	6.39(1.2)	0.28(4)	7.90(71)	0.40(12)	5.05(77)	0.40(4)	99.1
	pl	4	52.6(2)	-	29.1(8)	-	0.59(18)	0.54(46)	-	12.4(1)	0.09(-)	4.28(9)	-	99.6
	ol	4	39.5(9)	0.03(1)	0.06(1)	0.02(1)	18.4(3)	42.0(3)	0.21(5)	0.33(4)	-	-	-	100.5
	aug	10	50.8(1.)	0.98(13)	6.97(1.13)	0.15(3)	7.58(26)	18.3(7)	0.19(3)	14.2(9)	-	0.59(11)	-	99.6
	opx	10	52.9(1.1)	0.42(7)	6.30(1.58)	0.11(3)	9.96(33)	27.9(6)	0.21(6)	2.36(28)	-	0.12(2)	-	100.2
H165	gl	7	48.1(2)	1.30(4)	18.1(2)	0.04(3)	9.12(10)	9.38(17)	0.13(2)	10.3(1)	0.14(2)	3.33(2)	0.12(2)	100.0
	ol	4	40.7(3)	0.04(1)	0.06(1)	0.0	13.0(2)	46.6(5)	0.18(1)	0.32(1)	-	-	-	101.0
	aug	33	51.9(9)	0.37(7)	7.2(1.0)	0.14(7)	5.85(40)	21.5(1.4)	0.16(4)	12.0(1.3)	-	0.47(6)	-	99.5
	opx	13	54.4(1.5)	0.23(10)	5.24(2.71)	0.08(6)	7.71(57)	30.0(1.5)	0.16(3)	3.46(1.67)	-	0.16(8)	-	101.4
H178	gl	9	48.8(4)	1.13(3)	16.0(2)	0.04(1)	8.51(10)	11.4(2)	0.19(4)	10.8(9)	0.13(1)	2.72(13)	0.11(2)	99.9
	ol	2	40.9(2)	0.02(1)	0.07(1)	0.0	11.7(2)	48.5(4)	0.14(2)	0.35(1)	-	-	-	101.7
	aug	10	51.9(1.6)	0.48(27)	7.25(1.5)	0.19(3)	6.05(.39)	21.5(2.0)	0.18(4)	12.4(1.6)	-	0.48(14)	-	100.4
	opx	7	53.8(9)	0.24(3)	6.78(1.38)	0.14(2)	7.44(17)	30.2(4)	0.17(2)	2.55(33)	-	0.12(1)	-	101.4
H162	gl	10	48.9(5)	1.40(6)	17.7(3)	0.00	10.2(1)	7.93(2)	0.10(4)	9.13(2)	0.21(2)	4.11(12)	0.00	98.9
	pl	5	52.2(9)	-	29.8(2)	-	0.48(13)	0.29(13)	-	12.9(7)	0.04(1)	4.12(34)	-	99.8
	ol	4	39.7(3)	0.04(2)	0.06(-)	0.03(1)	17.3(4)	43.1(2)	0.20(2)	0.32(1)	-	-	-	100.9
	aug	31	50.5(7)	0.68(14)	8.42(1.24)	0.10(3)	7.66(40)	19.3(1.2)	0.18(3)	12.6(1.0)	-	0.67(17)	-	100.0
	opx	10	51.5(7)	0.33(7)	8.73(1.73)	0.05(3)	9.63(19)	28.0(6)	0.17(4)	2.22(16)	-	0.14(2)	-	100.8
	sp	3	0.20(6)	0.17(4)	64.4(6)	0.37(7)	12.6(8)	19.9(6)	0.11(3)	0.14(3)	-	-	-	97.3
H156	gl	7	48.0(3)	1.42(8)	19.3(4)	0.00	10.3(4)	6.28(90)	0.14(2)	8.64(45)	0.23(3)	5.27(25)	0.26(4)	99.8
	pl	5	53.8(1)	-	28.7(1)	-	0.55(28)	0.57(44)	-	11.7(1)	0.08(1)	4.83(1)	-	100.2
	ol	4	39.7(3)	0.03(1)	0.06(1)	0.00	16.9(3)	44.0(2)	0.20(1)	0.33(2)	-	-	-	101.3
	aug	12	50.2(1.1)	0.92(20)	8.55(1.47)	0.10(3)	8.19(55)	18.9(1.0)	0.19(4)	12.9(1.2)	-	0.65(13)	-	100.5
	opx	9	52.0(1.3)	0.39(8)	8.10(2.08)	0.07(2)	10.4(4)	27.5(1.2)	0.19(3)	2.51(47)	-	0.18(6)	-	101.2
	sp	3	0.41(38)	0.14(1)	64.8(2)	0.81(11)	11.7(4)	20.7(4)	0.12(2)	0.15(4)	-	-	-	98.0

Table 1-3 (cont.)

Run	Phase[a]	#	SiO_2	TiO_2	Al_2O_3	Cr_2O_3	FeO	MgO	MnO	CaO	K_2O	Na_2O	P_2O_5	total
H154	gl	7	47.8(4)	1.65(7)	19.1(4)	0.04(3)	11.0(3)	6.10(62)	0.16(2)	8.64(43)	0.27(3)	4.98(58)	0.28(3)	100.1
	pl	7	52.7(4)	-	29.2(6)	-	0.53(17)	0.46(38)	-	12.4(2)	0.08(1)	4.39(15)	-	99.8
	ol	4	39.8(5)	0.05(1)	0.06(1)	0.00	17.2(3)	43.1(8)	0.22(1)	0.38(7)	-	-	-	101.0
	aug	12	51.1(4)	0.72(12)	7.03(68)	0.13(3)	7.83(32)	19.7(8)	0.17(4)	13.3(9)	-	0.59(6)	-	100.4
	opx	10	51.2(7)	0.49(7)	8.63(1.1)	0.07(2)	10.5(2)	27.1(5)	0.16(4)	2.45(31)	-	0.15(1)	-	100.7
	sp	3	0.75(62)	0.15(1)	64.0(1.5)	0.77(5)	11.9(2)	20.0(1)	0.13(2)	0.19(12)	-	-	-	97.1
H181	gl	4	47.8(4)	1.98(18)	18.5(9)	0.02(1)	11.8(4)	5.70(16)	0.14(5)	7.38(29)	0.37(2)	5.94(26)	0.40(7)	100.2
	pl	4	52.8(2)	-	29.2(6)	-	0.58(22)	0.51(40)	-	12.1(4)	0.07(1)	4.52(19)	-	99.8
	ol	6	39.6(2)	0.04(1)	0.06(1)	0.00	18.7(3)	42.3(2)	0.19(2)	0.33(2)	-	-	-	101.2
	aug	10	50.2(1.3)	0.85(20)	8.76(1.36)	0.12(3)	7.86(27)	18.4(1.3)	0.18(5)	13.0(1.3)	-	0.75(21)	-	100.0
	opx	10	51.7(1.3)	0.45(9)	8.35(1.9)	0.07(4)	10.3(8)	27.4(8)	0.20(3)	2.22(21)	-	0.16(2)	-	100.8
	sp	3	0.38(31)	0.31(2)	65.9(5)	0.47(26)	13.4(3)	19.8(4)	0.13(1)	0.12(5)	-	-	-	100.5
H179	gl	4	47.4(7)	1.64(14)	18.6(4)	0.00	11.6(4)	7.07(48)	0.13(2)	8.36(22)	0.27(3)	5.12(83)	0.34(2)	100.0
	ol	4	40.2(3)	0.04(1)	0.22(11)	0.02(1)	15.3(2)	44.6(6)	0.15(2)	0.41(11)	-	-	-	100.9
	aug	10	50.2(1.2)	0.63(26)	10.5(2.2)	0.06(2)	7.90(87)	18.9(3.0)	0.15(2)	10.3(1.10)	-	1.23(62)	-	99.7
	opx	10	51.8(34)	0.34(2)	8.64(61)	0.05(2)	8.90(13)	28.2(6)	0.18(2)	2.28(20)	-	0.21(2)	-	100.6
	sp	2	0.61	0.21	65.8	0.49(3)	11.4	21.3	0.12	0.19	-	-	-	99.7
H193	gl	11	47.5(4)	1.22(5)	16.0(2)	0.03(2)	8.46(10)	11.7(3)	0.19(4)	10.7(1)	0.15(1)	3.03(15)	0.13(2)	99.1
	ol	5	40.5(2)	0.02(1)	0.10(1)	0.02(1)	10.6(1)	48.5(4)	0.15(1)	0.34(3)	-	-	-	100.2
	aug	9	52.5(4)	0.31(4)	7.48(5)	0.09(2)	5.94(34)	23.5(7)	0.15(3)	10.4(1.)	-	0.58(4)	-	101.0
	opx	6	54.0(7)	0.20(4)	6.77(1.35)	0.08(3)	6.86(33)	30.8(4)	0.11(4)	2.45(14)	-	0.13(3)	-	101.4
H253	gl	7	47.4(3)	1.19(4)	15.8(20)	0.02(1)	7.42(10)	12.3(2)	0.27(4)	10.6(9)	0.14(1)	2.72(10)	0.15(1)	98.0
	ol	3	40.5(3)	0.00	0.10(1)	0.00	9.41(31)	49.3(2)	0.10(5)	0.31(3)	-	-	-	99.7
	opx	11	54.3(3)	0.22(2)	5.34(20)	0.15(2)	6.22(7)	26.8(3)	0.13(6)	7.32(33)	-	0.35(5)	-	100.8

Table 1-3 (cont.)

Run	Phase[a]	#	SiO_2	TiO_2	Al_2O_3	Cr_2O_3	FeO	MgO	MnO	CaO	K_2O	Na_2O	P_2O_5	total
H200	gl	4	47.3(7)	1.42(2)	17.8(4)	0.03(1)	9.92(11)	8.90(73)	0.16(3)	9.94(38)	0.22(2)	3.86(31)	0.32(2)	99.3
	ol	5	40.5(2)	0.05(1)	0.10(1)	0.02(1)	13.2(2)	46.8(5)	0.18(2)	0.29(2)	-	-	-	101.1
	aug	19	51.5(5)	0.49(8)	8.97(69)	0.08(3)	6.53(26)	20.9(9)	11.1(9)	0.18(3)	-	0.74(7)	-	100.4
	opx	7	52.6(1.3)	0.28(7)	8.60(2.01)	0.00	7.91(16)	29.5(1)	0.12(3)	2.11(12)	-	0.15(2)	-	101.2
	sp	3	0.56(20)	0.18(1)	65.9(8)	0.21(4)	9.48(6)	21.8(1)	0.07(1)	0.15(9)	-	-	-	98.1
H199	gl	5	48.1(8)	1.77(17)	17.6(8)	0.03(1)	10.4(4)	7.83(65)	0.11(2)	7.69(65)	0.36(4)	5.61(51)	0.36(6)	99.8
	ol	5	39.7(2)	0.05(1)	0.11(1)	0.03(1)	15.6(2)	44.5(4)	0.18(2)	0.31(2)	-	-	-	100.5
	aug	8	51.3(5)	0.53(8)	9.15(6)	0.08(2)	7.15(41)	20.6(7)	0.19(3)	10.8(6)	-	0.93(8)	-	100.6
	opx	10	52.3(9)	0.38(8)	8.16(1.29)	0.06(2)	9.23(21)	20.6(6)	0.15(3)	2.16(21)	-	0.23(4)	-	100.5
	sp	3	0.09(8)	0.17(2)	65.7(2)	0.78(3)	11.2(2)	20.7(1)	0.09(1)	0.11(1)	-	-	-	98.1
H176	gl	8	47.3(7)	1.25(5)	16.5(5)	0.00	7.73(22)	11.8(2)	0.18(3)	10.9(2)	0.13(1)	2.98(17)	0.15(3)	98.9
	ol	4	41.3(1)	0.03(1)	0.11(1)	0.00	9.59(11)	50.2(3)	0.14(1)	0.31(1)	-	-	-	101.7
	aug	5	52.9(3)	0.35(6)	7.40(53)	0.12(1)	5.20(12)	23.1(4)	0.17(3)	11.6(4)	-	0.55(4)	-	101.4
	opx	6	54.9(7)	0.17(3)	6.22(1.04)	0.10(1)	6.03(11)	31.7(5)	0.15(3)	2.46(10)	-	0.14(2)	-	101.9
H195	gl	7	48.0(5)	0.66(3)	18.9(3)	0.02(1)	8.22(10)	9.36(25)	0.18(3)	10.6(1)	0.11(1)	2.76(11)	0.07(1)	98.8
	ol	6	40.5(1)	0.02(1)	0.08(1)	0.03(1)	12.4(2)	47.4(4)	0.17(2)	0.30(2)	-	-	-	101.0
	aug	10	51.4(1.2)	0.33(8)	8.17(1.8)	0.08(3)	5.56(63)	21.0(2.1)	0.17(3)	13.2(2.0)	-	0.47(6)	-	100.4
H196	gl	7	48.1(3)	0.66(2)	18.3(2)	0.03(1)	8.28(19)	9.70(20)	0.20(3)	10.7(1)	0.10(1)	2.72(9)	0.07(1)	98.8
	ol	5	40.5(3)	0.03(1)	0.09(3)	0.03(1)	12.3(3)	47.2(2)	0.18(2)	0.32(3)	-	-	-	100.7
	aug	8	51.2(4)	0.36(3)	8.44(66)	0.08(1)	5.54(21)	20.3(7)	0.15(3)	14.1(7)	-	0.52(10)	-	100.7
	opx	6	52.5(1.1)	0.21(2)	8.47(1.5)	0.06(3)	7.34(15)	30.1(7)	0.12(1)	2.35(29)	-	0.08(2)	-	101.2
H185	gl	9	47.1(3)	0.58(3)	16.6(2)	0.03(2)	7.75(10)	12.0(2)	0.19(3)	10.7(1)	0.12(1)	2.39(12)	0.04(3)	97.4
	ol	4	40.6(1)	0.03(1)	0.11(3)	0.04(1)	10.2(1)	49.4(4)	0.15(3)	0.34(3)	-	-	-	100.9
	aug	11	51.6(4)	0.25(3)	8.87(51)	0.08(2)	5.12(24)	21.8(9)	0.15(2)	11.9(1.)	-	0.55(4)	-	100.3
	opx	10	53.2(7)	0.19(4)	8.27(1.0)	0.06(2)	6.23(12)	31.2(5)	0.15(4)	2.45(15)	-	0.13(2)	-	100.9

Table 1-3 (cont.)

Run	Phase[a]	#	SiO_2	TiO_2	Al_2O_3	Cr_2O_3	FeO	MgO	MnO	CaO	K_2O	Na_2O	P_2O_5	total
B29	gl	7	48.1(6)	0.39(3)	17.0(8)	0.00	8.64(12)	13.6((4)	0.09(3)	10.4(1)	0.07(1)	1.35(7)	0.00	99.6
	ol	4	40.7(2)	0.00	0.13(1)	0.00	10.3(2)	49.2(3)	0.08(1)	0.29(1)	-	-	-	100.7
	opx	10	53.1(6)	0.10(2)	7.55(84)	0.10(3)	6.50(20)	31.2(5)	0.08(3)	1.85(28)	-	0.05(3)	-	100.6
B30	gl	7	46.9(3)	0.50(6)	18.1(1)	0.00	9.94(36)	10.5(1)	0.11(3)	11.2(1)	0.10(1)	1.99(25)	0.00	99.3
	ol	4	39.7(2)	0.00	0.11(1)	0.00	14.3(4)	45.5(4)	0.10(3)	0.36(2)	-	-	-	100.1
	aug	10	50.3(5)	0.20(3)	10.0(5)	0.04(2)	6.16(19)	20.0(6)	0.10(2)	13.4(7)	-	0.36(4)	-	100.6
	opx	10	52.8(6)	0.12(1)	7.88(77)	0.06(2)	7.37(8)	29.9(4)	0.09(3)	2.33(12)	-	0.05(1)	-	100.6
	sp	3	0.16(1)	0.05(1)	68.0(6)	0.18(6)	9.97(14)	21.8(4)	0.03(1)	0.07(1)	-	-	-	100.2
B32	gl	8	47.9(2)	0.61(3)	18.3(2)	0.00	11.8(2)	8.30(23)	0.09(6)	10.1(2)	0.18(3)	3.14(12)	0.00	100.6
	ol	4	39.7(7)	0.00	0.12(1)	0.00	17.3(2)	44.0(3)	0.11(2)	0.35(2)	-	-	-	101.6
	aug	15	50.2(4)	0.25(2)	10.2(5)	0.00	6.49(58)	19.0(5)	0.11(2)	13.7(8)	-	0.41(7)	-	100.3
	opx	6	52.2(9)	0.10(1)	9.35(1.25)	0.09(3)	7.96(52)	29.2(6)	0.12(2)	2.16(21)	-	0.07(1)	-	101.2
	sp	3	0.31(10)	0.07(2)	68.5(3)	0.14(8)	11.8(1)	20.6(1)	0.02(1)	0.12(1)	-	-	-	101.6
B52	gl	10	47.4(3)	0.47(2)	17.7(1)	0.12(5)	9.21(17)	10.8(1)	0.10(2)	11.7(1)	0.12(1)	1.87(12)	0.00	99.6
	ol	6	39.5(7)	0.00	0.11(1)	0.07(1)	12.4(1)	46.2(9)	0.12(1)	0.35(1)	-	-	-	98.8
	aug	19	50.4(1.1)	0.15(4)	7.54(1.55)	0.44(7)	5.32(33)	20.2(1.3)	0.11(3)	14.3(1.0)	-	0.42(6)	-	98.7
	opx	28	52.5(1.2)	0.10(2)	7.93(1.43)	0.57(10)	6.94(22)	30.3(9)	0.08(2)	1.70(23)	-	0.06(4)	-	100.2
	sp	5	0.09(8)	0.08(1)	58.9(1.9)	8.06(1.46)	9.75(30)	21.0(4)	0.04(2)	0.10(4)	-	-	-	98.04
B54	gl	8	49.2(3)	0.42(2)	18.8(2)	0.02(1)	7.83(16)	9.93(23)	0.11(4)	9.87(10)	0.12(1)	3.77(10)	0.00	100.2
	ol	4	40.8(4)	0.00	0.09(1)	0.02(1)	12.1(2)	47.8(3)	0.09(2)	0.30(1)	-	-	-	101.2
	aug	20	50.3(9)	0.31(4)	10.3(4)	0.04(2)	5.01(26)	18.8(1.0)	0.11(2)	14.6(9)	-	0.72(8)	-	100.2
	opx	22	52.4(1.0)	0.15(3)	9.28(1.27)	0.07(3)	6.77(23)	30.1(1.0)	0.09(3)	1.97(30)	-	0.15(11)	-	101.0
	sp	4	0.51(18)	0.05(1)	67.8(1.9)	0.45(14)	8.38(1)	22.4(36)	0.04(1)	0.13(4)	-	-	-	99.8
B55	gl	8	48.8(3)	0.44(3)	19.1(2)	0.00	7.91(12)	9.74(14)	0.13(3)	10.0(2)	0.13(2)	3.78(15)	0.00	100.2
	ol	5	40.9(4)	0.00	0.09(2)	0.02(1)	12.3(2)	47.9(6)	0.09(2)	0.30(2)	-	-	-	101.6
	aug	22	50.5(1.0)	0.24(4)	10.2(1.8)	0.05(2)	5.22(52)	19.2(1.8)	0.11(3)	13.5(1.3)	-	0.76(36)	-	99.9
	opx	22	52.5(7)	0.13(3)	9.43(84)	0.08(2)	6.98(18)	29.9(5)	0.10(3)	2.09(3)	-	0.14(4)	-	101.4
	sp	3	0.55(38)	0.06(1)	69.3(2)	0.43(4)	8.68(13)	22.6(4)	0.04(1)	0.10(7)	-	-	-	101.7

Table 1-3 (cont.)

Run	Phase[a]	#	SiO_2	TiO_2	Al_2O_3	Cr_2O_3	FeO	MgO	MnO	CaO	K_2O	Na_2O	P_2O_5	total
B59	gl	11	49.1(3)	0.42(2)	18.4(1)	0.00	8.12(13)	9.94(19)	0.06(4)	9.71(19)	0.14(1)	3.87(21)	0.00	99.9
	ol	5	40.2(6)	0.00	0.09(1)	0.05(1)	12.8(2)	46.1(4)	0.10(2)	0.30(1)	-	-	-	99.7
	aug	12	49.8(6)	0.27(2)	10.1(4)	0.19(3)	5.21(14)	18.7(6)	0.12(2)	14.8(5)	-	0.68(3)	-	100.2
	opx	12	51.9(9)	0.15(2)	9.08(98)	0.44(12)	6.88(26)	30.1(9)	0.12(2)	2.07(40)	-	0.15(14)	-	100.9
	sp	7	0.15(5)	0.06(1)	66.4(1.1)	1.38(10)	8.78(14)	22.3(6)	0.04(2)	0.09(2)	-	-	-	99.5
B56	gl	8	49.2(2)	0.48(3)	19.0(1)	0.00	8.70(33)	7.46(37)	0.11(3)	8.36(15)	0.19(1)	5.32(26)	0.00	98.8
	pl	6	55.0(7)	-	28.7(8)	-	0.43(19)	0.00	-	11.1(3)	0.06(1)	5.20(23)	-	100.9
	ol	3	39.7(5)	0.02(1)	0.08(1)	0.03(1)	15.4(1)	44.5(7)	0.11(1)	0.30(1)	-	-	-	100.1
	aug	25	50.4(8)	0.28(4)	9.84(99)	0.10(4)	5.61(41)	19.0(8)	0.20(3)	14.0(1.1)	-	0.72(7)	-	100.2
	opx	11	52.4(7)	0.16(3)	8.59(1.01)	0.40(11)	7.37(33)	29.9(3)	0.09(3)	2.15(19)	-	0.12(2)	-	101.2
	sp	3	0.29(23)	0.09(2)	67.6(5)	1.13(46)	10.8(1)	21.2(2)	0.04(1)	0.10(5)	-	-	-	101.3
B63	gl	8	50.9(1)	0.73(5)	18.2(1)	0.05(4)	8.09(28)	8.04(27)	0.13(5)	9.53(15)	0.19(2)	4.30(17)	0.00	100.1
	pl	10	53.9(6)	-	29.0(4)	-	0.40(9)	0.22(12)	-	11.9(2)	0.06(1)	4.60(19)	-	100.1
	ol	5	39.9(3)	0.00	0.09(1)	0.05(1)	14.0(3)	45.8(4)	0.14(3)	0.30(2)	-	-	-	100.3
	aug	10	51.5(9)	0.47(6)	7.34(1.19)	0.25(3)	5.44(26)	19.1(8)	0.14(2)	15.4(8)	-	0.61(5)	-	100.2
	opx	10	52.8(8)	0.19(2)	8.12(1.46)	0.25(3)	6.77(14)	30.4(5)	0.11(1)	2.25(26)	-	0.12(2)	-	101.0

[a] Abbreviations as in Table 2.
b Parenthesized units represent two standard deviations of replicate analyses in terms of least units cited. Thus, 48.1(4) should be read as 48.1 +/- 0.4.
c Element not analyzed.
[d] Element below detection limit.

Table 1-4 Experimentally constrained stoichiometric coefficients[a] for the mantle-melting equation over the pressure range of 0.001 - 16 kbar (wt. %) (abbreviations the same as in Table 2):

$$1.\ liq^{T1} = \zeta\ liq^{T2} + \alpha\ aug^{T2} + \beta\ opx^{T2} + \gamma\ ol^{T2} + \delta\ pl^{T2} + \epsilon\ sp^{T2}$$

calculated from experiments presented in this study:

Expt. T1	T2	P(kb)	Mg# (T1-T2)	α	β	γ	δ	ϵ	Σr^{2b}
H130	H13	9	0.64-0.51	0.25	0.21	-0.03[c]	0.57	-	0.92
H164	H13	9	0.65-0.51	0.31	0.16	-0.06	0.58	-	1.32
H162	H156	13	0.58-0.52	1.72	1.59	-1.35	-1.13	0.17	0.02
H162	H181	13	0.58-0.46	1.21	0.50	-0.57	-0.23	0.11	0.21
H154	H181	13	0.50-0.46	1.83	0.44	-0.98	-0.53	0.29	0.04
H200	H179	16	0.62-0.53	1.34	-0.15	-0.25	-	0.07	0.02
B52	B30	12	0.68-0.65	1.08	0.17	-0.36	-	0.07	0.005
Bartels et al. (1990)									
H192	H197	16	0.65-0.51	1.39	-0.17	-0.31	-	0.08	0.33
Falloon and Green (1987):									
2078	2138	10	0.71-0.67	0.76	0.60	-0.44	-	0.08	0.03
2136	2078	10	0.75-0.71	0.79	0.43	-0.29	-	0.07	0.12
2140	1511	10	0.72-0.69	0.73	0.40	-0.19	-	0.06	0.22
1493	1511	10	0.71-0.69	0.75	0.38	-0.22	-	0.08	0.14
For modelling spinel-lherzolite melting:									
avg of B52, and Falloon and Green experiments				0.82	0.40	-0.30	-	0.08	
For modelling plagioclase-lherzolite melting:									
avg of H130 and H164				0.28	0.19	-0.05	0.58	-	

[a] stoichiometric coefficients were esitmated with a mass balance calculation in which the major element compositions of the melt and mineral phases (wt. % oxides) in an experiment at a lower temperature (T2) on the multiple saturation boundary were balanced against a melt at a higher temperature (T1) on the multiple saturation 0.boundary. The equations were normalized to 1 unit mass of liquid (thus the mineral phase coefficients sum to 1.0).

[b] sum of residuals squared for mass balance calculation.

[c] negative coefficients imply that the phase belongs on the product side of the melt reaction, with the liquid.

Table 1-5 Sources of experimentally produced multiply saturated liquids incorporated into data set used in quantitative description of multiple saturation equilibria over the pressure range of 0.001 - 16 kb

Study	Pressure (kb)	Temp (^{o}C)	Phases[a]	Mg #[b]	NaK#[c]	TiO_2 (wt%)
Kushiro (1973)	8	1200	liq,ol,aug,pig,pl	0.57	0.27	1.97
Fujii & Kushiro (1977)	8	1230	liq,ol,aug,opx,pl	0.57	0.21	1.64
Presnall et al. (1979)	.001-14	1242-1374	liq,ol,aug,opx,pl liq,ol,aug,opx,pl,sp liq,ol,aug,opx,sp	1.00	0.00	0.00
Stolper (1980)	10	1275	liq,ol,aug,opx,pl[d]	0.67	0.28	0.84
Fujii & Bougault (1983)	10	1275	liq,ol,aug,opx,pl[e]	0.70	0.20	0.86
Grove & Bryan (1983b)	.001	1156-1167	liq,ol,aug,pig,pl	0.46-0.54	0.11-0.13	1.28-2.43
Takahashi & Kushiro (1983)	5-8	1200-1225	liq,ol,aug,opx,pl,sp liq,ol,aug,opx,sp	0.63-0.66	0.20-0.31	1.33-1.91
Elthon & Scarfe (1984)	15	1300	liq,ol,aug,opx,sp	0.69	0.10	1.19
Fujii & Scarfe (1985)	10	1250-1310	liq,ol,aug,opx,sp	0.70-0.82	0.00-0.16	0.04-1.14
Falloon & Green (1987,1988)	10-15	1230-1360	liq,ol,aug,opx,pl,sp liq,ol,aug,opx,sp	0.68-0.76	0.14-0.27	0.69-0.96
Baker & Eggler (1987)	8	1150-1175	liq,ol,aug,pig,pl[f]	0.41-0.45	0.28-0.41	1.43-1.65
Grove et al. (1990)	8	1210	liq,ol,aug,pig,pl	0.46	0.30	2.55
Bartels et al. (1990)	10-15	1270-1355	liq,ol,aug,opx,pl liq,ol,aug,opx,sp	0.58-0.65	0.24-0.38	0.64-0.88
Kinzler (this study)	9-16	1220-1340	liq,ol,aug,pig,pl liq,ol,aug,opx,pl liq,ol,aug,opx,pl,sp liq,ol,aug,opx,sp	0.46-0.65	0.20-0.46	1.15-2.56

a abbreviations same as in Table 2.
b mg# = $(Mg^{2+}/[Mg^{2+}+Fe^{2+}])$, total iron as Fe^{2+}.
c NaK# = $([Na_2O+K_2O]/[Na_2O+K_2O+CaO])$, in wt.%.
d liquid composition and temperature of multiple saturation estimated from experiments on ol-aug-pl and ol-opx cotectic surfaces.
e liquid composition assumed to be that of ARP-74-10-16, temperature estimated from liquidus experiments of Fujii and Bougault (1983).
f liquid composition and temperature of multiple saturation interpolated between higher temperature experiment saturated with ol, aug and pl; and a lower temperature experiment saturated with aug, pig, and pl.

Table 1-6 Melting experiments on synthetic analog[a] of glass from experiment # 10, 10 kbar at 1310°C, Table 6, of Fujii and Scarfe (1985).

Run Conditions:

Run #	Pressure (kbar)	Temp (°C)	Time (hrs)	Run products
B93	10	1310	12	gl
B102	10	1295	10	gl,cpx
B100	10	1265	24	gl,cpx

Starting composition:

	#[b]	SiO_2	TiO_2	Al_2O_3	Cr_2O_3	FeO	MgO	MnO	CaO	K_2O	Na_2O	Total
F&S#10		50.1	0.45	14.5	0.32	6.05	14.0	0.12	12.4	0.05	1.74	100.0
SYNF&S	8	51.2(2)[c]	0.39(2)	14.2(1)	0.20(13)	6.18(6)	14.0(1)	0.05(1)	12.0(2)	0.05(1)	1.54(7)	99.9

Run product compositions:

B93	gl	9	51.6(2)	0.36(3)	14.6(1)	0.28(5)	5.08(19)	14.2(12)	0.13(3)	12.1(1)	0.05(1)	1.44(8)	99.8
B102	gl	10	50.7(3)	0.44(4)	16.6(1)	0.22(4)	6.07(11)	11.3(2)	0.15(3)	12.3(1)	0.05(1)	1.76(8)	99.8
B102	cpx	22	53.1(6)	0.16(6)	5.93(1.7)	0.83(14)	4.56(31)	23.6(1.9)	0.11(2)	12.2(1.4)	-	0.34(16)	100.8
B100	gl	10	50.9(4)	0.47(3)	18.3(2)	0.23(3)	6.18(26)	9.95(38)	0.07(1)	11.8(1)	0.07(1)	1.97(10)	100.1
B100	cpx	37	52.9(6)	0.18(4)	6.07(70)	0.63(11)	4.64(39)	23.1(1.2)	0.11(2)	12.9(1.3)	-	0.31(7)	100.8

[a] composition synthesised from oxides as described in experimental techniques section for the type 3 experiments, and conditioned at 1 atm. at QFM at 1307 for 1 hour.

[b] number of analyses in average of electron microprobe analyses.

[c] parenthesized units represent two standard deviations of replicate analyses in terms of least units cites. Thus, 51.2(2) should be read as 51.1 +/- 0.2.

Table 1-7 Comparison between experimentally produced, multiply saturated experiments and compositions predicted with the descriptions of the spinel- and plagioclase-lherzolite melting equilibria.

Expt	Pressure	Temp	SiO_2	TiO_2	Al_2O_3	FeO	MgO	CaO	K_2O	Na_2O
B30	12	1300	47.3(3)	0.50(6)	18.2(1)	10.0(4)	10.6(1)	11.3(1)	0.10(1)	2.01(25)
model[a]		1311	48.3	0.49	16.1	10.4	10.7	11.7	0.10	2.18
B52	12	1315	47.4(3)	0.47(2)	17.8(1)	9.27(17)	10.9(1)	11.8(1)	0.12(1)	1.88(12)
model[a]		1314	48.4	0.46	16.3	9.51	11.2	11.9	0.12	2.03
B54	12	1285	49.2(3)	0.42(2)	18.8(2)	7.82(16)	9.92(23)	9.86(10)	0.12(1)	3.77(10)
model[a]		1297	49.1	0.42	18.7	7.76	9.54	10.3	0.12	4.07
B56	12	1255	49.8(2)	0.49(3)	19.3(1)	8.82(33)	7.56(37)	8.47(15)	0.19(1)	5.39(26)
model[a]		1277	49.2	0.47	19.5	8.98	7.42	8.59	0.19	5.65
B63	10	1267	50.9(1)	0.73(5)	18.2(1)	8.10(28)	8.05(27)	9.54(15)	0.19(2)	4.30(17)
model[b]		1260	52.1	0.72	17.5	7.93	7.68	9.44	0.19	4.44

[a] model calculated for the pressure of the experiment and the Mg#, NaK# and TiO_2 of the glass using the description of the spinel-lherzolite melting equilibrium.

[b] as in a but the model was calculated with the description of the plagioclase-lherzolite melting equilibrium.

Table 1-8 Model mantle and melt compositions

	Mantle compositions							
	SiO_2	TiO_2	Al_2O_3	FeO	MgO	CaO	K_2O	Na_2O
H&Z prim[a]	46.381	0.182	4.097	7.619	38.116	3.239	0.032	0.333
H&Z dep 1[b]	46.335	0.172	3.870	7.665	38.499	3.185	0.004	0.279
	Mantle modes							
	aug	opx	ol	pl	aug	opx	ol	sp
H&Z prim[a]	0.11	0.24	0.58	0.07	0.20	0.24	0.53	0.03
H&Z dep 1[b]	0.11	0.24	0.59	0.06	0.19	0.24	0.54	0.03

Melt compositions generated by melting H&Z dep 1 mantle source

Model 1: isobaric, batch melting

Pressure	5 kbar			8 kbar			10 kbar			15 kbar			20 kbar		
melt %	5%	10%	20%	5%	10%	20%	5%	10%	20%	5%	10%	20%	5%	10%	20%
SiO_2	53.9	53.5	53.0	51.8	51.4	50.9	50.2	49.9	49.5	47.9	47.5	47.1	45.5	45.1	44.6
TiO_2	1.11	0.87	0.61	1.11	0.87	0.61	0.94	0.81	0.64	0.94	0.81	0.64	0.94	0.81	0.64
Al_2O_3	16.0	16.0	15.9	17.2	17.1	17.1	17.6	16.6	15.6	18.8	17.8	16.8	19.9	18.9	18.0
FeO	6.07	6.31	6.68	6.45	6.70	7.06	6.90	7.55	8.17	7.33	7.97	8.59	7.75	8.38	9.00
MgO	8.88	9.24	9.78	9.44	9.81	10.3	10.2	11.2	12.1	10.8	11.8	12.7	11.5	12.41	13.3
CaO	11.3	11.6	12.1	11.3	11.6	12.1	10.5	11.5	12.4	10.7	11.6	12.6	10.8	11.8	12.7
K_2O	0.07	0.04	0.02	0.07	0.04	0.02	0.08	0.04	0.02	0.08	0.04	0.02	0.08	0.04	0.02
Na_2O	2.74	2.41	1.90	2.74	2.41	1.90	3.46	2.50	1.55	3.51	2.53	1.57	3.55	2.57	1.59
Temp (^oC)	1230	1235	1241	1257	1262	1268	1269	1278	1287	1349	1366	1367	1429	1438	1447

Table 1-8 (cont.)

Model 2: isobaric, incremental-batch, accumulative melting with incomplete melt withdrawal

Pressure	5 kbar			8 kbar			10 kbar			15 kbar			20 kbar		
melt %[c]	5.2%	10.3%	20.2%	5.2%	10.3%	20.2%	5.2%	10.3%	20.2%	5.2%	10.3%	20.2%	5.2%	10.3%	20.2%
SiO_2	53.9	53.6	52.2	51.8	51.4	50.1	50.4	50.1	49.6	48.0	47.6	47.2	45.7	45.2	44.8
TiO_2	1.21	1.02	0.73	1.21	1.02	0.73	1.00	0.90	0.67	1.00	0.90	0.72	1.00	0.90	0.72
Al_2O_3	16.0	15.9	15.8	17.1	17.1	17.0	17.8	16.5	15.7	19.0	17.7	16.6	20.1	18.9	17.8
FeO	5.94	6.14	6.68	6.32	6.50	7.02	6.66	7.32	8.09	7.09	7.73	8.18	7.51	8.14	8.54
MgO	8.82	9.26	10.5	9.39	9.83	11.1	10.0	11.2	12.0	10.7	11.9	13.2	11.3	12.5	13.9
CaO	11.2	11.6	12.7	11.2	11.6	12.7	10.3	11.4	12.6	10.4	11.5	12.8	10.6	11.7	13.0
K_2O	0.07	0.04	0.02	0.07	0.04	0.02	0.07	0.04	0.02	0.07	0.04	0.02	0.07	0.04	0.02
Na_2O	2.81	2.44	1.31	2.81	2.44	1.31	3.73	2.54	1.68	3.76	2.55	1.29	3.79	2.56	1.29
Temp (^oC)[d]	1233	1243	1259	1260	1270	1286	1278	1295	1303	1359	1376	1383	1438	1456	1463

a renormalized not to include Cr_2O_3, MnO, NiO, P_2O_5.

b calculated by melting a primitive mantle of the composition of Hart and Zindler (1986) over the pressure range 25-2 kbar, with the model 3 melting process (see text) for a total melt extent of 1.3%. Compositions of the residues of these melts over this pressure range were averaged to provide an estimate of a well-mixed depleted MORB-mantle source.

c each successive increment of batch melting is 0.01, of which 90 % is withdrawn after it is produced. The effective % melt extracted = $1-(.991)^n$ where n=number of steps.

d the temperature at which the last increment in the step-wise incremental-batch accumulative melting process with incomplete melt withdrawal was produced.

Table 1-9 Aggregate primary magmas produced by near-fractional, polybaric melting and accumulation

Model 3:	polybaric, incremental-batch, accumulative melting with incomplete melt withdrawal[a]					
	Hart & Zindler dep 1			Hart & Zindler prim		
	(1)	(2)	(3)	(4)	(5)	(6)
P_r(kbar)	25-4	20-4	15-4	25-4	20-4	15-4
F_T(%)	18	14	10	18	14	10
crust (km)	13	8	4	13	8	4
SiO_2	47.7	49.1	50.5	47.7	49.3	50.7
TiO_2	0.75	0.83	0.90	0.80	0.86	0.93
Al_2O_3	16.6	16.4	16.5	17.2	17.0	17.3
FeO	8.00	7.66	7.12	7.76	7.32	6.65
MgO	12.8	12.0	10.9	12.3	11.4	10.1
CaO	12.7	12.2	11.5	12.3	11.7	10.9
K_2O	0.02	0.03	0.04	0.17	0.21	0.30
Na_2O	1.46	1.88	2.55	1.83	2.25	3.00
$Temp_r$ (^oC)	1499-1207	1418-1206	1337-1200	1483-1223	1402-1205	1321-1197

Notes: Percent melting as a function of pressure is assumed to be a constant value of 1. % per kbar of pressure release, 90% of this melt is withdrawn after each increment (to allow for continuous melting). P_r provides the initial (P1) and final (P2) pressures associated with a given mean pressure. F_T, is the total extent of melt achieved from the column ($(0.991)^{(P1-P2+1)}$). $Temp_r$ provides the temperatures at which the first and last increment are produced, respectively. Crust refers to an approximation of the thickness of crust generated from each melting column ($= (P1 - P2 + 1)*3.3*F_T$).

Table 1-10 'Back-fractionation' calculations of sampled MORB lava compositions to hypothetical primary parents

sample[a]	SiO_2	TiO_2	Al_2O_3	FeO	MnO	MgO	CaO	Na_2O	K_2O	P[b] (Kb)	ol - aug - pl[c] (wt. fraction)	inc	F[d]
IOTJ	51.1	1.08	16.7	7.75	0.20	8.73	10.0	3.91	0.25				
	51.3	1.01	17.0	7.19	0.18	9.02	10.3	3.78	0.22		0.13,0.29,0.58	0.02	0.89
parent	51.2	0.93	17.4	6.85	0.17	9.25	10.2	3.76	0.21	9-10	0.25 - 0.75	0.02	0.82
MCR	51.7	1.58	16.6	8.78		7.80	10.4	3.48	0.25				
	51.3	1.26	17.3	7.14		8.60	11.0	3.16	0.18		0.13,0.29,0.58	0.02	0.72
parent	51.0	1.22	16.8	7.28		9.71	10.7	3.07	0.18	9-10	1.0 - -	0.02	0.65
KFZ	50.2	1.44	15.8	9.35	0.17	8.50	12.0	2.36	0.10				
	50.2	1.32	16.3	8.55	0.15	8.84	12.3	2.26	0.09		0.12,0.34,0.54	0.02	0.87
	49.9	1.19	17.1	8.04	0.13	9.12	12.2	2.25	0.08		0.25 - 0.75	0.02	0.78
parent	49.5	1.14	16.2	8.21	0.10	11.0	11.6	2.14	0.08	13-14	1.0 - -	0.01	0.75
RP	50.5	0.92	14.7	10.2	0.06	8.22	12.8	1.87	0.07				
	49.3	0.62	18.1	8.04	0.04	9.34	12.6	1.84	0.05		0.25 - 0.75	0.02	0.67
parent	49.0	0.60	17.4	8.18	0.04	10.8	12.1	1.77	0.05	10-11	1.0 - -	0.02	0.64
ELT65	49.1	1.18	17.4	8.54		9.03	11.8	2.95	0.05				
	49.0	1.01	18.3	7.73		9.44	11.6	2.91	0.04		0.25 - 0.75	0.02	0.85
parent	48.7	0.98	17.8	7.83		10.6	11.3	2.82	0.04	13-15	1.0 - -	0.01	0.83
ELT45	48.7	0.91	17.4	10.0		8.93	11.5	2.56	0.04				
	49.1	0.80	17.9	8.19		9.51	12.2	2.33	0.03		0.12,0.34,0.54	0.02	0.74
parent	48.7	0.77	17.2	8.32		11.0	11.7	2.24	0.03	13-15	1.0 - -	0.01	0.71
ELT72	49.6	0.85	16.1	8.97		9.87	12.4	2.07	0.17				
	49.3	0.76	17.1	8.30		10.1	12.3	2.06	0.15		0.25 - 0.75	0.02	0.89
parent	49.0	0.73	16.5	8.38		11.2	12.0	2.00	0.15	12-13	1.0 - -	0.01	0.86
ELT102	49.8	0.63	17.4	7.53		9.94	13.1	1.65	0.02				
parent	49.6	0.62	17.0	7.59		10.7	12.8	1.62	0.02	11-13	1.0 - -	0.02	0.98
ELT34	50.9	1.08	15.6	9.46		9.15	12.0	1.62	0.12				
	50.6	0.97	16.4	8.29		9.54	12.5	1.54	0.10		0.12,0.34,0.54	0.02	0.82
parent	50.2	0.93	15.6	8.44		11.4	11.9	1.46	0.09	13-15	1.0 - -	0.01	0.78

Notes for Table 1-10

[a] MORB sample abbreviations: IOTJ, Indian Ocean triple junction; MCR, mid-Cayman rise; KFZ, just south of the Kane Fracture Zone (23°N); RP, Reykjanes Peninsula; ELT#, # keyed to same # in Table 5, Elthon (1990).

[b] estimated pressure of separation of the parent magma from the mantle residue, inferred with the inverse method described in the text.

[c] weight fractions of phases added to lava.

[d] fraction of liquid remaining.

NOTE: $^{pl}K_D^{Na\text{-}Ca} = (Na_2O^{pl}*CaO^{liq})/(Na_2O^{liq}*CaO^{pl}) = 1.0$; $^{ol}K_D^{Fe\text{-}Mg} = (FeO^{ol}*MgO^{liq})/(FeO^{liq}*MgO^{ol}) = 0.293$; $^{aug}K_D^{Fe\text{-}Mg} = (FeO^{aug}*MgO^{liq})/(FeO^{liq}*MgO^{aug}) = 0.27$.

CHAPTER II

Magmatic diversity at the over-lapping spreading center at $11^{O}45'$ N on the East Pacific Rise

INTRODUCTION

Detailed geochemical sampling and marine tectonic studies over the past 10 years have revealed that mid-ocean ridges are segmented on the scale of tens to hundreds of kilometers (e.g., Macdonald et al., 1984; Lonsdale, 1985; Langmuir et al., 1986). Maxima in geochemical diversity typically occur near the end-points of ridge segments, and thus understanding the processes that yield the geochemically diverse signatures is important for understanding the overall formation of mid-ocean ridge crust. Data collected during a combined ALVIN submersible/dredging cruise aboard the Atlantis II in 1988 to the over-lapping spreading center (OSC) at $11^{O}45'$N on the East Pacific Rise (EPR) are combined with experimentally determined 1-atm. phase equilibria. The purpose of this study is to extend the work of Thompson et al. (1985, 1989) to evaluate and amplify the existing framework for understanding the processes that yield geochemical diversity at migrating tectonic offsets along mid-ocean ridges by applying it to this well characterized area.

Previous Work on the $11^{O}45'$ N OSC

The discontinuity at $11^{O}45'$ N of the EPR, at a depth maximum along the ridge between the Clipperton and Orozco transforms (Perram and Macdonald, 1990), was mapped with Sea Beam and recognized morphologically as an OSC by Macdonald and Fox (1983); and as a substantial petrologic discontinuity by Thompson et al. (1985, 1989) and Langmuir et al. (1986). Detailed sampling of the EPR between 10 and 12^{O}N (Thompson et al., 1985, 1989; and this study) provides excellent characterization of the lava types represented along the ridge segment to the south of the $11^{O}45'$ N OSC as well as at the southern tip of the eastern limb. Geochemical and camera-tow studies of the ridge segment to the north of the $11^{O}45'$ N OSC include those of Hekinian and Fouquet (1985), Langmuir et al. (1986) and Hekinian et al. (1989). Mapping of the $11^{O}45'$ N OSC with high-resolution SeaMARC I side scan sonar (Crane, 1987) and Argo and

Angus imaging systems (Thompson et al., 1985, 1989; Argo-Rise Group, 1988; Uchupi et al., 1988) revealed that the eastern limb is tectonically and volcanically more active than the western limb.

A recent detailed bathymetric, magnetic and side scan sonar study has determined that the $11^{O}45'$ OSC has existed near its current morphological expression for approximately 0.7 m.y., and that it migrated northward at 70 mm/yr for the first 0.2 m.y., then migrated slowly (less than 30 mm/yr) and then significantly more rapidly (140-200 mm/yr) southward (Perram and Macdonald, 1990). Thus the $11^{O}45'$ OSC represents a southward migrating, small-offset (8 km) ridge transform intersection (Perram and Macdonald; 1990).

Background

Over-lapping spreading centers (Macdonald and Fox, 1983; Lonsdale, 1983) are intermediate in the scale of tectonic offsets of mid-ocean ridge spreading centers, between large offset transforms, and zero offset transforms (Schouten and White, 1980; Schouten and Klitgord, 1982) or deviations in axial linearities (DEVALs) (Langmuir et al., 1986). OSCs are non-rigid (Macdonald et al., 1985), may migrate along strike and are thought to be rather transient features, although this point has been debated (Lonsdale, 1986; Macdonald et al., 1986; Perram and Macdonald, 1990). Previous investigators have observed that mid-ocean ridge basalt (MORB) erupted near tectonic offsets may show several petrologic signatures. These signatures include the occurrence of evolved lava compositions with cooler magmatic temperatures (Hekinian and Thompson, 1976; Schilling and Sigurdsson, 1979; Christie and Sinton, 1981); the eruption of a wider range of lava compositions over a limited geographic area (Natland, 1980; Sinton et al., 1983; Perfit et al., 1983; Bender et al., 1984; Christie and Sinton, 1986); and the effects of higher-pressure fractionation (Langmuir and Bender, 1984; Sinton and Christie, 1985) and varying extents of melting in the underlying mantle (Bender et al., 1984; Langmuir and Bender, 1984; Christie and Sinton, 1986, Karsten, et

al., 1991). Collectively labelled 'a transform fault effect' (Langmuir et al., 1986) the petrologic signatures associated with tectonic offsets have been understood in the context of the cooling of the lithosphere and asthenosphere that results from the truncation or disruption of a spreading ridge by the offset (Fox and Gallo, 1984; Langmuir and Bender, 1984). Macdonald et al. (1988), however, stress the observation that as the offset at the 11°45'N OSC on the EPR is so small, the axial morphological and geochemical expression of the OSC must be controlled by processes at depth (i.e. related to magma supply) beneath each of the spreading segments, rather than by the near-surface boundary conditions imposed by the small offset in the lithospheric plates.

Sinton et al. (1983) extended the framework which considered the thermal affects associated with ridge truncation to include the magma supply effects associated with the migration of a ridge-transform intersection relative to the underlying mantle, in order to evaluate the magnitude and distribution of geochemical signatures associated with migrating ridge transform intersections. Several tectonic variables are considered within their framework, including local spreading rates; proximity to 'hot spots'; propagation rate (if any); migration rate of the intersection, relative to the underlying mantle; and the length of the transform truncating the ridge segment.

This paper presents geochemical and geologic observations from the east and west limbs of the OSC at 11°45'N on the EPR (Fig. 1). In the context of the existing frameworks for evaluating the geochemical effects of the tectonic environments associated with offsets along mid-ocean ridges (Sinton et al., 1983; Langmuir et al., 1986, Macdonald et al., 1988), the work of Thompson et al. (1989) is extended to address three general questions for the migrating OSC at 11°45'N: 1) What are the geochemical signatures observed in lavas erupted proximal to the migrating OSC? 2) What roles in generating the geochemical diversity observed on both limbs of the 11°45'N OSC are played by crystal fractionation and magma mixing over a range of crustal pressures? 3) What role do the tectonic variables governing the morphological expression of the

$11^{o}45'$N OSC play in generating the magnitude and distribution of geochemical anomalies observed, and how do these anomalies compare to the geochemical anomalies observed at other nearby OSCs (i.e. $12^{o}37'$N and $12^{o}54'$N) and propagating, or migrating rift systems (i.e. Galapagos, Juan de Fuca)? These questions are addressed and constrained by new experimental data and geochemical data on lavas recently recovered in the 1988 ALVIN dive series.

MAJOR ELEMENT COMPOSITIONS OF LAVAS FROM THE $11^{o}45'$N OSC

Analytical Methods

Chemical analyses were performed with an electron microprobe at an accelerating potential of 15 kV and a sample current of approximately 10 nA. Beam spot size was nominally 1 micron for mineral analyses and 10 microns for glass analyses. All data was collected using wavelength dispersive spectrometers and Tracor Northern 5500-5600 automation and reduced using the Bence and Albee (1968) matrix corrections with modifications of Albee and Ray (1970). The relatively low beam current of 10 nA was used to minimize errors resulting from sodium migration in the glass caused by impingement of the electron beam. Counting times were 10 - 40 seconds. A natural MORB glass (PROTEA-9-70-002, Table 3) was analyzed during every probe session to check the consistency of the calibration throughout the time over which the analytical data were collected. We have augmented the data presented in this study with the data presented for the same area by Thompson et al. (1989), as well as additional data for 10 - 13^{o}N on the EPR from the Smithsonian Institution Volcanic Glass File (this additional data is only used for the discussion of the geochemical anomalies associated with OSC tectonic segmentation). Systematic differences outside of electron microprobe counting statistic errors for SiO_2, MgO and Na_2O exist between data obtained on the MIT electron microprobe and the Smithsonian electron microprobe. Therefore, correction

factors obtained by analyzing the same set of glasses on both microprobes (provided in Table 3) were applied to the data from the Smithsonian electron microprobe facility.

Data Presentation

Major element compositions of fresh glass chips from 79 lavas sampled during the 1988 ALVIN and dredging cruise aboard the Atlantis II on the EPR from $11^{o}40'$ to $12^{o}00'$N on the east and west limbs of the $11^{o}45'$N OSC were determined as described above on the MIT electron microprobe. The dive tracks and dredge locations for 8 ALVIN dives and 2 dredges are shown in Fig. 1 (dredge locations from the Thompson et al. (1989) study are also provided in Fig. 1). For the purposes of discussion, the compositional mean and sample standard deviation were compiled for chemical groups observed in the data set (including the data of Thompson et al., 1989) (Table 2). These groups were chosen on the basis of similarity of major element compositions (the only exception is group F, which was also identified based on field observations). In general, the sample standard deviations for the chemical groups are similar in magnitude or smaller relative to the sample standard deviations associated with 7 replicate analyses collected for a single MORB glass with the electron microprobe (compare 1 sigma values for chemical group averages in Table 2 with 1 sigma values for individual analyses in Table 1).

Normalized SiO_2, TiO_2, Al_2O_3, FeO* (total Fe as FeO), CaO, K_2O, Na_2O, and P_2O_5 for glasses from the eastern and western rifts of the $11^{o}45'$N OSC are plotted verses MgO in Fig. 2. The glasses from the eastern rift of the OSC (EOSC) show a significantly greater range in MgO content than those of the western rift of the OSC (WOSC), defining both the more primitive and more evolved ends of the total range. The highest MgO glasses from both the EOSC and the WOSC overlap in their Al_2O_3, FeO, CaO and TiO_2 contents. As the MgO contents of the glasses decrease the trends defined by Al_2O_3, FeO and CaO for the two suites diverge, although some overlap is observed. In general, the EOSC glasses contain lower amounts of Al_2O_3 and CaO, and

higher amounts of FeO, relative to the WOSC glasses, at a given MgO content. Glasses from the EOSC define a lower K_2O trend with decreasing MgO than those from the WOSC, although, again, overlap is observed. Mineralogically, the lavas sampled from both rifts of the OSC are aphyric to sparsely phyric, containing micro-phenocrysts and rare phenocrysts of plagioclase and lesser amounts of olivine.

GEOLOGICAL OBSERVATIONS AND DISTRIBUTIONS OF GEOCHEMICAL GROUPS

Western Rift

Three ALVIN dives (1997, 1998 and 2000) and two dredges (17 and 18) were carried out between roughly $11^{O}43'$ N and $11^{O}52'$ N on the western rift of the $11^{O}45'$N OSC during the 1988 Atlantis II-118 cruise (Fig. 1, dredges 64, 65, 66 and 68 from the PROTEA-009 cruise reported by Thompson et al., 1989 are also shown). The WOSC is narrower and topographically higher than the eastern rift and is composed of pillowed terrain with occasional lobate pillows and sheet flows in flatter regions. To the north there is no simple axial graben, however there is a well developed axial graben to the south (Bryan et al., 1988). The age of the lavas corresponds to approximately 1.5 on the sediment scale (inter-connected sediment pockets observed). The southern portion of the west rift is marked by fissuring, while the northern portion is dominated by relatively un-fissured, constructional volcanism; the transition between the dominantly fissured and un-fissured terrain was observed at approximately $11^{O}45'$N (north of ALVIN dive 1998). Tectonism also dominates the portion of the EPR south of the WOSC (south of $11^{O}40'$N) to the topographic high at $11^{O}25'$N, with the most recent locus of volcanic activity observed at $11^{O}29'$N (age corresponding to 1.2 on the sediment scale, light dusting of sediment observed) (Thompson, Bryan et al., in prep).

The northernmost tip of the western rift (ALVIN dive 2000, Fig. 1) is marked by small volcanic cones cut by only minor fissures, and a final volcanic event that partially filled in earlier fissures. The ages of lavas at the tip are similar to those further south, (also corresponding to roughly 1.5 on the sediment scale); lavas collected along dive 2000 from glassy flows that partly fill the older fissures probably represent the last volcanic event (Bryan et al., 1988). In general, the western rift of the OSC to the north of approximately 11°45'N is relatively quiet with respect to both tectonic and volcanic processes, and most likely is a dieing rift. No evidence of hydrothermal activity was observed north of 11°40'N.

Eastern Rift

Five ALVIN dives were carried out between roughly 11°43'N and 11°50'N on the eastern rift of the 11°45'N OSC (Fig. 1). Some areas of the EOSC are marked by local constructional highs that were centers of eruption. The ages of the fissured lavas correspond roughly to 1.5 on the sediment scale. To the north on the EOSC the axial region lacks a well defined axial graben; and is wide and highly fissured. Southwards, the axial region narrows, and has a better developed graben at 11°44'N. The tip of the EOSC consists mainly of fissured volcanic ridges and local constructional highs. Lavas with a range of compositions (groups A, B, C, H, K and P, Tables 1 and 2) were emplaced along the EOSC from approximately 11°55' N (Dr-20) to 11°43'N (ALVIN dive 2002) relatively recently (ages corresponding to 1.5-1.1 on the sediment scale; interconnected sediment pockets - light dusting of sediment). At the southern tip of the EOSC, the more recent volcanic events (chemical groups A, C, H; dive 2002) took the form of small, thin pillow eruptions on the western flank of the axial region near 11°42'N that override the older pillow terrain (chemical group O, 2002), whereas to the north local flooding and lava lake formation occurred in the bottom of the deeper and wider fissures. These lava lakes (chemical groups A and C; dive 2004), cut by only rare

fissures, cover and abut the older pillowed terrain seen in the walls of the fissures (chemical group P, dive 2004).

The most recent volcanic event observed on the EOSC emplaced lavas (ages corresponding to 1.0 on the sediment scale; no sediment observed) of a nearly uniform composition (chemical group F (+E), Table 2; Fig. 1) (Kinzler et al., 1988) along the EOSC from 11°43'N (ALVIN dive 2002) to 11°57'N (Dr-19). Samples in Group F were erupted as thin sheet flows in the bottoms of fissures and were identified from the ALVIN submersible to be similar in their very fresh and highly glossy, black appearance. In addition, the group F lavas were identified as the youngest lavas sampled during the course of dives 1999, 2001, 2002, 2003 and 2004, and were observed to have flowed over the older sheet and pillow flows described above. Group E was recognized after the major element compositions of the lavas were determined (as were the other groups listed in Table 2) on the basis of their compositional similarity to the younger group F lavas. Lavas in group E were collected along dives 1999 and 2001, and were recovered in dredges 70 and 19. The group E lavas are interpreted to be slightly older than the group F lavas, based on direct observation of their field relations in 5 ALVIN dives. Because of their similarity in composition, however, we suggest that groups E and F were emplaced fairly closely in time. This emplacement event occurred over a distance of approximately 24 km. The lavas were erupted onto the floors of fissures, which may suggest that the hydraulic head associated with the recent eruptions was relatively low, as the levels of the flows were not observed to rise far above the floors of the older fissures.

In general, the EOSC now appears to be in a moderately active volcanic phase which has followed a period dominated by tectonic fissuring of yet older constructional volcanism. Hydrothermal activity is not developed in the current phase, although fossil hydrothermal sites consisting of inactive sulfide chimneys and hydrothermally stained talus were observed. This phase is very similar to the final stage in the ridge segment tectonic and volcanic cycle outlined by Thompson et al. (1988), where tectonism is on the

decrease and renewed volcanism is restricted to low level filling in of fissures in the floor of the axial graben. The implication is that the cycle is about to start anew on the eastern rift of the OSC, with a fresh influx of magma to the spreading axis.

Three chemical groups (H, K and N) are observed in common between the WOSC and the EOSC (see also Thompson et al., 1989). Interestingly, chemical group K is relatively common on the EOSC (sampled at dredge-20, and on ALVIN dives 1999, 2001 and 2003) and is sampled at only one location on the WOSC (ALVIN dive 2000); while chemical group N is relatively common on the WOSC (sampled at dredge-65, and on ALVIN dives 1998 and 2000) and is sampled at only one location on the EOSC (dr-70). The observed, uneven distributions of these lava types support the inference of Thompson et al. (1989) that magma may have 'leaked' across the small (roughly 8 km) basin that separates the two rifts of the OSC. Lavas in the third, shared chemical group (H) only occur at two sampled locations, near the northernmost part of the WOSC (dredge-68) and at the southernmost part of the EOSC (ALVIN dive 2002). On the basis of major element considerations alone, it would be hard to justify that these spatially disparate lavas were physically related to the same magma body. Rather, it is likely that they evolved from similar parent magmas by similar magmatic processes (see below).

Primitive Lavas

Primitive lavas (defined here as lavas containing > 8 wt.% MgO) were sampled at several locations on both the WOSC and the EOSC. Grouped together in the P group (Table 2), 7 different primitive lava types with Mg# (100*Mg/[Mg+Fe]) of 61 - 65 were identified. Lava types P2, P3, P4 and P5 were sampled on the WOSC, P1, P6 and P7 were sampled on the EOSC. The highest MgO glass (ALV-2004-3-1, MgOn=9.23) was sampled approximately 8 km north of the southern tip of the EOSC. In general, the P group lavas sampled from the ALVIN were observed to be older than the nearby, more evolved lavas.

Propagation vs. Migration?

Thompson et al. (1985, 1989) suggested that the eastern rift of the 11°45'N OSC was propagating southwards and that the western rift constituted a failing rift. This interpretation was based on the observation of recent volcanic and tectonic activity on the EOSC, and a lack thereof on the WOSC. The ALVIN dive observations presented here confirm the previous observations that within the zone of overlap, the eastern rift is more volcanically and tectonically active relative to the northern portion of the western rift. The southern portion (south of 11°45') of the WOSC is marked by recent fissuring, indicating extension. Perram and Macdonald (1990) suggested that the migrating offset at 11°45'N is the result of a reorientation of the ridge axes to the north and south to accommodate a slight rotation in the spreading direction over the past 1 m.y. (3-4°. Perram and Macdonald (1990) suggest that active, asymmetric extension is occurring to the north (on the EOSC) and to the south (on the southern portion of the WOSC) of 11°45'N. The observations of possibly recent fissuring along the southern portion of the WOSC (ALVIN dive 1998), and lack thereof along the northern portion of the WOSC; and recent fissuring along the whole length of the EOSC are consistent with this interpretation.

PETROLOGIC EVOLUTION OF THE LAVA TYPES SAMPLED ON THE 11°45'N OSC

Experimental Study

We carried out a 1-atm. experimental study using natural lava compositions collected from 11°40'N to 11°50'N on the EPR. These experiments locate the 1-atm. olivine - augite - plagioclase - liquid boundary (4-phase boundary) in composition space for the bulk compositions sampled at the 11°45'N OSC. These data will be used to quantify the effects of shallow level (near 0.001 kbar) crystallization on the magma

compositions and to assess the roles played by crystal fractionation processes and mixing of magmas in the generation of the observed geochemical signatures at the $11^{o}45'$N OSC

Experimental Methods All five lavas used in our experiments consist of fresh glassy to aphyric pillow fragments. Four of the lavas (PROTEA-9-70-002, 67-032, 64-002 and 61-002) were collected during a dredging program between 10 and 12^{o} N in 1984 (Thompson et al., 1985; 1989). The fifth (ALVIN 2004-3-1) was sampled on ALVIN dive 2004 (Fig. 1). The freshest parts of the pillows were reduced to powder by grinding in a SPEX shatterbox for 3 minutes and then used as starting material for the anhydrous, 1-atm. melting experiments. Table 3 provides chemical analyses of the starting compositions used in this study. Two analyses of PROTEA-9-70-002 are provided in Table 3; one carried out on the Smithsonian electron microprobe and the other carried out on the MIT. electron microprobe. Experimental run conditions are reported in Table 4.

The experiments were carried out at 1 atm. using techniques similar to those described in Tormey et al. (1987). Pellets of natural lava powder (0.08-0.10 g) were prepared using elvanol as a binder, and sintered to 0.008" PtFe alloy loops fabricated to minimize Fe exchange between the loop and silicate sample (Grove, 1981). Experiments were carried out in Deltech DT31VT quenching furnaces in a CO_2-H_2 gas atmosphere maintained near the quartz-fayalite-magnetite buffer, using gas flow rates of 0.1 mL/s. Oxygen fugacity was monitored using ZrO_2-CaO electrolyte cells calibrated at the Fe-FeO, Cu-Cu_2O and Ni-NiO buffers. Temperature was monitored using Pt-$Pt_{90}Rh_{10}$ thermocouples calibrated against the melting points of NaCl, Au and Pt on the IPTS 1968 temperature scale (Biggar, 1972). Temperatures were held constant to within plus or minus 1^{o}. The exchange of Fe between loop and silicate charge, and the loss of Na from the silicate charge by volatilization in these 1-atm wire loop experiments

have been essentially eliminated by using PtFe alloys, extremely low gas flow rates, and "large" sample sizes (Tormey et al., 1987).

Analytical Methods Run products were mounted in epoxy and polished for examination under reflected light and for characterization of the chemical compositions of all the phases (provided in Table 5) with the MIT 4-spectrometer JEOL model 733 electron microprobe (see analytical methods section above).

Balance of Mass In order to evaluate how mass was conserved during each experiment, the compositions of all the phases present (Table 5) were balanced against the bulk composition of each experiment (Table 3), using unweighted materials balance (Bryan et al., 1969). These mass balance calculations provide estimates of the proportions of phases present in each experiment (reported in Table 4 with the sum of the residuals squared for each mass balance). FeO loss from the charge as estimated with the mass balance technique was typically < 1% to 3% relative, never more than 5% relative. Na_2O loss was typically 1 - 5% relative, never more than 10 % relative.

Achievement of Near Equilibrium Conditions The average values of experimental Fe-Mg K_Ds ($FeO^{xtl}MgO^{liquid}/MgO^{xtl}FeO^{liquid}$) observed in the melting experiments reported in Table 4 for olivine/liquid (20 experiments) and augite/liquid (17 experiments) are approximately constant at 0.28 +/- 0.1 (1 sigma) and 0.24 +/-0.2 (1 sigma), respectively. The olivine/liquid Fe-Mg K_D is within 1 sigma of the equilibrium value determined by Roeder and Emslie (1970) and both the olivine/liquid and augite/liquid Fe-Mg K_Ds are similar to those obtained in similar 1-atm. experimental studies on tholeiitic and low-potassium, high-alumina basalt compositions (Grove et al., 1982; Grove and Bryan, 1983; Tormey et al., 1987), indicating that near-equilibrium conditions were obtained in the experiments, at least with respect to Fe-Mg exchange. The average experimental Na-Ca K_D ($Na_2O^{xtl}CaO^{liquid}/CaO^{xtl}Na_2O^{liquid}$) observed for plagioclase/liquid (20 experiments) is 1.05 +/- 0.15 (1 sigma). The larger 1 sigma on the average plagioclase/liquid Na-Ca K_D, relative to the 1 sigmas on the Fe-Mg K_Ds

stems from a systematic increase in the plagioclase/liquid Na-Ca K_D as the temperature of experiment decreases (Table 5). The glass, olivine and plagioclase produced in the experiments are generally homogeneous in composition, again indicating near-equilibrium conditions. Experimentally produced augites are compositionally the most heterogeneous, as reflected in the higher standard deviations associated with the average compositions reported in Table 5. This compositional heterogeneity stems from sector and patchy zoning developed in the pyroxenes and was not observed to diminish significantly with increased run time (augite saturated experiments were carried out for approximately 4 to 11 days, Table 3). Nonetheless, the small standard deviation of the values observed for the augite/liquid Fe-Mg K_D, and the similarity of the average augite/liquid Fe-Mg K_D to that obtained in similar experimental studies suggests that an approach to equilibrium was achieved.

Experimental Results

Crystallizing Phase Proportions Cotectic proportions of the minerals crystallizing along the 4-phase boundary are provided in Table 6. The olivine-plagioclase-augite phase proportions were determined by computing mass balances between higher-temperature liquids and lower-temperature liquid + crystalline phase assemblages (both experiments carried out on the same starting composition). This mass balance estimates the proportions of olivine, plagioclase and augite that crystallized from the higher-temperature liquid to form the composition of the lower-temperature liquid. If the 4-phase boundary curves with decreasing temperature, then an increase in the difference in temperature (ΔT) between the experiments on either side of the mass balance results should yield different coefficients of the crystallization reaction. As ΔT increases for the estimates provided in Table 6, the proportion of olivine and augite decreases, and the proportion of plagioclase increases, indicating some curvature. The variation is slight, however, and thus the average is calculated to best approximate the crystallization reaction.

Phase Relationships The low pressure 4-phase boundary defined by the melting experiments is shown in projection schemes in Fig. 3. Experimentally produced olivine-augite-plagioclase saturated glass compositions and the coexisting augite compositions are projected into the Olivine (Oliv) - high-Ca Clinopxroxene (Cpx) - Plagioclase (Plag) - Quartz (Qtz) pseudo-quaternary, using oxygen units and the mineral component scheme of Grove et al. (1991), and further projected from Plag onto the Oliv-Cpx-Qtz pseudo-ternary in Fig. 4a and from Qtz onto the Oliv-Cpx-Plag pseudo-ternary in Fig. 4b. The lavas used as starting compositions are also plotted. The liquid line of descent for ALVIN 2004-3-1 is shown in Fig. 4a as a solid curve. Olivine and plagioclase are on the liquidus at approximately 1225 ^{o}C, thus 1-atm. crystallization involves the precipitation of olivine + plagioclase, in proportions of roughly 30 % and 70% respectively, moving the magma composition away from the Oliv apex in the Oliv - Cpx - Qtz pseudo-ternary, towards the 4-phase boundary. Upon intersection with the 4-phase boundary, the magma saturates with augite, and further crystallization involves olivine + plagioclase + augite, moving the magma composition away from the plane defined by the Oliv apex, the Plag apex and the compositions of the coexisting augites. Magmas evolving from all the starting compositions chosen in this study move towards the Qtz apex of the Oliv - Cpx - Qtz pseudo-ternary as they fractionally crystallize along the olivine-plagioclase-augite-liquid boundary. Although the liquidus assemblages were not determined for the other 4 starting compositions, the highest temperature experiments on each of these 4 compositions contain olivine + plagioclase. Thus, none of the 5 compositions have the assemblage olivine + plagioclase + augite on their liquidus, although PROTEA-9-61-002 crystallizes augite within < 20 wt.% crystallization (Table 3). This observation is consistent with the phenocryst mineralogy for these nearly aphyric samples which contain only small amounts of olivine and plagioclase.

Petrogenetic Models

The chemical groups from the east and west rifts of the 11°45'N OSC (Table 2) are projected onto portions of the Oliv - Cpx - Qtz and Oliv - Cpx - Plag pseudo-ternaries in Fig. 4 (using the same projection scheme as described for Fig. 3), along with the experimentally determined 1-atm. 4-phase and 3-phase (olivine + plagioclase + liquid) boundaries. Primitive lava groups P7, P6 and P1 plot towards the Oliv-Cpx join in Fig. 4a and generally follow an olivine - plagioclase crystallization control line, similar to that observed for the higher temperature, olivine + plagioclase saturated experiments on lava P7, ALVIN 2004-3-1 (see below for discussion of models). Primitive lavas P2, P3, P4 and P5 from the WOSC are lower in CaOn relative to the primitive lavas on the EOSC (Fig. 5a), and do not appear to follow an olivine + plagioclase fractionation control line (see below for discussion of models). Chemical group N (labelled n in Fig. 4a), which is dominantly sampled on the WOSC (Fig. 1), is the most evolved lava type (Mg# = 59) that appears to have formed by olivine + plagioclase fractionation (see Table 8) from the primitive lava type P3, also sampled on the WOSC. Many of the lava groups sampled from both rifts of the OSC, however, contain elevated FeO and TiO_2 contents, low Al_2O_3 and CaO contents, and are displaced towards the Qtz apex in Fig. 4a relative to the primitive (MgO > 8 wt.%) lavas. These characteristics (in particular the diminishment of both Al_2O_3 and CaO with increasing extents of evolution) suggest that fractionation of augite as well as olivine + plagioclase played a role in the creation of the evolved lavas sampled at the OSC. With the exception of perhaps two lavas, however, most of the OSC lavas do not coincide with the 1-atm., experimentally determined 4-phase boundary, either in the projection schemes shown in Fig. 4 or in most major element variation diagrams comparing the experimental data and natural glasses. (In Fig. 5, neither the WOSC or the EOSC lava groups fall on the 1-atm., experimentally determined 4-phase boundary on the CaOn vs. MgOn variation diagram, and only the WOSC lavas coincide with the 1-atm. 4-phase boundary on the FeOn vs.

MgOn variation diagram) Furthermore, the majority of the OSC lavas do not contain augite as a phenocryst phase. Therefore although the major element chemistry indicates a role for the crystallization of augite, the displacement of the lava compositions from the 1-atm. olivine + augite + plagioclase + liquid boundary, and the lack of augite as a phenocryst phase suggest that the lavas were not saturated with augite at near 1-atm. conditions. Two alternative models for generating the diversity of the chemical groups sampled at the OSC are evaluated in the following sections: 1) mixing of primitive magmas with moderately evolved magmas fractionated in shallow magma chambers (~ 1 km below the ridge axis) along the near-1-atm. 4-phase boundary, and 2) fractionation of olivine + augite + plagioclase from primitive magmas at greater pressures (~ 6 km below the ridge axis).

1) Mixing of primitive magma with moderately evolved magma during magma chamber replenishment at shallow levels within the spreading axis

In this model, magma is emplaced in a chamber at shallow levels where it evolves by low-pressure fractional crystallization (along the experimentally determined 4-phase boundary). After some time, fresh, parental magma is re-injected into the chamber (O'Hara, 1977), mixed homogeneously with the fractionated magma, and then some fraction of the mixed magma is erupted. The proposed model is similar to a cycle of the open magma chamber model B proposed by Albarede (1985). Model B proceeds as follows: 1) fresh magma is injected into a chamber that contains residual magma created by fractional crystallization, and mixing occurs; 2) part of the mixed magma is immediately erupted; 3) closed system fractional crystallization takes place within the reservoir and the system returns to step 1. We will test whether any of the chemical groups sampled at the OSC represent the mixed magma erupted during step 2.

The chemical groups from the $11^{o}45'$N OSC are plotted in Fig. 5 on a CaOn vs. MgOn and FeOn vs. MgOn. diagram, along with the experimentally produced, 1-atm. olivine + plagioclase saturated liquids, and olivine + plagioclase + augite saturated

liquids. The displacement of the evolved lava groups away from the 1-atm. 4-phase boundary relative to the Cpx apex observed in Fig. 4 is also apparent in Fig. 5 on the CaOn vs. MgOn diagram. The lava groups are generally characterized by lower CaOn, and higher FeOn contents, relative to the experimental liquids on the 1-atm. 4-phase boundary, at equivalent MgOn contents. The array of lava compositions on the CaOn and FeOn vs. MgOn diagrams shown in Fig. 5 encourages the interpretation that, in fact, the sampled lavas may be two component mixtures of the MgO-rich parental magmas and magmas similar to the experimentally produced, olivine + augite + plagioclase saturated liquids.

The primitive chemical groups (P1-P7) from the OSC and the experimentally produced liquids on the 4-phase boundary were the components available for mixing in weighted, least squares, mass balance calculations used to test the mixing hypothesis for generating the major element compositions of the OSC chemical groups (Table 7). In general, the lavas sampled on the western rift of the $11^{O}45'$N OSC (mixing lines for evolved groups I, J, and primitive group P3 are shown on Fig. 5a) lie within the mixing 'envelop' defined by the moderately evolved experimentally produced olivine + augite + plagioclase saturated liquids and the inferred parental magmas. The FeOn vs. MgOn variation diagram in Fig. 5b shows that most of the lava groups of the WOSC coincide with the array of liquids along the 1-atm. phase boundaries. This coincidence might be interpreted as evidence of shallow level, closed system fractionation. However fractionation and subsequent mixing are required to explain both the FeOn and the CaOn vs. MgOn variations for the WOSC lavas. The mismatches in the models relative to the lava groups (Table 7), particularly the poor fits for the K_2O contents, most likely reflect the lack of a fully representative set of parental and experimental compositions available for mixing.

Groups K and H are found on both rifts of the OSC (Fig. 1); group K was sampled in several locations on the EOSC, but in only one location on the WOSC, and

group H was sampled near the northernmost tip of the WOSC and at the southernmost tip of the EOSC. The major element chemistries of both of these better modelled within the elevated pressure fractionation framework discussed below for the EOSC.

The mixing scenario discussed above for the generation of much of the chemical diversity of the WOSC lavas requires a magma chamber or complex of pipes at shallow levels either at or relatively proximal to the WOSC, prior to and at the time of emplacement of the lavas. Detrick et al. (1987) reported the presence of a continuous seismic reflector from ~11°30'N that terminates abruptly at ~11°40'N, and is then picked up for a very short distance at ~11°42'N, just underneath the sample site of the P3 lava group (Dredge 64, Thompson et al., 1989). This seismic reflector is interpreted as indicative of a shallow magma chamber situated roughly 1 km beneath the ridge axis. For the simple model suggested by the major element mixing calculations, parental magmas such as lava types P2, P3 and P4 are emplaced into this shallow magma chamber (and perhaps erupted at the ridge axis at the same time) where they undergo fractional crystallization, reaching the low-pressure, 4-phase boundary. The 'best fit' experimental liquids in the mass balance calculations (Table 7) from parental-type starting compositions (64-002=P3, ALV2004-3-1=P7) contain roughly 50 % liquid (Table 4), suggesting for this simple model that re-injection of fresh parental magma is intermittent, and only occurs after approximately 50 % crystallization of the prior batch.

With the exception of chemical group O on the EOSC, none of the major element compositions of the chemical groups on the EOSC are adequately explained by mixing of any of the parental lava types sampled with magmas similar to the evolved, 1-atm. experimentally produced liquids. Group O is, in fact, an exceptional composition, relative to the other lavas sampled on the EOSC (see, for example, TiO_2n vs. MgOn, Fig. 3, the EOSC lavas at ~2.00 wt.% TiO_2n and 7.90 wt.% MgOn). The major element composition of Group O, which was sampled at the southernmost tip of the eastern rift of the 11°45'N OSC (ALVIN dive 2002, Fig. 1), is well approximated as a mixture of lava

type P7, the most primitive lava sampled at the OSC (ALVIN dive 2004, just north of ALVIN dive 2002, Fig. 1), and the most evolved experimental liquid (61-002-150, Table 5). The following model is suggested for its petrogenesis. A single batch of parental magma was emplaced at shallow depths at the rift tip, and was then able to fractionate to very high FeO and TiO_2, and low Al_2O_3 and CaO contents by crystallizing olivine + augite + plagioclase contents in the relatively cool rift tip environment. As discussed below, the thermal environment and magma supply conditions associated with the rapidly southward migrating EOSC are expected to favor high degrees of fractionation (as at the Galapagos, Christie and Sinton; 1981). This is in contrast with the processes inferred across the OSC for the lavas on the WOSC, where the evolved components present in the mixtures do not appear to reach such high levels of fractionation. At a later stage, another batch of parental magma, not necessarily of the same composition as the first batch but similar in composition to lava type P7 was injected through the chamber, mixed with the highly evolved liquid and then erupted. Interestingly, Group O lavas were only sampled in three closely spaced locations, on the eastern portion of the eastern rift tip. Furthermore, the most evolved lavas sampled on the EOSC (Groups A and B, sampled in close proximity to Group O on ALVIN dives 2002 and 2004) do not resemble the highly evolved, low-pressure, experimentally produced liquids that are inferred to have been present for the formation of the Group O lavas. These observations suggest that the low-pressure fractionation process that produced the evolved component present in the Group O lavas was not a common one on the EOSC, or at least that the evolved magmas that are the products of this process are not commonly erupted at the EOSC.

2) Fractionation of olivine + augite + plagioclase at pressures > 1 atm

In this model, emplacement of parental magmas occurs at greater depths (~ 6 km = ~ 2 kbar pressure) in the spreading axis, relative to the shallow level (~ 1 km) fractionation, re-injection and mixing model inferred for the WOSC. The parental

magmas then fractionate at pressures greater than 1-atm. Several reasons exist for exploring this model for the lavas sampled at the EOSC. 1) Lava groups A, B, C, D, E, F, and G are moderately to highly evolved in terms of their major elements (12.0 - 14.1 wt.% FeO, 1.98 - 2.65 wt.% TiO_2). With decreasing MgO, the lavas show increasing FeO and TiO_2, with decreasing CaO and Al_2O_3, with little change in SiO_2 contents, characteristics similar to those associated with magmas evolving along the experimentally determined, 1-atm. 4-phase boundary. However, augite is not observed as a phenocryst phase in the lavas sampled at the EOSC. Furthermore, as is apparent in Fig. 5, the evolved major element signatures are linked with higher MgO contents, relative to the experimentally determined 1-atm. 4-phase boundary. Two additional groups, H and K, that are sampled on both rifts of the OSC, have similar characteristics. Group K is more common on the EOSC, and thus might be expected to have been formed by the petrologic processes that dominated on the eastern rift. Group H is sampled only at the tips of both rifts, and its chemistry appears to be better explained by elevated pressure fractionation than by the mixing scenario proposed for the WOSC lavas. 2) The lava groups are displaced away from the 4-phase boundary in the Oliv-Cpx-Qtz pseudo-ternary (towards the Oliv apex in Fig. 4a and towards the Oliv-Plag join in Fig. 4b), a shift that is consistent with the effect of increased pressure on the position of the 4-phase boundary in composition space (Presnall et al., 1979; Stolper, 1980; Grove et al., 1990; Bartels et al., 1991). 3) Simple two-component mixing models similar to those inferred for the WOSC lavas fail to reproduce the major element chemistry of these EOSC lavas. The fact that the shallow level fractionation, re-injection and mixing model fails for the EOSC lavas suggests that shallow level magma chambers are not common on the EOSC. This interpretation is consistent with the observations of Detrick et al. (1987) that there is a break in the shallow level seismic reflector between $11^{o}40'$N and $12^{o}10'$N on the EPR. 4) The evolved lavas on the EOSC coincide with the 4-phase boundary at ~ 2 kbar predicted by the expressions of Kinzler and Grove (1991) which

track the phase boundary position in composition and temperature space as a function of pressure and melt composition. This line of evidence will be explored in detail in the next section.

Grove and Juster (1989) and Kinzler and Grove (1991) devised a method that predicts the influence of compositional variables and pressure on the compositions of liquids saturated with olivine, plagioclase, augite and a low-Ca pyroxene. This 5-phase boundary lies at the terminus of the 4-phase olivine + augite + plagioclase + liquid boundary. The key compositional parameters that control the position of the 5-phase boundary in composition space are: Mg#, A# ($[Na_2O+K_2O]/[Na_2O+K_2O+CaO]$) and TiO_2 content. Longhi and Pan (1988) have shown the systematic effects of variations in Mg# on the positions of saturation boundaries in projection schemes; Grove et al. (1991) and Kinzler and Grove (1991) discuss the effects of variations in A# in light of natural system experiments and the simple system ($CaO-MgO-Al_2O_3-SiO_2-Na_2O$) experiments of Biggar and Humphries (1981); and TiO_2 was the other compositional variable in MORB systems that Grove and Juster (1989) and Kinzler and Grove (1991) found to be significant. Given some simplifying assumptions about the shape of the 4-phase boundary that extends from the 5-phase boundary, we can use the predictive method of Kinzler and Grove (1991) to estimate the position of the 4-phase olivine - plagioclase - augite - liquid boundary in composition space as a function of pressure, Mg#, A# and TiO_2 content of the magma.

We have used a subset of the experimentally produced liquids on the 4-phase boundary presented in this study to test the ability of the expressions of Kinzler and Grove (1991) to accurately locate the 4-phase boundary for the EPR lava compositions. Fig. 6 shows 4 experimentally produced liquids saturated with olivine + augite + plagioclase in the projection schemes described in Fig. 4. In the projection through Qtz onto the Oliv-Cpx-Plag pseudo-ternary (Fig. 6b), a liquid composition saturated with olivine + augite + plagioclase should project approximately on top of liquid

compositions saturated with olivine + augite + plagioclase + low-Ca pyroxene. The projected positions of the experimentally produced liquids on the 1-atm. 4-phase boundary coincide with the projected positions of the liquid compositions predicted by the Kinzler and Grove (1991) expressions to be on the 5-phase boundary at 1 atm., which suggests that the expressions work very well for the EPR lavas. The boundaries predicted at 2 and 4 kbar are shifted towards the Oliv-Plag join. In the projection through Plag onto the Oliv-Cpx-Qtz pseudo-ternary (Fig. 6a) the experimentally produced liquids define the 1-atm. 4-phase boundary that trends away from the predicted liquids on the 5-phase boundary towards the Oliv-Cpx join. The combination of the 1-atm. experimentally determined 4-phase boundary, which provides the general slope, and the predicted 5-phase boundary, which fixes the location, allows us to infer the positions of the olivine - augite - plagioclase - liquid boundary at 1 atm., and 2 and 4 kbar for the compositions of the experimentally produced liquids.

Four of the evolved lava groups sampled on the EOSC (Groups A, B, C and E) and two groups from both the EOSC and the WOSC (Groups H and K) are shown in the Oliv-Cpx-Plag and Oliv-Cpx-Qtz pseudo-ternaries in Fig. 7 and 8, respectively, along with the phase boundaries predicted for these compositions with the method of Kinzler and Grove (1991) as described above at 1 atm., and 2 and 4 kbar. The Group B, C and E lavas project onto the predicted 2-kbar 4-phase boundary in both the Oliv-Cpx-Qtz (Fig. 7a) and the Oliv-Cpx-Plag pseudo-ternaries (Fig. 7b). The Group A lavas projected onto a predicted 4-phase boundary at slightly higher pressures ($\sim$3 kbar). Groups H and K project onto the 4-predicted phase boundary at $\sim$1 kbar. Fractionation of olivine + plagioclase + augite at pressures of 1 - 3 kbar may have been responsible for the evolved character of these lava groups. To test the higher pressure fractionation hypothesis for the generation of these lavas further, models were calculated relating several of the evolved chemical groups on the EOSC back to the parental type lavas (Table 8, models 1 - 7). These are 'reverse' fractionation models,

estimated by adding back the phases that were inferred to have crystallized from their parental magmas in their generation. Compositions of augites (in terms of Wollastonite-(Enstatite,Ferrosilite)) added in the 2-3 kbar models were similar to the estimates of Grove et al. (1991) except that the calculations presented in Table 8 used slightly more aluminous pyroxenes. We used the K_Ds and cotectic proportions for the assemblage olivine + augite + plagioclase determined experimentally at 1-atm. (Tables 5 and 7).

The model parents estimated by 1- and 2-kbar 'reverse fractionation' from groups S, H and K (models 1, 6 and 7, respectively, Table 8) are good approximations to the major element composition of lava P7, the most primitive, parental lava type. With the exception of Na_2O, K_2O and P_2O_5, the models estimated by 3- and 2-kbar 'reverse fractionation' from Groups A, B, D, and E in Table 8 are also similar to the most primitive parental lava type P7. The success of these 'reverse fractionation' models in returning the evolved lavas to the major element composition of the most primitive parental lava type, particularly with respect to CaO, Al_2O_3, FeO, TiO_2 and SiO_2, supports the hypothesis that fractionation of olivine + augite + plagioclase at pressures equivalent to ~6 km generated the evolved compositions sampled on the EOSC. In models 3 - 5, the Na_2O and K_2O contents are lower in the model parent, relative to the primitive P7 lava. Given that the K_2O contents of both the parental lava P7 (Mg# = 65) and, for example, Group E lavas (Mg# = 52) are the same (0.10 wt.%), it comes as no surprise that in detail, P7 could not have been parental to Group E lavas by fractional crystallization. The major element compositions of these evolved lavas at the EOSC require a parental magma type with lower K_2O and Na_2O, relative to the parental lavas identified at the EOSC. Hekinian and Fouquet (1985) report a composition for a parental type lava sampled to the north of the EOSC at approximately $12^{o}50'N$ that is similar to lava P7, but has lower K_2O and Na_2O (0.05 and 2.38 wt.%, respectively; Table 3, sample CL-H-6). We suggest that a magma type similar to that sampled further north on the EPR must be playing a role in the magmatism at the EOSC, and that we just have

not sampled it. Forward fractionation models 8 and 9 demonstrate that the compositions of lava groups C and G are well explained as the more fractionated products of the same ~2-kbar fractionation process inferred for types E and S, respectively.

Primitive Lavas primitive lava types (P1-P7 and N, Table 2) have been identified, 4 on the WOSC (P2-P5), 3 (P1, P6 and P7) on the EOSC and 1, group N, which occurs on both. Forward fractionation models 8 and 9 (Table 8) successfully relate lava types P6 and N to lava types P7 and P3, respectively, by olivine and plagioclase fractionation. Lava type P1 is similarly related to P7. These models indicate that much of the chemical diversity observed in the more mafic lavas on both the WOSC and the EOSC is generally well explained by the fractionation of olivine + plagioclase from a primitive (high-MgO) lava such as P7. Of the parental lava types on the WOSC, P3 is well modelled as a mixture of P7 and the experimentally produced, 1-atm. liquid ALV-2004-3-1-10. Lava types P2, P4 and P5 do not appear to be related to the other parental group lavas through the simple mixing and fractionation models developed for the EOSC and WOSC.

The petrologic models for the evolved lavas on the EOSC suggest that the tectonic environment associated with the migrating rift tip favors staging of magma batches at greater depths in the oceanic crust, relative to the WOSC and more central portions of the tectonic segments to the south on the EPR. Christie and Sinton (1981) identified 2 highly fractionated lavas (Mg# = ~53) at the 95.5°W propagating rift in the Galapagos region (18B and 18C) that are offset from the inferred 1-atm. 4-phase boundary towards the Oliv apex of the Oliv-Cpx-Qtz pseudo-ternary and contain rare micro-phenocrysts of olivine and plagioclase. These two lavas are similar to the evolved lavas at the EOSC in that they have major element signatures suggestive of fractionation along the 4-phase boundary. However they contain elevated FeO and TiO_2 and low Al_2O_3 and CaO, given their MgO contents, relative to what would be anticipated for

fractionation along the 1-atm. 4-phase boundary, and are saturated with only olivine and plagioclase upon eruption. The predicted phase boundaries for the Galapagos lavas are shown in Fig. 9 using the method of Kinzler and Grove (1991) and Grove et al. (1991) described above for the EOSC lava groups. The Galapagos lavas (filled circles) are closely similar to melts predicted to be on the 4-phase boundary (possibly also saturated with low-Ca pyroxene) at pressures between 3 and 4 kbar. The propagating rift tip at 95.5^{o}W may provide a tectonic environment similar to that of the migrating eastern rift at the 11^{o}45'N OSC, that favors staging of magma batches near the base of the oceanic crust, and/or in the upper-most oceanic mantle. In these tectonic environments magma may be emplaced to the system before rifting is sufficiently developed to allow rapid Ascension to shallow levels in the crust or extrusion on the sea floor.

The chemical diversity of the evolved lavas at the EOSC is well explained by processes of fractional crystallization at slightly elevated pressures. The major element chemistries of the evolved lavas indicate that they are the products of ~45 - ~55 % crystal fractionation (Table 8) at pressures of ~2 kbar (= ~6 km depth) from parental lavas similar to those sampled at the EOSC and further north on the EPR. The pressures and extents of fractionation inferred from the models suggest that isolated magma batches are emplaced at or near the base of the oceanic crust beneath the EOSC, where they cool and fractionate to relatively high extents, before being erupted. This process is consistent with the suggestion of Christie and Sinton (1981) and Sinton et al. (1983) that propagating rift tips are characterized by isolated magma chambers, not interconnected or continuous magma chambers, and of Macdonald et al. (1988) that rifts near migrating offsets suffer from diminished magma supply, or 'magma starvation'.

Evolved lavas with major element signatures of ~2-kbar crystal fractionation of olivine + plagioclase + augite are sampled all along the EOSC between 11^{o}40'N and 11^{o}57'N (Fig. 1, chemical groups A, B, C, D, E, F, G, and S). As mentioned above, Detrick et al. (1987) identified a break in the shallow level seismic reflector along the

EPR that roughly coincides with the portion over which these evolved magmas were sampled. Detrick et al. (1987) did, however, observe two discontinuous seismic reflectors at greater depths (~ 1 km deeper) at 11°45'N and 11°55'N on the EOSC. These deeper seismic reflectors are consistent with the petrologic evidence that magma chamber processes are occurring deeper in the oceanic crust beneath the EOSC, relative to the WOSC and the rise axis to the north.

Chemical groups E and F (identical in chemistry, group E is slightly older than group F) were sampled along a ~ 26 km segment of the EOSC (between ~ 11°43'N and ~ 11°57'N). The lack of a continuous seismic reflector and a well defined axial graben along this same portion of the EPR, as well as the occurrence of a wide diversity of lavas erupted in the neo-volcanic zone, argue against a continuous magma chamber at 6 km depth from ~ 11°45'N and ~ 11°57'N (Detrick et al., 1987; Macdonald et al., 1988). The preferred interpretation is that parental magma was injected beneath the EOSC at ~ 11°57'N and staged at ~ 6 km depth. Approximately 40 - 50 % fractionation occurred to produce the E magma, which was then emplaced vertically and laterally along the EOSC, forming lava lakes and flooding the bottoms of larger preexisting fissures to the south. The group C lavas, sampled at the southern tip of the EOSC (ALVIN dives 2002 and 2004) and interpreted as having been formed by fractionation along the 4-phase boundary at 2 kbar from the group E and F magma type (Table 8, model 8), were also erupted at this time. The more evolved, 2-kbar signature of the group C lavas relative to the E and F lavas suggests that the lateral injection of the group E magma occurred at relatively deep levels. Group F lavas were then emplaced shortly thereafter as a second pulse of the same magma type that erupted to form group E and C lavas.

TECTONIC VARIABLES GOVERNING THE OSC AT $11^{O}45$'N ON THE EPR

This final section explores the relationship between the tectonic variables associated with migrating ridge-offset intersections (Sinton et al., 1983) and the magnitude and distribution of the associated geochemical signature for the migrating OSC at $11^{O}45$'N. These tectonic variables are local spreading rates; proximity to 'hot spots'; propagation rate (if any); migration rate of the intersection, relative to the underlying mantle; and the length of the transform truncating the ridge segment. Table 9 provides a compilation of these variables for the $11^{O}45$' N OSC, as well as for three other OSCs on the EPR at 9^{O}N, $12^{O}37$'N and $12^{O}54$'N, and two propagating rift tips from the Galapagos area and two from the Juan de Fuca (data sources are in notes for Table 9) For the purposes of this comparison, the geochemical anomaly associated with a given ridge offset is considered in terms of the FeO*/MgO (FeO* implies total Fe as Fe^{2+}) ratio. 'Normal MORB' are considered to have FeO*/MgO ratios < 1.75, thus any lavas sampled with FeO*/MgO ratios > 1.75 are considered to be anomalously fractionated (Sinton et al., 1983). FeO*/MgO is chosen as the geochemical anomaly indicator because it reflects the degree of fractionation achieved by erupted lavas, which in turn will be a function of the thermal and magmatic budgets associated with the rifts. The actual value of the anomalous FeO*/MgO associated with a particular offset feature (from 1.9 to 5 in Table 9) is likely to be affected by petrologic considerations including the parent magma composition, the oxygen fugacity of the fractionally crystallizing magma bodies (Sinton et al., 1983), and the petrologic processes causing the fractionation.

An important effect of the elevated pressure fractionation processs that appears to have generated the compositional diversity in the lavas sampled along the EOSC at the $11^{O}45$'N OSC is that it lowers the magnitude of the FeO*/MgO ratio associated with the evolved lavas, relative to that which would result from near-1-atm. fractionation.

The maximum FeO*/MgO value observed at the EOSC is 2.25, for lava group A (Table 2), which is inferred to have evolved by crystallization along the 4-phase boundary at approximately 3 kbar. This lava group contains 14.1 wt.% FeO, and 6.26 wt.% MgO. Experimentally produced melts on the 1-atm. 4-phase boundary with similar FeO contents contain less MgO (see, for example, the glass composition in experiment 64-002-140; at 14.0 wt.% FeO this glass contains only 5.43 wt.% MgO, and thus has an FeO*/MgO ratio of 2.58). The lower MgO contents in magmas that evolve at 1 atm. result because parental magmas that evolve near 1-atm. crystallize more olivine, and olivine + plagioclase before reaching the 4-phase boundary, as compared to parental magmas evolving by crystallization at higher pressures. FeO is enriched more as magmas evolve along the 4-phase boundary, relative to the olivine-liquid and olivine-plagioclase-liquid boundaries.

Observed FeO/MgO anomaly*

The FeO*/MgO ratio for glasses is plotted vs. latitude in Fig. 10 for the tectonic segments to the north and south of the $11^{o}45'$N OSC on the EPR. The maximum FeO*/MgO values ($\sim$2.3) are observed in lavas sampled along ALVIN dive 2002 (Fig. 1) at the very tip of the eastern rift of the OSC. The most primitive lavas associated with the $11^{o}45'$N OSC (lowest FeO*/MgO) are erupted approximately 8 km behind the tip of the eastern rift. The FeO*/MgO ratio remains elevated above that of 'normal' MORB throughout the portion of the EOSC sampled ($\sim$ 28 km). Data directly to the north of 12^{o} on the EPR are sparse, and thus it is difficult to evaluate where the FeO*/MgO ratio drops to a 'normal' MORB level of 1.75. Lavas at $12^{o}6'$N on the EPR range up to 1.9 in FeO*/MgO (Langmuir et al., 1986), however, this range has been interpreted by Langmuir et al. (1986) as being caused by a small deval. Thus the FeO*/MgO geochemical anomaly associated with the OSC at $11^{o}45'$N is inferred to have a distribution along the rift to the north of the OSC of > 30 but < 50 km.

Lavas sampled from the western rift show a more limited overall range of FeO*/MgO variation (maximum value ~1.7, Fig. 4), although the ratio still varies considerably at a given latitude. The more limited range in FeO*/MgO is consistent with the mixing scenario proposed above for generating the WOSC lavas. Fractionation of magma batches in the shallow level magma chambers inferred to be present on the WOSC is dampened by the repeated influx of fresh, unfractionated parental magma.

Nearby OSCs at 12°37'N and 12°54'N (Fig. 3) show less range in FeO*/MgO relative to those on the east rift of the 11°45'N OSC (Langmuir et al., 1986; show ranges in the FeO*/MgO ratio for the portions of the northern segment from 11°45'N to 12°27'N and 12°37'N to 13°30'N of 1.38-1.79 and 1.09-1.86, respectively).

Comparison

Macdonald et al (1988) point out important distinctions between first-order segmentation of the mid-ocean ridge by major transform faults and propagating rifts, whose offsets are large enough that the lithosphere along the plate boundary behaves rigidly (0.5-1.0 M.y. old), second-order segmentation by large-offset (>3-5 km) OSCs and small-offset, non-rigid transform faults, and third-order segmentation by smaller offset (<3 km) OSCs. It is important to bear in mind that in Table 9 we are comparing first- (the propagating rift systems from the Galapagos Spreading Center and the Juan de Fuca), second- (the OSCs at 11°45'N and 9°N on the EPR) and third- order (the OSCs at 12°37'N and 12°54'N on the EPR) discontinuities. Note that the magnitude and distribution of the geochemical anomaly along the ridge segment to the north (in terms of FeO*/MgO) associated with the second-order discontinuity at 11°45'N (2.3, 30 - 50 km) is of the order observed at several of the first-order propagating rift tip discontinuities considered. Furthermore, the geochemical anomaly associated with the OSC at 11°45'N is more significant than that observed at the similarly sized OSC at 9°N (1.9, <20 km). In contrast, geochemical anomalies (in terms of elevated FeO*/MgO) are very small, if present at all at the third-order discontinuities at 12°37'N and 12°54'N.

All of the OSCs considered in Table 9 are on intermediate to fast spreading ridges (5-6 cm/yr, half spreading rate), in contrast to the propagating rifts which are on intermediate spreading ridges (~ 3 cm/yr, half spreading rate). The geochemical signatures associated with both propagating rift tips and OSCs on ridges with similar spreading rates vary widely, thus spreading rate variations of the scale covered by the features in Table 9 are not particularly diagnostic. The propagating ridge tip at 93°W in the Galapagos area is the only ridge offset feature considered in Table 9 that appears to be fed by a 'hot spot'. The fact that no anomalous FeO*/MgO ratios are observed in lavas from this area suggests that even though the rift is currently propagating, the diminished magma supply effects associate with propagating rifts ('starvation') are swamped by the flooding of the rift tip with an over-supply of the 'hot spot' derived magmas (Sinton et al., 1983). Thus, no observed geochemical anomaly is associated with the propagating rift at 93°W.

The length of the transform is anticipated to be directly related to the magnitude of the thermal edge effects it imposes on the truncated rifts (Langmuir et al., 1986). Thus the transform length might be diagnostic of the geochemical anomalies associated with the tectonic offset features considered in Table 9. In fact, propagating rifts and OSCs (95°W and Cobb; 9°N and 11°45'N, respectively) with similar truncating transform lengths (and half spreading rates) show very different distributions of lavas with anomalous FeO*/MgO. Whether or not the ridge offset features in Table 9 are currently propagating, or have propagating rifts on one side of the OSC also does not appear to be diagnostic of the magnitude or distribution of geochemical anomaly associated with the offset.

The most significant variable shown in Table 9 is the migration rate of the particular offset feature relative to the underlying mantle. Lavas sampled from propagating rift and OSC offsets with more rapid migration rates relative to the underlying mantle show anomalous FeO*/MgO over greater lengths behind the rift tips.

A rapid migration rate may imply that the rift(s) at the migrating offset feature is 'out-running' its supply of magma from the mantle, and is thus suffering 'starvation' (Macdonald et al., 1988). A shortage of incoming primitive (less fractionated, lower FeO*/MgO) magma related to the rapid migration of the offset away from the mantle-derived magma supply zone results in a greater extent of fractionation of the magma at the migrating rifts, as well as lesser amounts of mixing between fractionated magmas and fresh inputs of primitive magma. The $11^{O}45'$N OSC is migrating roughly twice as fast as the most rapidly migrating propagating rift tips, which probably explains the similar order of associated geochemical anomaly between these first and second order ridge segmentation features. Similarly, the three-fold increase in migration rate associated with the $11^{O}45'$N OSC over that associated with the similar sized 9^{O}N OSC is most likely responsible for the more substantial anomaly associated with the $11^{O}45'$N OSC. The results of this comparison between the tectonic variables associated with ridge offsets and the occurrence of geochemical anomalies are consistent with the suggestion of Sinton et al. (1983) and Macdonald et al. (1988) that migration rates of rifts relative to their magma sources are the key factors controlling the formation and distribution of geochemical anomalies such as elevated FeO*/MgO.

SUMMARY AND FURTHER STUDY

This study combines detailed geochemical sampling with geological observations and experimentally determined phase equilibria to examine in detail the petrologic processes that operated to produce the observed geochemical diversity at the large offset, rapidly migrating OSC at $11^{O}45'$N on the EPR. The major observations of this study are: 1) The geochemical signatures in the lavas erupted on both the eastern and western rifts of the OSC require the operation of crystallization by magmas along the olivine - augite - plagioclase - liquid boundary, however, few, if any of the lavas erupted

at the OSC contain augite as a phenocryst phase. 2) Lavas on the eastern rift of the OSC show a greater diversity in major element composition relative to those on the western rift. 3) The major element chemistry of the lavas sampled from the currently volcanically and tectonically quiet western rift is well explained by simple mixing between moderately evolved magmas saturated with olivine + augite + plagioclase near 1-atm. and parental magma. The resulting mixed magma is no longer saturated with augite at 1-atm., however the magma composition retains the signature of the fractionation of augite contributed by the evolved component in the mixture. The identification of a shallow level seismic reflector under the southern portion of the western rift of the OSC (Detrick et al., 1987) indicates the presence of a shallow level magma chamber in which the magma injection, fractionation, re-injection and mixing process inferred for the western rift lavas took place. 4) The major element compositions of lavas sampled from the eastern rift is well explained by fractionation from parental magmas similar to the primitive lavas sampled at the eastern rift and further to the north on the EPR, at pressures equivalent to ~6 km depth in the oceanic crust. The diversity of chemical compositions erupted during the recent history of the eastern rift and the lack of a continuous seismic reflector along this portion of the EPR preclude the existence of a continuous magma chamber beneath the eastern rift of the EOSC, however, the occurrence of lavas of identical major element chemistry and similar age along approximately 25 km of ridge requires extensive lateral injection from the magma source, possible at pressures equivalent to the base of the oceanic crust. 5) No anomalous FeO*/MgO lavas were observed on the western rift of the OSC, which is consistent with the mixing scenario proposed for the generation of the compositional diversity of the WOSC lavas. Anomalously high FeO*/MgO (~2.3) values were observed for the lavas on the eastern rift over a relatively great length of ridge axis (30 - 50 km). These characteristics are comparable to those observed at first order tectonic discontinuities such as the 95.5^{o}W and Blanco propagating rift tips, and more substantial

than the geochemical anomalies observed at nearby OSCs, and are attributed at least in part to the very rapid migration rate of the $11^{o}45'N$, relative to the underlying mantle (Perram and Macdonald, 1990). The rapid migration rate relative to the underlying mantle and magma source(s) results in the staging of isolated magma batches at pressures equivalent to the base of the oceanic crust where they are able to evolve to fractionated compositions.

Two further studies are required to test the inferences made in this study based solely on the geological observations and major element compositions of the glasses sampled. These include: 1) Electron microprobe study of the phenocryst assemblages present in a representative set of the lavas, particularly to examine the phenocryst evidence to test the mixing hypothesis for several of the western rift lava groups, as well to test the ~2-kbar fractionation hypothesis for many of the eastern rift lava groups. 2) The trace element data for the lavas (which is coming soon!) needs to be integrated into the present work, both to test the integrity of the lava groups identified on the basis of field observation and major element chemistry and to further test the mixing and fractionation models.

REFERENCES

Albarede, F., Regime and trace-element evolution of open magma chambers. Nature, 318, 356-358, 1985.

Albee, A. L. and Ray, L., Correction factors for electron microprobe analysis of silicates, oxides, carbonates, phosphates and sulfates. Anal. Chem., 42, 1408-1414, 1970.

Antrim, L., Sempere, J.-C. and Macdonald, K. C., Fine Scale Study of a Small Overlapping Spreading Center System at $12^{o}54'$N on the East Pacific Rise. Marine Geophys. Res., 9, 115-130, 1988.

Argo-Rise Group, Geological mapping of the East Pacific Rise axis ($10^{o}19'$ - $11^{o}53'$N) using the Argo and Angus imaging systems. Can. Mineral., 26, 467-486, 1988.

Bartels, K. S., Kinzler, R. J. and Grove, T. L., High pressure phase relations of a near primary high alumina basalt from Medicine Lake Highland, N. California. Contrib. Mineral. Petrol., in press, 1991.

Bence, A. E., and Albee, A. L., Empirical correction factors for the electron microanalysis of silicates and oxides. J. Geol., 76, 382-403, 1968.

Bender, J. F., Langmuir, C. H. and Hanson, G., J. Petrol.., 25, 213-254, 1984.

Biggar, G. M., Diopside, lithium metasilicate and the 1968 temperature scale. Mineral. Mag., 38, 768-770, 1972.

Biggar, G. M. and Humphries, D. J., The plagioclase, forsterite, diopside, liquid equilibrium in the system CaO-Na_2O-MgO-Al_2O_3-SiO_2. Mineral. Mag., 44, 309-314, 1981.

Bryan, W. B., Finger, L. W., and Chayes, F., Estimating proportions in petrographic mixing equation by least squares approximation. Science, 163, 926-927, 1969.

Bryan, W. B., Kinzler, R. J., Hekinian, R. and Edwards, M., Geologic and petrologic contrasts in rift tips at the $11^{o}45'$N OSC, East Pacific Rise (abs). EOS, 69, 1477, 1988.

Christie, D. M. and Sinton, J. M., Evolution of abyssal lavas along propagating segments of the Galapagos spreading center. Earth and Planet. Sci. Lett., 56, 321-335, 1981.

Christie, D. M. and Sinton, J. M., Major element constraints on melting, differentiation and mixing of magmas from the Galapagos 95.5^{o} W propagating rift system. Contrib. Mineral. Petrol., 94, 274-288, 1986.

Crane, K., Alkman III, F., and Foucher, J. P., The Distribution of Geothermal Fields Along the East Pacific Rise from $13^{o}10'$N to $8^{o}20'$N: Implications for Deep Seated Origins. Marine Geophys. Res. 9, 211-236, 1987.

Detrick, R.S., Buhl, P., Vera, E., Mutter, J., Orcutt, J., Madsen, J., and Brocher, T., Multi-channel seismic imaging of a crustal magma chamber along the East Pacific Rise. Nature, 326, 35-41, (1987).

Fox, P. J. and Gallo, D. G., A tectonic model for Ridge-transform-ridge plate boundaries: implications for the structure of oceanic lithosphere. Tectonophysics, 104, 205-242, 1984.

Grove, T. L., Use of FePt alloys to eliminate the iron loss problem in 1 atmosphere gas mixing experiments: Theoretical and practical considerations. Contrib. Mineral. Petrol., 78, 298-304, 1981.

Grove, T. L. and Bryan, W. B., Fractionation of pyroxene-phyric MORB at low pressure: an experimental study. Contrib. Mineral. Petrol., 84, 293-309, 1983.

Grove, T. L., Gerlach, D. C. and Sando, T. W., Origin of calc-alkaline series lavas at Medicine Lake volcano by fractionation, assimilation and mixing. Contrib. Mineral. Petrol., 80, 160-182, 1982.

Grove, T. L. and Juster, T. C., Experimental investigations of low-Ca pyroxene stability and olivine - pyroxene - liquid equilibria at 1-atm in natural basaltic and andesitic liquids. Contrib. Mineral. Petrol., 103, 287-305, 1989.

Grove, T. L., Kinzler, R. J. and Bryan, W. B., Natural and experimental phase relations of lavas from Serocki volcano. in Proc. Ocean Drilling Prgrm. Sci. Res., eds. Detrick, R., Honnores, J, Bryan, W. B., Juteau, T., et al., 106/109, 9-17.

Grove, T. L., Kinzler, R. J. and Bryan, W. B., Fractionation of mid-ocean ridge basalt (MORB). Submitted to RIDGE Summer Inst. 1990 Vol, special A.G.U. publication, 1991.

Hekinian, R., Auzende, J. M., Francheteau, J., Gente, P., Ryan, W. B. F. and Kappel, E. S., Offset spreading centers near 12°53'N on the East Pacific Rise: submersible observations and composition of the volcanics. Marine Geophys. Res., 7, 359-377, 1985.

Hekinian, R. and Fouquet, Y., Volcanism and Metallogenesis of Axial and Off-Axial Structures on the East Pacific Rise near 13° N. Economic Geology, 80, 221-249, 1985.

Hekinian, R. and Thompson, G., Comparative Geochemistry of Volcanics from Rift Valleys, Transform Faults and Aseismic Ridges. Contrib. Mineral. Petrol., 57, 145-162, 1976.

Hekinian, R., Thompson, G. and Bideau, D., Axial and Off-Axial Heterogeneity of Basaltic Rocks From the East Pacific Rise at 12°35'N - 12°51'N and 11°26'N-11°30'N, J. Geophys. Res., 94, 17,437-17,463, 1989.

Hey, R., Johnson, G. L., Lowrie, A., Recent plate motions in the Galapagos area. Geol.. Soc. Amer. Bull., 88, 1385-1403, 1977.

Karsten, J. L., Delaney, J. R., Rhodes, J. M. and Liias, R. A., Spatial and temporal evolution of magmatic systems beneath the Endeavour segment, Juan de Fuca Ridge: Tectonic and petrologic constraints, in press for J. Geophys. Res., 1991.

Kinzler, R. J. and Grove, T. L., Primary magmas of mid-ocean ridge basalts. J. Geophys. Res., submitted, 1991.

Kinzler, R. J., Grove, T. L., Bryan, W. B. and Humphries, S., Magmatic diversity in space and time at the eastern over-lapping spreading center (EOSC), East Pacific Rise (abs). EOS, 69, 1477, 1989.

Langmuir, C. H. and Bender, J. F., The geochemistry of oceanic basalts in the vicinity of transform faults: observations and implications. Earth and Planet. Sci. Lett., 69, 107-127, 1984.

Langmuir, C. H., Bender, J. F., and Batiza, R., Petrological and tectonic segmentation of the East Pacific Rise, $5^{o}30'N$ - $14^{o}30'N$. Nature, 322, 422-429, 1986.

Longhi, J. and Pan, F., A reconnaissance study of phase boundaries in low-alkali basaltic liquids. J. Petrol., 115-148, 1988.

Lonsdale, P., Overlapping rift zones at the $5.5^{o}S$ offset of the East Pacific Rise, J. Geophys. Res., 88, 9393-9406, 1983.

Lonsdale, P., Linear volcanoes along the Pacific-Cocos plate boundary, 9=oN to the Galapagos triple junction. Tectonophysics, 116, 255-279, 1985.

Lonsdale, P., Comments on "East Pacific Rise from Siqueiros to Orozco fracture zones: Along-strike continuity of axial neo-volcanic zone and structure and evolution of overlapping spreading centers" by K. C. Macdonald, J. C. Sempere, and P. J. Fox. J. Geophys. Res., 91, 10,493-10,499, 1986.

Macdonald, K. C. and Fox, P. J., Overlapping spreading centers: A new kind of accretionary geometry on the East Pacific Rise. Nature, 302, 55-58, 1983.

Macdonald, K. C., Sempere, J.-C. and Fox, P. J., East Pacific Rise from Siqueiros to Orozco fracture zones: Along-strike continuity of axial neo-volcanic zone and structure and evolution of overlapping spreading centers. J. Geophys. Res., 89, 6049-6069, 1984.

Macdonald, K. C., Fox, P. J., Perram, L J., Eisen, M F., Haymon, R. M., Miller, S. P., Carbotte, Sm M., Cormier, M.-H. and Shor, A. N., A new view of the mid-ocean ridge from the behaviour of ridge-axis discontinuities. Nature, 335, 217-225, 1988.

Natland, J. H., Effect of axial magma chambers beneath spreading centers on the compositions of basaltic rocks. 1980.

O'Hara, M. J., Geochemical evolution during fractional crystallization of a periodically refilled magma chamber. Nature, 266, 503-507, 1977.

Perfit, M. R., Fornari, D. J., Malahoff, A. and Embley, R. W., Geochemical Studies of Abyssal Lavas Recovered by DSRV Alvin From Eastern Galapagos Rift, Inca Transform, and Ecuador Rift. 1. Major Element Variations in Natural Glasses and Spacial Distribution of Lavas. J. Geophys. Res., 88, 10,519-10,529, 1983.

Perram, L. J. and Macdonald, K. C., A One-Million-Year History of the 11°45'N East Pacific Rise Discontinuity. J. Geophys. Res., 95, 21,363-21,381, 1990.

Presnall, D. C., Dixon, T. H., O'Donnell, T. H., and Dixon, S. A., Generation of mid-ocean ridge tholeiites. J. Petrol., 20, 3-35, 1979.

Roeder, P. L. and Emslie, R. F., Olivine-Liquid Equilibrium. Contrib. Mineral. Petrol., 29, 275-289, 1970.

Schilling, J-G. and Sigurdsson, H., Thermal minima along the axis of the Mid-Atlantic Ridge. Nature, 282, 370-374, 1979.

Schouten, H. and Klitgord, K. D., The memory of the accreting plate boundary and the continuity of fracture zones. Earth Planet. Sci. Lett., 59, 255-266, 1982.

Schouten, H. and White, R. S., Zero-offset fracture zones. Geology, 8, 175-179, 1980.

Sinton, J. M. and Christie, D. M., Petrological Effects at Ocean Ridge-Transform Intersections (abs). EOS, 65, 1138, 1985.

Sinton, J. M., Wilson, D S., Christie, D. M., Hey, R. N. and Delaney, J. R., Petrologic consequences of rift propagation on oceanic spreading ridges. Earth and Planet. Sci. Lett., 62, 193-207, 1983.

Stolper, E., Phase diagram for mid-ocean ridge basalts: preliminary results and implications for petrogenesis. Contrib. Mineral. Petrol., 74, 13-27, 1980.

Thompson, G., Bryan, W. B., Ballard, r. D., Hamuro, K., and Melson, W. G., Axial processes along a segment of the East Pacific Rise, 10-12°N. Nature, 318, 429-433, 1985.

Thompson, G., Bryan, W. B. and Humphris, S. E., Axial volcanism on the East Pacific Rise, 10-12°N. *Magmatism in the Ocean Basins*, Saunders, A. D. and Norry, M. J. (eds), Geological Soc. Spec. Pub. No. 42, 1989.

Thompson, G., Bryan, W. B., Humphris, S., Ryan, W. B. F., Hekinian, R. and Grove, T., Volcanic and tectonic evolution of the East Pacific Rise, 10° - 12°N (abs). EOS, 69, 1477, 1988.

Tormey, D. R., Grove, T. L. and Bryan, W. B., Experimental petrology of normal MORB near the Kane Fracture Zone: 22°-25°N, mid-Atlantic ridge. Contrib. Mineral. Petrol., 96, 121-139, 1987.

Uchupi, E., Schwab, W. C., Ballard, R. D., Cheminee, J. L., Francheteau, J., Hekinian, R., Blackman, D. K. and Sigurdsson. An Angus/Argo study of the neo-volcanic zone along the East Pacific Rise from the Clipperton fracture zone to 12°N. Geo. Mar. Lett., 8, 131-138, 1988.

Fig. 2-1 Bathymetry and sample locations for the $11^{o}45'$N OSC on the EPR (inset, from Perram and Macdonald, 1990, provides general location), with tracks (arrows) of ALVIN dives 1997 - 2004, and locations of dredges 17 - 20 from the 1988 Atlantis II - leg 119 cruise. Dredge locations (labelled dr-) for samples from Thompson et al. (1989) are also shown. Capitol letters signify chemical groups (Tables 1 and 2) sampled at each dive or dredge location.

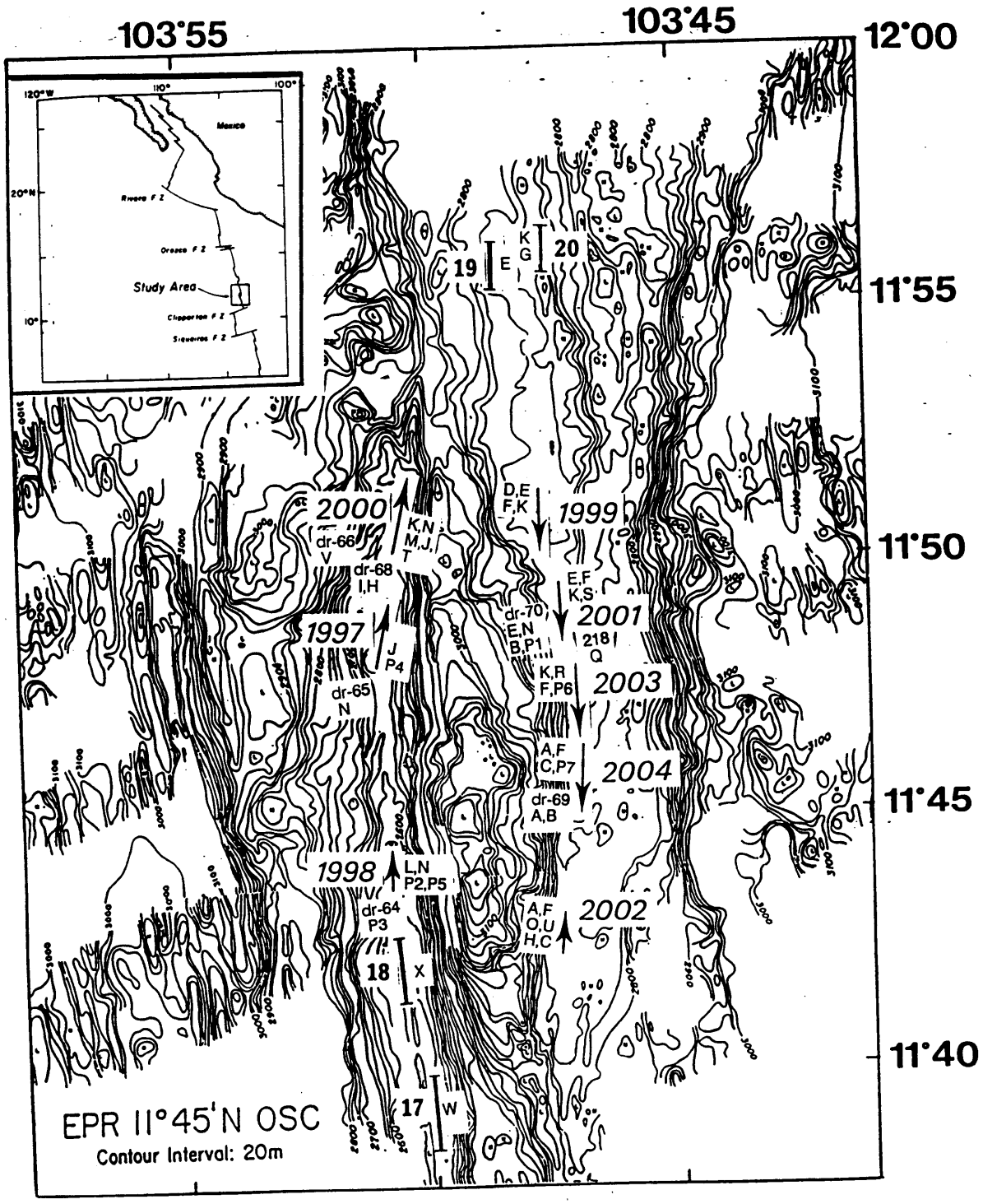
103°55
103°45
12°00
11°55
11°50
11°45
11°40
120°W
110°
100°
20°N
10°
Mexico
Rivera F Z
Orozco F Z
Study Area
Clipperton F Z
Siqueiros F Z
2000
dr-66
V
dr-68
I,H
K,N
M,J
T
1997
dr-65
N
J
P4
1998
dr-64
P3
L,N
P2,P5
18
X
17
W
19
E
K
G
20
D,E
F,K
1999
E,F
K,S
2001
dr-70
E,N
B,P1
218
Q
K,R
F,P6
2003
A,F
C,P7
2004
dr-69
A,B
A,F
O,U
H,C
2002
EPR 11°45'N OSC
Contour Interval: 20m

Fig. 2-2 Major element variation diagrams vs. MgO for the glasses sampled on the eastern and western rifts of the 11°45'N OSC (EOSC=open squares and WOSC=closed squares). Data are from Table 1 and Thompson et al. (1989). Correction factors (see Table 3) were applied to the data of Thompson et al. (1989) and all analyses were normalized to 100% (indicated by subscript n).

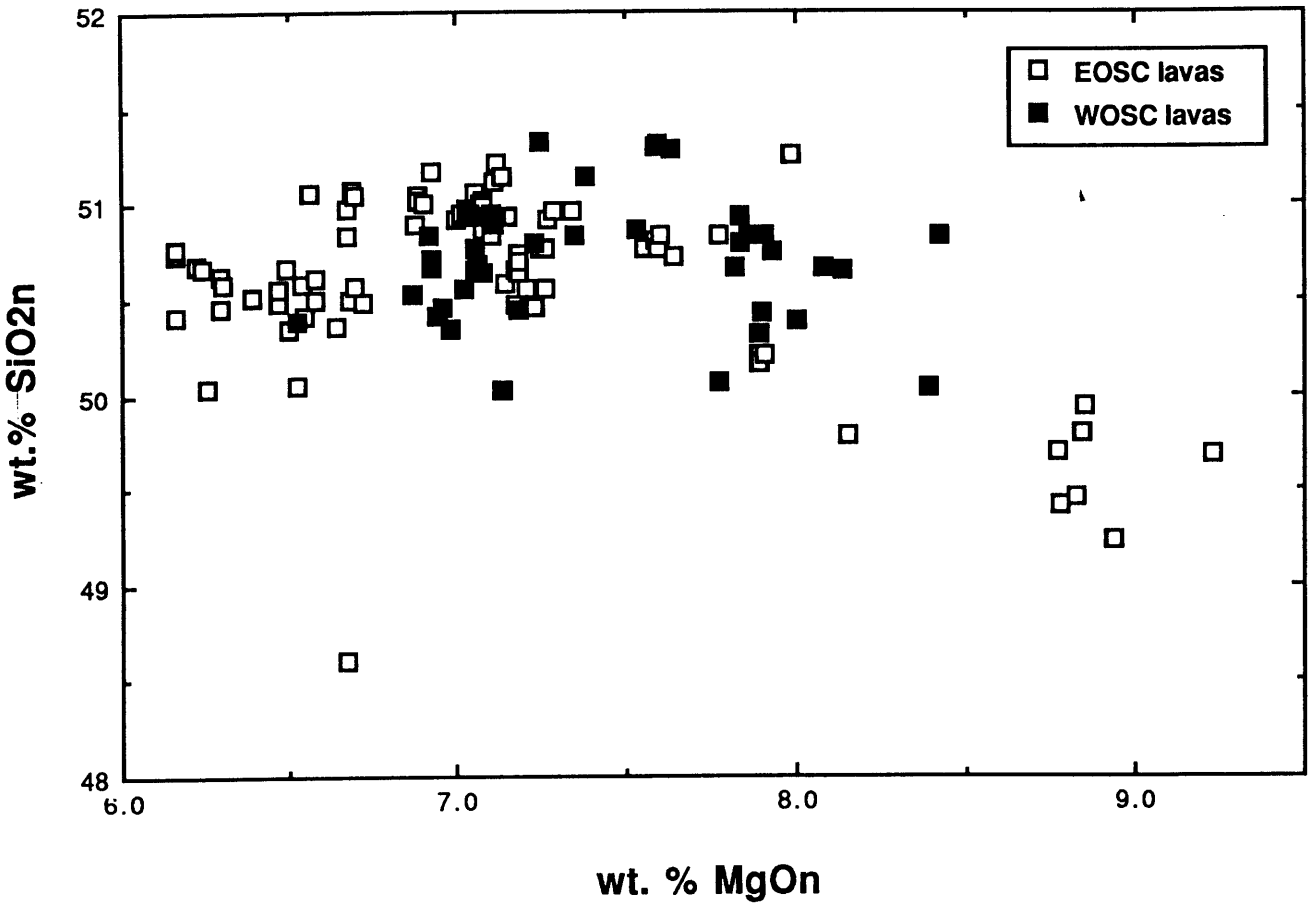
EOSC lavas
WOSC lavas
wt.% SiO2n
wt. % MgOn
52
51
50
49
48
6.0
7.0
8.0
9.0

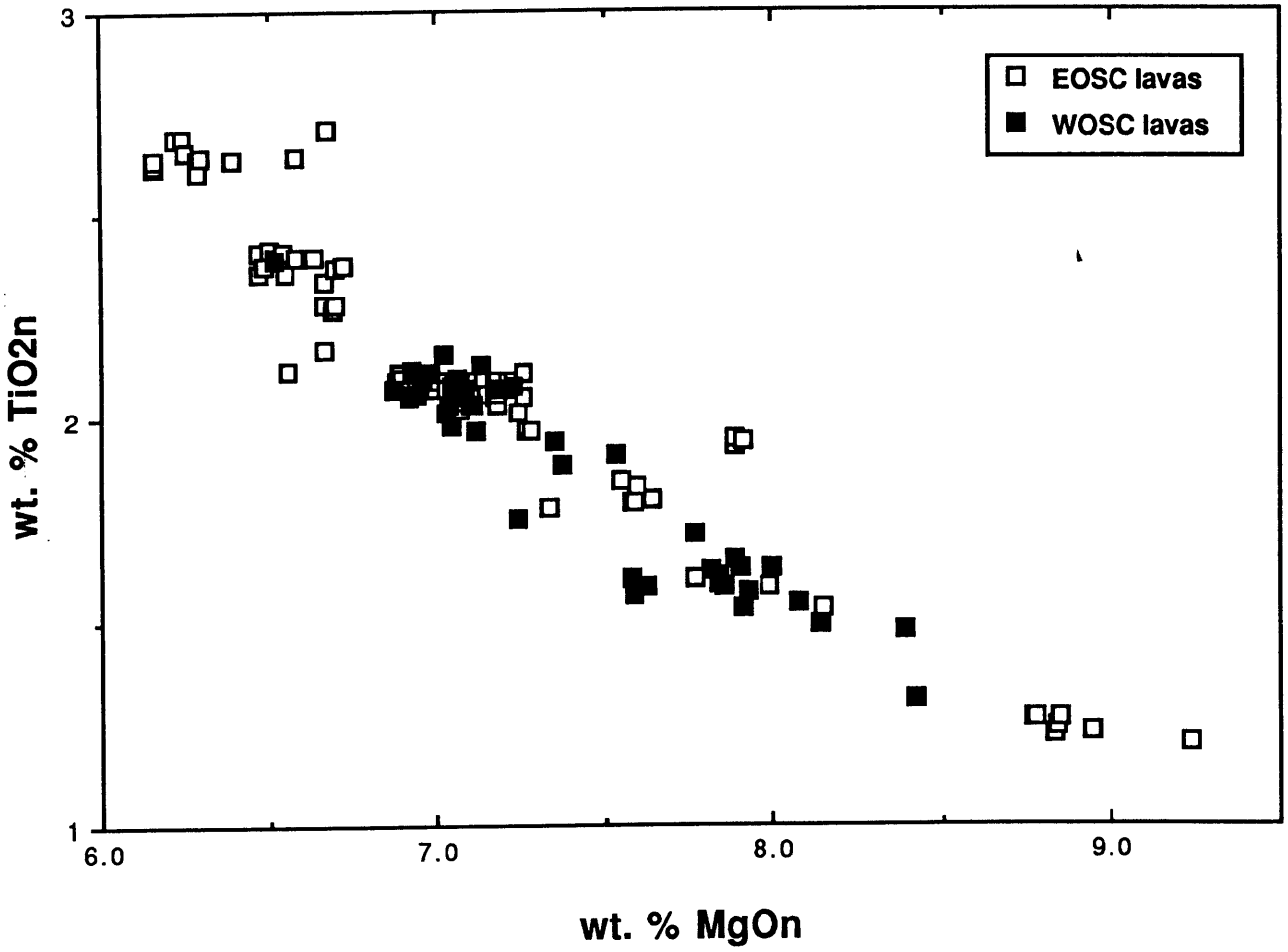
EOSC lavas
WOSC lavas
wt. % TiO2n
wt. % MgOn
3
2
1
6.0
7.0
8.0
9.0

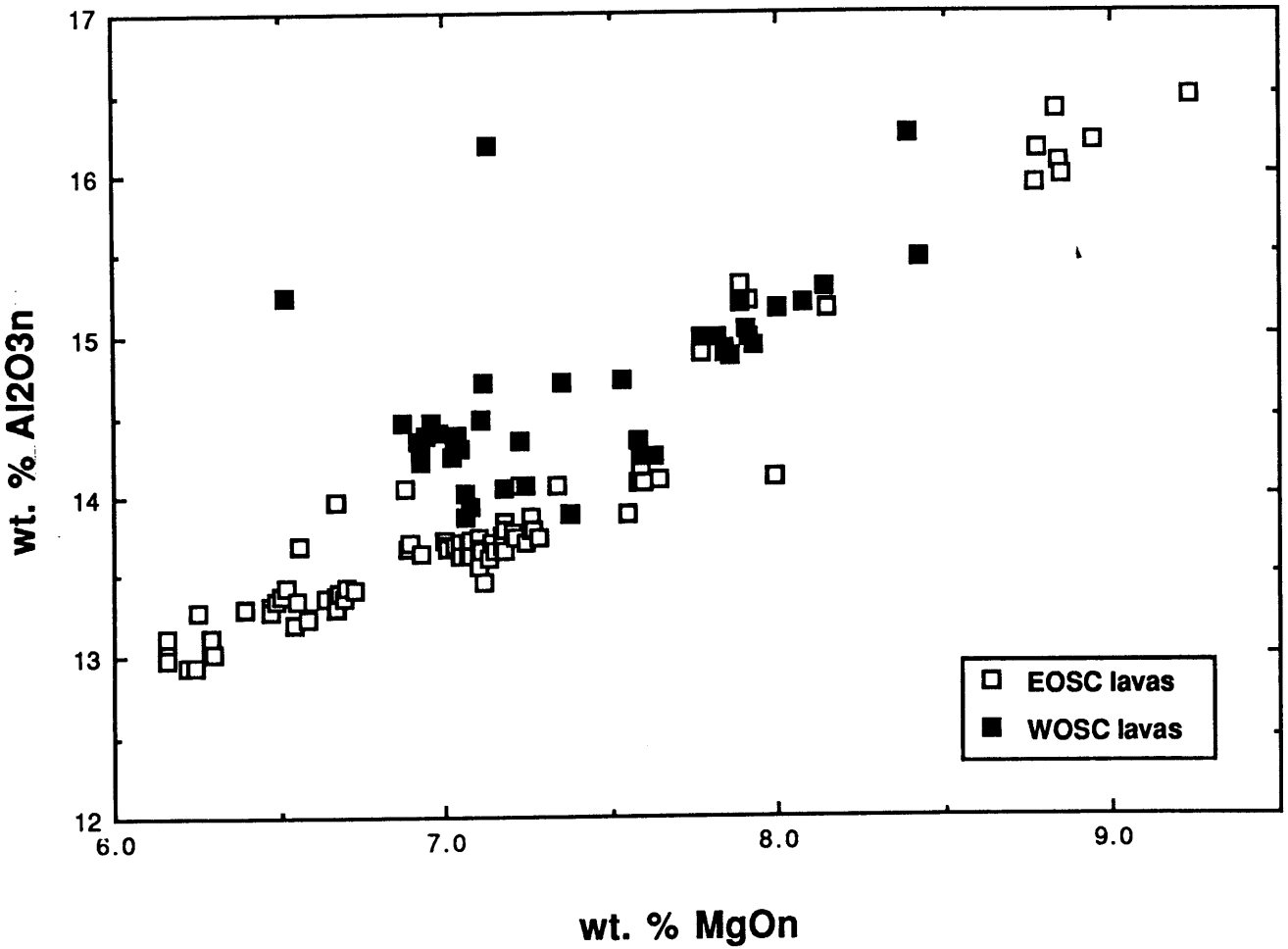
17
16
15
14
13
12
6.0
7.0
8.0
9.0
wt. % Al2O3n
wt. % MgOn
EOSC lavas
WOSC lavas

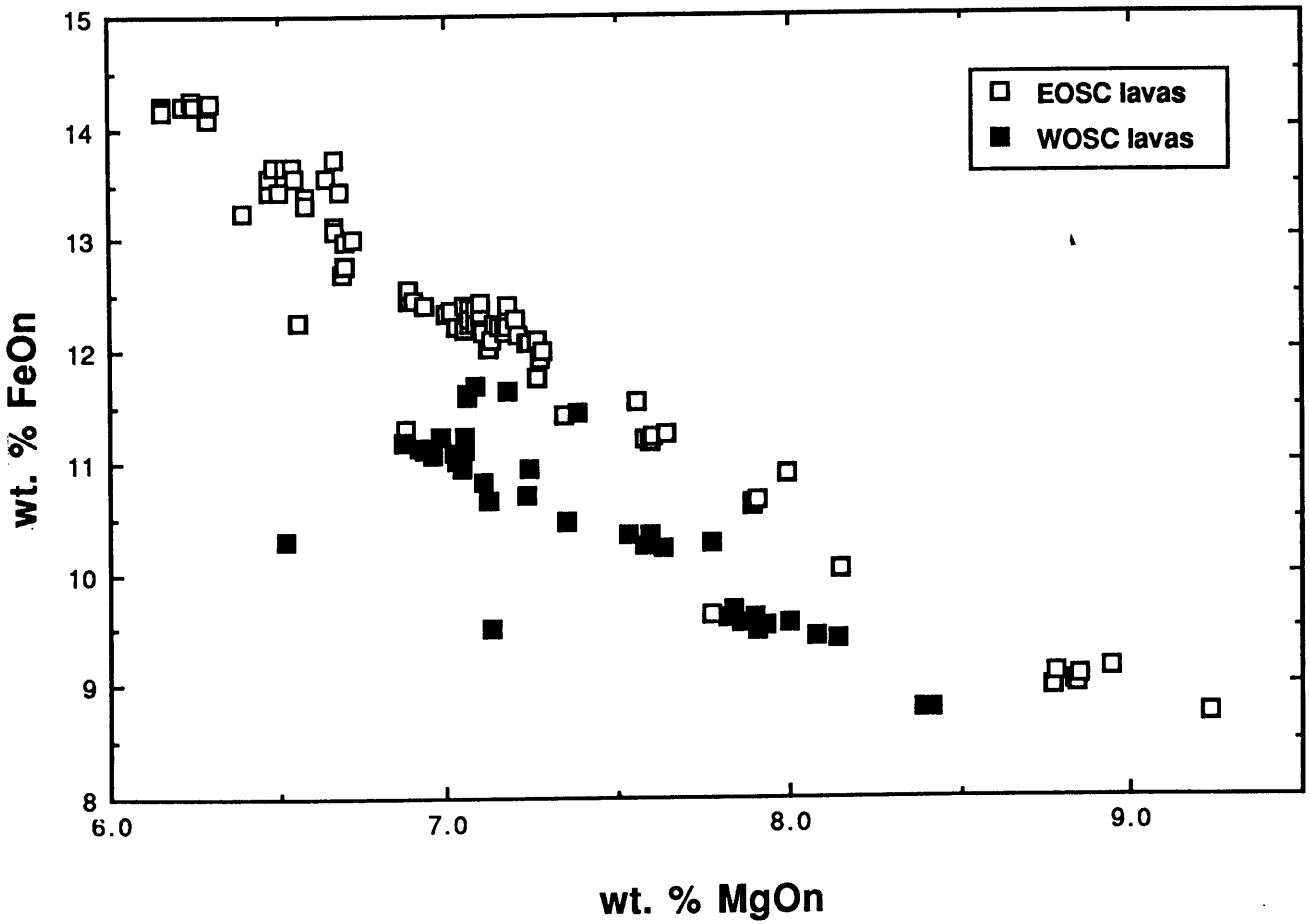
EOSC lavas
WOSC lavas
wt. % FeOn
wt. % MgOn
15
14
13
12
11
10
9
8
6.0
7.0
8.0
9.0

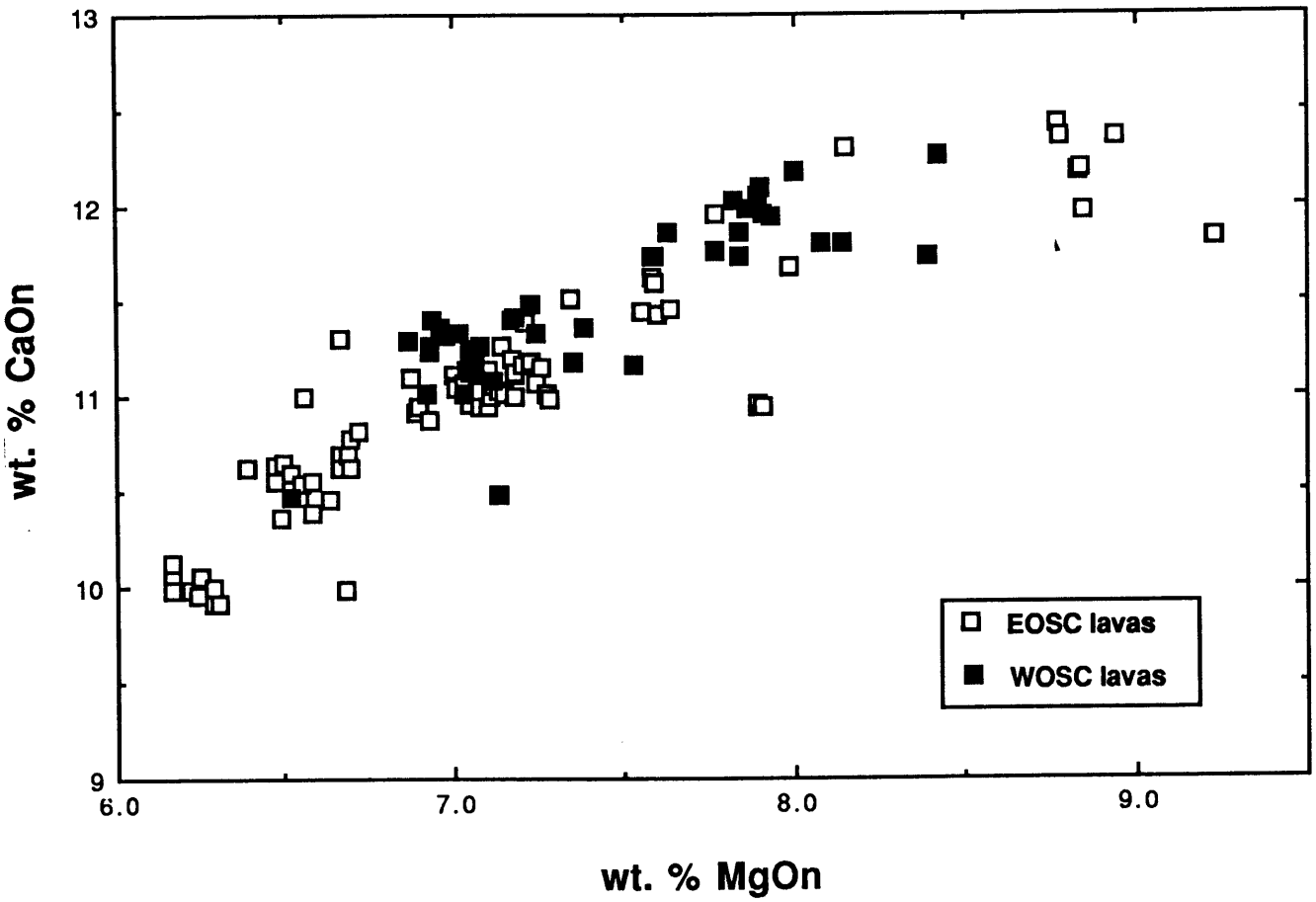
13
12
11
10
9
6.0
7.0
8.0
9.0
wt. % CaOn
wt. % MgOn
EOSC lavas
WOSC lavas

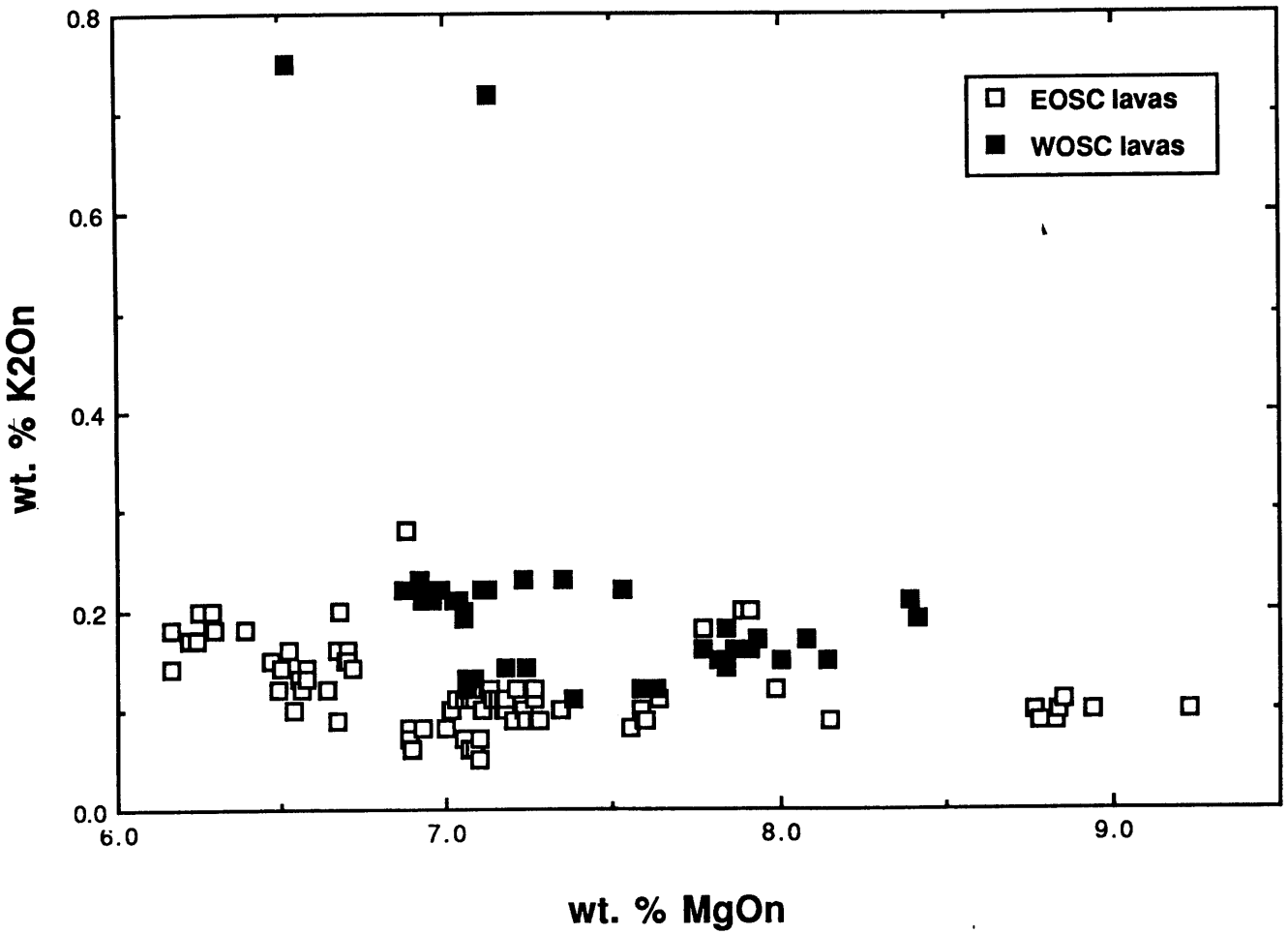
EOSC lavas
WOSC lavas
wt. % K2On
wt. % MgOn
0.0
0.2
0.4
0.6
0.8
6.0
7.0
8.0
9.0

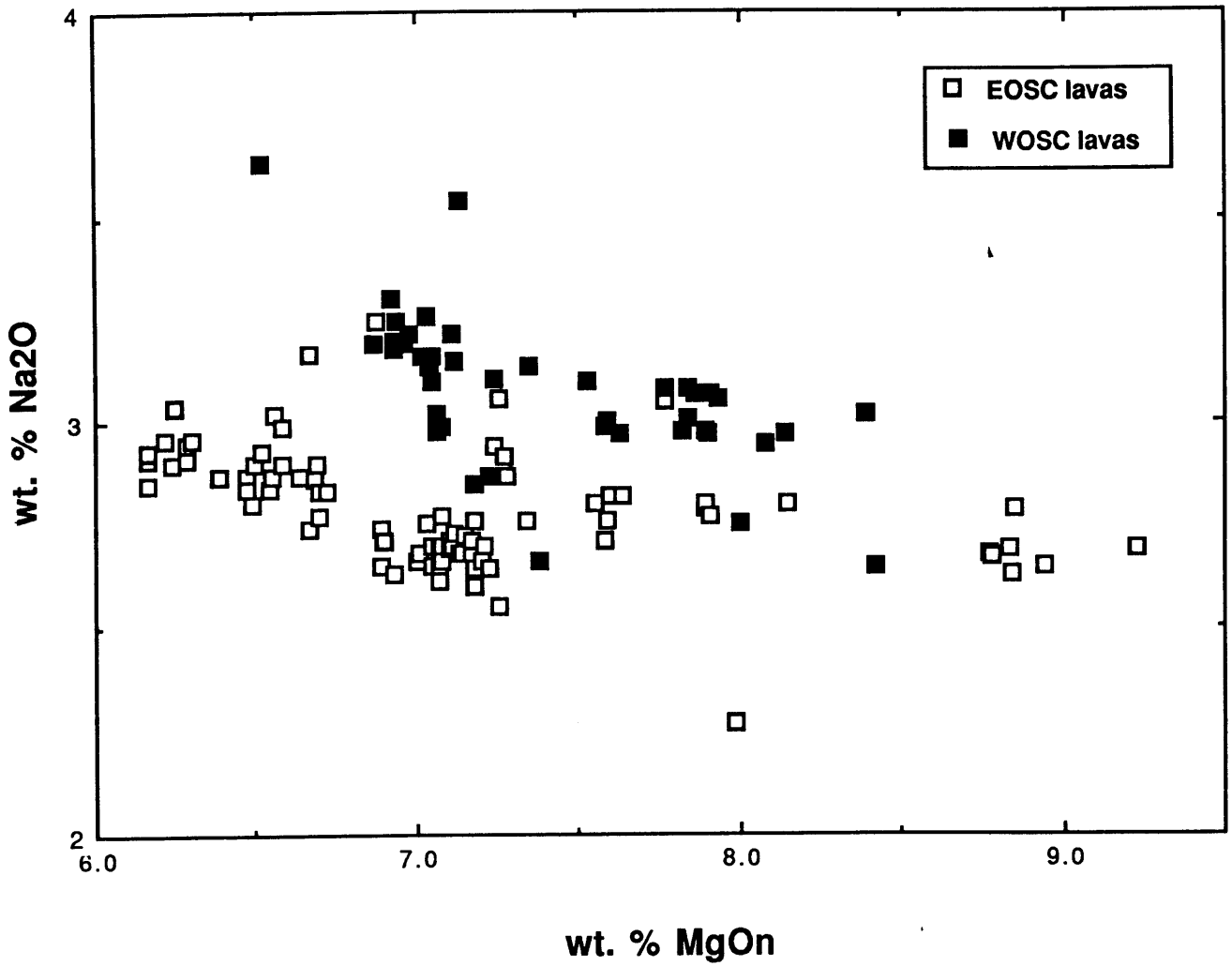
EOSC lavas
WOSC lavas
wt. % Na2O
wt. % MgOn
4
3
2
6.0
7.0
8.0
9.0

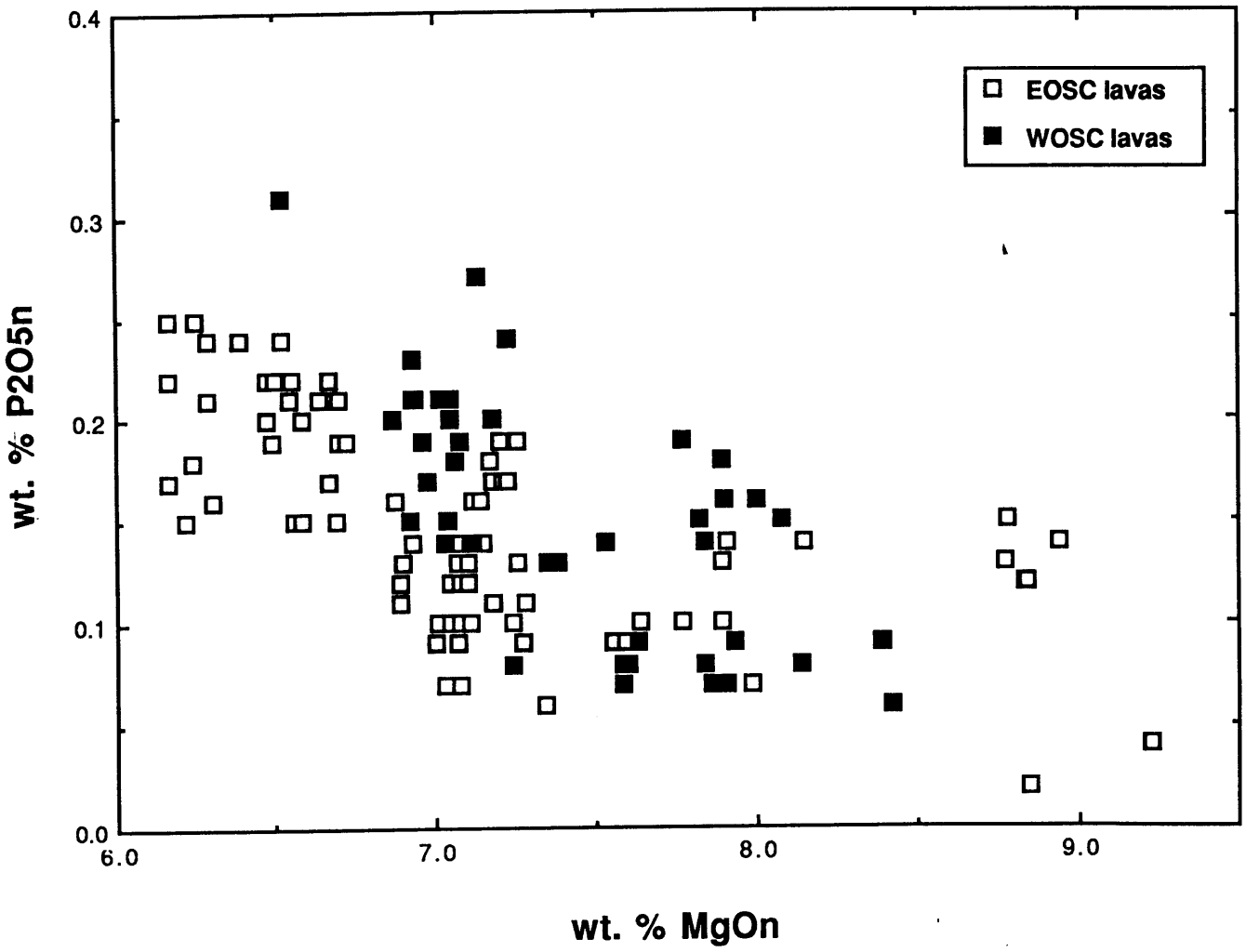
EOSC lavas
WOSC lavas
wt. % P2O5n
wt. % MgOn
0.0
0.1
0.2
0.3
0.4
6.0
7.0
8.0
9.0

Fig. 2-3 (A) Starting compositions (triangles), and experimentally produced olivine + plagioclase, and olivine + plagioclase + augite saturated liquids (pluses) and augites (squares) projected into the pseudo-quaternary Oliv - Cpx - Plag - Qtz using oxygen normalized mineral components (projection scheme of Grove et al., 1991) and further projected through Plag onto the Oliv - Cpx - Qtz pseudo-ternary. The two pluses that project into the olivine primary phase volume are liquids saturated with olivine and plagioclase (from experiments on ALVIN 2004-3-1), the remaining pluses define the 4-phase boundary (from experiments on all five starting compositions provided in Table 3). The solid curve shows the 1-atm. liquid line of descent for the most MgO-rich lava sampled (ALVIN 2004-3-1). The pluses on the 4-phase boundary at lower normative Qtz in the projection are olivine - plagioclase - augite saturated experiments on the other lavas. The projected position of the MORB glass ALVIN 2004-3-1 (the triangle that plots closest to the Oliv apex) is shifted away from the experimentally determined liquid line of descent for ALVIN 2004-3-1 (solid line) in the Oliv - Cpx - Qtz pseudo-ternary because of a slight amount of sodium loss in the higher-temperature melting experiments. The experimentally produced augite compositions closest to the Cpx apex are from the highest temperature experiments, as temperature decreases, the augite compositions move away from the Cpx apex towards the Oliv - Qtz join. The thermal divide on the 4-phase boundary is very close to the Oliv - Plag - Cpx join, and the 'down-temperature' direction along the experimentally determined 4-phase boundary for the EPR lavas is always towards Qtz.

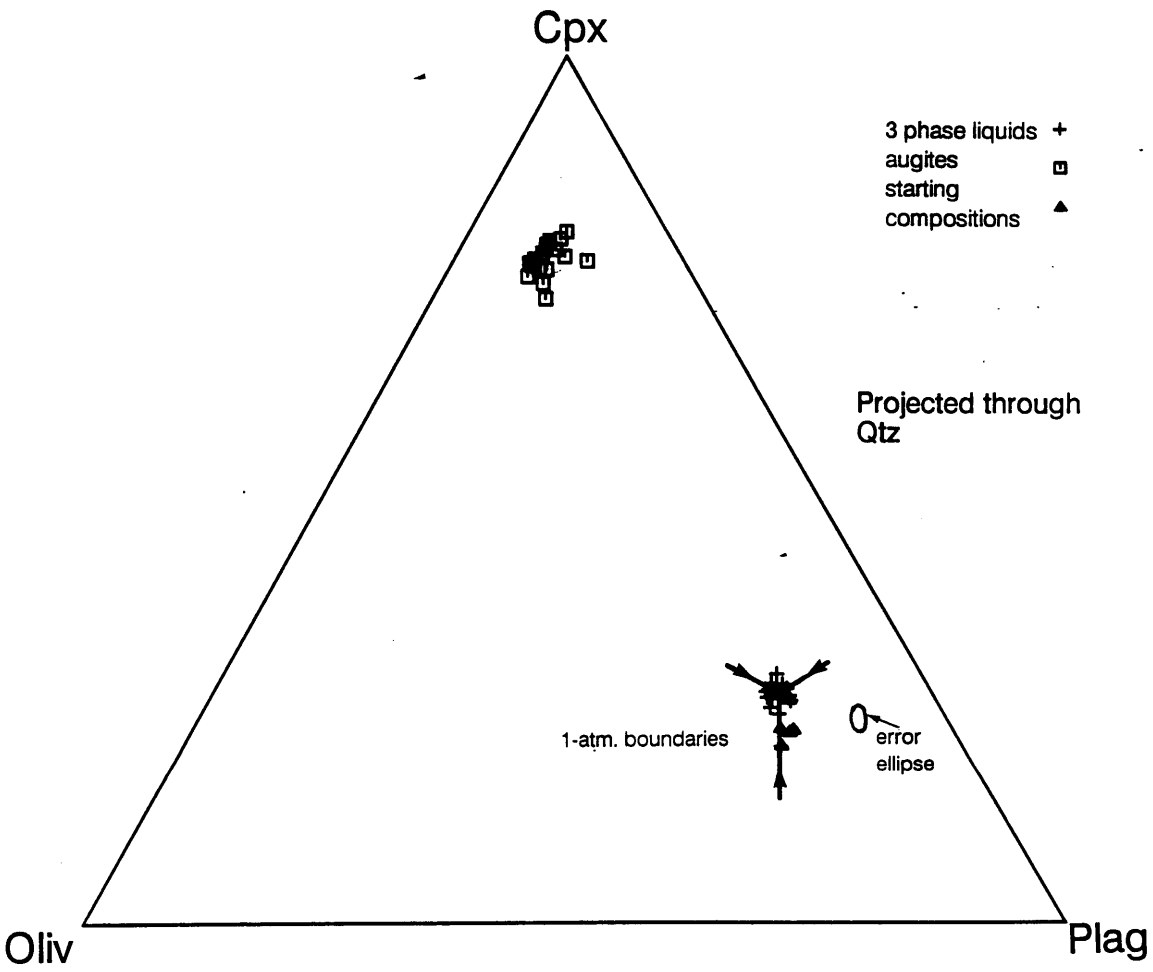
Cpx
3 phase liquids
augites
starting compositions
Projected through Qtz
1-atm. boundaries
error ellipse
Oliv
Plag

Fig. 2-3 (B) As in (A) however projected through Qtz onto the pseudo-ternary Oliv - Cpx - Plag. The 4-phase boundary olivine + plagioclase + augite + liquid collapses to a cluster to constrain the temperature minimum or 'point' in the Oliv - Cpx - Plag pseudo-ternary. The olivine + plagioclase + liquid boundary is constrained as well by experiment, the olivine + augite + liquid and the plagioclase + augite + liquid boundaries are inferred. Two of the starting compositions fall on the 1-atm. olivine + plagioclase + liquid 3-phase boundary, one is near the 1-atm. 4-phase boundary and the other two are shifted slightly towards the Plag apex.

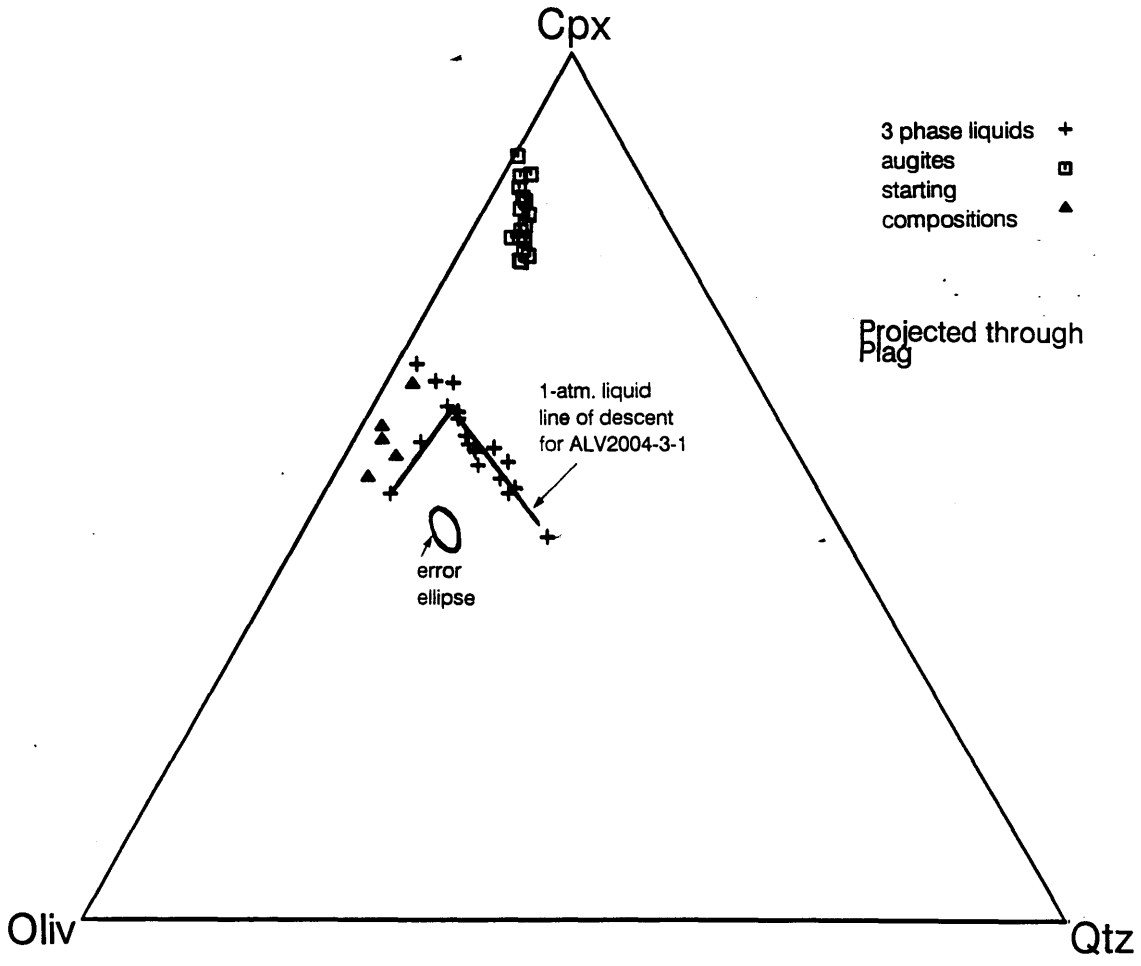
Cpx
3 phase liquids
augites
starting
compositions
Projected through Plag
1-atm. liquid
line of descent
for ALV2004-3-1
error
ellipse
Oliv
Qtz

Fig. 2-4 (A) Comparison of the OSC lava groups (open squares) to the 1-atm. experimentally determined phase boundaries (experimental liquids shown as pluses) in an expanded portion of the same projection described in Fig. 3a caption. Note the displacement towards the Oliv apex of most of the OSC lava groups from the solid line fit by eye to the 3-phase saturated experimental liquids in the Oliv - Cpx - Qtz pseudo-ternary. The two pluses in the Oliv phase volume are the olivine + plagioclase saturated experiments on ALVIN 2004-3-1.

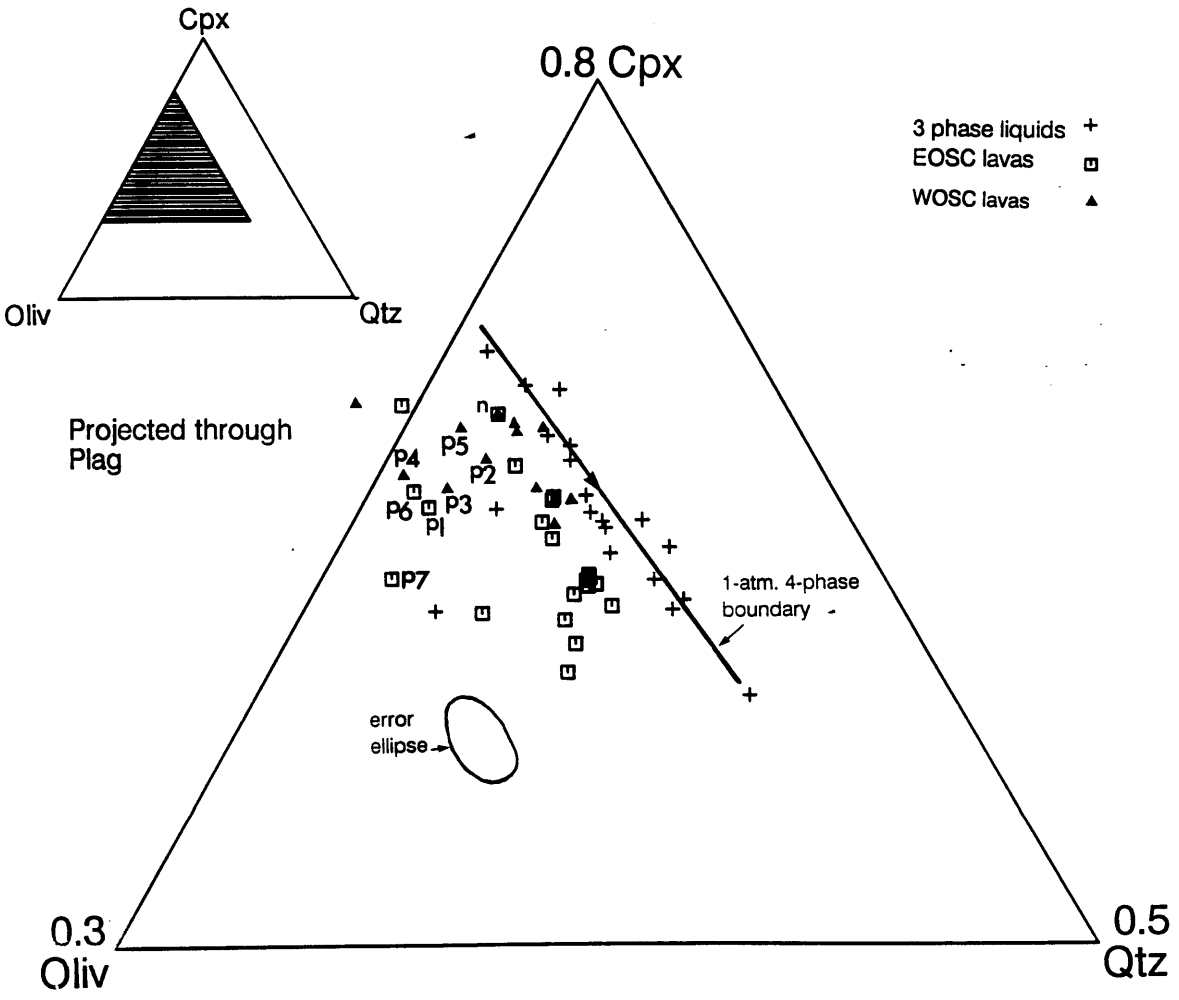
Cpx
Oliv
Qtz
Projected through Plag
0.8 Cpx
3 phase liquids
EOSC lavas
WOSC lavas
n
p5
p4
p2
p6
p3
p1
P7
1-atm. 4-phase boundary
error ellipse
0.3 Oliv
0.5 Qtz

Fig. 2-4 (B) As in (A) however in an expanded portion of the same projection described in Fig. 3b caption. The parental type lavas on the EOSC fall along the olivine + plagioclase + liquid boundary in the Oliv - Cpx - Plag pseudo-ternary, however several of the EOSC lava groups are shifted away from the 1-atm. boundaries toward the Oliv apex.

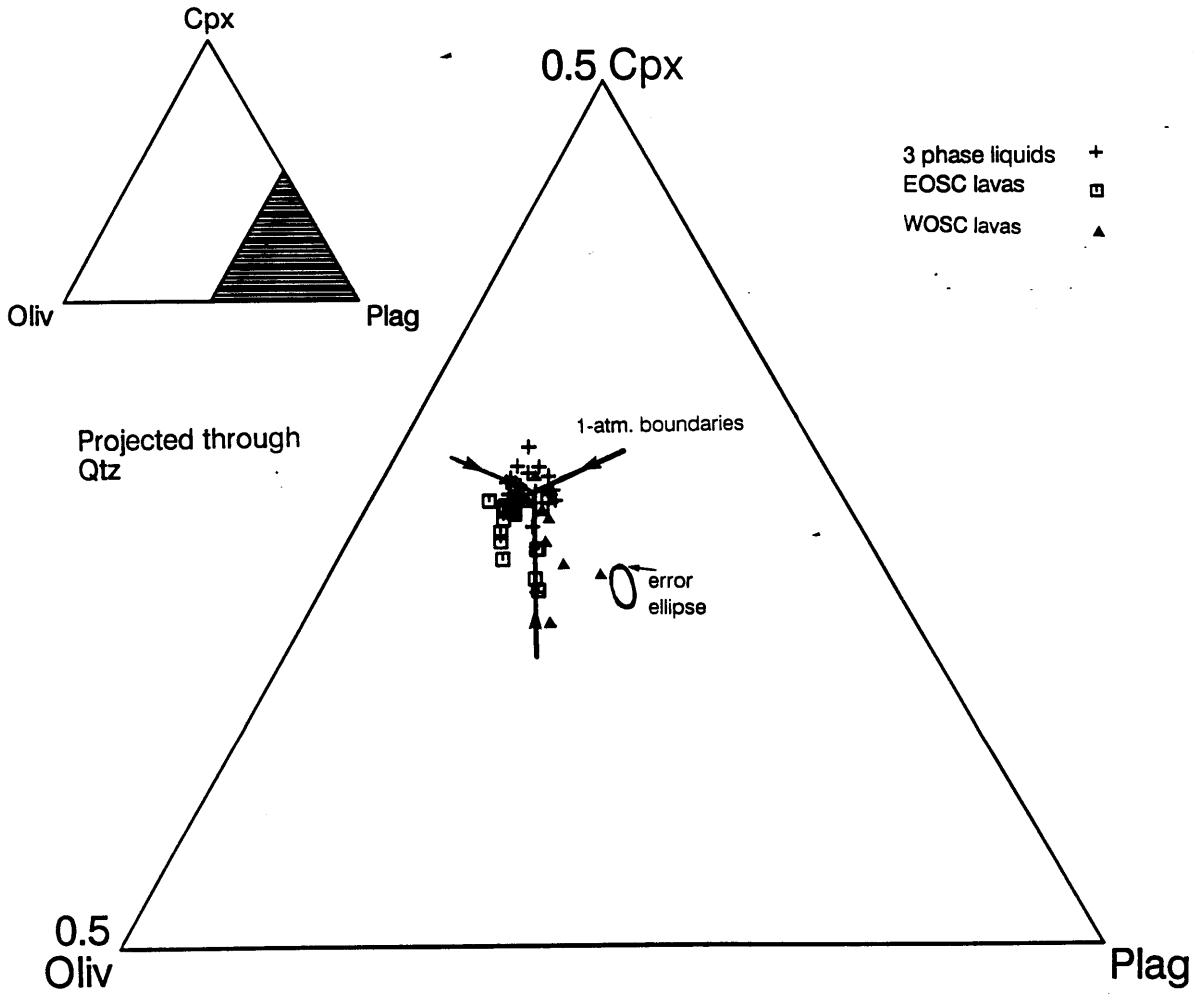
Cpx
Oliv
Plag
Projected through
Qtz
0.5 Cpx
3 phase liquids
EOSC lavas
WOSC lavas
1-atm. boundaries
error
ellipse
0.5
Oliv
Plag

Fig. 2-5 (A) Normalized wt.% CaO vs. wt.% MgO (CaOn vs. MgOn) for lava types sampled at the EOSC (open squares) and WOSC (filled squares, 3 lava types that occur on both rifts are shown as open circles). The pluses are 1-atm. experimentally produced liquids saturated with olivine + plagioclase (wt.% MgO>7.5), and olivine + plagioclase + augite. The lines show 3 shallow level mixing models (Table 7) between parental lava types and liquids along the 1-atm. experimentally determined 4-phase boundary for lava types P3, I and J on the WOSC. Lava type L contains 2 lavas (Table 1 and 2) on the WOSC that are 'E' type MORB similar to MORBs recognized from this portion of the EPR by Thompson et al. (1989), with elevated K_2O and Na_2O.

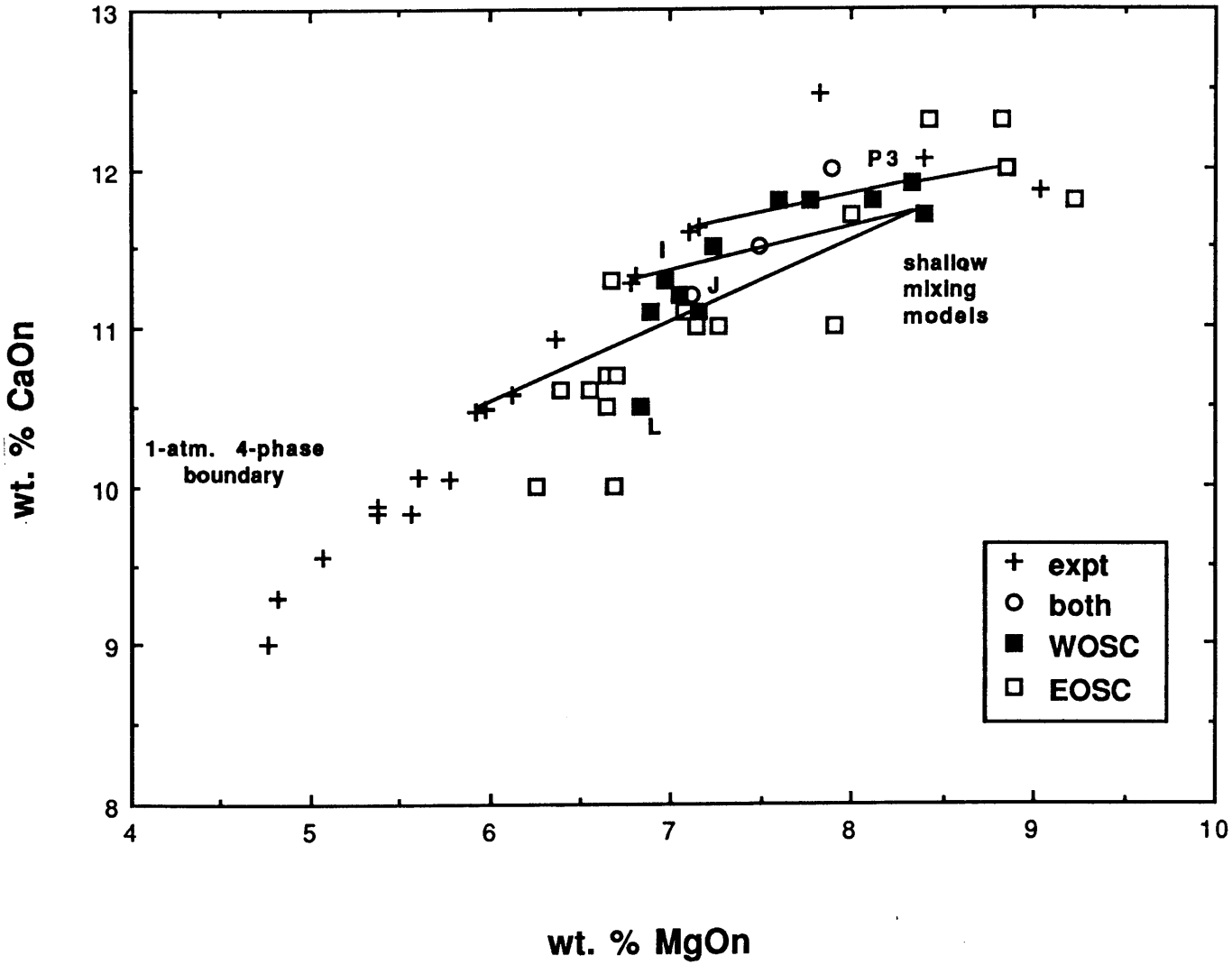
wt. % CaOn
wt. % MgOn
13
12
11
10
9
8
4
5
6
7
8
9
10
P3
I
J
L
shallow
mixing
models
1-atm. 4-phase
boundary
expt
both
WOSC
EOSC

Fig. 2-5 (B) Normalized wt.% FeO vs. wt.% MgO (FeOn vs. MgOn) for lava types sampled at the EOSC (open squares) and WOSC (filled squares, 3 lava types that occur on both rifts are shown as open circles). The pluses are 1-atm. experimentally produced liquids saturated with olivine + plagioclase (wt.% MgO > 7.5), and olivine + plagioclase + augite. The WOSC lava types coincide with the experimentally determined 1-atm. liquids on the olivine + plagioclase and olivine + plagioclase + augite boundaries (with the exception of the enriched L lava type which has lower FeOn than all other lavas and experiments). The arrow drawn through the EOSC lavas indicates an inferred fractionation trend along the same boundaries determined experimentally at 1-atm. but at ~2 kbar pressure (~6 km depth).

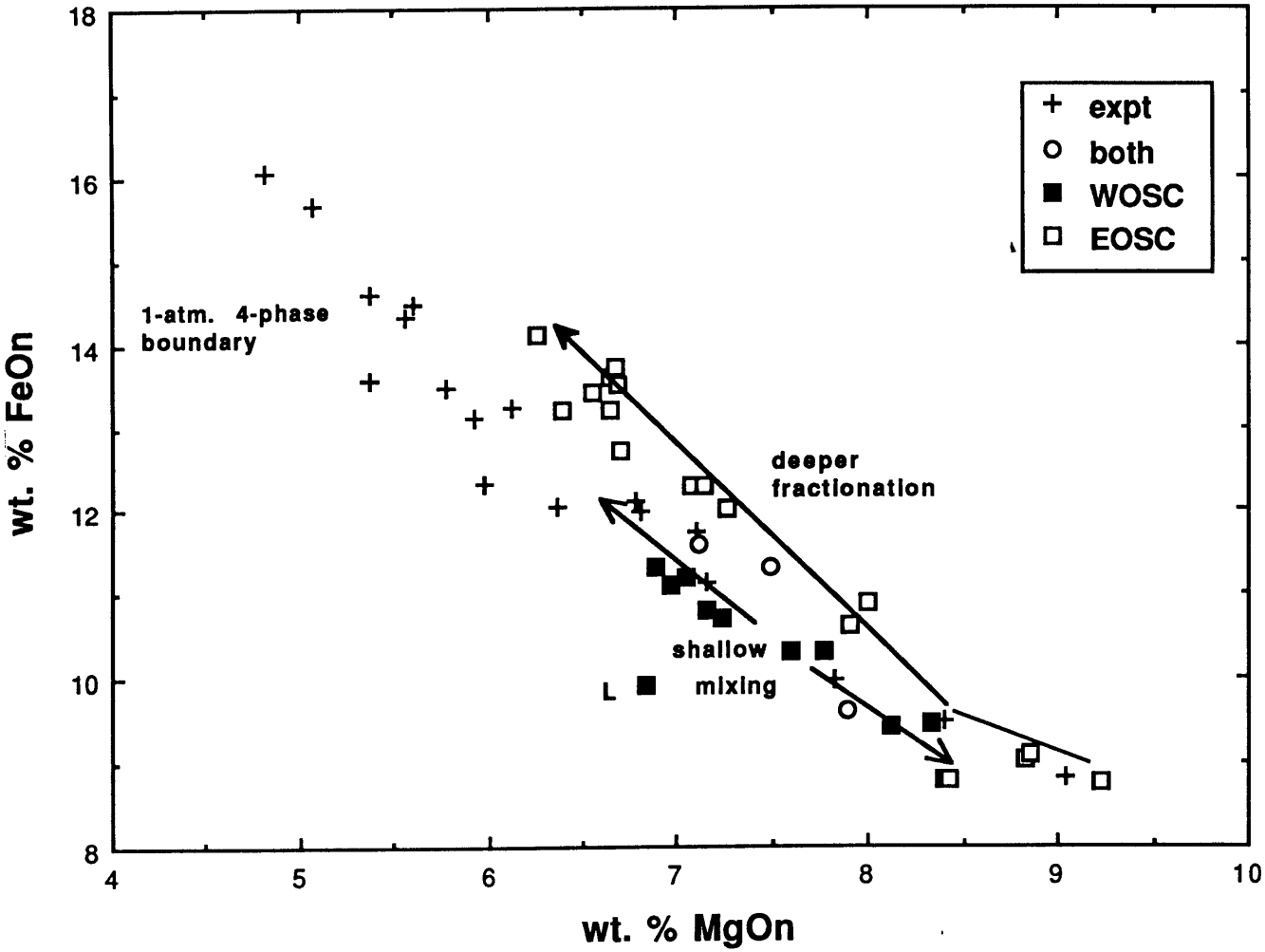
18
16
14
12
10
8
4
5
6
7
8
9
10
wt. % FeOn
wt. % MgOn
expt
both
WOSC
EOSC
1-atm. 4-phase
boundary
deeper
fractionation
shallow
mixing
L

Fig. 2-6 (A) Application of the method of estimating the effect of pressure and composition on the positions of phase boundaries described in Chapter I to 4 of the experimentally produced olivine + plagioclase + augite saturated liquids (4-phase boundary) to infer the effect of increased pressure on the phase boundaries shown in an expanded portion of the projection described in the caption for Fig. 3a. Solid symbols indicate the 1-atm. experimental liquid compositions, open symbols of the same shape indicate the predicted positions for these liquid compositions of the olivine + plagioclase + augite + low-Ca pyroxene + liquid (5-phase) boundaries at 0.001, 2 and 4 kbar. Solid lines connect the 1-atm. olivine + plagioclase + augite saturated liquids with the 1-atm., predicted 5-phase boundaries for each composition. The 1-atm. experiments provide the slope of the 4-phase boundary, and the 5-phase boundary marks the terminus. We have inferred the position of the 4-phase boundary at 2 and 4 kbar by assuming the slope remains the same as that determined experimentally at 1-atm. and fixing the position with the predicted 5-phase boundary.

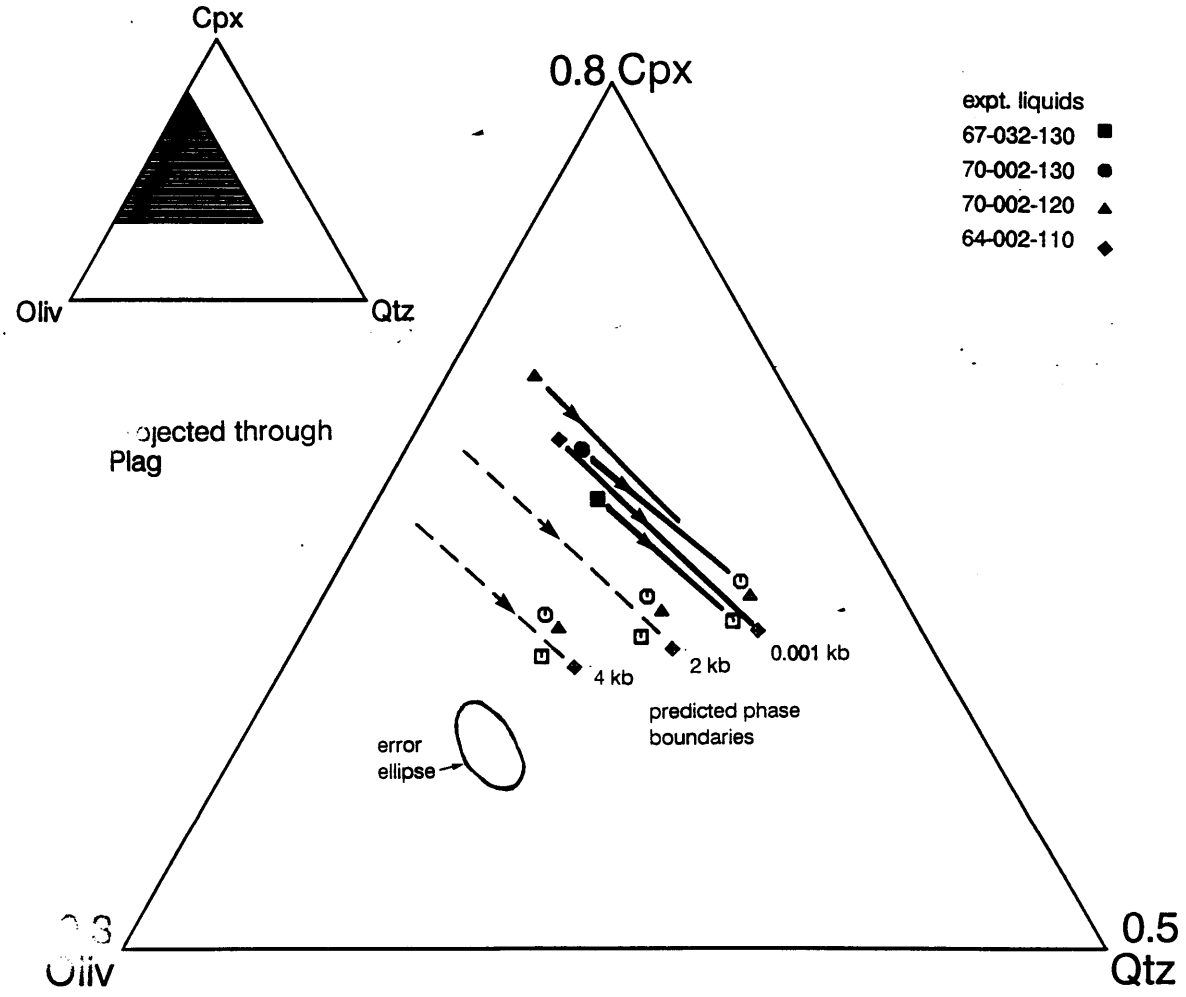
Cpx
Oliv
Qtz
0.8 Cpx
expt. liquids
67-032-130
70-002-130
70-002-120
64-002-110
ojected through
Plag
0.001 kb
2 kb
4 kb
predicted phase
boundaries
error
ellipse
0.5
Qtz

Fig. 2-6 (B) The same estimated boundaries described in the caption for Fig. 6a are shown in an expanded portion of the projection described in the caption for Fig.3b. The close correspondence between the experimentally produced liquids on the 4-phase boundary at 1-atm. and the predicted positions of the 1-atm. 5-phase boundaries for each of the experimental liquid compositions occurs because the 4-phase boundary essentially collapses onto the 5-phase boundary in this projection. Thus, the predicted 5-phase boundary can be used to track the position of the 4-phase boundary in this projection. The topology of the 3-phase boundaries (dashed lines) are inferred. The predicted positions of the 4- and 5- phase boundaries track along the olivine + plagioclase + liquid boundary with increasing pressure, moving towards the Oliv - Plag join.

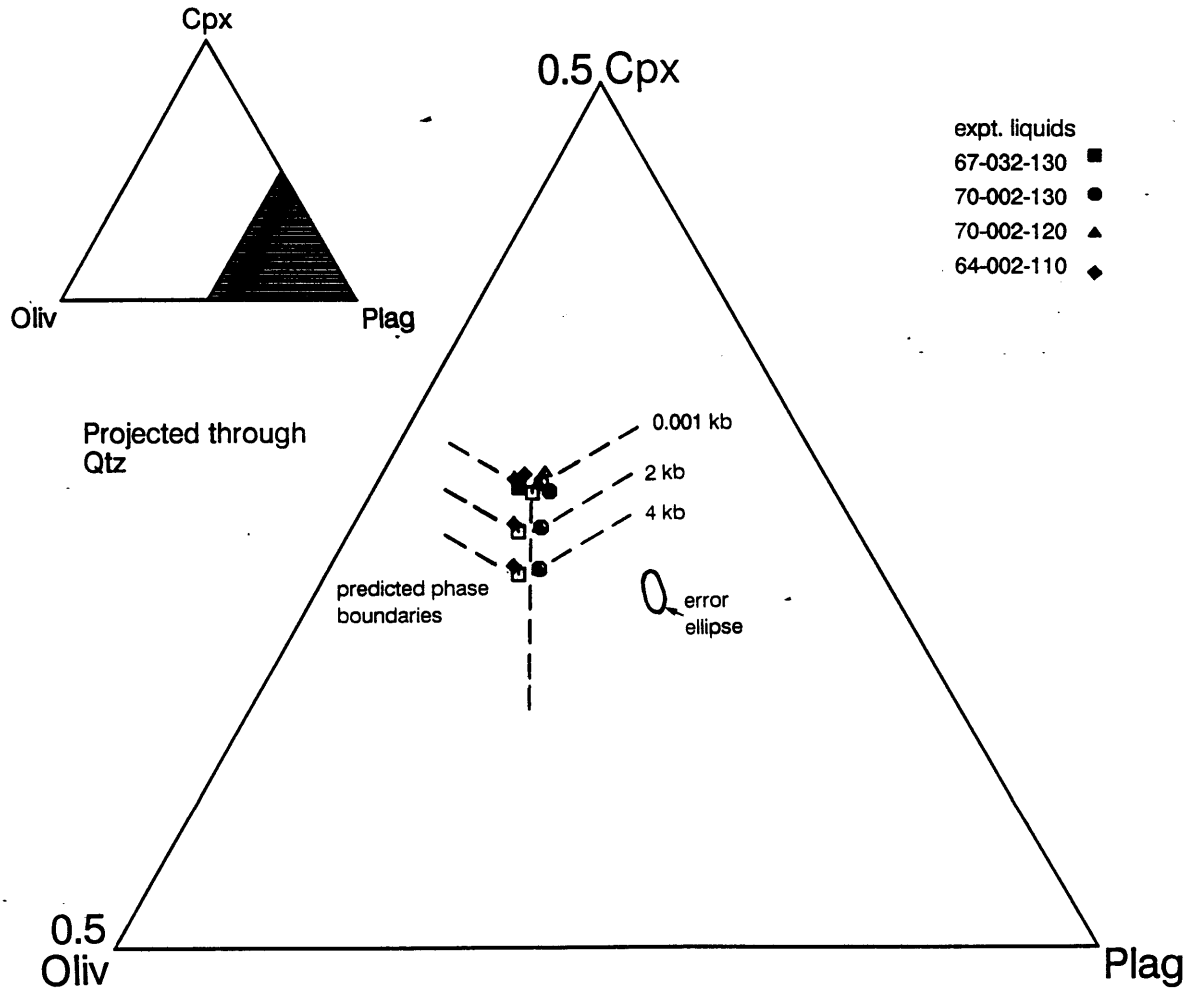
Cpx
Oliv
Plag
0.5 Cpx
0.5 Oliv
Plag
expt. liquids
67-032-130
70-002-130
70-002-120
64-002-110
Projected through Qtz
0.001 kb
2 kb
4 kb
predicted phase boundaries
error ellipse

Fig. 2-7 (A) Application of the method of estimating the effect of pressure and composition on the positions of phase boundaries described in Chapter I to estimate the phase boundaries for 4 of the lava groups from the EOSC (A, B, C and E, Table 2) shown in an expanded portion of the projection described in the caption for Fig. 3a. The solid symbols indicate the lava group compositions (labelled in each projection), open, like symbols indicate the predicted positions of the 5-phase boundary for each of these compositions at 0.001, 2 and 4 kbar. Solid curves in the Oliv - Cpx - Qtz projection (a) show the inferred 0.001, 2 kbar and 4 kbar 4-phase boundaries.

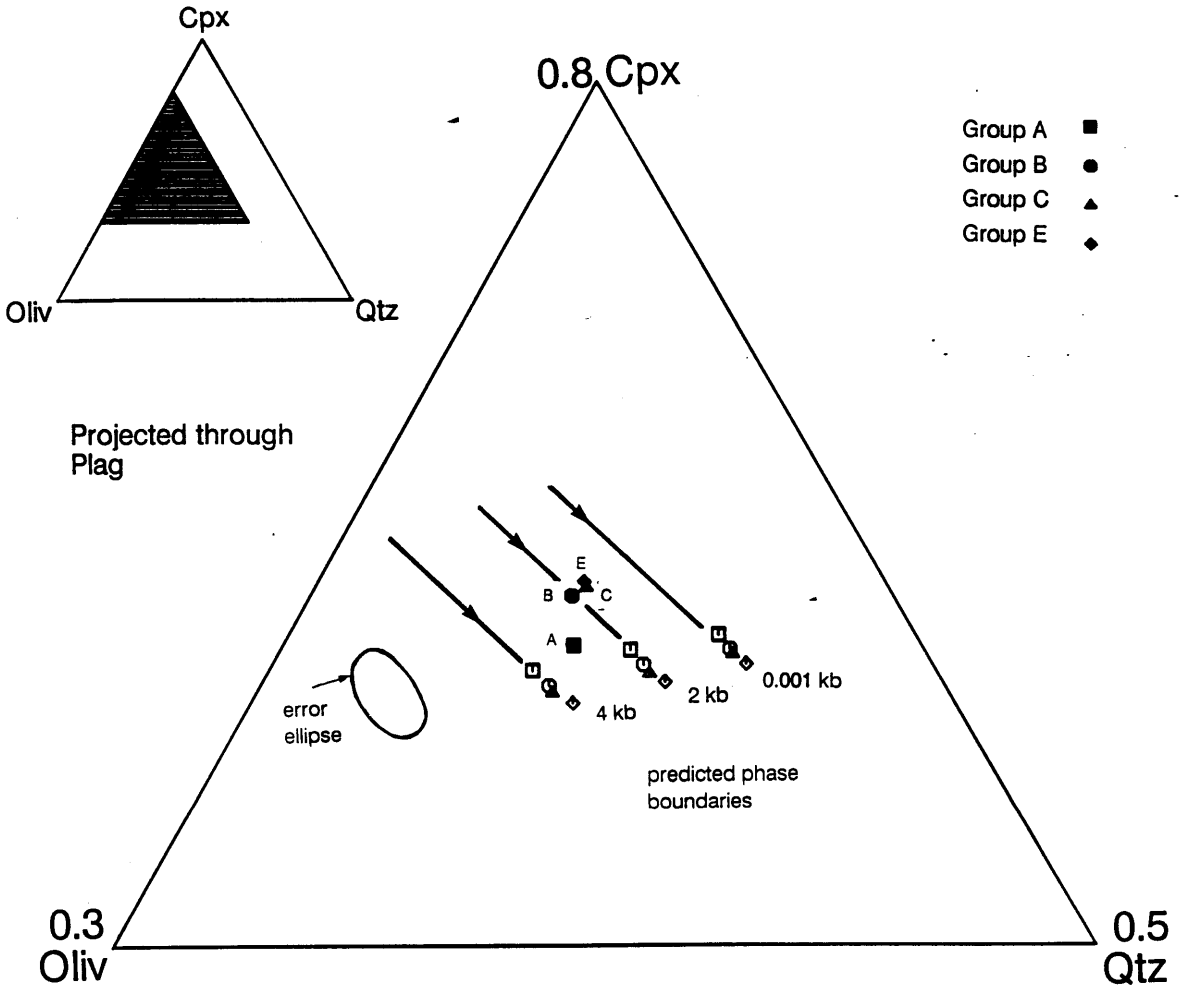
Cpx
Oliv
Qtz
Projected through Plag
0.8 Cpx
Group A
Group B
Group C
Group E
E
B
C
A
0.001 kb
2 kb
4 kb
error ellipse
predicted phase boundaries
0.3 Oliv
0.5 Qtz

Fig. 2-7 (B) As in (A), however the estimated boundaries are shown in an expanded portion of the same projection described in the caption for Fig. 3b. The projected positions of the 4-phase-boundaries are assumed to be the same as the projected positions of the predicted 5-phase boundary. The topology of the 3-phase boundaries (solid curves with arrows) are inferred. The close correspondence between lava groups B, C and E and the predicted 2-kbar, 4-phase boundary in both the Oliv - Cpx - Qtz projection (A) and the Oliv - Cpx - Plag projection (B) suggests that these compositions are olivine + plagioclase + augite saturated at ~2 kbar. Lava group A is shifted to slightly higher pressures (~3 kbar) in both projections.

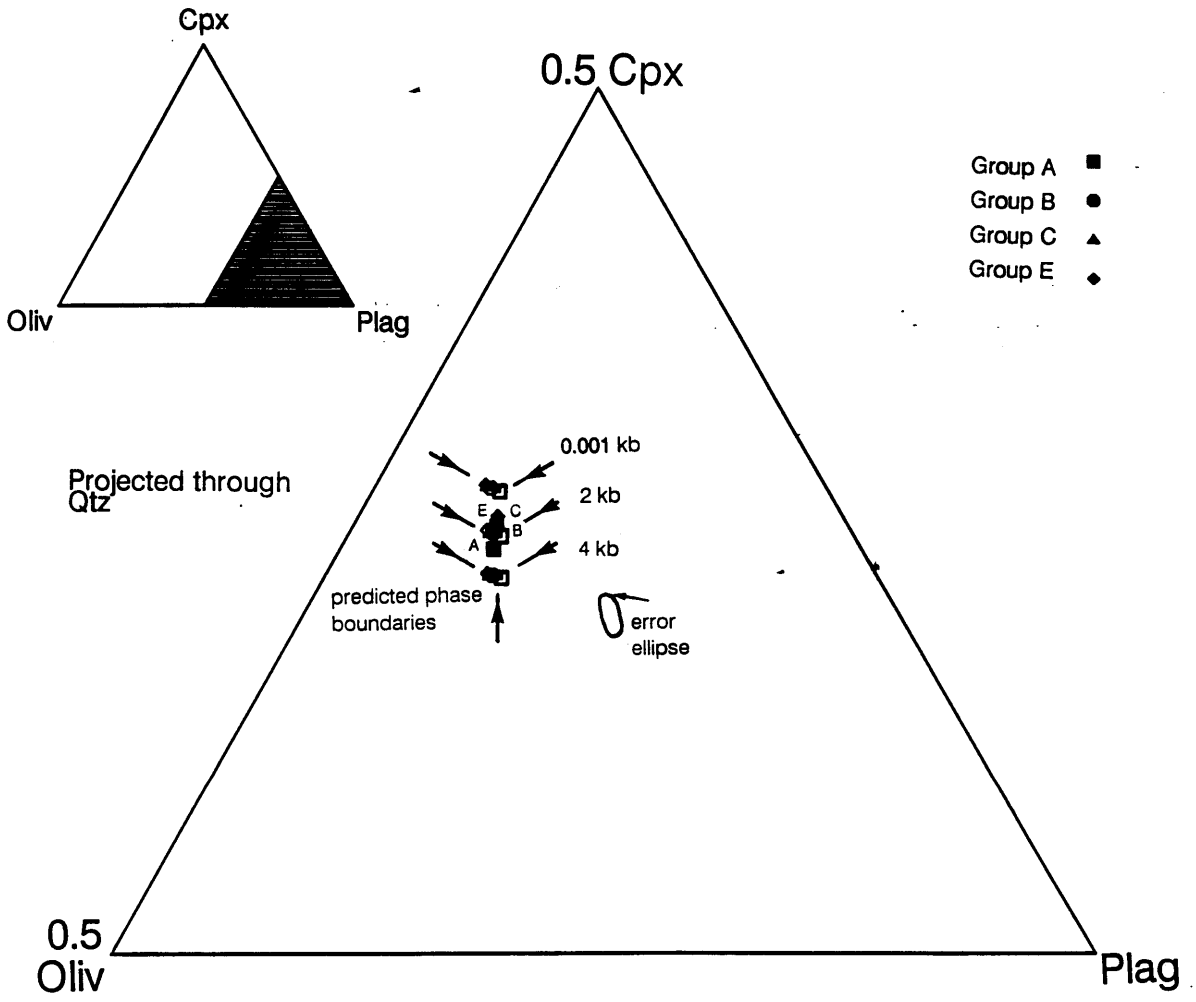
Cpx
Oliv
Plag
0.5 Cpx
0.5
Oliv
Plag
Group A
Group B
Group C
Group E
Projected through
Qtz
0.001 kb
2 kb
4 kb
E
C
B
A
predicted phase
boundaries
error
ellipse

Fig. 2-8 (A) Same construction as in Fig. 7a for 2 lava groups that contain lavas from both the EOSC and the WOSC (H and K, Table 2) shown in an expanded portion of the projection described in the caption for Fig. 3a. The solid symbols indicate the lava group compositions (labelled in each projection), open, like symbols indicate the predicted positions of the 5-phase boundary for lava groups H and K at 0.001, 2 and 4 kbar. These lava groups are inferred to be crystallizing on the 4-phase boundary at ~1 kbar.

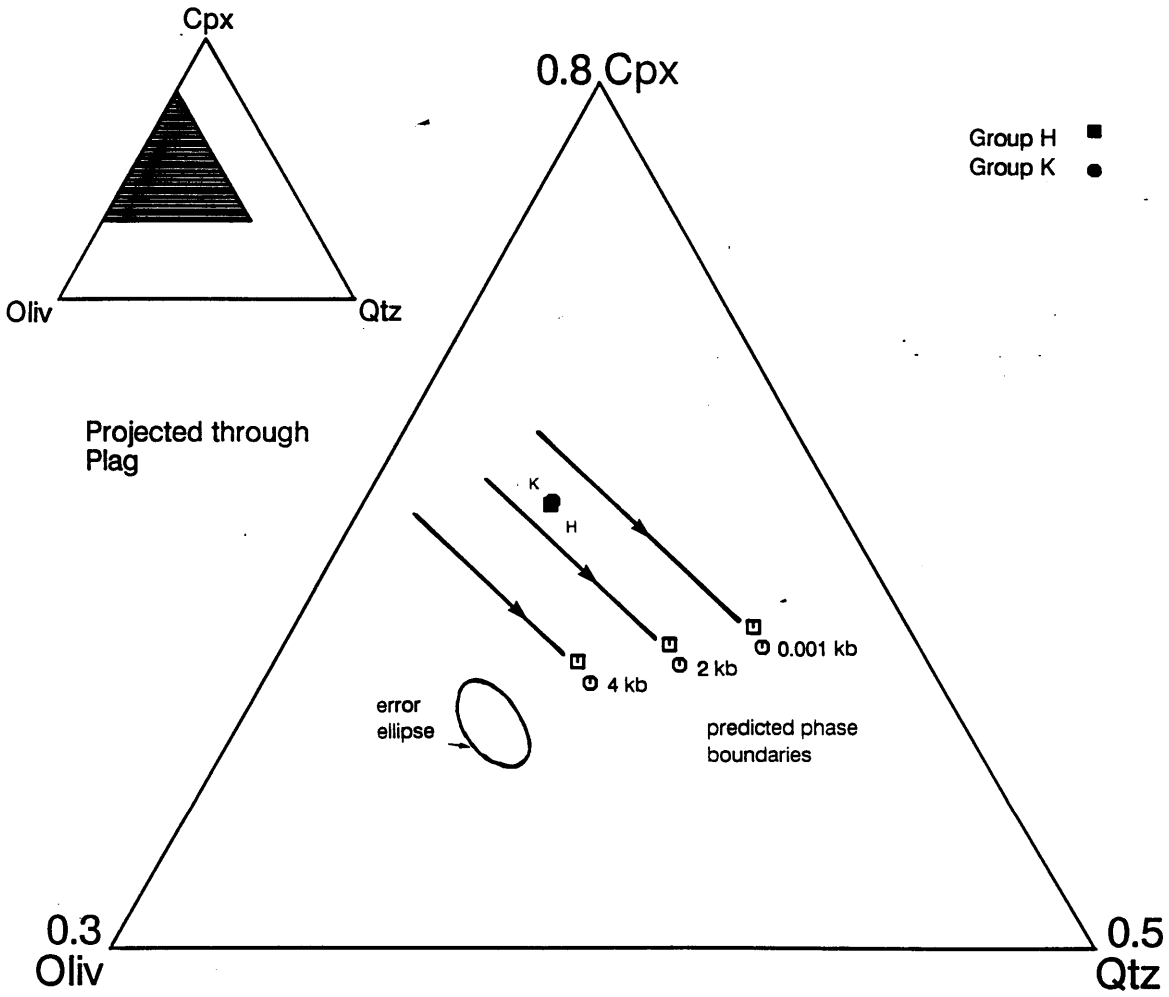
Cpx
Oliv
Qtz
Projected through Plag
0.8 Cpx
Group H
Group K
K
H
0.001 kb
2 kb
4 kb
error ellipse
predicted phase boundaries
0.3 Oliv
0.5 Qtz

Fig. 2-8 (B) Same construction as in Fig. 7b for 2 lava groups that contain lavas from both the EOSC and the WOSC (H and K, Table 2) shown in an expanded portion of the projection described in the caption for Fig. 3b. Symbols as described in the caption for Fig. 8a.

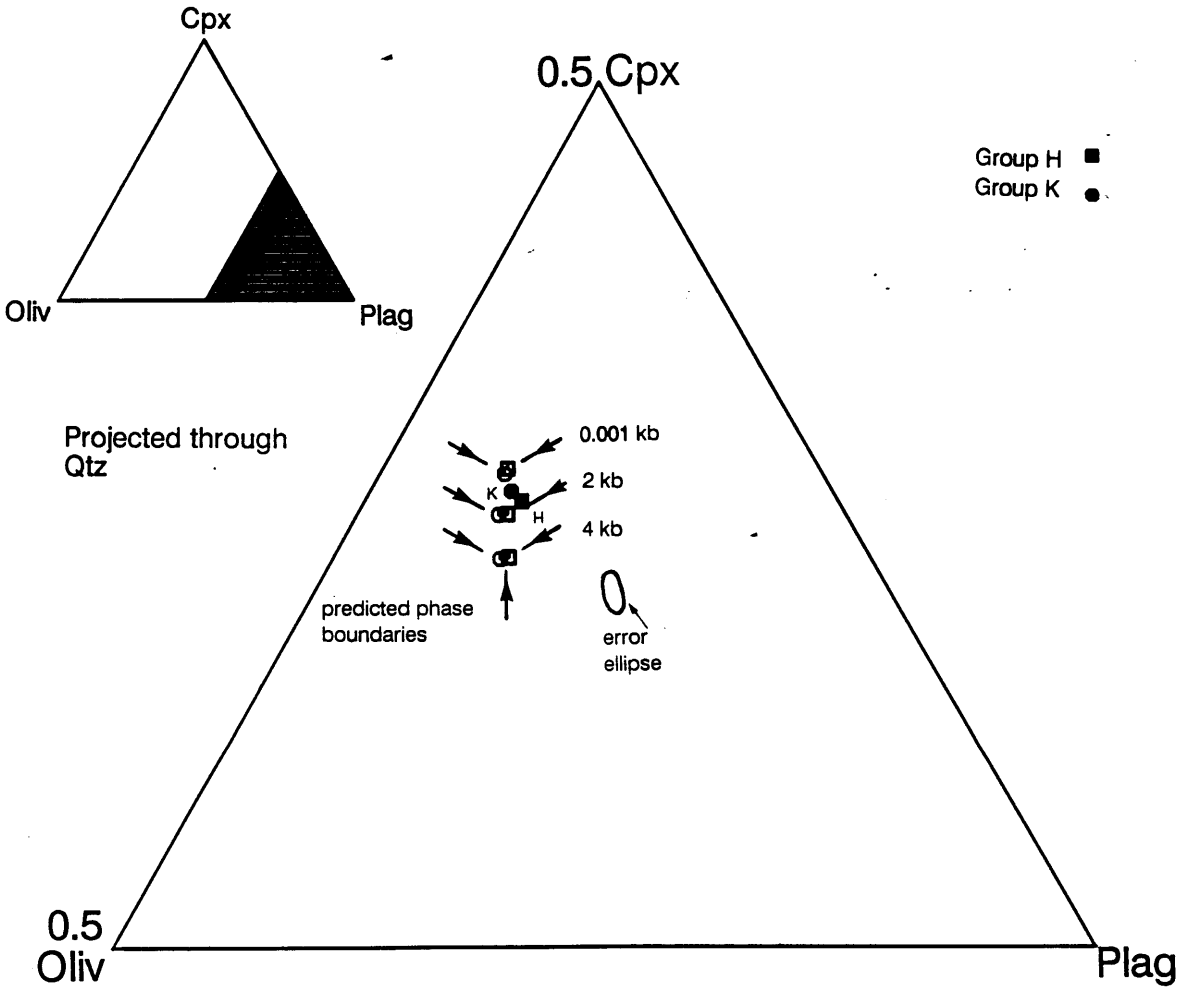
Cpx
Oliv
Plag
Projected through
Qtz
0.5 Cpx
Group H
Group K
0.001 kb
2 kb
4 kb
K
H
predicted phase
boundaries
0
error
ellipse
0.5
Oliv
Plag

Fig. 2-9 (A) Same construction as in Fig. 7a for 2 lava compositions (K18B and K18C, Christie and Sinton, 1986) from the 95.5°W propagating rift at the Galapagos shown in an expanded portion of the projection described in Fig. 3a. The lavas are shown as filled circles, the predicted 5-phase boundaries for these two lavas at 0.001, 2 and 4 kbar are shown as open squares. These inferred phase boundaries suggest that the Galapagos lava compositions are saturated with olivine + plagioclase + augite (+ low-Ca pyroxene?) at ~3 - 4 kbar.

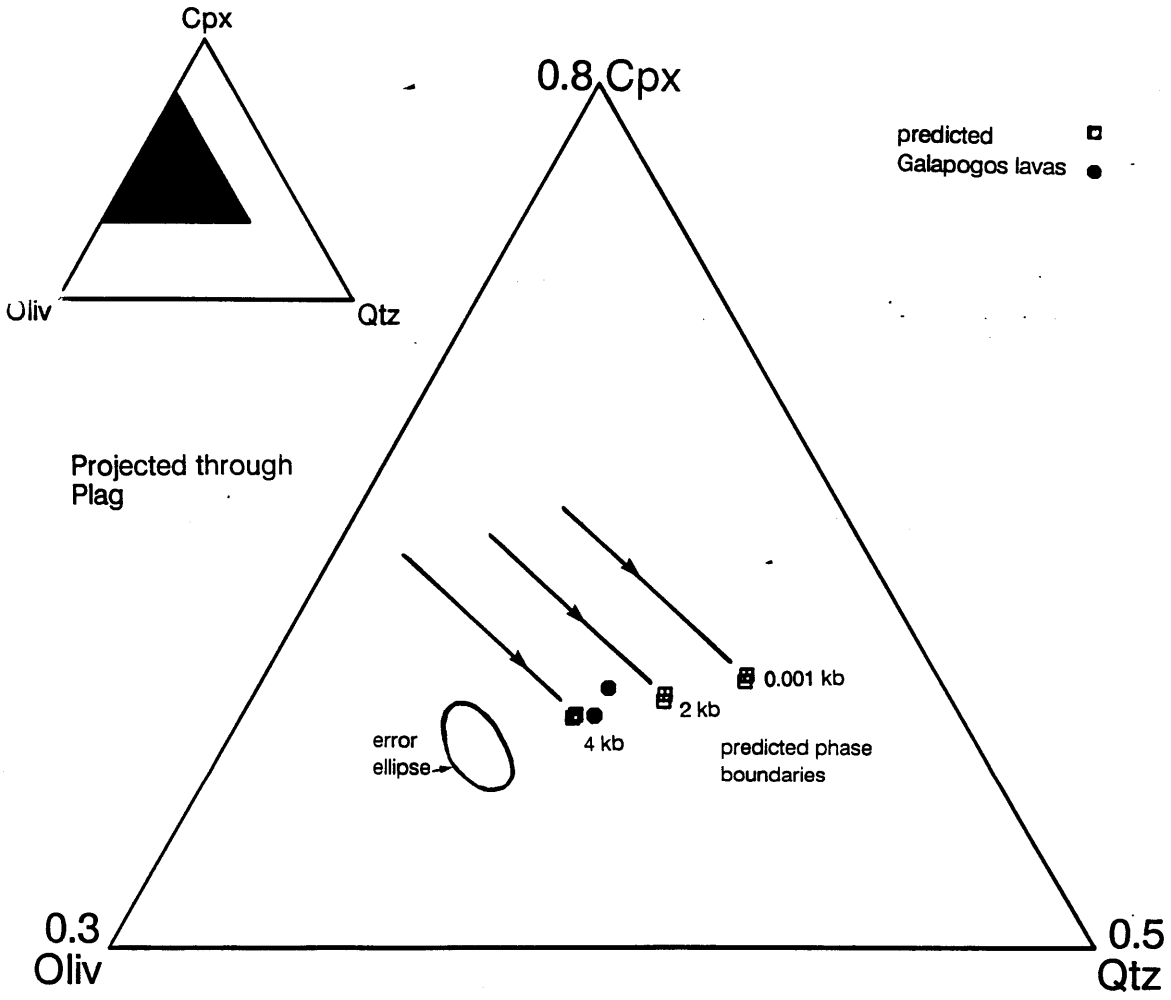
Cpx
Oliv
Qtz
0.8 Cpx
predicted
Galapogos lavas
Projected through
Plag
0.001 kb
2 kb
4 kb
error
ellipse
predicted phase
boundaries
0.3
Oliv
0.5
Qtz

Fig. 2-9 (B) Same construction as in Fig. 7b for 2 lava compositions (K18B and K18C, Christie and Sinton, 1986) from the 95.5°W propagating rift at the Galapagos shown in an expanded portion of the projection described in Fig. 3b. Symbols as described in the caption for Fig. 9a.

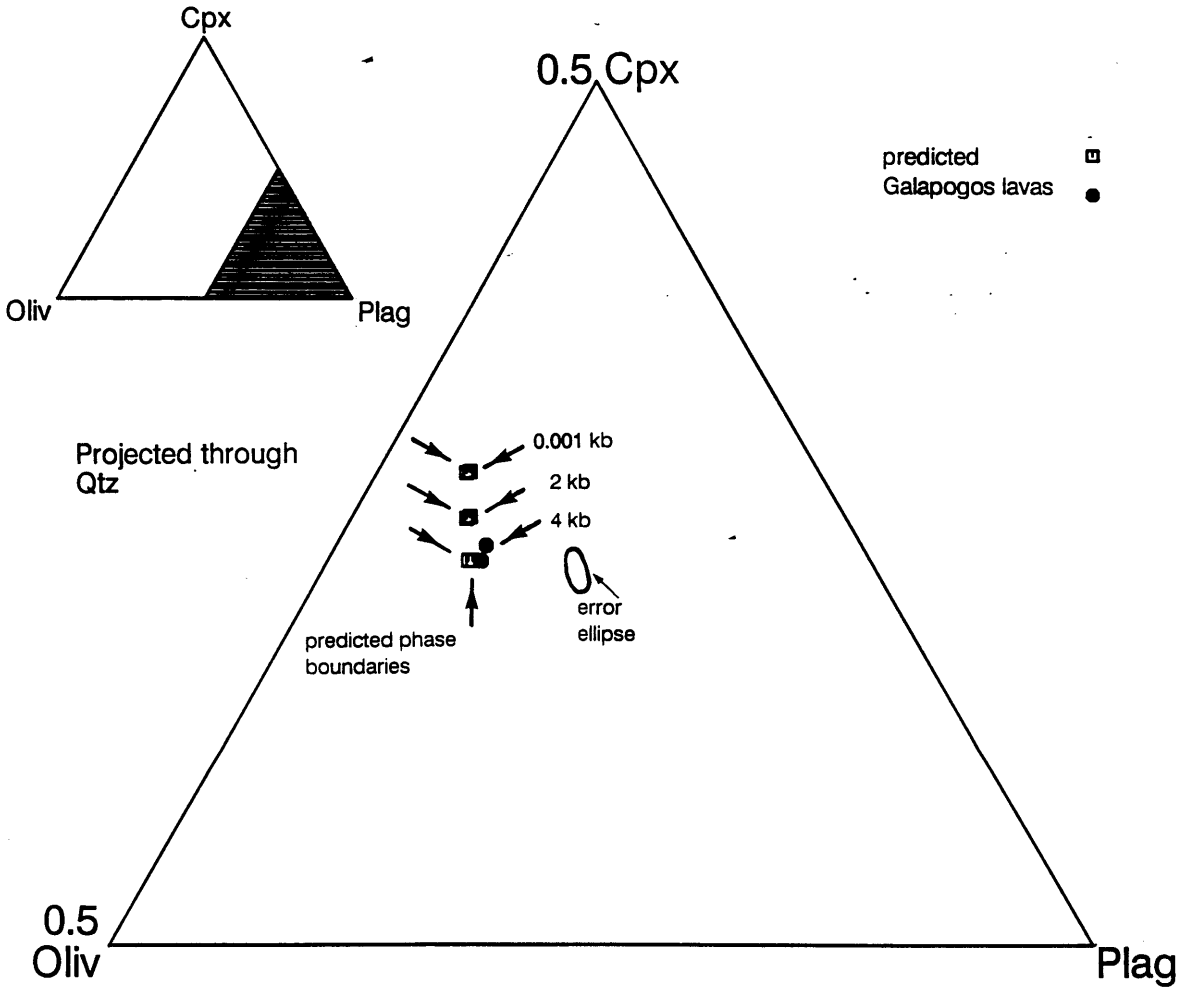
Cpx
Oliv
Plag
0.5 Cpx
predicted
Galapogos lavas
Projected through
Qtz
0.001 kb
2 kb
4 kb
error
ellipse
predicted phase
boundaries
0.5
Oliv
Plag

Fig. 2-10 (A) Normalized FeO/MgO (FeOn/MgOn) of lavas from the EPR up to and including the western rift of the 11°45'N OSC between ~11.2°N and 12°N. Data are from Table 1, Thompson et al. (1989) and the Smithsonian Institution Volcanic Glass File (data from both Thompson et al., 1989, and the Smithsonian Institution Volcanic Glass File were corrected with the factors provided in Table 3, and all analyses were normalized to 100%).

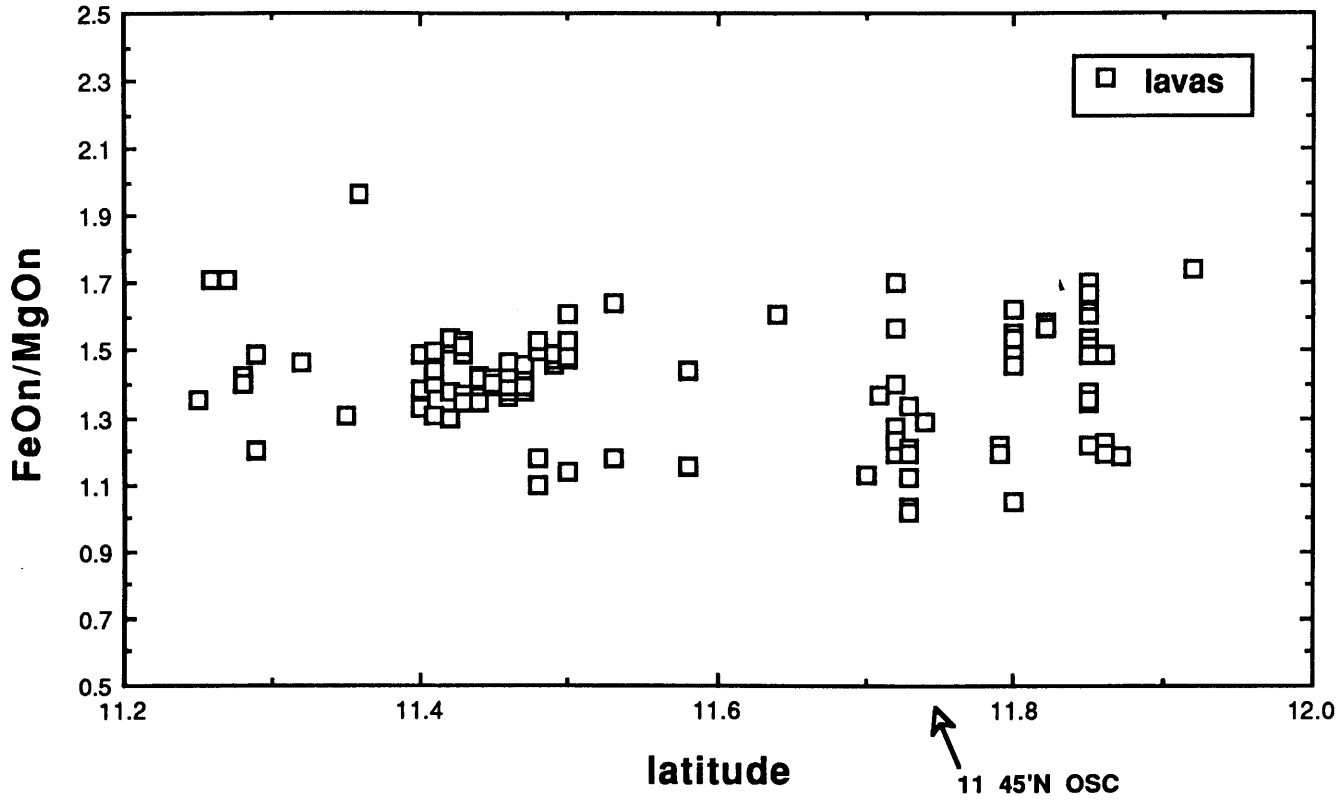
lavas
FeOn/MgOn
2.5
2.3
2.1
1.9
1.7
1.5
1.3
1.1
0.9
0.7
0.5
11.2
11.4
11.6
11.8
12.0
latitude
11 45'N OSC

Fig. 2-10 (B) Normalized FeO/MgO (FeOn/MgOn) of lavas from the eastern rift of the $11^{O}45'$N OSC and the EPR to the north, from ~ 11.75^{O}N - ~ 13^{O}N. Locations of the $12^{O}37'$N and the $12^{O}54'$N OSCs are also shown.

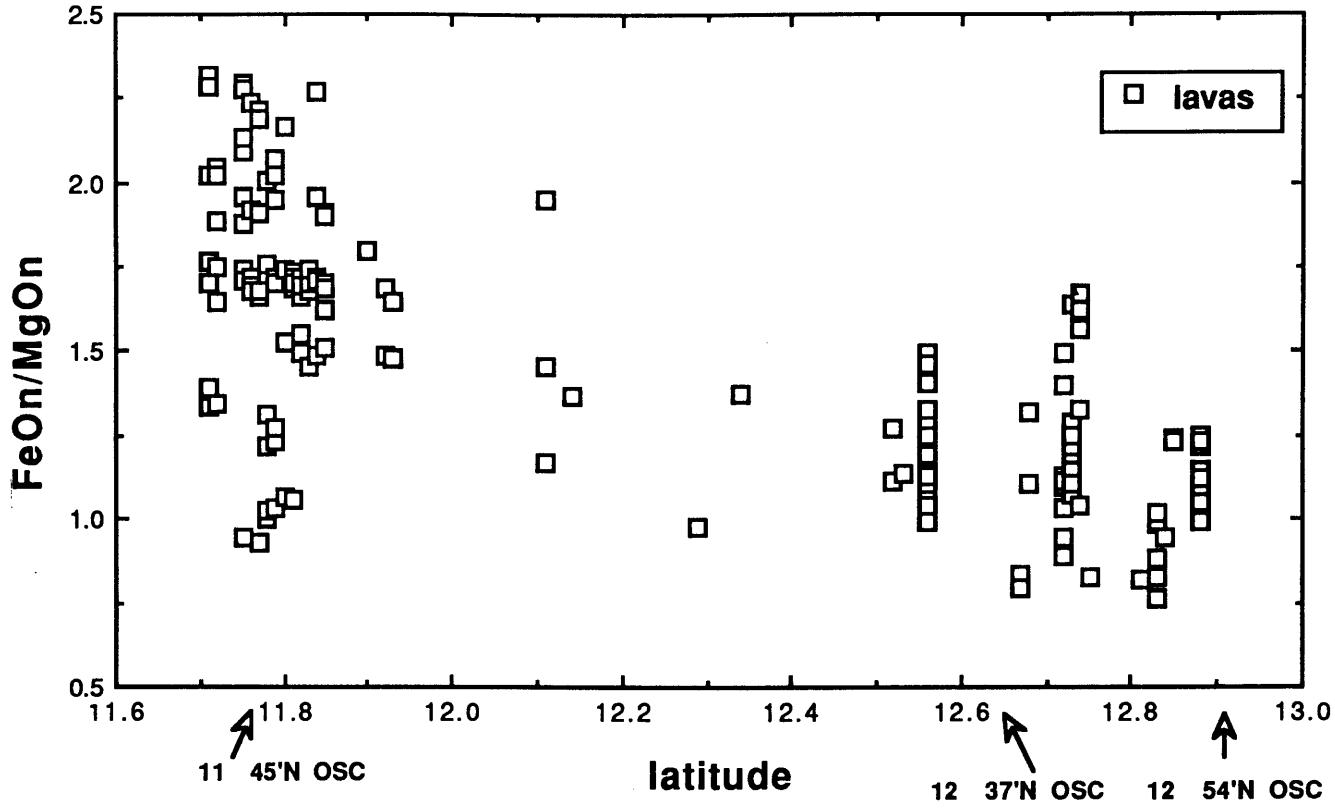
FeOn/MgOn
2.5
2.0
1.5
1.0
0.5
11.6
11.8
12.0
12.2
12.4
12.6
12.8
13.0
latitude
lavas
11 45'N OSC
12 37'N OSC
12 54'N OSC

Table 2-1 Electron microprobe analyses of glasses from the eastern and western rifts of the 11°45'N OSC

Alvin	#	SiO_2	TiO_2	Al_2O_3	FeO[a]	MgO	MnO	CaO	K_2O	Na_2O	P_2O_5	Total	Tag[b]
1997	1-1	50.1(1)[c]	2.02(7)	14.2(1)	11.0(1)	6.83(8)	0.20(3)	10.9(2)	0.23(2)	3.25(13)	0.15(3)	98.83	J
1997	3-1	50.0(2)	1.93(4)	14.4(1)	10.5(2)	6.99(9)	0.17(4)	10.9(1)	0.22(2)	3.09(4)	0.14(4)	98.31	J
1997	4-1	50.1(1)	1.88(5)	14.5(1)	10.2(1)	7.24(10)	0.19(5)	11.0(1)	0.22(2)	3.05(5)	0.14(2)	98.81	J
1997	5-1	50.1(2)	1.91(5)	14.5(2)	10.3(1)	7.24(10)	0.17(5)	11.0(1)	0.23(2)	3.09(9)	0.13(2)	98.65	J
1997	6-1	49.4(1)	1.46(4)	16.0(1)	8.68(11)	8.29(8)	0.14(5)	11.6(1)	0.21(2)	2.98(12)	0.09(3)	98.92	P4
1997	7-1	50.0(1)	1.97(4)	14.1(1)	10.8(1)	6.90(3)	0.20(4)	10.8(2)	0.21(1)	3.20(2)	0.14(4)	98.35	J
1997	7-2	50.0(2)	1.99(3)	14.1(1)	10.8(1)	6.90(6)	0.22(4)	10.9(1)	0.21(1)	3.08(8)	0.15(5)	98.26	J
1997	9-1	49.9(1)	1.99(5)	14.2(1)	10.6(1)	6.97(5)	0.20(6)	10.9(1)	0.22(1)	3.16(10)	0.14(4)	98.28	J
1998	2-1	49.0(2)	2.09(6)	15.9(1)	9.33(10)	6.99(5)	0.14(4)	10.3(1)	0.71(3)	3.47(10)	0.26(4)	98.13	L
1998	4-1	49.4(1)	2.34(4)	15.0(1)	10.1(1)	6.39(8)	0.16(4)	10.3(1)	0.74(2)	3.56(11)	0.30(3)	98.23	L
1998	6-1	50.1(2)	1.57(8)	14.7(1)	9.56(10)	7.73(9)	0.18(2)	11.7(1)	0.14(2)	3.04(9)	0.08(5)	97.82	N
1998	7-1	49.9(2)	1.47(9)	15.1(1)	9.28(27)	8.03(11)	0.20(3)	11.6(2)	0.15(2)	2.93(9)	0.08(3)	98.79	P2
1998	9-1	50.1(2)	1.29(4)	15.2(2)	8.66(8)	8.29(6)	0.15(3)	12.1(1)	0.19(2)	2.61(9)	0.06(3)	98.66	P5
1998	10-1	49.9(2)	1.52(5)	15.0(1)	9.30(9)	7.96(8)	0.17(3)	11.6(1)	0.17(1)	2.91(13)	0.15(3)	98.73	P2
1998	11-1	50.2(1)	1.59(3)	14.7(1)	9.54(13)	7.73(6)	0.13(6)	11.6(2)	0.18(2)	2.97(10)	0.14(4)	98.78	N
1999	2-1	50.1(1)	1.84(10)	13.6(2)	11.2(4)	7.23(16)	0.23(4)	11.1(3)	0.11(2)	2.61(8)	0.13(4)	98.24	K
1999	3-2	50.2(1)	2.03(4)	13.4(1)	11.9(1)	7.00(8)	0.23(2)	10.8(1)	0.12(2)	2.63(10)	0.14(4)	98.46	E
1999	6-1	50.1(1)	2.24(4)	13.2(1)	12.5(1)	6.57(6)	0.18(5)	10.4(1)	0.15(1)	2.78(10)	0.19(3)	98.25	D
1999	7-1	50.1(1)	2.22(7)	13.1(1)	12.5(2)	6.56(9)	0.18(8)	10.5(1)	0.15(1)	2.84(5)	0.15(4)	98.18	D
1999	8-1	50.2(1)	2.05(8)	13.4(1)	11.8(2)	6.98(9)	0.22(4)	10.8(1)	0.12(2)	2.67(7)	0.16(4)	98.19	F
2000	2-2	50.0(1)	2.05(7)	13.8(1)	11.1(1)	6.75(10)	0.17(5)	10.9(1)	0.27(2)	3.19(10)	0.16(4)	98.35	T
2000	4-2	50.0(2)	1.93(4)	14.4(1)	10.5(2)	6.99(9)	0.17(4)	10.9(1)	0.22(2)	3.09(6)	0.14(5)	98.31	J
2000	5-1	50.4(1)	1.55(4)	14.0(1)	10.0(2)	7.50(10)	0.21(3)	11.7(1)	0.12(1)	2.92(7)	0.09(2)	98.47	M
2000	6-1	50.5(2)	1.54(5)	14.0(3)	10.2(1)	7.47(4)	0.17(3)	11.6(1)	0.12(2)	2.95(9)	0.08(3)	98.63	M
2000	7-1	50.3(2)	1.71(3)	13.8(1)	10.7(1)	7.09(10)	0.18(5)	11.1(1)	0.14(1)	3.05(10)	0.08(3)	98.11	K
2000	8-1	50.3(2)	1.57(4)	14.1(1)	10.1(1)	7.44(5)	0.18(4)	11.5(1)	0.12(1)	2.93(10)	0.07(2)	98.29	M
2000	9-1	49.9(2)	1.57(3)	14.6(1)	9.45(10)	7.62(10)	0.16(7)	11.7(1)	0.18(1)	2.99(9)	0.10(3)	98.28	N
2000	10-1	49.9(1)	1.54(3)	14.7(1)	9.38(8)	7.80(8)	0.16(3)	11.8(1)	0.17(2)	3.01(7)	0.09(5)	98.50	N
2000	10-2	49.9(1)	1.55(5)	14.6(1)	9.39(14)	7.72(7)	0.17(5)	11.8(1)	0.16(1)	3.01(9)	0.07(3)	98.33	N
2000	11-1	50.0(1)	1.50(2)	14.7(1)	9.33(15)	7.78(6)	0.14(2)	11.8(1)	0.16(1)	3.02(6)	0.07(4)	98.50	N
2001	1-1	49.8(2)	2.07(8)	13.3(1)	12.0(2)	6.96(11)	0.21(3)	10.7(1)	0.12(2)	2.94(10)	0.15(3)	97.66	S
2001	3-1	50.0(1)	2.02(3)	13.3(1)	12.2(1)	6.97(10)	0.23(2)	10.7(1)	0.12(1)	2.66(10)	0.13(4)	98.44	E
2001	3-2	49.9(2)	2.02(3)	13.4(1)	12.0(2)	7.00(8)	0.22(1)	10.8(1)	0.11(2)	2.66(10)	0.14(4)	98.10	F
2001	4-1	50.1(2)	2.00(5)	13.4(1)	12.0(2)	6.95(6)	0.24(3)	10.9(1)	0.11(1)	2.65(11)	0.07(3)	98.46	E
2001	5-1	50.1(1)	2.01(7)	13.4(1)	12.0(1)	6.95(5)	0.25(3)	10.8(1)	0.11(1)	2.72(16)	0.10(6)	98.47	E
2001	7-1	50.1(1)	1.99(5)	13.4(1)	12.0(2)	6.97(9)	0.23(2)	10.8(1)	0.10(1)	2.65(9)	0.10(3)	98.31	F
2001	7-2	50.0(2)	2.03(6)	13.4(1)	12.0(2)	6.90(4)	0.27(3)	10.9(1)	0.11(1)	2.70(2)	0.07(2)	98.44	F
2001	8-1	50.1(1)	1.98(5)	13.4(1)	12.0(1)	6.94(7)	0.27(4)	10.9(1)	0.11(1)	2.64(16)	0.09(3)	98.48	F
2001	thr	50.1(2)	1.75(6)	13.8(1)	11.2(2)	7.21(11)	0.23(3)	11.3(1)	0.10(1)	2.71(16)	0.06(5)	98.52	K
2002	1-1	49.3(1)	1.90(5)	14.9(1)	10.5(1)	7.76(9)	0.22(3)	10.8(1)	0.20(2)	2.72(8)	0.14(4)	98.36	O
2002	2-1	49.3(1)	1.90(3)	15.0(1)	10.4(2)	7.75(6)	0.22(4)	10.8(1)	0.20(1)	2.74(14)	0.13(4)	98.46	O
2002	3-1	49.2(2)	1.91(3)	15.0(1)	10.4(1)	7.74(9)	0.24(3)	10.8(1)	0.20(2)	2.75(14)	0.10(4)	98.45	O
2002	5-1	49.6(2)	2.63(7)	12.7(1)	13.9(1)	6.09(6)	0.26(4)	9.78(9)	0.17(1)	2.90(16)	0.15(2)	98.13	A
2002	6-1	50.0(1)	2.03(4)	13.4(1)	12.1(1)	6.93(7)	0.24(3)	10.8(1)	0.11(1)	2.56(14)	0.09(2)	98.23	F
2002	6-3	49.5(2)	2.63(4)	12.6(1)	13.9(1)	6.10(5)	0.28(3)	9.73(13)	0.17(2)	2.83(8)	0.18(4)	97.99	A
2002	7-1	50.0(2)	2.03(5)	13.4(1)	12.2(1)	6.91(6)	0.23(3)	10.7(1)	0.11(2)	2.65(7)	0.10(3)	98.22	F
2002	8-1	49.7(1)	2.61(4)	13.0(2)	13.2(1)	6.47(5)	0.15(4)	10.2(2)	0.14(2)	2.85(14)	0.20(3)	98.50	A

Table 2-1 (cont.)

Alvin #	SiO_2	TiO_2	Al_2O_3	FeO[a]	MgO	MnO	CaO	K_2O	Na_2O	P_2O_5	Total	Tag[b]
2002 9-1	50.5(2)	1.56(4)	13.9(1)	10.8(1)	7.87(4)	0.10(4)	11.5(1)	0.12(1)	2.24(16)	0.07(4)	98.65	U
2002 10-1	49.9(1)	2.08(7)	13.7(1)	11.6(1)	7.17(11)	0.13(7)	11.0(1)	0.11(1)	3.02(13)	0.13(4)	98.89	H
2002 12-2	49.9(1)	2.37(4)	13.0(1)	13.1(1)	6.48(10)	0.15(5)	10.4(1)	0.13(1)	2.95(9)	0.15(4)	98.70	C
2003 2-1	50.1(2)	1.82(7)	13.7(1)	11.4(1)	7.45(6)	0.12(5)	11.3(1)	0.08(3)	2.76(10)	0.09(2)	99.63	K
2003 4-1	49.7(1)	2.67(5)	13.2(1)	13.2(2)	6.57(9)	0.16(6)	9.83(17)	0.20(2)	2.81(9)	0.21(2)	98.53	R
2003 5-1	50.2(2)	2.08(3)	13.4(1)	12.1(3)	7.02(7)	0.13(6)	10.9(1)	0.10(3)	2.65(13)	0.11(3)	97.95	F
2003 6-1	49.5(3)	1.25(4)	15.8(1)	9.00(8)	8.77(6)	0.10(4)	11.9(1)	0.11(2)	2.77(5)	0.02(1)	99.22	P6
2003 8-1	50.3(1)	2.06(4)	13.5(1)	12.2(2)	6.92(8)	0.10(5)	10.9(1)	0.10(2)	2.65(13)	0.10(5)	98.83	F
2004 2-1	49.9(2)	2.57(8)	12.8(1)	14.0(2)	6.20(8)	0.17(5)	9.77(4)	0.18(2)	2.87(13)	0.21(5)	98.68	A
2004 3-1	49.1(2)	1.19(2)	16.3(1)	8.65(9)	9.13(5)	0.09(5)	11.7(2)	0.10(1)	2.66(14)	0.04(2)	98.99	P7
2004 3-2	50.1(1)	2.07(7)	13.5(1)	12.3(1)	7.10(7)	0.10(7)	10.9(1)	0.11(1)	2.73(1)	0.11(5)	99.01	F
2004 4-1	49.8(2)	2.61(4)	12.8(1)	14.0(1)	6.20(7)	0.17(6)	9.77(8)	0.18(2)	2.91(12)	0.16(3)	98.64	A
2004 5-1	49.9(1)	2.29(3)	13.0(1)	12.8(1)	6.53(6)	0.22(5)	10.4(1)	0.09(1)	2.68(15)	0.17(4)	98.05	C
2004 6-1	50.0(1)	2.03(4)	13.5(1)	12.1(1)	6.87(7)	0.22(3)	10.9(1)	0.08(1)	2.61(10)	0.09(1)	98.31	F
2004 7-2	49.6(2)	2.57(4)	12.7(1)	13.9(1)	6.02(10)	0.23(3)	9.75(15)	0.14(3)	2.84(17)	0.21(4)	97.90	A
2004 8-1	49.8(2)	1.99(4)	13.5(1)	12.1(2)	6.96(5)	0.19(3)	10.9(1)	0.05(4)	2.64(20)	0.12(2)	98.21	F
2004 9-1	49.7(1)	2.23(4)	13.1(1)	12.8(2)	6.53(8)	0.21(3)	10.5(2)	0.09(2)	2.68(12)	0.17()	98.05	C
2004 9-2	49.9(1)	2.00(5)	13.4(1)	11.9(2)	6.95(10)	0.22(2)	10.9(1)	0.07(1)	2.65(15)	0.12(4)	98.14	F
2004 10-1	50.0(2)	2.01(5)	13.4(1)	12.0(1)	6.94(2)	0.21(3)	10.9(1)	0.06(3)	2.61(7)	0.12(3)	98.28	F
2004 11-1	50.0(2)	1.98(4)	13.4(1)	12.0(1)	6.90(6)	0.20(2)	10.9(1)	0.07(3)	2.60(11)	0.12(3)	98.13	F
2004 12-1	49.8(2)	2.57(5)	12.8(1)	14.0(2)	6.04(4)	0.24(5)	9.88(9)	0.14(1)	2.80(13)	0.17(5)	98.33	A
2004 12-2	49.9(2)	2.04(1)	13.4(4)	12.0(1)	6.92(8)	0.19(2)	10.8(1)	0.06(2)	2.59(9)	0.13(3)	98.10	F
Dr-20 2	49.9(3)	1.76(3)	13.9(1)	11.0(2)	7.46(10)	0.13(3)	11.4(1)	0.09(2)	2.71(9)	0.09((4)	98.44	K
Dr-20 3	49.8(1)	1.75(4)	13.8(1)	11.0(1)	7.43(7)	0.11(6)	11.4(1)	0.10(2)	2.66(11)	0.08(5)	98.13	K
Dr-20 6	49.8(3)	1.76(2)	13.8(1)	11.0(1)	7.44(10)	0.10(5)	11.3(1)	0.09(1)	2.65(9)	0.08(3)	98.01	K
Dr-20 8	49.9(2)	1.93(6)	13.5(1)	11.7(2)	7.12(12)	0.13(3)	10.8(1)	0.09(2)	2.86(11)	0.09(3)	98.12	G
Dr-20 9	50.1(2)	1.94(5)	13.5(1)	11.8(1)	7.16(7)	0.16(2)	10.8(2)	0.09(2)	2.82(14)	0.11(4)	98.48	G
Dr-20 15	50.0(2)	1.77(3)	13.9(1)	11.1(1)	7.53(10)	0.14(4)	11.3(1)	0.11(1)	2.78(15)	0.10(5)	98.73	K
Dr-20 33	50.0(2)	1.98(6)	13.5(1)	11.9(1)	7.13(9)	0.11(4)	10.9(1)	0.09(3)	2.90(9)	0.10(3)	98.61	G
Dr-20 34	49.8(1)	1.79(5)	13.8(6)	11.0(1)	7.45(7)	0.11(4)	11.2(2)	0.09(1)	2.76(11)	0.08(3)	98.08	K
Dr-19 1	49.9(2)	2.05(3)	13.4(1)	12.2(1)	6.75(5)	0.21(3)	10.7(1)	0.06(2)	2.65(15)	0.13(4)	98.05	E
Dr-19 7	50.0(2)	2.05(4)	13.4(1)	12.2(1)	6.75(11)	0.22(5)	10.7(1)	0.08(2)	2.68(9)	0.11(5)	98.19	E
Dr-19 9	50.0(1)	2.07(6)	13.4(1)	12.3(1)	6.75(7)	0.21(5)	10.7(1)	0.07(1)	2.60(12)	0.12(2)	98.22	E
Dr-19 15	49.9(3)	2.07(7)	13.3(1)	12.1(1)	6.76(6)	0.22(3)	10.6(1)	0.08(2)	2.56(12)	0.14(2)	97.73	E
Dr-19 16	49.7(1)	2.03(12)	13.4(2)	12.1(2)	6.92(9)	0.13(6)	10.7(2)	0.11(2)	2.60(4)	0.14(3)	97.83	E

[a] total Fe as FeO

[b] Tag refers to chemical group to which the glass belongs

[c] each composition represents the average of 7 replicate analyses; parentheses represent 1 standard deviation of the sample in terms of least units cited, thus 50.1(1) should be read as 50.1+/-0.1

Table 2-2 Chemical groups described by glasses from the 11°45'N OSC reported in Table 1 and Thompson et al. (1989), locations shown in Figure 1

Group	n[a]	SiO_2n	TiO_2n	Al_2O_3n	FeOn	MgOn	CaOn	K_2On	Na_2On	P_2O_5n	data[b]	setting[c]
A	10	50.6(1)[d]	2.65(3)	13.1(1)	14.1(3)	6.26(12)	10.0(1)	0.17(2)	2.93(5)	0.20(3)	3	EOSC
B	11	50.6(2)	2.41(8)	13.3(1)	13.4(2)	6.55(10)	10.6(1)	0.14(2)	2.85(5)	0.21(5)	1	EOSC
C	3	50.8(2)	2.34(6)	13.3(1)	13.2(1)	6.64(5)	10.7(1)	0.10(2)	2.82(14)	0.16(1)	2	EOSC
D	2	51.0(1)	2.28(1)	13.4(1)	12.7(1)	6.70(1)	10.7(1)	0.15(1)	2.87(4)	0.17(2)	2	EOSC
E	18	50.9(1)	2.07(3)	13.7(1)	12.3(1)	7.08(11)	11.1(1)	0.10(2)	2.68(4)	0.14(2)	3	EOSC
F	15	51.0(1)	2.06(3)	13.7(1)	12.3(1)	7.08(5)	11.1(1)	0.09(2)	2.69(4)	0.10(2)	2	EOSC
G	3	50.9(1)	1.98(2)	13.7(1)	12.0(1)	7.26(2)	11.0(1)	0.09(1)	2.91(4)	0.10(1)	2	EOSC
H	5	50.8(2)	2.08(2)	13.9(1)	11.6(1)	7.11(9)	11.2(1)	0.13(1)	2.97(8)	0.17(2)	3	both
I	8	50.7(1)	2.10(3)	14.3(1)	11.1(1)	6.96(6)	11.3(1)	0.21(1)	3.19(3)	0.20(1)	1	WOSC
J	8	50.9(1)	1.99(5)	14.5(2)	10.8(3)	7.15(20)	11.1(1)	0.22(1)	3.18(7)	0.14(1)	2	WOSC
K	9	50.9(2)	1.81(4)	14.0(1)	11.3(2)	7.49(15)	11.5(1)	0.10(2)	2.81(14)	0.08(2)	2	both
L	2	50.2(2)	2.26(18)	15.7(6)	9.91(55)	6.83(43)	10.5(1)	0.74(2)	3.59(6)	0.30(2)	2	WOSC
M	3	51.3(1)	1.58(2)	14.3(1)	10.3(1)	7.60(3)	11.8(1)	0.12(1)	2.99(2)	0.08(1)	3	WOSC
N	11	50.7(2)	1.59(4)	15.0(1)	9.62(14)	7.89(10)	12.0(1)	0.15(3)	2.98(11)	0.12(4)	3	both
O	3	50.2(1)	1.94(1)	15.3(1)	10.6(1)	7.90(1)	11.0(1)	0.20(1)	2.79(2)	0.12(2)	2	EOSC
P1	5	49.8(2)	1.24(2)	16.1(2)	9.04(7)	8.83(7)	12.3(1)	0.10(1)	2.66(2)	0.13(1)	1	EOSC
P2	2	50.7(1)	1.52(4)	15.2(1)	9.43(2)	8.11(4)	11.8(1)	0.16(1)	2.96(1)	0.12(5)	2	WOSC
P3	16	50.0(3)	1.53(6)	15.6(4)	9.45(25)	8.33(22)	11.9(1)	0.15(1)	2.85(12)	0.17(1)	1	WOSC
P4	1	50.0	1.48	16.2	8.79	8.39	11.7	0.21	3.02	0.09	2	WOSC
P5	1	50.8	1.31	15.5	8.79	8.42	12.3	0.19	2.65	0.06	2	WOSC
P6	1	49.9	1.26	16.0	9.08	8.85	12.0	0.11	2.79	0.02	2	EOSC
P7	1	49.7	1.20	16.5	8.75	9.23	11.8	0.10	2.69	0.04	2	EOSC
Q	1	48.9	2.17	14.0	13.7	6.67	11.3	0.16	3.17	0.22	1	EOSC
R	1	50.5	2.71	13.4	13.5	6.68	9.99	0.20	2.86	0.21	2	EOSC
S	1	51.1	2.12	13.7	12.3	7.14	11.0	0.12	3.02	0.15	2	EOSC
T	1	50.9	2.09	14.1	11.3	6.88	11.1	0.28	3.25	0.16	2	WOSC
U	1	51.3	1.58	14.1	10.9	7.99	11.7	0.12	2.27	0.07	2	EOSC
V	1	51.1	2.08	14.3	10.7	7.23	11.5	0.23	2.87	0.24	1	WOSC
W	1	51.1	1.98	14.3	11.2	7.05	11.2	0.19	3.10	0.21	1	WOSC
X	1	50.4	1.7115.0	15.0	10.3	7.77	11.8	0.16	3.08	0.19	1	WOSC
Y	1	50.7	2.40	13.4	13.6	6.64	10.5	0.12	2.86	0.21	1	EOSC
Z	1	50.8	2.64	13.3	13.2	6.39	10.6	0.18	2.87	0.24	1	EOSC

[a] number of samples included in group

[b] 1=analyses from Thompson et al., 1989; 2=analyses from Table 1, this study; 3=analyses from both sources

[c] EOSC = chemical group sampled on the eastern rift of the 11°45'N OSC, WOSC = sampled on the western rift, both = sampled on both rifts.

[d] parenthesized units represent 1 standard deviation of the chemical group population, in terms of least units cited, thus 50.6(1) should be read as 50.6+/-0.1.

Table 2-3 Starting compositions used in 1-atm. melting experiments

Composition	SiO_2	TiO_2	Al_2O_3	FeO	MgO	MnO	CaO	K_2O	Na_2O	P_2O_5	Total
67-032[a]	50.2	1.59	15.8	9.50	7.52	-	11.6	0.15	2.88	0.17	99.4
64-002[a]	50.2	1.50	16.1	9.21	7.91	-	11.9	0.12	2.68	0.16	99.8
61-002[a]	50.4	1.84	14.7	10.3	6.96	-	11.7	0.17	2.90	0.18	99.2
70-002[a]	50.2	1.26	16.0	9.04	8.24	-	12.5	0.10	2.50	0.13	100.0
70-002[b]	49.6(1)	1.20(2)	15.8(2)	8.98(7)	8.66(6)	0.17(3)	11.9(1)	0.10(1)	2.67(6)	0.12(4)	99.2
70-002[c]	50.1	1.22	15.9	9.07	8.74		12.0	0.10	2.70	0.12	100.0
70-002[d]	49.8	1.25	15.9	8.96	8.75		12.4	0.10	2.67	0.13	100.0
2004-3-1[d]	49.1(2)	1.19(2)	16.3(8)	8.65(9)	9.13(5)	0.09(5)	11.7(2)	0.10(1)	2.66(14)	0.04(2)	99.0

[a] determined with the Smithsonian electron microprobe

[b] average of 368 electron microprobe analyses collected with the MIT JEOL electron microprobe, numbers in parentheses represent 1 sigma deviation in terms of least units cited, thus 49.6(1) should be read as 49.6 +/- 0.1

[c] 70-002[b] normalized to 100%, excluding MnO

[d] 70-002[a], after the following correction factors were applied: SiO_2:0.9944; MgO: 1.0686; Na_2O: 1.076, and then renormalized to 100 %; these correction factors were determined by comparing analyses of the same set of 8 natural glass chips collected on each microprobe, and applying corrections for oxides that were 2 sigma or greater outside of electron microprobe counting statistics.

[d] as in b but average of 7 microprobe analyses

Table 2-4 Run conditions for melting experiments (see Table 3 for starting compositions and Table 5 for run product compositions)

Composition	Run #	T °C	log f_{O2}	Time (hrs)	Run products[a]	K_D[b] ol/lig FeMg	aug/liq FeMg	pl/liq CaNa	Phase proportions (wt. %)	ΣR^2[c]
2004-3-1	50	1223	-8.25	18.6	gl,pl,ol	0.26		0.81	97:2:1	0.77
	40	1213	-8.36	46.0	gl,pl,ol	0.27		0.75	84:12:4	0.70
	20	1188	-8.72	77.8	gl,pl,ol	0.27		0.91	70:22:8	1.04
	10	1170	-8.95	164.2	gl,pl,ol,aug	0.28	0.24	1.02	57:28:13:2	1.11
	60	1152	-9.39	170.2	gl,pl,ol,aug	0.28	0.23	1.18	34:40:14:13	0.94
	70	1134	-9.24	166	gl,pl,ol,aug	0.29	0.23	1.23	26:43:14:17	0.69
70-002	110	1160	-8.58	93.5	gl,pl,ol					
	120	1152	-9.02	93.5	gl,pl,ol,aug	0.29	0.25	0.96	48:31:9:12	0.18
	130	1140	-9.20	142.3	gl,pl,ol,aug	0.30	0.24	0.89	41:34:10:15	0.13
	140	1128	-9.38	165	gl,pl,ol,aug	0.29	0.25	1.17	25:42:11:22	0.11
67-037	100	1191	-8.52	114.3	gl,pl,ol					
	110	1171	-8.58	93.5	gl,pl,ol,aug	0.29	0.24	0.92	73:20:4:3	0.27
	130	1140	-9.20	142.3	gl,pl,ol,aug	0.27	0.30	1.13	48:32:7:13	0.05
	140	1128	-9.38	165	gl,pl,ol,aug	0.29	0.25	1.09	40:36:8:16	0.19
	150	1110	-9.76	269.8	gl,pl,ol,aug	0.29	0.22	1.00	29:42:9:19	0.51
64-002	100	1190	-8.71	94.5	gl,pl,ol					
	110	1160	-8.95	99.8	gl,pl,ol,aug	0.26	0.23	1.04	59:28:6:7	0.13
	140	1128	-9.40	166.3	gl,pl,ol,aug	0.29	0.22	1.08	40:36:8:16	0.19
	150	1110	-9.66	218.5	gl,pl,ol,aug	0.29	0.21	1.28	23:47:10:20	0.34
61-002	100	1190	-8.71	94.5	gl,pl,ol					
	110	1160	-8.95	99.8	gl,pl,ol,aug	0.26	0.26	1.06	80:14:4:2	0.05
	130	1140	-9.14	146.5	gl,pl,ol,aug	0.29	0.22	1.14	64:22:3:11	0.07
	140	1128	-9.38	165	gl,pl,ol,aug	0.30	0.21	1.13	48:30:5:15	0.92
	150	1110	-9.66	218.5	gl,pl,ol,aug	0.30	0.21	1.30	35:36:6:22	0.13

[a] gl=glass,pl=plagioclase,ol=olivine,aug=augite

[b] liq = glass, $K_D^{xtl/liq} = (FeO^{xtl}MgO^{liq}/FeO^{liq}MgO^{xtl})$, $(Na_2O^{xtl}CaO^{liq}/Na_2O^{liq}CaO^{xtl})$

[c] sum of the residuals squared for an unweighted least squares fit of the run product compositions to the starting composition

Table 2-5 Run product compositions for melting experiments on EPR compositions (see Table 4 for run conditions)

Run	Phase[a]	# of anals	SiO_2	TiO_2	Al_2O_3	FeO	MgO	MnO	CaO	K_2O	Na_2O	P_2O_5	Total
2004-	gl	7	49.7(1)[b]	1.18(2)	16.4(1)	8.78(12)	9.00(10)	0.15(2)	11.8(2)	0.10(1)	2.53(10)	0.04(1)	99.7
3-1-50	pl	3	49.6(6)	-[c]	31.8(6)	0.55(5)	0.30(6)	-	15.5(2)	0.02(1)	2.68(11)	-	100.4
	ol	3	50.5(3)	0.0[d]	0.09(2)	12.3(2)	46.9(5)	0.10(1)	0.50(1)	-	-	-	100.3
2004-	gl	7	50.2(2)	1.38(6)	15.4(2)	9.46(10)	8.35(7)	0.14(4)	12.0(1)	0.11(2)	2.63(11)	0.04(1)	99.7
3-1-40	pl	4	49.3(1)	-	31.7(1)	0.65(4)	0.30(7)	-	15.7(1)	0.02(1)	2.59(6)	-	100.3
	ol	3	39.9(4)	0.0	0.12(4)	14.1(2)	45.8(2)	0.17(1)	0.47(2)	-	-	-	100.6
2004-	gl	6	50.2(3)	1.58(4)	14.2(9)	9.84(13)	7.71(12)	0.19(7)	12.3(1)	0.14(1)	2.64(21)	0.04(1)	98.8
3-1-20	pl	4	50.3(9)	-	29.8(11)	0.95(22)	0.54(24)	-	14.9(4)	0.03(1)	2.91(21)	-	99.4
	ol	3	39.7(4)	0.03(1)	0.12(3)	15.3(1)	43.9(2)	0.28(1)	0.50(1)	-	-	-	99.7
2004-	gl	6	50.8(3)	2.17(10)	13.5(2)	11.0(1)	7.08(7)	0.27(2)	11.5(1)	0.17(2)	2.52(2)	0.11(5)	99.2
3-1-10	pl	4	50.7(4)	-	29.9(4)	0.71(11)	0.40(10)	-	14.4(2)	0.04(1)	3.23(8)	-	99.4
	ol	4	39.6(5)	0.05(1)	0.08(2)	18.1(6)	42.1(5)	0.31(3)	0.46(3)	-	-	-	100.7
	aug	8	51.5(1.1)	0.72(21)	2.92(78)	6.36(88)	16.7(6)	0.16(4)	20.8(2)	-	0.21(6)	-	99.3
2004-	gl	10	50.4(4)	3.33(20)	12.5(2)	12.9(3)	6.22(13)	0.22(3)	10.4(2)	0.25(1)	2.51(9)	0.48(6)	99.4
3-1-60	pl	3	52.3(5)	-	29.5(4)	0.75(4)	0.36(18)	-	13.5(3)	0.03(2)	3.83(17)	-	100.3
	ol	4	38.8(1)	0.07(4)	0.06(4)	22.8(2)	38.7(2)	0.36(3)	0.41(3)	-	-	-	101.2
	aug	13	51.8(4)	0.94(14)	2.46(57)	7.94(36)	16.4(5)	0.12(4)	19.8(3)	-	0.26(6)	-	99.7
2004-	gl	10	50.0(7)	4.14(44)	12.1(5)	13.4(7)	5.75(3)	0.23(3)	10.0(2)	0.28(3)	2.55(12)	0.54(5)	99.0
3-1-70	pl	3	52.3(5)	-	29.1(1)	0.78(8)	0.30(5)	-	13.4(3)	0.02(2)	3.88(22)	-	99.8
	ol	5	38.5(4)	0.10(1)	0.06(5)	24.9(12)	36.9(9)	0.38(1)	0.45(2)	-	-	-	101.3
	aug	7	51.3(7)	1.28(29)	2.86(72)	8.89(81)	16.3(6)	0.18(6)	18.8(11)	-	0.32(13)	-	99.9
70-002	gl	9	50.1(4)	2.52(13)	13.4(1)	11.9(1)	6.30(6)	0.16(3)	10.8(1)	0.38(2)	3.31(9)	0.19(3)	99.1
120	pl	6	52.5(8)	-	29.2(6)	0.86(11)	0.32(5)	-	13.2(6)	0.11(3)	3.90(33)	-	100.1
	ol	6	38.9(3)	0.04(3)	0.38(26)	20.8(1)	39.9(3)	0.35(2)	0.53(6)	-	-	-	100.9
	aug	10	51.7(1.1)	1.10(49)	2.84(82)	7.29(1.4)	15.7(1.2)	0.13(4)	20.6(4)	-	0.28(7)	-	99.6

Table 2-5 (cont.)

Run	Phase[a]	# of anals	SiO_2	TiO_2	Al_2O_3	FeO	MgO	MnO	CaO	K_2O	Na_2O	P_2O_5	Total
70-002	gl	9	50.3(8)	2.80(3)	13.2(3)	12.2(6)	5.90(15)	0.28(11)	10.3(3)	0.45(4)	3.25(21)	0.25(7)	98.9
130	pl	5	51.9(9)	-	29.4(2)	0.70(10)	0.27(4)	-	13.4(3)	0.10(1)	3.75(7)	-	99.5
	ol	5	38.5(2)	0.00[d]	0.19(4)	23.4(3)	38.0(2)	0.37(1)	0.29(17)	-	-	-	100.8
	aug	8	52.1(2)	0.96(13)	2.48(3)	8.06(29)	16.3(4)	0.21(7)	19.5(4)	-	0.21(4)	-	99.8
70-002	gl	8	49.2(3)	4.17(26)	12.0(2)	14.3(3)	5.51(13)	0.30(5)	9.90(16)	0.32(6)	2.68(21)	0.37(5)	98.7
140	pl	3	53.2(3)	-	28.9(1)	0.73(9)	0.22(3)	-	12.8(2)	0.13(1)	4.07(22)	-	100.1
	ol	5	37.4(2)	0.03(3)	0.21(5)	26.4(3)	35.5(2)	0.41(2)	0.42(2)	-	-	-	100.4
	aug	4	51.0(1.5)	1.27(27)	3.14(11)	9.70(1.4)	15.2(1.2)	0.24(5)	18.0(6)	-	0.31(8)	-	98.9
67-032	gl	8	50.4(6)	2.10(21)	13.5(2)	11.7(3)	7.05(18)	0.22(4)	11.5(3)	0.17(3)	2.66(21)	0.26(6)	99.6
110	pl	4	50.9(3)	-	30.2(6)	0.75(22)	0.34(16)	-	14.6(3)	0.08(1)	3.11(15)	-	100.0
	ol	5	38.8(3)	0.00	0.21(10)	19.6(4)	41.2(4)	0.29(4)	0.39(6)	-	-	-	100.5
	aug	7	52.5(1)	0.74(25)	2.47(61)	6.59(70)	16.9(4)	0.17(5)	19.9(3)	-	0.21(5)	-	99.5
67-032	gl	7	50.4(5)	2.62(11)	13.0(2)	13.0(2)	5.85(17)	0.27(4)	10.4(2)	0.29(5)	3.16(18)	0.23(5)	99.2
130	pl	4	53.7(7)	-	28.3(4)	0.88(10)	0.31(6)	-	12.4(4)	0.15(1)	4.26(23)	-	100.0
	ol	5	38.1(2)	0.00	0.22(7)	22.8(3)	38.0(5)	0.39(4)	0.50(7)	-	-	-	100.0
	aug	9	49.5(2.2)	1.74(77)	3.91(1.47)	9.43(1.37)	13.9(1.9)	0.23(8)	20.2(4)	-	0.37(10)	-	99.3
67-032	gl	7	49.8(6)	3.56(14)	12.6(1)	13.4(2)	5.31(9)	0.31(7)	9.70(16)	0.57(8)	3.38(13)	0.34(7)	99.0
140	pl	3	53.8(1)	-	28.4(2)	0.63(2)	0.18(1)	-	12.0(2)	0.18(0)	4.54(1)	-	99.7
	ol	5	37.8(2)	0.08(5)	0.22(5)	25.8(4)	35.6(2)	0.43(1)	0.52(14)	-	-	-	100.5
	aug	10	50.6(1.7)	1.42(46)	3.16(1.20)	9.47(1.42)	14.8(1.4)	0.22(5)	19.9(9)	-	0.31(6)	-	99.9
67-032	gl	9	49.8(4)	4.92(9)	11.7(2)	14.2(3)	4.70(3)	0.21(3)	8.88(17)	0.68(5)	3.32(13)	0.45(9)	98.9
150	pl	3	53.7(3)	-	27.9(5)	0.97(4)	0.66(60)	-	11.8(3)	0.17(1)	4.42(8)	-	99.6
	ol	5	37.1(2)	0.08(6)	0.21(7)	29.0(2)	33.3(3)	0.45(5)	0.45(14)	-	-	-	100.6
	aug	8	51.2(6)	1.50(15)	2.28(38)	10.2(5)	15.6(5)	0.24(2)	18.1(6)	-	0.23(3)	-	99.4

Table 2-5 (cont.)

Run	Phase[a]	# of anals	SiO_2	TiO_2	Al_2O_3	FeO	MgO	MnO	CaO	K_2O	Na_2O	P_2O_5	Total
64-002	gl	8	50.2(2)	2.30(29)	13.4(2)	11.9(5)	6.76(27)	0.22(6)	11.2(3)	0.22(2)	3.03(18)	0.26(4)	99.5
110	pl	4	52.8(7)	-	28.3(5)	1.14(14)	0.53(7)	-	13.3(5)	0.10(1)	3.74(27)	-	99.9
	ol	5	38.9(2)	0.00	0.21(8)	19.1(4)	41.4(2)	0.31(3)	0.45(3)	-	-	-	100.4
	aug	17	51.8(8)	0.76(21)	2.83(66)	6.70(91)	16.6(7)	0.15(6)	20.1(5)	-	0.27(11)	-	99.2
64-002	gl	11	49.3(2)	3.92(7)	11.8(1)	14.0(1)	5.43(4)	0.28(1)	9.59(12)	0.35(1)	2.93(7)	0.36(1)	97.9
140	pl	4	53.3(2)	-	28.5(4)	0.80(20)	0.25(9)	-	12.6(2)	0.14(1)	4.14(7)	-	99.7
	ol	5	37.3(1)	0.06(4)	0.18(8)	26.6(3)	35.3(2)	0.41(5)	0.41(4)	-	-	-	100.3
	aug	4	51.5(1.1)	1.17(25)	2.57(63)	9.16(69)	15.9(6)	0.18(5)	18.9(2)	-	0.25(5)	-	99.6
64-002	gl	7	48.4(5)	5.28(18)	11.2(2)	15.4(4)	4.99(3)	0.23(4)	9.40(4)	0.43(3)	2.76(13)	0.49(7)	98.6
150	pl	4	54.1(6)	-	27.8(1.0)	0.85(22)	0.47(41)	-	12.0(3)	0.17(2)	4.50(7)	-	99.9
	ol	5	36.8(3)	0.05(7)	0.20(4)	29.2(2)	33.2(2)	0.46(3)	0.44(1)	-	-	-	100.5
	aug	9	51.4(3)	1.36(10)	2.05(23)	9.92(24)	15.6(2)	0.19(6)	18.4(4)	-	0.26(4)	-	99.2
61-002	gl	8	50.4(6)	2.27(18)	13.3(4)	11.9(6)	6.71(35)	0.23(7)	11.2(2)	0.19(3)	2.73(21)	0.26(8)	99.2
110	pl	3	52.1(3)	-	28.4(5)	1.12(18)	0.56(10)	-	13.7(3)	0.10(1)	3.53(17)	-	99.5
	ol	5	38.7(3)	0.00	0.17(4)	19.2(3)	41.2(5)	0.26(8)	0.44(3)	-	-	-	100.0
	aug	8	52.3(5)	0.72(5)	2.50(29)	6.40(43)	17.0(1)	0.15(5)	20.2(3)	-	0.24(4)	-	99.5
61-002	gl	7	50.0(7)	2.98(48)	12.8(4)	13.1(5)	6.06(16)	0.28(6)	10.5(34)	0.31(3)	2.91(15)	0.26(4)	99.2
130	pl	4	53.3(6)	-	28.7(7)	0.87(31)	0.29(14)	-	12.9(2)	0.12(0)	4.09(14)	-	100.3
	ol	5	38.3(3)	0.00	0.20(6)	23.8(3)	37.9(3)	0.35(3)	0.45(4)	-	-	-	101.0
	aug	8	52.6(8)	0.81(9)	2.29(44)	7.86(34)	16.8(3)	0.24(2)	19.2(4)	-	0.22(3)	-	100.0
61-002	gl	7	49.8(4)	3.33(31)	12.2(3)	14.3(4)	5.29(23)	0.25(6)	9.73(40)	0.37(4)	3.08(21)	0.32(6)	98.7
140	pl	4	54.8(4)	-	28.2(8)	0.94(31)	0.24(13)	-	12.2(2)	0.13(1)	4.38(14)	-	100.9
	ol	5	37.4(2)	0.10(5)	0.28(8)	27.5(4)	34.3(4)	0.44(2)	0.49(7)	-	-	-	100.5
	aug	5	52.1(4)	0.94(7)	2.17(37)	8.91(27)	15.9(2)	0.18(2)	18.4(3)	-	0.27(2)	-	98.9

Table 2-5 (cont.)

Run	Phase[a]	# of anals	SiO_2	TiO_2	Al_2O_3	FeO	MgO	MnO	CaO	K_2O	Na_2O	P_2O_5	Total
61-002	gl	8	49.2(2)	4.33(12)	11.4(1)	15.8(2)	4.74(3)	0.26(4)	9.16(10)	0.43(1)	3.02(11)	0.44(4)	98.8
150	pl	3	55.0(2)	-	27.9(2)	0.78(5)	0.16(2)	-	11.3(1)	0.17(1)	4.85(8)	-	100.2
	ol	5	36.7(4)	0.16(6)	0.24(6)	31.3(3)	31.5(4)	0.47(5)	0.45(1)	-	-	-	100.8
	aug	20	50.8(1.0)	1.43(3)	2.69(94)	10.5(1.0)	14.7(9)	0.24(5)	18.7(7)	-	0.30(7)	-	99.4

[a] Abbreviations as in Table 4
[b] Parenthesized units represent 1 sigma of the sample of replicate analyses in terms of least units cited. Thus, 49.7(1) should be read as 49.7 +/- 0.1
[c] Element not analyzed
[d] Element below detection limit

Table 2-6 Crystallizing proportions along the olivine - plagioclase - augite - liquid boundary estimated[a] from experiments reported in Tables 5 and 6.

High T Expt	Low T Expt	ΔT (°)	est. liq wt. frac.	Proportions[b] oliv	plag	aug	ΣR^{2} [c]
70-120	70-130	12	0.92	0.12	0.50	0.38	0.10
"	70-140	24	0.71	0.09	0.56	0.35	1.01
70-130	70-140	12	0.78	0.09	0.61	0.30	1.13
avg (3) for	70-002			0.10(4)	0.56(7)	0.35(1)	
67-110	67-130	31	0.75	0.12	0.44	0.44	0.10
"	67-140	43	0.65	0.11	0.46	0.43	0.59
"	67-150	61	0.51	0.12	0.50	0.38	1.52
67-130	67-140	12	0.88	0.13	0.48	0.40	0.52
"	67-150	30	0.71	0.13	0.54	0.33	1.87
67-140	67-150	18	0.83	0.14	0.58	0.28	0.67
avg (6) for	67-037			0.13(1)	0.50(5)	0.38(6)	
64-110	64-140	32	0.72	0.11	0.54	0.36	0.41
"	64-150	50	0.54	0.11	0.55	0.34	0.92
64-140	64-150	18	0.81	0.12	0.58	0.30	0.65
avg (3) for	64-002			0.11(1)	0.56(3)	0.33(3)	
61-110	61-130	20	0.83	0.08	0.51	0.41	0.09
"	61-140	32	0.66	0.10	0.53	0.37	0.32
"	61-150	50	0.51	0.10	0.51	0.39	0.09
61-130	61-140	12	0.58	0.27	0.44	0.29	1.21
"	61-150	20	0.66	0.10	0.52	0.38	0.02
61-140	61-150	18	0.82	0.10	0.56	0.34	0.16
avg (6) for	61-002			0.13(7)	0.52(4)	0.36(5)	
AVERAGE OVER ALL ESTIMATES				0.12(4)	0.53(5)	0.35(5)	

[a] proportions estimated by solving for the coefficients a,b,c,d in the equation: 1 High T liq = a Low T liq + b Low T oliv + c Low T plag + d Low T aug, using unweighted least squares. Thus the reported 'est. liq wt. fraction = a. High T and Low T experiments were selected from down temperature sequences of experiments on the same composition

[b] crystalline phase proportions, (wt. fraction) (b,c,d) normalized to 1

[c] sum of the residuals squared for the unweighted least squares estimation described in note [a]

Table 2-7 Mixing models for chemical groups sampled from the 11°45'N OSC

	Σr^{2a}	SiO_2n	TiO_2n	Al_2O_3n	FeOn	MgOn	CaOn	K_2On	Na_2On	P_2O_5n	setting[c]
Group H		50.8(2)[b]	2.08(2)	13.9(1)	11.6(1)	7.11(9)	11.2(1)	0.13(1)	2.97(8)	0.17(2)	both
model	0.19	50.7	2.11	14.3	11.6	7.06	11.2	0.22	3.00	0.19	
		mixing components: 39% P1 + 61% 62-037-130 liquid									
Group I		50.7(1)	2.10(3)	14.3(1)	11.1(1)	6.96(6)	11.3(1)	0.21(1)	3.19(3)	0.20(1)	WOSC
model	0.16	50.5	2.12	14.2	11.2	7.21	11.4	0.22	3.05	0.22	
		mixing components: 25% P4 + 75% 64-002-110 liquid									
Group J		50.9(1)	1.99(5)	14.5(2)	10.8(3)	7.15(20)	11.1(1)	0.22(1)	3.18(7)	0.14(1)	WOSC
model	0.14	50.7	2.06	14.8	10.9	7.22	11.1	0.25	3.12	0.16	
		mixing components: 52% P4 + 48% 62-037-110 liquid									
Group K		50.9(2)	1.81(4)	14.0(1)	11.3(2)	7.49(15)	11.5(1)	0.10(2)	2.81(14)	0.08(2)	both
model	0.24	50.7	1.97	14.2	11.1	7.42	11.6	0.18	2.77	0.22	
		mixing components: 23% P4 + 77% 62-037-110 liquid									
Group M		51.3(1)	1.58(2)	14.3(1)	10.3(1)	7.60(3)	11.8(1)	0.12(1)	2.99(2)	0.08(1)	WOSC
model	0.38	51.1	1.75	14.7	10.0	7.82	11.8	0.16	2.83	0.12	
		mixing components: 66% P2 + 34% 200431-10 liquid									
Group P2		50.7(1)	1.52(4)	15.2(1)	9.43(2)	8.11(4)	11.8(1)	0.16(1)	2.96(1)	0.12(5)	WOSC
model	0.28	50.5	1.57	15.3	9.77	8.32	11.9	0.13	2.72	0.05	
		mixing components: 68% P6 + 32% 200431-10 liquid									
Group P3		50.0(3)	1.53(6)	15.6(4)	9.45(25)	8.33(22)	11.9(1)	0.15(1)	2.85(12)	0.17(1)	WOSC
model	0.11	51.1	1.48	15.4	9.54	8.41	11.9	0.12	2.72	0.04	
		mixing components: 75% P6 + 25% 200431-10 liquid									
Group T		50.9	2.09	14.1	11.3	6.88	11.1	0.28	3.25	0.16	WOSC
model	0.04	50.9	2.12	14.1	11.4	6.95	11.1	0.23	3.09	0.18	
		mixing components: 47% P2 + 53% 67-037-130 liquid									
Group V		51.1	2.08	14.3	10.7	7.23	11.5	0.23	2.87	0.24	WOSC
model	0.19	51.0	1.99	14.2	11.1	7.34	11.5	0.18	2.85	0.21	
		mixing components: 47% P2 + 53% 61-002-110 liquid									
Group W		51.1	1.98	14.3	11.2	7.05	11.2	0.19	3.10	0.21	WOSC
model	0.25	50.9	2.08	14.4	10.9	7.21	11.4	0.28	3.18	0.16	
		mixing components: 47% P2 + 53% 70-002-120 liquid									
Group X		50.4	1.71	15.0	10.3	7.77	11.8	0.16	3.08	0.18	WOSC
model	0.11	50.4	1.74	15.0	10.3	7.93	11.8	0.16	2.80	0.20	
		mixing components: 66% P3 + 34% 67-037-110 liquid									
Group O		50.2(1)	1.94(1)	15.3(1)	10.6(1)	7.90(1)	11.0(1)	0.20(1)	2.79(2)	0.12(2)	EOSC
model	0.18	49.9	2.03	15.3	10.6	8.12	11.2	0.19	2.80	0.15	
		mixing components: 39% P1 + 61% 61-002-150 liquid									

[a] Σr^2 = sum of the residuals squared for the weighted least squares mass balance calculation models
[b] parenthesized units represent 1 standard deviation of the chemical group population, in terms of least units cited, thus 50.8(2) should be read as 50.8+/-0.2.

Table 2-8 Fractionation models for chemical groups sampled from the 11°45'N OSC

	SiO_2n	TiO_2n	Al_2O_3n	FeOn	MgOn	CaOn	K_2On	Na_2On	P_2O_5n	phase prop[a] oliv - aug - plag	%Δmass[b]	P (kbar) inferred[c]
Lava S	51.1	2.12	13.7	12.3	7.14	11.0	0.12	3.02	0.15			
	50.4	1.44	15.6	9.33	8.54	11.9	0.08	2.66	0.10	-0.12-0.33-0.55	+36	~2
model 1	**49.9**	**1.26**	**16.5**	**8.65**	**9.23**	**11.8**	**0.07**	**2.57**	**0.08**	-0.30- -0.70	+44	
Lava P7	**49.7**	**1.20**	**16.5**	**8.75**	**9.23**	**11.8**	**0.10**	**2.69**	**0.04**			
Group A	50.6	2.65	13.1	14.1	6.26	10.0	0.17	2.93	0.20			
	50.1	1.50	15.7	9.52	8.71	11.8	0.09	2.46	0.10	-0.12-0.35-0.53	+49	~3
model 2	**49.7**	**1.35**	**16.4**	**9.02**	**9.19**	**11.7**	**0.08**	**2.41**	**0.09**	-0.30- -0.70	+54	
Lava P7	**49.7**	**1.20**	**16.5**	**8.75**	**9.23**	**11.8**	**0.10**	**2.69**	**0.04**			
Group B	50.6	2.41	13.3	13.4	6.55	10.6	0.14	2.85	0.21			
	50.1	1.49	15.6	9.56	8.59	12.1	0.08	2.44	0.12	-0.12-0.35-0.53	+43	~2
model 3	**49.6**	**1.29**	**16.6**	**8.88**	**9.26**	**11.9**	**0.07**	**2.36**	**0.11**	-0.30- -0.70	+51	
Lava P7	**49.7**	**1.20**	**16.5**	**8.75**	**9.23**	**11.8**	**0.10**	**2.69**	**0.04**			
Group D	51.0	2.28	13.4	12.7	6.70	10.7	0.15	2.87	0.17			
	50.4	1.49	15.5	9.42	8.55	12.0	0.09	2.49	0.10	-0.12-0.35-0.53	+40	~2
model 4	**49.9**	**1.29**	**16.4**	**8.74**	**9.23**	**11.8**	**0.08**	**2.41**	**0.09**	-0.30- -0.70	+52	
Lava P7	**49.7**	**1.20**	**16.5**	**8.75**	**9.23**	**11.8**	**0.10**	**2.69**	**0.04**			
Group E	50.9	2.07	13.7	12.3	7.08	11.1	0.10	2.68	0.14			
	50.3	1.42	15.7	9.38	8.52	12.2	0.07	2.39	0.09	-0.12-0.35-0.53	+36	~2
model 5	**49.7**	**1.24**	**16.6**	**8.70**	**9.21**	**12.0**	**0.06**	**2.31**	**0.08**	-0.30- -0.70	+44	
Lava P7	**49.7**	**1.20**	**16.5**	**8.75**	**9.23**	**11.8**	**0.10**	**2.69**	**0.04**			
Group H	50.8	2.08	13.9	11.6	7.11	11.2	0.13	2.97	0.17			
	50.4	1.50	15.6	9.25	8.51	11.9	0.09	2.68	0.12	-0.14-0.31-0.55	+32	~1
model 6	**49.9**	**1.30**	**16.5**	**8.58**	**9.21**	**11.8**	**0.08**	**2.59**	**0.10**	-0.30- -0.70	+41	
Lava P7	**49.7**	**1.20**	**16.5**	**8.75**	**9.23**	**11.8**	**0.10**	**2.69**	**0.04**			
Group K	50.9	1.81	14.0	11.3	7.49	11.5	0.10	2.81	0.08			
	50.5	1.43	15.3	9.51	8.41	12.1	0.08	2.60	0.06	-0.12-0.33-0.55	+25	~1
model 7	**49.9**	**1.22**	**16.4**	**8.73**	**9.20**	**11.9**	**0.07**	**2.50**	**0.05**	-0.30- -0.70	+36	
Lava P7	**49.7**	**1.20**	**16.5**	**8.75**	**9.23**	**11.8**	**0.10**	**2.69**	**0.04**			

Table 2-8 (cont.)

	SiO_2n	TiO_2n	Al_2O_3n	FeOn	MgOn	CaOn	K_2On	Na_2On	P_2O_5n	phase prop[a] oliv - aug - plag	%Δmass[b] inferred[c]	P (kbar)
Lava P7	49.7	1.20	16.5	8.75	9.23	11.8	0.10	2.69	0.04			
model 8	**49.9**	**1.30**	**16.0**	**9.15**	**8.83**	**11.9**	**0.11**	**2.75**	**0.04**	0.30 - 0.70	-8	~0.001
Lava P6	**49.9**	**1.26**	**16.0**	**9.08**	**8.85**	**12.0**	**0.11**	**2.79**	**0.02**			
Lava P3	50.3	1.53	15.6	9.45	8.33	11.9	0.15	2.85	0.17			
model 9	**50.4**	**1.65**	**15.0**	**9.83**	**7.87**	**12.0**	**0.16**	**2.90**	**0.18**	0.70 - 0.30	-8	~0.001
Group N	**50.7**	**1.59**	**15.0**	**9.62**	**7.89**	**12.0**	**0.15**	**2.98**	**0.12**			
Group E	50.9	2.07	13.7	12.3	7.08	11.1	0.10	2.68	0.14			
model 10	**51.0**	**2.30**	**13.1**	**13.2**	**6.60**	**10.7**	**0.11**	**2.77**	**0.16**	0.12 0.35 0.53	-11	~2
Group C	**50.8**	**2.34**	**13.3**	**13.2**	**6.64**	**10.7**	**0.10**	**2.82**	**0.16**			
Lava S	51.1	2.12	13.7	12.3	7.14	11.0	0.12	3.02	0.15			
model 11	**50.7**	**1.99**	**13.9**	**11.8**	**7.30**	**11.0**	**0.11**	**2.95**	**0.14**	-0.12 -0.33 -0.55	-6	~2
Group G	**50.9**	**1.98**	**13.7**	**12.0**	**7.26**	**11.0**	**0.09**	**2.91**	**0.10**			

[a] phase proportions being subtracted or added in the model (wt.%). The fractionation calculation uses weight units and removes variable proportions of olivine, augite and plagioclase in increments of 0.02; Fe-Mg $K_d^{oliv} = 0.29$, Fe-Mg $K_d^{augite} = 0.23$; Ca-Na $K_d^{plag} = 0.9$ for assemblages of olivine + plagioclase and 1.1 for assemblages of olivine + plagioclase + augite. Augite compositions for 2 - 3 kbar fractionation models were estimated from experiments at 1 atm., 2 kbar and 8 kbar (see Grove et al., 1991)

[b] change in mass of system for step, for example in fractionation model for Group A lavas, the first step involves addition of 33 increments of 2% of the assemblage 0.12 olivine + 0.35 augite + 0.53 plagioclase, which is equivalent to adding 49 % to the changing model magma ($= 100*(1.0 - (0.98)^{33})$).

[c] see text for discussion

Table 2-9 Comparison of values of tectonic variables and resulting geochemical effects for the 11°45'N OSC and other nearby OSCs and migrating ridge-offset intersections

Location	Half Spreading Rate (cm/yr)	'Hot Spot' Influence?	Propagating?	Migration Rate (mm/yr)	Transform Length (km)	Geochemical Signature
95°W GSC	2.1-3.6	no	yes	37	~ 30	LS = < 100 km MS = ~ 3.5 XS = ~ 20 km
85°W GSC	2.1-3.6	no	stopped ~ 2 m.y. ago	60 - 90	~ 80	LS = ~ 200 km MS = ~ 5 XS = 0 km
93°W GSC	2.1-3.6	yes	Yes	?	~ 10	none
Blanco JdF	~ 3	no	stopped ~ 2 m.y. ago	24 - 30	~ 250	LS = < 75 MS = ~ 3 XS = 0 km
COBB JdF	~ 3	no	yes	60 - 80	~ 30	LS = ~ 200 MS = ~ 2.5 XS = 50 km
12°37'N EPR	~ 5-6	no	?	no evidence for migration in magnetics	< 3	none
12°54'N EPR	~ 5-6	no	? WOSC prop. S	no evidence for migration in magnetics	1.6	none
11°45'N EPR	~ 5-6	no	no	~ 75 N < 30 S >145 S	~ 8	LS = 60 km MS = 2.3 XS = 15 km
9° N EPR	~ 5-6	no	? EOSC prop. S	45 - 55	~ 8	LS = < 20 km MS = 1.9 XS = 0 km (?)

GSC = Galapogos Spreading Center, JDF = Jaun de Fuca Spreading Center, EPR = East Pacific Rise.

TABLE NOTES: 'Hot Spot' influence? refers to whether or not the major element chemistry reflects a significant hot spot signature; Propagating? to whether or not the either rift tip of the MROT is currently propagating through the oceanic crust; Migration Rate to the average migration rate of the rift tips relative to the underlying mantle (hot spot reference) over the past 2 m.y., except for the 11°45'N OSC, in this case the migration rate is 75 mm/yr to the north, followed by < 30 mm/yr to the south for 0.7 to 0.2 m.y.b.p., followed by >145 mm/yr to the S for 0.2 m.y. to present; Transform Length to the length of the offset that truncates the rift; Geochemical Signature is defined in terms of FeO*/MgO in lavas sampled in area, LS = length of ridge segment behind offset over which the geochemical signature of the offset is observed, MS = maximum value of geochemical signature, if MS < 1.75, then no geochemical analomy is observed, XS = distance behind offset of MS. (Data for GSC and JdF estimated from Sinton et al., 1983; Hey, 1977; Karston et al., 1991; Data for 11°45'N EPR from Perram and Macdonald, 1991; Thompson et al., 1989; Langmuir et al., 1986; this study; Data for 12°54'N from Hekinian et al., 1985, Antrim et al., 1988; Data for 9°N from Natland et al., 1986; Smithsonian Institution Volcanic Glass File).